Long-term analysis of the global water vapour distribution based on satellite measurements

Dissertation submitted
for the award of the title
“Doctor
of the Natural Sciences”
to the Faculty of Physics, Mathematics, and Computer Science
of Johannes Gutenberg University
in Mainz

Christian Borger
born in Karlsruhe

Mainz, 5 December 2022

MAX PLANCK INSTITUTE FOR CHEMISTRY
JOHANNES GUTENBERG UNIVERSITY MAINZ

1. Referee:	[redacted]
2. Referee:	[redacted]
Supervisor:	[redacted]
Oral examination:	14 April 2023

Abstract

Water vapour is one of the most important trace gases in the Earth's atmosphere and plays a key role in atmospheric processes from a few micrometres up to climate-relevant scales. In this work, the long-term changes (2005-2020) of the global water vapour distribution were investigated using satellite measurements.

To this end, first a retrieval algorithm was developed to determine the total vertical column of water vapour (TCWV) in the visible blue spectral range. This spectral range is particularly well suited for TCWV retrievals, as it provides a similar sensitivity over land and ocean surfaces. The retrieval is based on measurements of the novel satellite instrument TROPOMI, which combines an unprecedented signal-to-noise ratio with a high spatial resolution and a daily global coverage. In the new retrieval, for the first time an iterative scheme was implemented, which finds an optimal a priori profile shape of water vapour. Furthermore, an optimised surface albedo was developed. The novel, iterative approach provides reliable results even under high cloud cover and thus also enables the investigation of atmospheric water vapour phenomena (e.g. atmospheric rivers) on a fine spatial scale. Moreover, comparisons with microwave satellites, reanalyses models and GPS measurements show an excellent agreement.

This new retrieval was then modified such that it could be applied to the long-term measurement series of the OMI instrument (2005-2020). From these retrieval results the MPIC OMI TCWV climate data record (CDR) was generated. This CDR is unique as it is solely based on one instrument so that cross-calibrations between different sensors are not necessary, but it still provides a global coverage with an almost homogeneous and high surface sensitivity. An extensive validation study with various reference data sets demonstrates a very good agreement over ocean, but also a systematic overestimation over land surfaces. Nevertheless, the CDR proves to be highly temporally stable and is therefore predestined for climate studies.

The trend analyses based on the MPIC OMI TCWV CDR revealed on average a global TCWV increase, with almost all local, statistically significant trends being positive. It was shown that the assumption of temporally constant relative humidity is not always fulfilled even over ocean and that indirectly determined precipitation trends do not correspond to the "dry-gets-drier, wet-gets-wetter" paradigm. Furthermore, an increase in the water vapour residence time was found, implying a slow down of the atmospheric branch of the hydrological cycle.

In addition, the CDR has been used to investigate changes in the (global) meridional circulation which revealed a poleward expansion of the southern tropical width across the entire Pacific Ocean.

Zusammenfassung

Wasserdampf ist eines der wichtigsten Spurengase in der Erdatmosphäre und spielt eine Schlüsselrolle bei atmosphärischen Prozessen von wenigen Mikrometern bis hin zu klimarelevanten Skalen. Das Ziel dieser Arbeit war, die langfristigen Veränderungen (2005-2020) der globalen Wasserdampf-Verteilung anhand von Satellitenmessungen zu untersuchen.

Zu diesem Zweck wurde zunächst ein Auswerte-Algorithmus entwickelt, um die vertikal integrierte Wasserdampfsäule (engl. total column water vapour, TCWV) im sichtbaren blauen Spektralbereich zu bestimmen. Dieser Spektralbereich ist besonders gut für solche Retrievals geeignet, da er beispielsweise eine ähnliche Empfindlichkeit über Land- und Meeresoberflächen vorweist. Für die Entwicklung des Retrievals wurden die Messungen des neuen Satelliteninstruments TROPOMI verwendet, welches ein noch nie dagewesenes Signal-zu-Rausch-Verhältnis mit einer hohen räumlichen Auflösung und einer täglichen globalen Abdeckung kombiniert. Bei dem neuen Retrieval wurde zum ersten Mal eine iterative Methode implementiert, die eine optimale a priori Profilform des Wasserdampfs findet. Darüber hinaus wurde eine neue, optimierte Oberflächenalbedo erstellt. Der neuartige, iterative Ansatz liefert selbst bei hohen Bewölkungsgraden zuverlässige Ergebnisse und ermöglicht somit auch die Untersuchung von atmosphärischen Wasserdampfphänomenen (z.B. atmosphärische Flüsse) auf einer kleinsträumlichen Skala. Außerdem zeigen Vergleiche mit Mikrowellensatelliten, Reanalysen-Modellen und GPS-Messungen eine hervorragende Übereinstimmung.

Der Algorithmus wurde dann so modifiziert, dass er auf die Langzeitmessreihen des OMI-Instruments (2005-2020) angewendet werden konnte. Aus den Ergebnissen dieser Auswertung wurde der MPIC OMI TCWV Klimadatensatz (CDR) erstellt. Dieser CDR ist ein einzigartiger TCWV-Datensatz, da er nur auf einem einzigen Instrument basiert, sodass keine Kreuzkalibrierungen zwischen verschiedenen Satellitensensoren erforderlich sind. Dennoch bietet er eine globale Abdeckung mit einer nahezu homogenen und hohen Oberflächenempfindlichkeit. Eine umfangreiche Validierungsstudie mit verschiedenen Referenzdatensätzen zeigt eine sehr gute Übereinstimmung über den Ozeanen, jedoch auch eine systematische Überschätzung über Landflächen. Gleichzeitig erweist sich der CDR als zeitlich sehr stabil und ist daher für Klimastudien prädestiniert.

Aus den Trendanalysen des MPIC OMI TCWV CDR wurde im Mittel ein globaler TCWV-Anstieg ermittelt, wobei fast alle lokalen, statistisch signifikanten Trends positiv sind. Es wurde auch gezeigt, dass die Annahme einer zeitlich konstanten relativen Luftfeuchtigkeit selbst über Ozean nicht immer erfüllt ist und dass indirekt ermittelte Niederschlagstrends nicht dem Paradigma "dry-gets-drier, wet-gets-wetter" folgen. Außerdem wurde eine Zunahme der Lebenszeit des Wasserdampfs festgestellt, was auf eine Verlangsamung des atmosphärischen Zweigs des hydrologischen Kreislaufs hindeutet.

Darüber hinaus wurde der CDR auch zur Untersuchung von Veränderungen in der (globalen) meridionalen Zirkulation verwendet, wobei eine polwärtige Ausdehnung der südlichen Tropen über den gesamten Pazifischen Ozean festgestellt wurde.

Contents

1 Introduction

Water is an essential element for life on Earth, which mankind has been fascinated with for thousands of years. For example, the ancient Greek philosophers Plato in "Timaeus" and Aristotle in his writings "On Generation and Corruption" included water among the components of the "concept of four basic elements".

The total mass of water on planet Earth is estimated to be approximately 1.4–1.5 $\times$ 10^9 km^3, with the largest reservoir being in the ocean with about 1.3–1.4 $\times$ 10^9 km^3 (e.g. Peixoto and Oort, 1992; Bengtsson, 2010). In contrast, only around 12.7 $\times$ 10^3 km^3 or 0.001% of the total water mass is found in the Earth's atmosphere mainly in the form of water vapour (Trenberth et al., 2007). However, despite its negligible role in the overall hydrological cycle in terms of mass, atmospheric water vapour is a key component of the Earth system.

Water vapour is the most important trace gas in the Earth's atmosphere and as such is involved in various atmospheric processes across all atmospheric scales: starting from phenomena like cloud droplet growth on the microscale (e.g. Pruppacher and Klett, 2010), to thunderstorms on the mesoscale (e.g. Stevens, 2005; Markowski and Richardson, 2010), and to hurricanes on the synoptic scale (e.g. Emanuel et al., 1994; Sherwood et al., 2010). On global or climate scale, water vapour acts as the most important natural greenhouse gas altering the Earth's energy balance by playing a dominant role in the atmospheric thermal opacity or the greenhouse effect. Moreover, it has a major amplifying influence on several factors of anthropogenic climate change through various feedback mechanisms such as cloud, lapse rate, and water vapour feedback mechanisms (Manabe and Wetherald, 1967; Kiehl and Trenberth, 1997; Randall et al., 2007; Trenberth et al., 2009). Furthermore, it also affects the energy balance via the transport of latent heat (e.g. Held and Soden, 2000) and therefore exerts an influence on the general circulation of the atmosphere (e.g. Schneider et al., 2010). However, despite its great importance on processes across all atmospheric scales, the complex interactions between the components of the hydrological cycle (including water vapour) and the atmosphere are still among the major challenges for climate modelling and for a better understanding of the Earth's climate system in general (Chahine, 1992; Stevens and Bony, 2013).

According to the Clausius-Clapeyron (CC) equation, changes in saturated water vapour are closely linked to changes in air temperature:

$$\frac{dE}{E} = \frac{L_v(T)}{R_v}\frac{dT}{T^2} \tag{1.1}$$

with the saturation water vapour pressure E, the latent heat of vaporization L_v, the specific heat capacity of water vapour R_v, and the air temperature T. For typical atmospheric conditions the CC-equation yields that for a temperature increase of 1 K it can be expected that the water vapour concentration increases by approximately 6-7$\%$ if relative humidity remains unchanged (Held and Soden, 2000). Thus, given its key role in many atmospheric processes and considering the global warming of the atmosphere and ocean within the last decades, accurate monitoring of the variability and changes of the amount and distribution of water vapour on a global scale is essential not only for a better understanding of the Earth's hydrological cycle, but also of the climate system.

Several different metrics exist to characterise the atmospheric water vapour content (Seinfeld and Pandis, 2016): for example, the volume and mass mixing ratio, the so-called specific humidity q (the ratio of the water vapour mass to the total (humid) air mass) or the so-called relative humidity RH, which is the ratio of the partial pressure of water vapour e to the saturation vapour pressure of water E at the ambient temperature T:

$$\mathrm{RH} = \frac{e}{E(T)} \tag{1.2}$$

Another important quantity is the water vapour concentration $\rho_{\mathrm{H_2O}}$ integrated over the complete atmospheric column, also known as "integrated water vapour", "(vertical) column density", or "total column water vapour" (TCWV), which is also directly related to the specific humidity:

$$\mathrm{TCWV} = \int_0^{\mathrm{TOA}} \rho_{\mathrm{H_2O}}\, dz = -\frac{1}{g}\int_{p_0}^{0} q\, dp \tag{1.3}$$

In the past decades, a large variety of in situ and remote sensing measurement techniques have been developed, enabling the observation of the water vapour distribution from platforms like radiosondes, balloons, aircrafts, and satellites (Kämpfer, 2012). Due to its spectral absorption properties, water vapour can be retrieved from satellite spectra in various spectral ranges, thus providing invaluable information on global scale and hence offering great scientific opportunities. As an example, in the microwave and thermal infrared spectral range it is possible to retrieve information of the vertical profile of the water vapour concentration or the water vapour volume mixing ratio, respectively (e.g. Kursinski et al., 1997; Rosenkranz, 2001; Susskind et al., 2003; Schlüssel et al., 2005; Schneider and Hase, 2011). In addition to profile algorithms, a large number of TCWV satellite retrievals exist, which typically operate in the microwave spectral range (e.g. Wentz, 1997), in the shortwave and near-infrared spectral range (e.g. Bennartz and Fischer, 2001; Gao and Kaufman, 2003; Schrijver et al., 2009; Dupuy et al., 2016; Schneider et al., 2020), and in the visible (red) spectral range (e.g. Noël et al., 1999; Lang et al., 2003; Wagner et al., 2003; Grossi et al., 2015). A detailed overview of several different water vapour satellite products (used within the framework of the GEWEX Water Vapor Assessment project G-VAP) is available in Schröder et al. (2018).

The visible spectral range is particularly interesting for the retrieval of total column water vapour: in contrast to the microwave spectral range, it allows for retrievals over the ocean and land surface, which means that global coverage can be achieved. Also, in comparison to the thermal infrared, it has a much higher sensitivity for the near-surface layers and it allows for retrievals under partly-cloudy conditions.

So far, TCWV retrievals in the visible spectral range mostly used the "red" spectral range because the absorption is strongest there. However, for this spectral range the ocean surface albedo is relatively low, leading to a low sensitivity for the lowermost troposphere, where the highest water vapour concentrations occur. In addition, current and past satellite sensors cannot spectrally resolve the fine absorption structures of water vapour in this spectral range, causing non-linear absorption effects (e.g. saturation effects) which have to be accounted for in post-processing. Also, this spectral range is covered only by a limited number of past and future satellite missions.

To overcome these limitations, Wagner et al. (2013) suggested applying TCWV retrievals in the "blue" spectral range (around 442 nm) where the absorption is much weaker than in the red, making the retrieval problem quasi-linear. In addition, the ocean surface albedo is much higher, leading to a higher sensitivity of the near-surface layers. Moreover, the surface albedo distribution is more homogenous compared to longer wavelengths (Koelemeijer et al., 2003; Wagner et al., 2013; Tilstra et al., 2017), which leads to a similar sensitivity for the near-surface layers over land and ocean. Furthermore, any satellite mission dedicated to NO_2 monitoring is covering this spectral range, i.e. the GOME series (Global Ozone Monitoring Experiment; Burrows et al., 1999; Munro et al., 2016), SCIAMACHY (SCanning Imaging Absorption spectroMeter for Atmospheric CHartographY; Bovensmann et al., 1999) as well as OMI (Ozone Monitoring Instrument; Levelt et al., 2006, 2018) and TROPOMI (TROPOspheric Monitoring Instrument; Veefkind et al., 2012).

Based on TCWV data sets from satellite observations, several studies in the past have investigated trends or changes in the global water vapour distribution (e.g. Trenberth et al., 2005; Wagner et al., 2006; Mieruch et al., 2008; Wang et al., 2016) and found rates of change that correspond to the CC-response (e.g. Trenberth et al., 2005). Trenberth et al. (2005) analyzed trends for the time period of 1988 to 2003 from a TCWV data set of merged microwave satellite sensors and found generally positive trends that are consistent with assumption of fairly constant relative humidity. Mieruch et al. (2008) combined TCWV measurements from GOME and SCIAMACHY in the visible red spectral range and determined also positive TCWV trends for the time period January 1996 to December 2003. More recently, Wang et al. (2016) investigated TCWV trends for the time period from 1995 to 2011 for a TCWV data set combining measurements from radiosondes, GPS radio occultation, and microwave satellite instruments. They found positive but slightly weaker TCWV trends which they attributed to the slowdown in the global warming rate since 2000 that terminated in 2014.

Nevertheless, a major limitation of the assumption of a CC-response is the supposition of temporally invariant relative humidity. More precisely, this presumes that the relative humidity close to the surface (especially over the ocean) remains constant, which was also confirmed by Dai (2006). Over land surfaces, however, this assumption is not always fulfilled (Simmons et al., 2010; Fasullo, 2012): for instance, Dunn et al. (2017) showed with their observational data first a gradual increase from 1973 to 2000, followed by a steep decrease in near-surface relative humidity over land masses since 2000. In contrast, for various climate models, relative humidity remained constant over the complete period.

In addition to global warming, several studies have shown that the tropics are expanding polewards, which is accompanied by an expansion of the so-called Hadley circulation (Seidel et al., 2008; Staten et al., 2018). Changes in the Hadley circulation have a direct impact on the atmospheric water cycle, for example in the distribution of rainfall areas (e.g. Sharmila and Walsh, 2018) or the expansion of subtropical deserts (Feng and Fu, 2013). Due to the direct impact on the hydrological cycle and the relationships between atmospheric dynamics and TCWV (Brogniez and Pierrehumbert, 2007; Singh et al., 2016), the question arises to what extent (satellite) measurements of the global TCWV distribution can contribute to detect changes in global circulation patterns.

The TCWV algorithm developed in this thesis makes use of the advantages of the blue spectral range compared to satellite products from other spectral ranges and investigates the long-term changes of the global water vapour distribution on the global scale.

The thesis is structured as follows: First, the development of a TCWV retrieval for the visible blue spectral range is presented in Chapter 2, making use of measurements from the state-of-the-art instrument TROPOMI. Building on this retrieval, Chapter 3 presents modifications to the retrieval algorithm so that it can be applied to long-term measurements from the Ozone Monitoring Instrument (OMI), from which a TCWV climate data set is generated. Using this new climate data record, Chapter 4 then investigates to what extent the TCWV distribution has changed within the last few years, whether there are particular patterns in the distribution of linear trends and how these relate to the earlier trend studies, and to what extent the assumption of temporally invariant relative humidity near the ground is fulfilled. In addition, Chapter 5 examines the poleward tropical expansion using the meridional TCWV distribution on both global and regional scales and the extent to which the results found are consistent with observations using established metrics for characterizing the width of the Hadley cell. Finally, Chapter 6 draws conclusions and gives an outlook.

2 Total column water vapour retrieval from S-5P/TROPOMI in the visible blue spectral range

The following chapter is based largely verbatim on the publication by Borger et al. (2020) and has only been restructured in a few places compared to this publication so that the Appendix and Supplement are included directly in the publication text.

2.1 Introduction

The particular absorption properties of water vapour allow for the retrieval of the water vapour content via satellites for several different spectral ranges from the microwave, e.g. AMSU (Rosenkranz, 2001), thermal infrared, e.g. AIRS (Susskind et al., 2003), near and shortwave infrared, e.g. MODIS (Gao and Kaufman, 2003) and MERIS (Bennartz and Fischer, 2001), to the visible, e.g. GOME (Noël et al., 1999; Wagner et al., 2003; Lang et al., 2007), SCIAMACHY (Noël et al., 2004), and GOME-2 (Grossi et al., 2015).

In the visible spectral range, TCWV was only retrieved in the red spectral range for a long time. It was only at the suggestion of Wagner et al. (2013) that the visible blue spectral range aroused interest, as it has some advantages over the red spectral range (see e.g. Chapter 1 or Wagner et al. (2013)). The first operational analyses of a similar approach have been performed by Wang et al. (2014, 2019) for measurements of the Ozone Monitoring Instrument (OMI; Levelt et al., 2006, 2018).

In October 2017 the TROPOspheric Monitoring Instrument (TROPOMI; Veefkind et al., 2012) onboard ESA's Sentinel-5 Precursor (S-5P) satellite was launched in a Sun-synchronous polar orbit with an Equator crossing time of 13:30 LT (local time). TROPOMI is a UV-Vis-NIR push-broom spectrometer and consists of 450 detectors/rows covering a swath width of 2600 km. The outstanding property of TROPOMI is that its spectral bands in the visible combine a high signal-to-noise ratio with an unprecedented spatial resolution of $3.5 \times 7.5\,km^2$ (and $3.5 \times 5.6\,km^2$ since August 2019; Rozemeijer and Kleipool, 2019) at nadir, which allows for the performance of spectral analyses at a never seen before accuracy even on small spatial scales.

This chapter introduces a TCWV retrieval based on the spectral analysis approach of Wagner et al. (2013) to S-5P/TROPOMI observations and is organized as follows: Sect. 2.2 gives an overview of the retrieval describing general retrieval principles and presenting the retrieval setup. Sect. 2.3 presents an empirical parameterization of the a priori water vapour profile shape and an iterative scheme making use of the relation between the water vapour profile shape and TCWV. Sect. 2.4 evaluates different input albedo products and Sect. 2.5 performs a detailed uncertainty analysis including a variety of different error sources. Sect. 2.6 presents first TCWV results retrieved from TROPOMI measurements and performs a validation study using data sets from satellites, ground-based measurements, and reanalysis models as reference. Sect. 2.7 draws conclusions and summarizes the outcomes of the investigations.

2.2 Retrieval principles

2.2.1 Wavelength calibration and spectral analysis

In a first step the wavelength alignment of the daily measured irradiance is calibrated for each of the 450 TROPOMI detectors/rows via a non-linear least-squares fit in intensity space using the solar spectrum from Kurucz et al. (1984) as reference. Simultaneously, the instrumental spectral response function (ISRF) is approximated assuming an asymmetric Super-Gaussian following the definition of Beirle et al. (2017):

$$S_{\text{asym}}(x) = \begin{cases} \exp\left(-\left|\frac{x}{w-a_w}\right|^k\right) & \text{for } x \leq 0, \\ \exp\left(-\left|\frac{x}{w+a_w}\right|^k\right) & \text{for } x > 0 \end{cases} \tag{2.1}$$

Next, a spectral analysis is performed using the Differential Optical Absorption Spectroscopy (DOAS; Platt and Stutz, 2008) scheme in which the attenuation along the light path is calculated via the Beer-Lambert law in optical depth space:

$$\ln\left(\frac{I}{I_0}\right) \approx -\sum_i \sigma_i(\lambda) \cdot \text{SCD}_i + \Psi + \Phi \tag{2.2}$$

where I_0 and I represent the solar irradiance and the radiance backscattered from Earth, respectively, and i denotes the index of a trace gas of interest, $\sigma_i(\lambda)$ its respective molecular absorption cross section, $\text{SCD}_i = \int_s c_i ds$ its concentration integrated along the light path s (the so called slant column density), Ψ summarizing terms accounting for the Ring effect and additional pseudo-absorbers, and Φ a closure polynomial accounting for Mie and Rayleigh scattering as well as parts of the low-frequency contributions of the trace gas cross sections.

Table 2.1: DOAS fit settings for the H_2O slant column retrievals.

Parameter	Description
Fit window	430–450 nm
Absorption cross sections	Water vapour, 296 K (Rothman et al., 2009) NO_2, 220 K (Vandaele et al., 1998) O_3, 243 K (Serdyuchenko et al., 2014) O_4, 293 K (Thalman and Volkamer, 2013)
Ring effect	Two Ring spectra calculated from daily irradiance
Polynomial	5th order
Pseudo-absorbers	intensity offset (inverse spectrum) shift and stretch (Beirle et al., 2013) ISRF parameter changes (Beirle et al., 2017)

Table 2.1 summarizes the fit setup of the retrieval's spectral analysis. The retrieval's fit window ranges from 430 to 450 nm and accounts for molecular absorption by water vapour (HITRAN 2008; Rothman et al., 2009), NO_2 (Vandaele et al., 1998), ozone (Serdyuchenko et al., 2014), and the O_2–O_2 dimer (Thalman and Volkamer, 2013). To account for the Ring effect (Grainger and Ring, 1962; Joiner et al., 1995) two Ring spectra are included (Wagner et al., 2009), and for Φ a fifth-order polynomial is used. Furthermore, the analysis includes pseudo-absorbers accounting for intensity offset, for shift and stretch effects (Beirle et al., 2013), and for ISRF changes along the orbit (Beirle et al., 2017) for ISRF parameters w and k in Eq. (2.1). All molecular absorption cross sections are convolved with the ISRF of the corresponding TROPOMI row/detector determined during the calibration process.

Figure 2.1 illustrates a typical example of such a spectral analysis of a TROPOMI measurement spectrum in which the absorption structures of water vapour, NO_2, and the Ring effect can be well identified and the residual spectrum shows a highly volatile pattern, containing noise and a high-frequency systematic structures.

Figure 2.2 depicts the distribution of the H_2O SCD from one TROPOMI orbit (orbit number 6930) on 13 February 2019. It demonstrates that the TROPOMI retrieval is able to capture the meso- to macro-scale water vapour patterns like convective updrafts in the tropics and atmospheric rivers in the midlatitudes, whereby the small H_2O SCD values in the tropics are caused by cloud shielding.

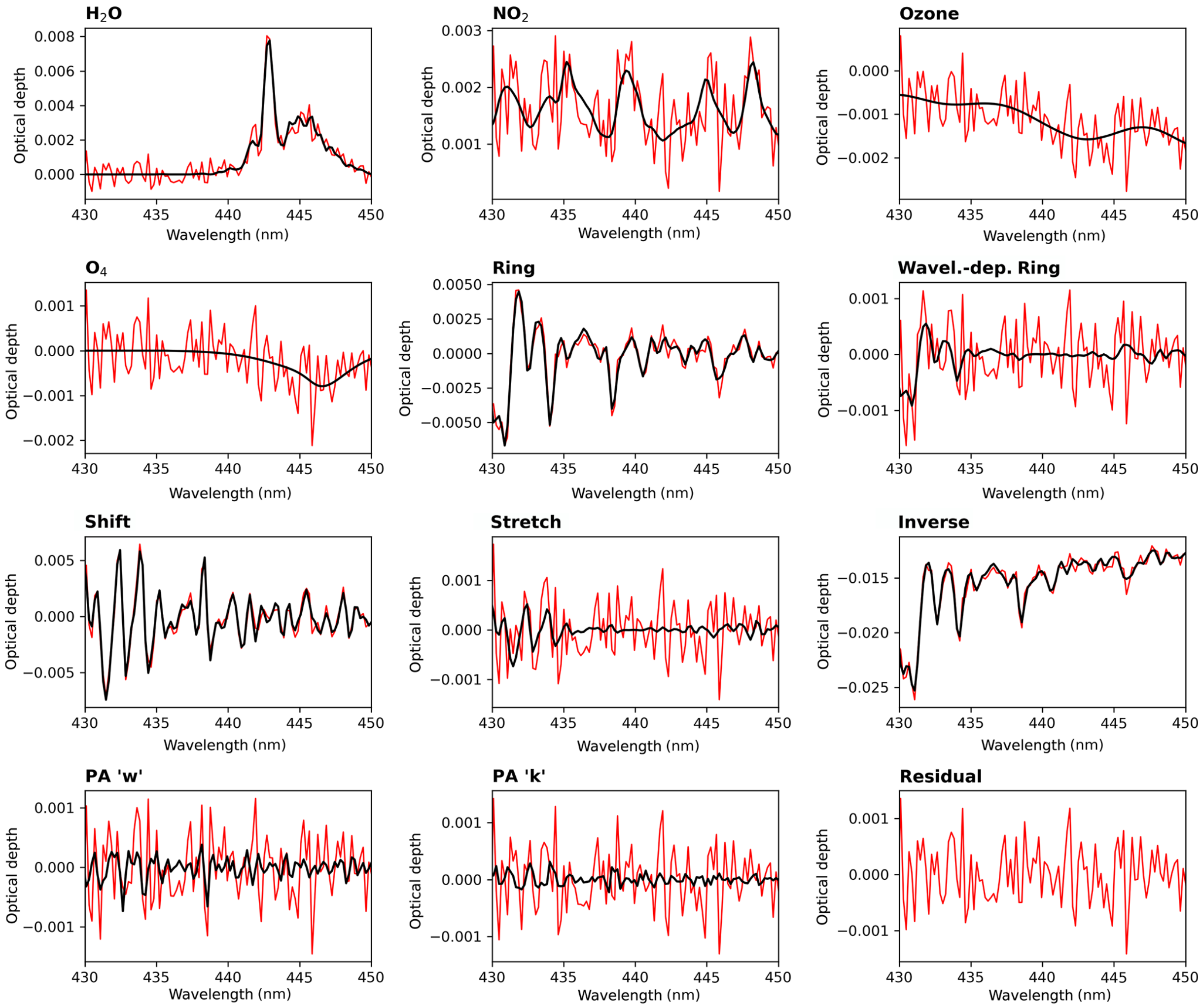

Figure 2.1: Example of a typical spectral analysis of a TROPOMI measurement spectrum (rms: 0.5 ‰, orbit: 6930, −7.41°N, −111.97°E). The black line indicates the fit result for the respective trace gas and the red line indicates the residual spectrum of the fit (bottom right panel) and residual noise for each constituent.

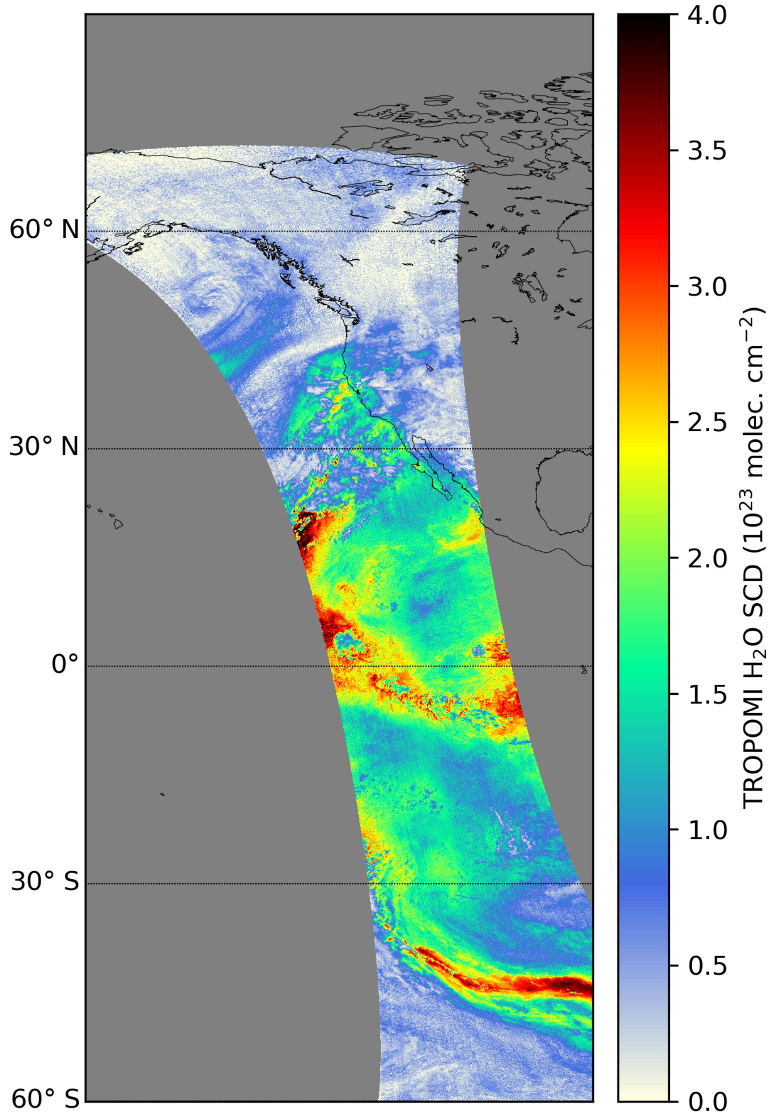

Figure 2.2: H_2O SCD distribution retrieved from TROPOMI measurements (orbit: 6930) on 13 February 2019 during an atmospheric river event at the western US coast and in the Southern Pacific ocean.

2.2.1.1 Weighted linear least-squares fit for spectral analysis

Due to the high daily data volume of the TROPOMI L1B radiances, the execution of a non-linear fit without high-performance infrastructure is demanding in computation time. For instance, TROPOMI's UVIS Band 4, which covers the spectral range of 400–499 nm, generates about 40 GB every day. Therefore, a weighted linear least-squares fit is implemented for the retrieval, in which the weights are the fractional coverage of the spectral pixel within the fit window.

The weights W are the fractional coverage of the pixel within the fit window (see also Fig. 2.3):

$$W(\lambda) = \begin{cases} 1 - \frac{|\lambda - \lambda_{\text{low}}|}{\Delta\lambda} & \frac{|\lambda - \lambda_{\text{low}}|}{\Delta\lambda} < 1 \wedge \lambda - \lambda_{\text{low}} < 0, \\ 1 & \lambda_{\text{low}} < \lambda < \lambda_{\text{up}} \\ 1 - \frac{|\lambda - \lambda_{\text{up}}|}{\Delta\lambda} & \frac{|\lambda - \lambda_{\text{up}}|}{\Delta\lambda} < 1 \wedge \lambda - \lambda_{\text{up}} > 0, \\ 0 & \text{else} \end{cases} \tag{2.3}$$

with λ_{low} and λ_{up} the lower and upper boundaries of the fit window and $\Delta\lambda$ the average wavelength increment within the fit window. The elements of the weight matrix are then given as $w_{ii} = \sqrt{W(\lambda_i)}$. Hence Eq. (2.2) can be solved by simple linear algebra:

$$\begin{aligned}
&\mathbf{y}' = \mathbf{M}'\mathbf{x}, \\
&\hat{\mathbf{x}} = \left(\mathbf{M}'^T\mathbf{M}'\right)^{-1}\mathbf{M}'^T\mathbf{y}', \\
&\mathbf{S} = \left(\mathbf{M}'^T\mathbf{M}'\right)^{-1}\chi^2, \\
&\beta_i = \sqrt{S_{ii}},
\end{aligned}$$

with the solution of the linear problem $\hat{\mathbf{x}}$ containing the SCDs, $\mathbf{y}' = \text{diag}(\mathbf{w})\mathbf{y}$ the weighted measurement spectrum, $\mathbf{M}' = \text{diag}(\mathbf{w})\mathbf{M}$ the weighted absorption structures to fit, β_i the estimated 1σ fit error of the results for each fitted parameter, and χ^2 the reduced chi square.

This weighting of the outermost pixels of the fit window avoids "jumps" of pixels included in the DOAS fit, as they would occur for a fixed fit window due to the changing pixel-to-

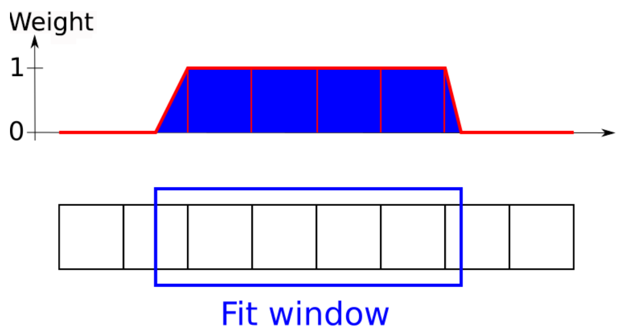

Figure 2.3: Schematic illustration of the weights used during the retrieval's spectral analysis.

wavelength mapping across-track. Thus, across-track "stripes" in the SCDs are reduced. According to Beirle et al. (2013) the computational speed increases by 3 orders of magnitude by going from non-linear to linear fits for their MATLAB routine (see Table 3 in their paper).

2.2.1.2 Evaluation of the water vapour absorption cross section

The molecular absorption by water vapour within the fit window is relatively weak, and hence the modelled line lists vary systematically from HITRAN 2008 to HITRAN 2012 (Rothman et al., 2013) and to HITRAN 2016 (Gordon et al., 2017). Thus, the choice of line list is afflicted by a high degree of uncertainty. Lampel et al. (2015) found that HITRAN 2012 underestimates the water vapour concentration derived from long-path DOAS (LP-DOAS) observations by approximately 10 % and that the previous version, HITRAN 2008, agrees better with the reference measurements.

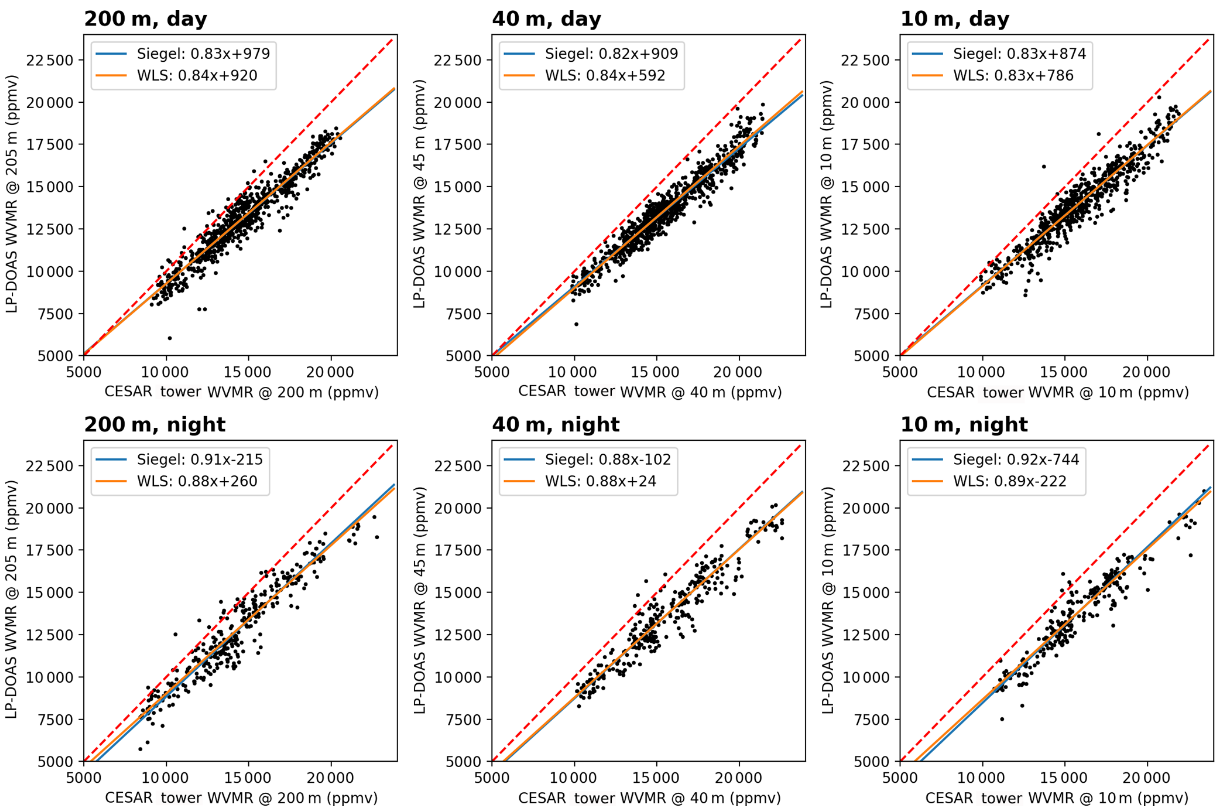

Figure 2.4: Scatter plots of water vapour volume mixing ratios (WVMRs) derived from LP-DOAS measurements and meteorological measurements at different altitudes (10 m, 40 m and 200 m) at the CESAR Tower for day and night during the CINDI-2 campaign. Water vapour absorption cross sections have been calculated from the HITRAN 2012 line list. The dashed red line represents the 1-to-1 diagonal, the solid blue line the results from the robust regression (Siegel, 1982), and the solid orange line the results from the weighted linear regression.

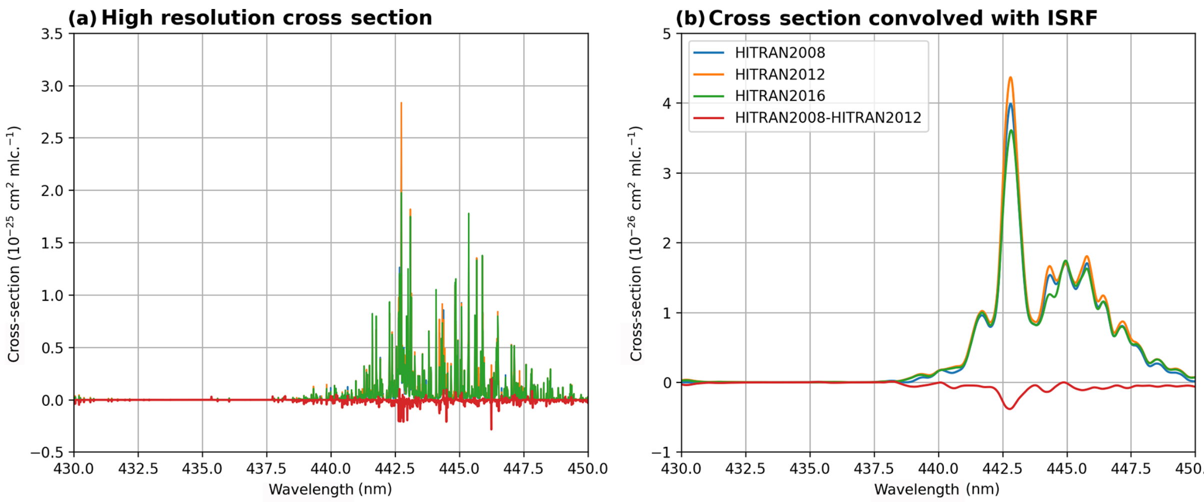

Figure 2.5: Comparison of the water vapour absorption cross section derived from different HITRAN versions (2008, 2012, and 2016) for a temperature of 296 K. Panel **(a)** depicts the high-resolution cross sections and the difference between HITRAN2008 and HITRAN2012. Panel **(b)** depicts the same cross sections but convolved with a typical TROPOMI Super-Gaussian ISRF (values from Beirle et al., 2017).

Figure 2.4 depicts intercomparisons between LP-DOAS and meteorological measurements of water vapour volume mixing ratios (WVMRs) at different altitudes (10 m, 40 m and 200 m) at the CESAR Tower for daytime and nighttime during the Cabauw Intercomparison of Nitrogen Dioxide Measuring Instruments 2 campaign (CINDI-2; Kreher et al., 2020). The results of the regression methods indicate that for every altitude the LP-DOAS underestimates WVMRs by around 17 % during day and 11 % during night. These findings independently confirm the results of further LP-DOAS measurements taken at the Cape Verde Atmospheric Observatory, for which Lampel et al. (2015) observed an underestimation of around 8 % when using the water vapour line lists from HITRAN 2012. However, when using the water vapour line lists from HITRAN 2008, Lampel et al. (2015) observe an excellent agreement with the reference meteorological measurements at the observatory (see Table 8 in their paper).

Figure 2.5 compares the absorption cross sections of the different HITRAN versions. For the high-resolution cross section (Panel a), the differences between the versions are hardly visible; however, after the convolution with the TROPOMI ISRF (Panel b), distinctive differences in the peak absorption are clearly visible: in comparison to HITRAN 2008, the absorption peak of HITRAN 2012 is approximately 7–9% higher than HITRAN 2008, and the absorption peak of HITRAN 2016 is approximately 7–9% lower than HITRAN 2008.

At this point, it should also be mentioned that the H_2O cross-section of HITRAN 2020 (Gordon et al., 2022) is now also available. However, it has not yet been used because the quality of this version cannot yet be sufficiently assessed. However, first comparisons show that the

HITRAN 2020 cross-section is significantly stronger than that of HITRAN 2016 and will therefore lead to an even greater underestimation of the H_2O column.

Combining these findings with the shortcomings of HITRAN 2016 indicated by Wang et al. (2019) and the observational evidence from the LP-DOAS measurements, the conclusion is that it is most adequate to use the water vapour line list from HITRAN 2008.

2.2.2 Vertical column density conversion and Box-AMF simulations

To convert the slant column density to a vertical column density (VCD), the so-called air-mass factor (AMF) must be applied:

$$\mathrm{VCD} = \frac{\mathrm{SCD}}{\mathrm{AMF}} \tag{2.4}$$

The air-mass factor accounts for the non-trivial effects of the atmospheric radiative transfer and is usually based on radiative transfer model (RTM) simulations. In this case, the RTM simulations with the 3D Monte Carlo RTM McArtim (Deutschmann et al., 2011) have been performed at a wavelength of 442 nm for different retrieval scenarios (summarized in Table 2.2) assuming an aerosol-free atmosphere. These simulations yield a Jacobian vector $\vec{J} = \frac{\partial \ln I}{\partial \mu}$ (with the absorption coefficient μ and the simulated intensity I at TOA normalized by the solar spectrum I_0) defined at each vertical grid box k. The altitude-dependent AMFs, so called box-AMF (BAMF), can then be calculated according to the formula

$$\mathrm{BAMF}_k = -\frac{1}{\Delta h}\frac{\partial \ln I}{\partial \mu_k} = \frac{-\vec{J}_k}{\Delta h} \tag{2.5}$$

with the box thickness Δh. These BAMF profiles have to be combined with the partial vertical columns c_k of an a priori water vapour profile (e.g. Palmer et al., 2001; Eskes and Boersma, 2003):

$$\mathrm{AMF} = \frac{\sum_k \mathrm{BAMF}_k \cdot c_k}{\sum_k c_k} \tag{2.6}$$

with $\sum_k c_k = \mathrm{VCD}$. For the case of a cloud-contaminated pixel it is assumed that the cloud is a Lambertian reflector with an albedo of 80 % and the cloud top height is used as surface altitude input for the AMF. Under the assumption of the independent pixel approximation (Cahalan et al., 1994), the resulting cloud-affected AMF can then be calculated as a linear combination of the AMF for a clear-sky scenario and the AMF for a cloudy-sky scenario weighted by the

Table 2.2: Parameter list and nodes for the BAMF profile simulations.

Parameter	Nodes
Wavelength (nm)	442
Sensor altitude (km)	720
Surface altitude (km)	0.0, 0.5, 1.0, 1.5, 2.0, 2.5, 3.0, 4.0, 5.0, 6.0, 8.0, 12.0
Surface albedo (%)	0, 1, 2, 3, 4, 5, 6, 7, 8, 9, 10, 12, 14, 16, 18, 20, 25, 30, 40, 50, 80, 100
Solar zenith angle (°)	0, 10, 20, 30, 40, 50, 60, 65, 70, 80, 85, 87, 88
Line-of-sight angle (°)	-90, -86, -82, -78, -74, -70, -66, -62, -58, -54, -50, -46, -42, -38
Solar relative azimuth angle (°)	0, 20, 40, 60, 80, 100, 120, 140, 160, 180

respective simulated intensities I and the effective cloud fractions ζ as follows (Chambers et al., 1997; Martin et al., 2002):

$$\mathrm{AMF} = \frac{(1-\zeta)\, I_{clear}\, \mathrm{AMF}_{clear} + \zeta \cdot I_{cloud}\, \mathrm{AMF}_{cloud}}{(1-\zeta)\, I_{clear} + \zeta \cdot I_{cloud}} \tag{2.7}$$

Figure 2.6 depicts typical examples of BAMF profiles for different clear- and cloudy-sky scenarios. The AMFs for the cloudy-sky scenarios were calculated assuming a surface albedo of 7 % and an effective cloud fraction of 20 %. For the clear-sky scenario (Panel a) the sensitivity decreases towards the surface. For the cloudy-sky scenarios (Panel b) the BAMF profiles slightly increase towards the (bright) cloud top surface of the respective scenario. Below the cloud, the sensitivity is 0, because the atmosphere is shielded. Since high clouds shield large fractions of the atmosphere and hence also of the water vapour column below the cloud (see the black dashed curve), the AMF has to be corrected correspondingly and thus decreases for increasing cloud top heights.

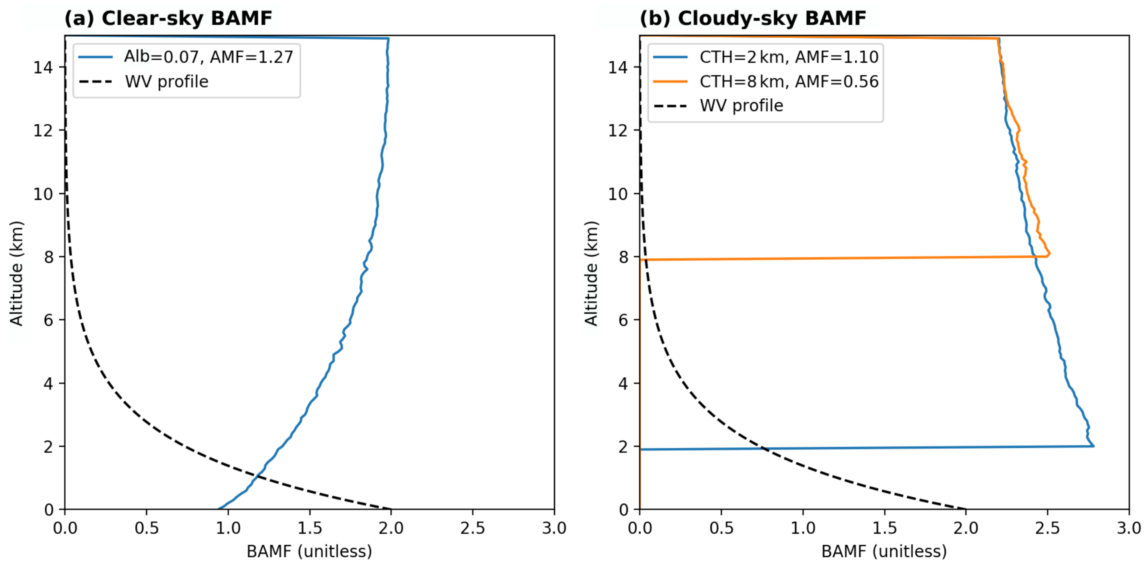

Figure 2.6: Examples of typical BAMF profiles for different observation scenarios under clear- **(a)** and cloudy-sky **(b)** conditions. For all simulations a solar zenith angle of 0° and a line-of-sight angle of –90° are assumed. For the clear-sky case the BAMF profile is illustrated for a surface albedo of 7%. For the cloudy-sky cases the profiles are depicted for cloud top heights of 2 and 8 km and the respective AMFs are calculated assuming a surface albedo of 7% and an effective cloud fraction of 20%. The black dashed lines indicate relative water vapour concentrations with a scale height of 2 km.

2.3 A priori water vapour profile shape

As described in Sect. 2.2.2 and Eq. (2.6), knowledge of the a priori water vapour profile shape is necessary for accurate calculations of the AMF from the BAMF profile. However, simply assuming the same a priori profile shape for the whole globe might cause biases because it cannot account for the atmospheric variability of water vapour, such as latitudinal variations, seasonal cycles, or different profile shapes over maritime and continental regions due to different water vapour sources (e.g. evapotranspiration by plants). Also, simply using profiles from numerical weather models is not uncritical: for instance, Wang et al. (2019) found out that their calculated AMF changes strongly, depending on which reanalysis model data they were using.

Weaver and Ramanathan (1995) approximated the water vapour profile by an exponential decay with altitude:

$$n_{\mathrm{v}}(z) = n_0 e^{-z/H_{\mathrm{v}}} \tag{2.8}$$

where H_v is the scale height of water vapour, which they defined as

$$H_\mathrm{v} = \frac{R_\mathrm{v} \langle T \rangle^2}{L \langle \Gamma \rangle} \qquad (2.9)$$

where $\langle T \rangle$ denotes the mean air temperature within an atmospheric column, $\langle \Gamma \rangle$ the mean lapse rate within the same atmospheric column, R_v the gas constant of water vapour, and L the specific latent heat. However, this definition requires knowledge of the mean air temperature and/or the lapse rate and that the relative humidity is assumed as constant with altitude. The former can be only estimated using numerical weather models and the latter is very unlikely to occur in the atmosphere.

Thus, this Section aims to find an empirical parameterization of the scale height and thereby focuses on its dependency on the H_2O VCD and the aforementioned atmospheric variabilities, i.e. dependencies of latitude, seasonal cycle, and surface properties (such as vegetation effects).

The Section is structured as follows: first, it is evaluated how well the method used to calculate the water vapour scale height can reproduce the COSMIC profiles via an AMF comparison. Then it is examined how the scale height can be parameterized globally and investigate for a parameterization over ocean and land separately. Finally, the parameterization is implemented in an iterative retrieval scheme and the new estimates of the H_2O VCD are evaluated.

2.3.1 COSMIC water vapour profiles

For the following investigations profile data retrieved from measurements of the Constellation Observing System for Meteorology, Ionosphere, and Climate (COSMIC, Anthes et al., 2008) program provided by the Radio Occultation Meteorology Satellite Application Facility (ROM-SAF) is used. The COSMIC data are based on the GPS radio occultation (RO) technique, which provides high-resolution vertical profiles of bending angles (Hajj et al., 2002) that can be used to retrieve the atmospheric refractivity. Since the atmospheric refractivity is dependent on the air pressure, the air temperature, and the water vapour pressure (Smith and Weintraub, 1953), GPS RO allows for the retrieval of profile information under all-weather conditions with a high vertical resolution of approximately 100 m in the lower troposphere up to 1 km in the stratosphere (Anthes, 2011) and an accuracy of around 1 g kg^{-1} (Heise et al., 2006; Ho et al., 2010b) while having an almost uniform global distribution (Ho et al., 2010a).

The ROMSAF profiles have been retrieved via a 1D-VAR scheme within a reprocessing initiative for creating climate data record (CDR) v1.0. Given the strict product requirements and the validation studies with ERA-Interim and radiosondes (Nielsen et al., 2018), biases associated with using COSMIC should be negligible, especially their impact on the profile shape (which is important for this task).

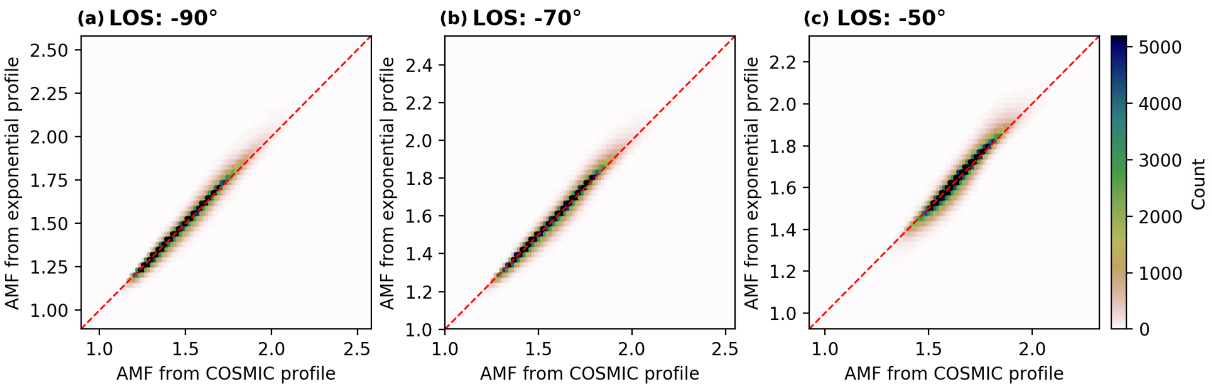

Figure 2.7: 2D histograms comparing synthetic AMFs (calculated via the sum method) for different line-of-sight angles (**a**: −90°, **b**: −70°, and **c**: −50°) assuming clear-sky conditions. The colour depicts the number of observations within one defined bin of the 2D histogram and the red dashed line represents the 1-to-1 diagonal.

The investigations are based on COSMIC data retrieved between 2013 and 2016, which accumulates to approximately 1.6×10^6 profiles.

2.3.2 Calculation of scale height

For the calculation of the scale height the COSMIC profile are high-sampled to a 100 m grid up to 14 km, or rather only consider profile data below 150 hPa (close to the tropopause height). Then all the partial columns of the COSMIC profile data are summed up from the ground up to a (scale) height H_{sum} where the H_2O VCD reaches $1 - \frac{1}{e}$:

$$\frac{\int_0^{H_{\text{sum}}} n(z)\mathrm{d}z}{\int_0^{\text{TOA}} n(z)\mathrm{d}z} > 1 - \frac{1}{e} \approx 63\,\% \tag{2.10}$$

To evaluate this scale height approach, a synthetic study has been performed in which AMFs calculated for the original COSMIC water vapour profile measurements are compared to AMFs for an exponential profile using the corresponding calculated scale height H_{sum}. For the simulation of the BAMF profiles an albedo of 7% is assumed, which is a representative value for the ocean surface albedo (Tilstra et al., 2017). The solar zenith angle is calculated for the location of the COSMIC profile assuming an hour angle of 90°, and the line-of-sight angles (LOS) are prescribed for −90°, −70° and −50°. Here, an LOS of −90° means a nadir viewing geometry.

The results of the intercomparison are given in Fig. 2.7. The 2D histograms reveal that the AMFs derived with the exponential profile agree well with the AMFs calculated directly from the COSMIC profiles, indicating that the chosen method can well reproduce the overall shapes of the COSMIC profiles. This good agreement can also be observed in the histograms of Fig. 2.8, which illustrate distributions of relative deviation between the AMFs for selected

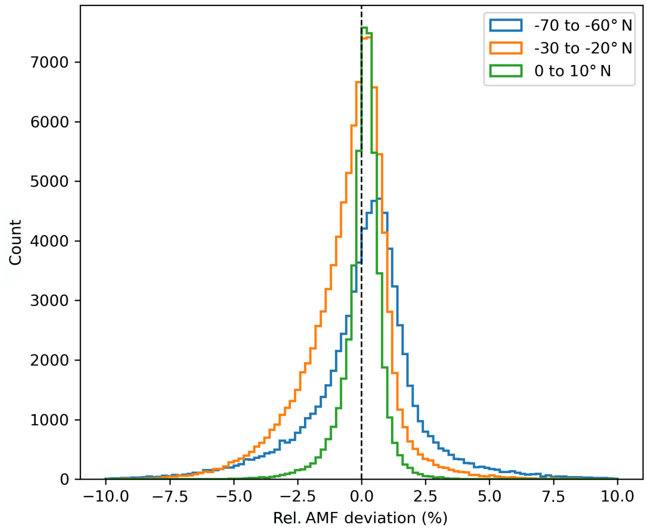

Figure 2.8: Histograms of the relative deviation of the calculated synthetic AMFs between the exponential profile and COSMIC profile for selected latitude bins (0 to 10, −30 to −20, and −70 to −60°N) assuming clear-sky conditions and nadir-viewing geometry.

latitude bins. These distributions have a clear peak around values of 0%, indicating that the AMFs from the exponential shape are almost unbiased to the reference AMFs.

In addition, Fig. 2.9 shows exemplary profiles for cases of good and bad agreement with the reference AMFs for the same selected latitude bins as in Fig. 2.8. In general, bad agreement (left column) occurs for profile shapes in which a sharp gradient is observed in the lower troposphere and from there the values remain quasi-constant with altitude. Such profiles usually occur when a moist boundary layer is topped by a dry free atmosphere. Nevertheless, the maximal absolute relative AMF deviations only have values around 15%. In contrast, good agreement (right column) is found for profile shapes following an approximate exponential decay with altitude, which indicates a well-mixed troposphere.

The results of the intercomparison for prescribed cloudy-sky conditions and nadir-viewing geometry are illustrated in Fig. 2.10, in which the panels show histograms of the relative AMF deviation for the same selected latitude bins as in Fig. 2.8 but for different cloud fractions (10%, 20% and 50%; left to right column) and cloud top heights (1, 2, and 5 km; top to bottom row) scenarios. For a cloud top height of 1 km the AMFs calculated from the exponential profiles are generally biased negative for all cloud fractions, in particular for the latitude bin of −30 to −20°N. However, for higher clouds the AMFs agree well with the reference AMFs for almost all cloud scenarios except the extreme cases with a cloud fraction of 50% and a cloud top height of 5 km or more.

Alternative methods for calculating the scale height yielded systematic overestimations of the AMF for clear-sky conditions (Fig. 2.15) and higher scatter within the AMF for cloudy-sky conditions (Fig. 2.16) in comparison to the sum method, as shown in detail in Section 2.3.3.

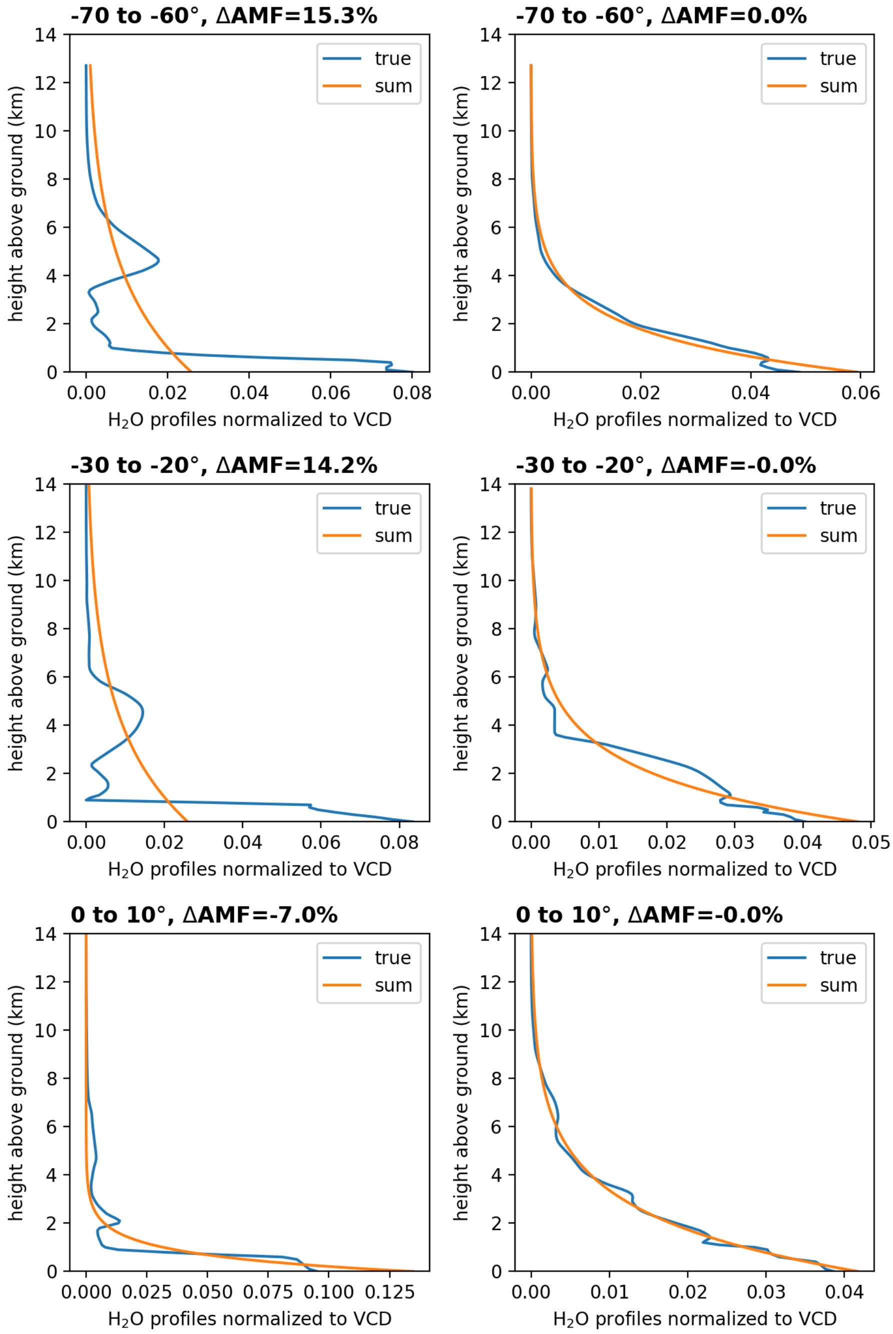

Figure 2.9: Comparison of profile shapes for selected latitude bins illustrating the maximal (left column) and minimal (right column) absolute relative AMF deviations. The blue line represents the "true" water vapour profile shape as measured from COSMIC and the orange line represents the exponential profile with a scale height H calculated from the sum method.

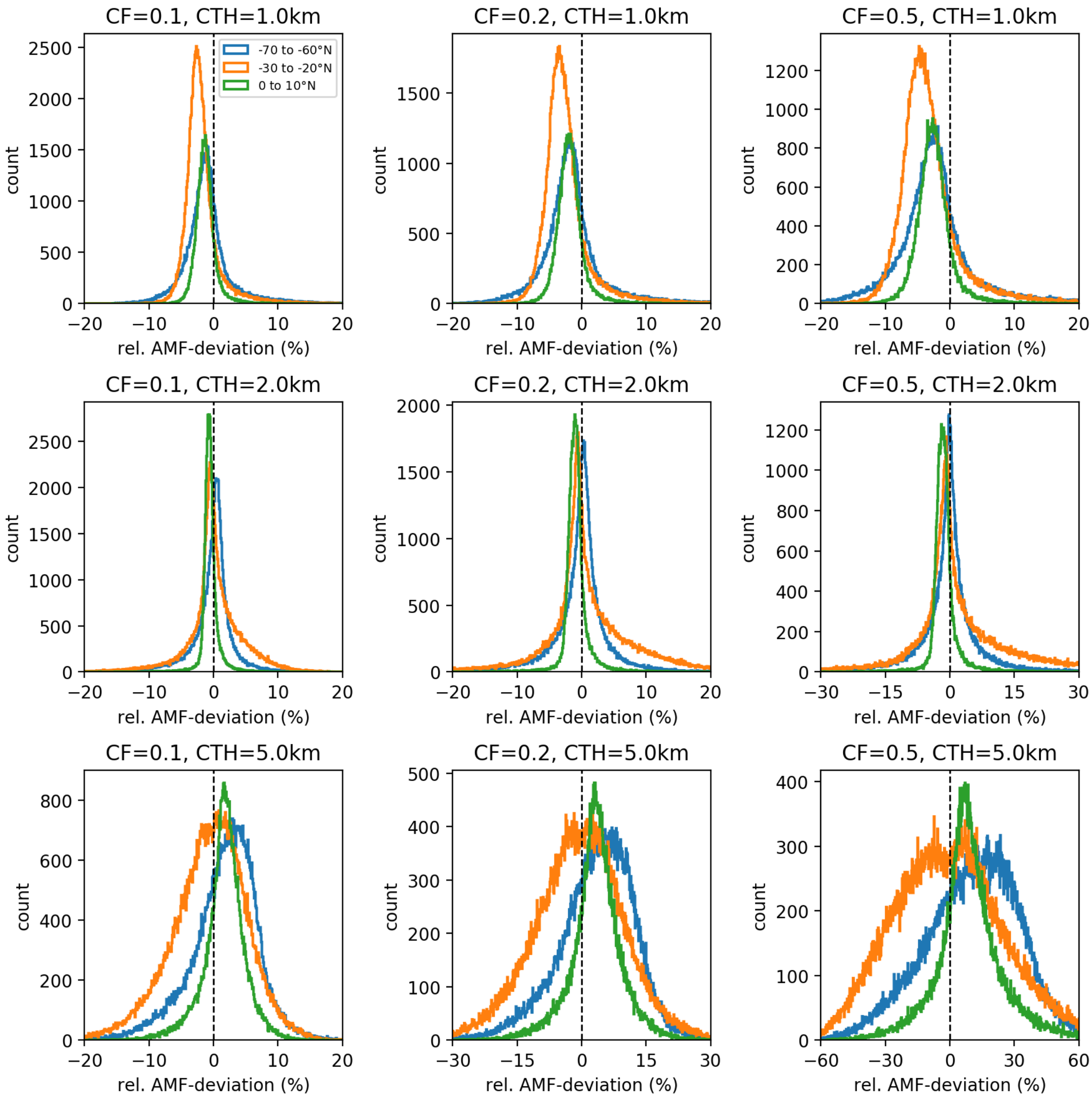

Figure 2.10: Histograms of the relative AMF deviations between exponential profile and COSMIC profile for the same latitude bins as in Fig. 2.8 for different cloud scenarios (cloud fraction 10, 20 and 50 % (left to right); cloud top height 1 km, 2 km and 5 km (top to bottom)) and a nadir viewing geometry.

2.3.3 Evaluation of methods for calculating the water vapour scale height

The water vapour scale height can be calculated in different ways. Here, two different approaches are compared: the first method is the calculation of the scale height via a weighted non-linear fit:

$$\min \sum_i \frac{\left(y_i - f\left(z_i, n_0, H_{\mathrm{nl}}\right)\right)^2}{\sigma_i^2}$$
$$f\left(z, n_0, H_{\mathrm{nl}}\right) = n_0 e^{-\frac{z}{H_{\mathrm{nl}}}}$$

where y_i are the COSMIC profile data points, $f(z, n_0, H)$ is the approximation of the exponential function, and σ_i is the inverse of the layer thickness at the observation y_i. The second method consists of summing up all the partial columns of the COSMIC profile data until a defined threshold is reached, which in our case is 63% of the H_2O VCD:

$$\frac{\int_0^{H_{\mathrm{sum}}} n(z)\mathrm{d}z}{\int_0^{\mathrm{TOA}} n(z)\mathrm{d}z} > 1 - \frac{1}{e} \approx 63\,\% \tag{2.11}$$

Figure 2.11 depicts the mean profile shapes calculated using both methods as well as the mean profile shape of the COSMIC data for different latitude bins for the year 2013 for which the sample size is largest. Further statistics of goodness are given in Fig. 2.12 (bias), Fig. 2.13 (mean absolute error), and Fig. 2.14 (standard deviation). In general, the profile shapes of both methods agree well with the COSMIC measurements; however, Figs. 2.12 and 2.13 also reveal that the largest deviations occur in the lowermost troposphere, in particular for the southern polar regions. Nevertheless, the profiles of standard deviations in Fig. 2.14 also demonstrate that both methods are able to well capture the vertical and temporal variations in the water vapour profile shape and that these variations are within the same range of the variation of the COSMIC profile data.

Figure 2.15 depicts histograms of the relative AMF deviation for both methods for selected latitude regions assuming nadir-viewing geometry and clear-sky conditions (like in Sect. 2.3.2 and Fig. 2.8). The peaks of the histograms for the sum method are close to the 0 % line, indicating very good agreement with AMF calculated from the COSMIC profiles. In contrast, the histograms for the non-linear fit peak at values around 2 % and show a broader distribution than the histograms of the sum method, thus revealing an inferior agreement with the reference AMFs. For cloudy-sky conditions (see Fig. 2.16), both methods are biased to smaller AMF values (deviations of around $-5\,\%$) for a cloud top height of 1 km, but for higher clouds both methods show similar good agreement with the reference AMFs. However, the variance in the AMFs for the sum method is much smaller than in the AMFs for the non-linear fit.

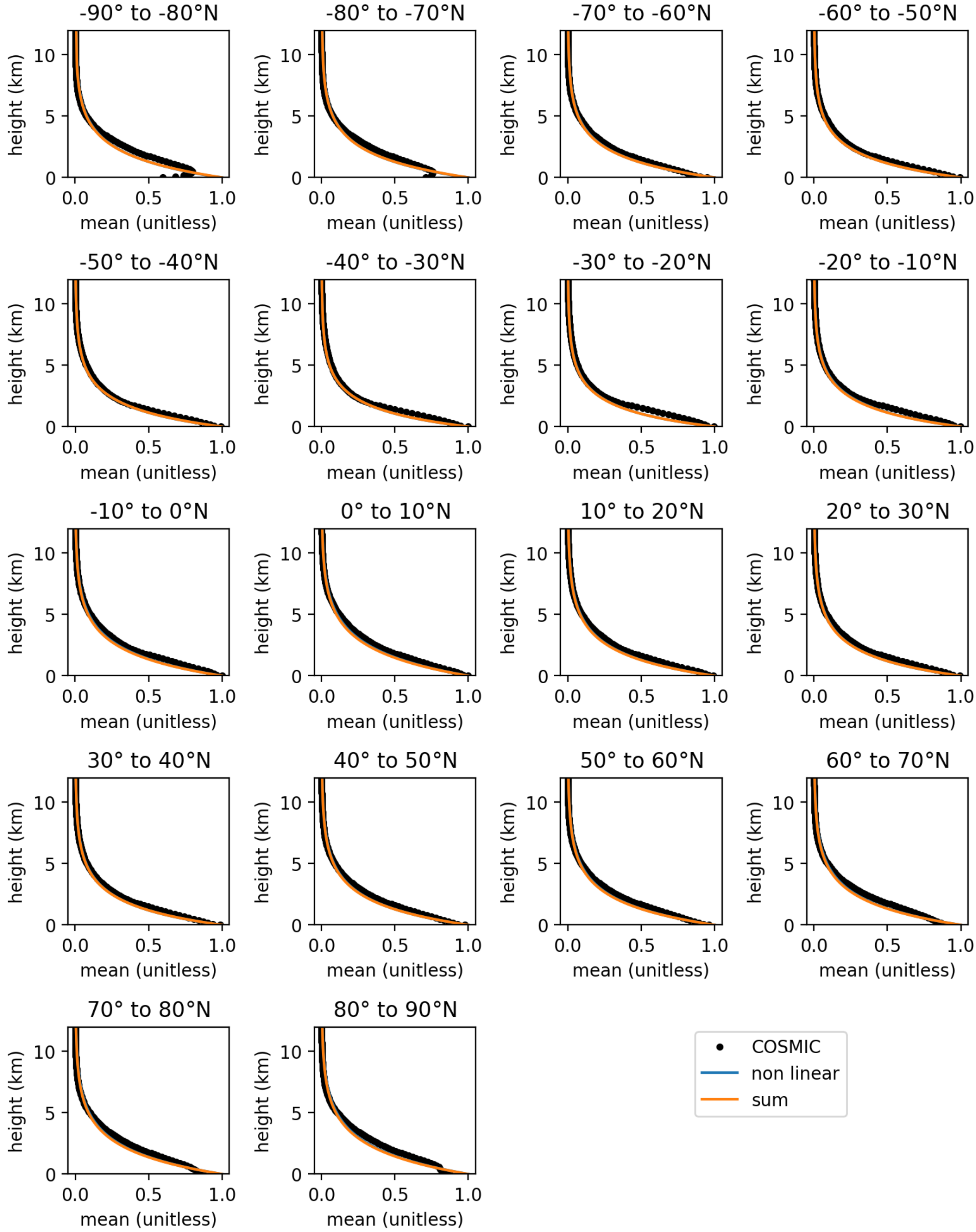

Figure 2.11: Mean water vapour profile shapes for data in 2013 for latitude bins of 10°. The solid lines represent the results from the exponential scale height approaches (blue: non-linear fit; orange: sum method) and the black dots represent the COSMIC measurements.

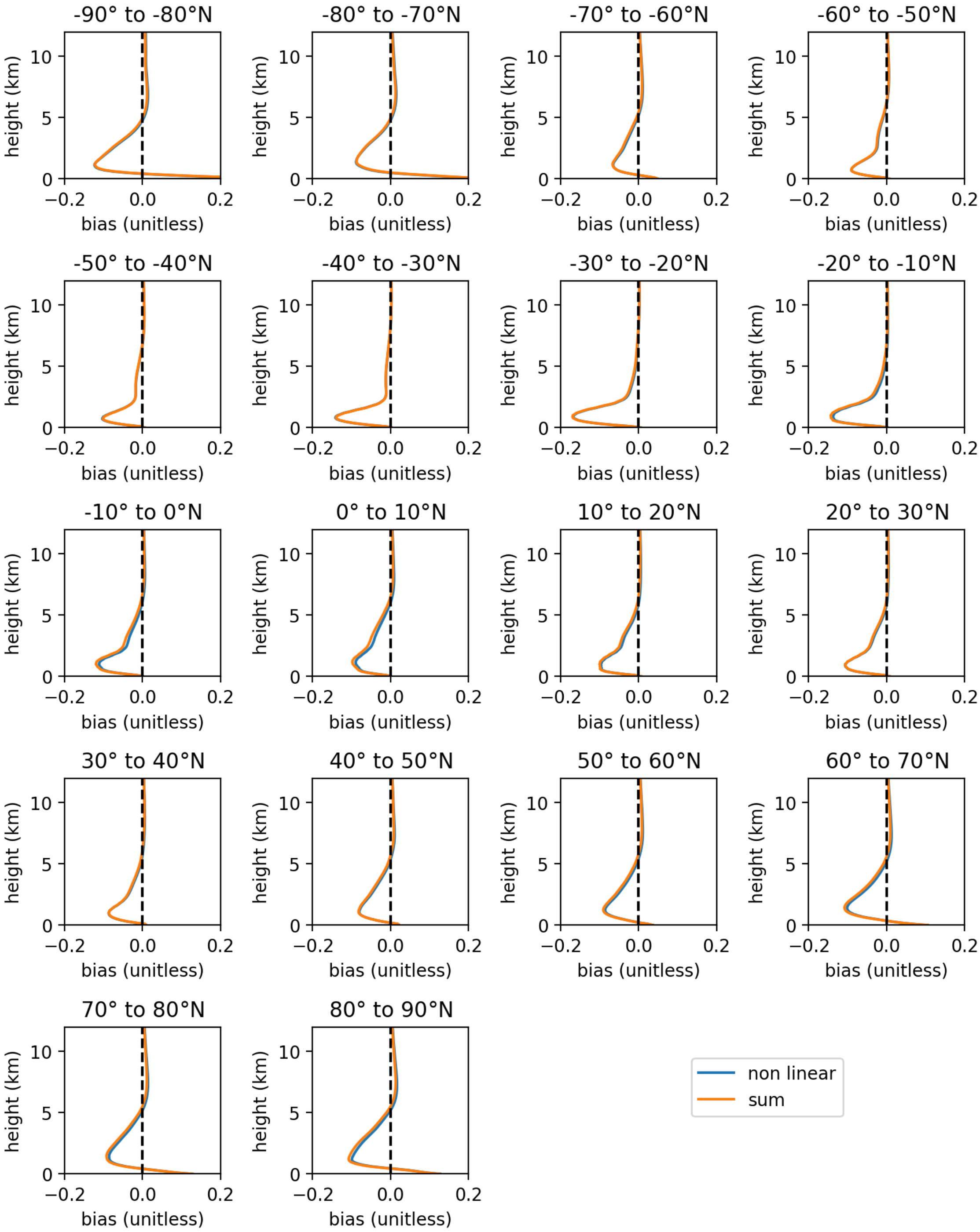

Figure 2.12: Bias of the profile shapes with respect to COSMIC profile shapes for the same data as in Fig. 2.11 (blue: non-linear fit; orange: sum method). The dashed black line represents the zero bias line.

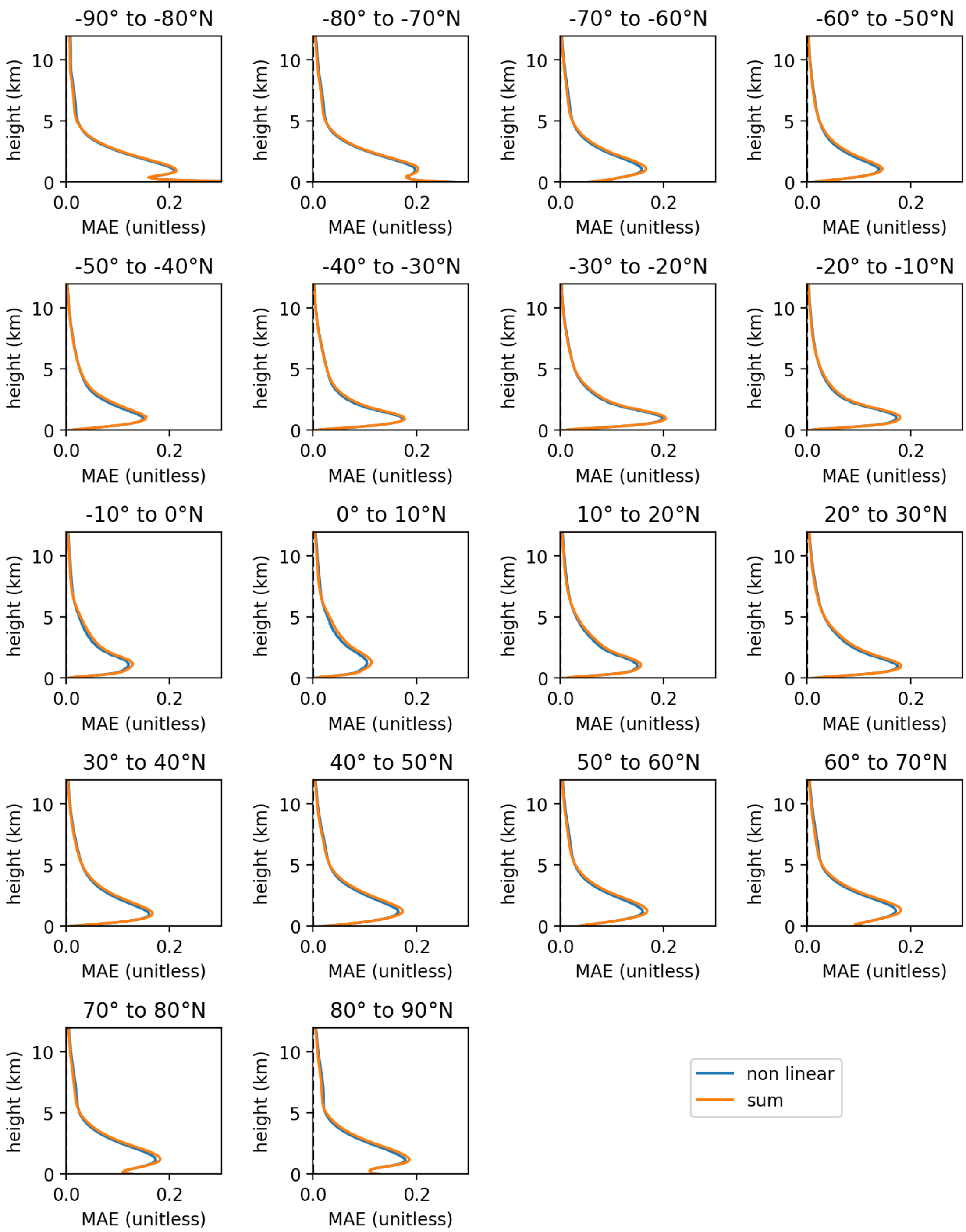

Figure 2.13: Mean absolute error of exponential profile shapes with respect to COSMIC profiles for the same data as in Fig. 2.11 (blue: non-linear fit; orange: sum method).

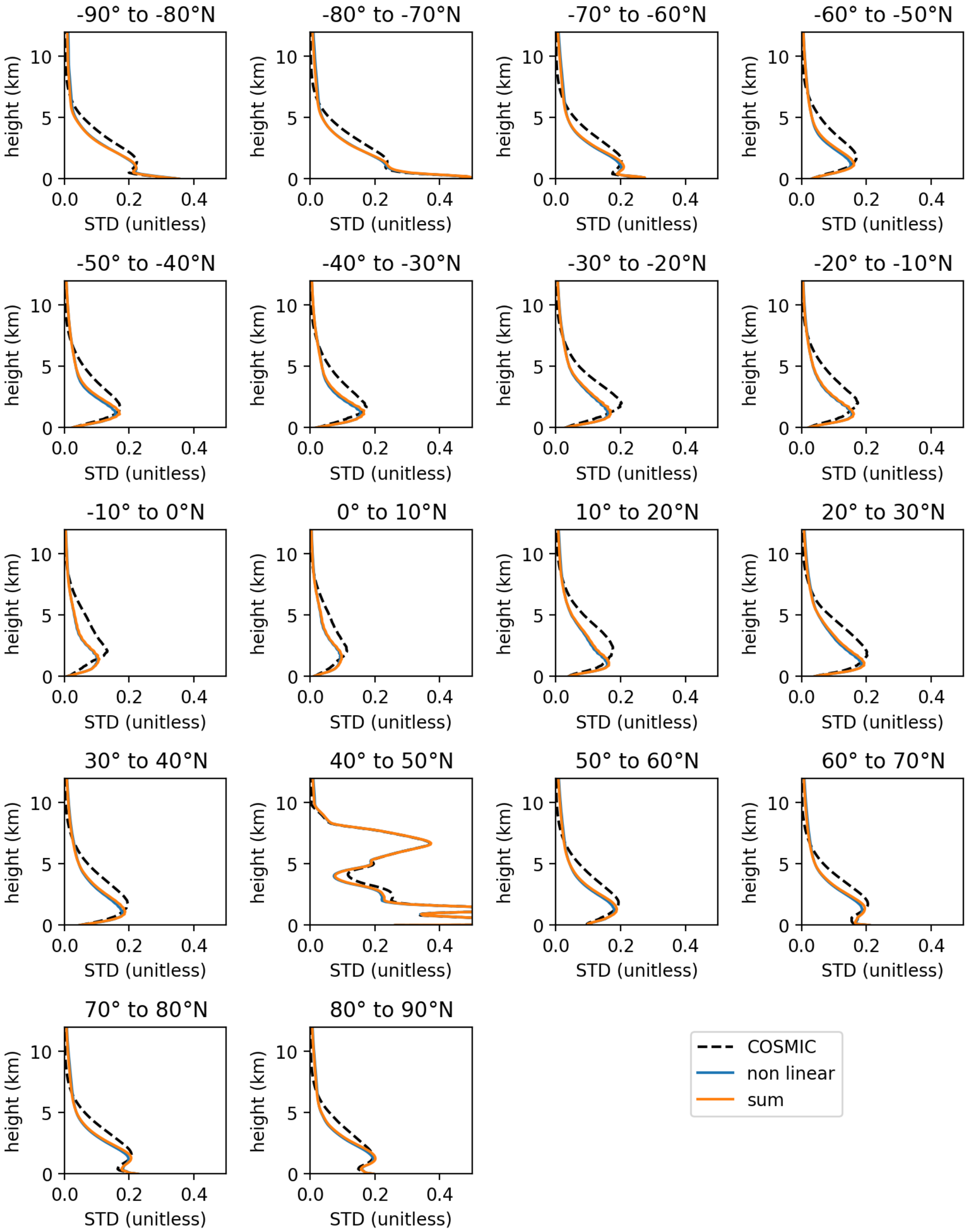

Figure 2.14: Standard deviations of the exponential and measured COSMIC profile shapes for the same data as in Figure 2.11. The blue solid line represents the results for the non-linear fit and the orange line for the sum method. The dashed black line represents the results for the COSMIC measurements.

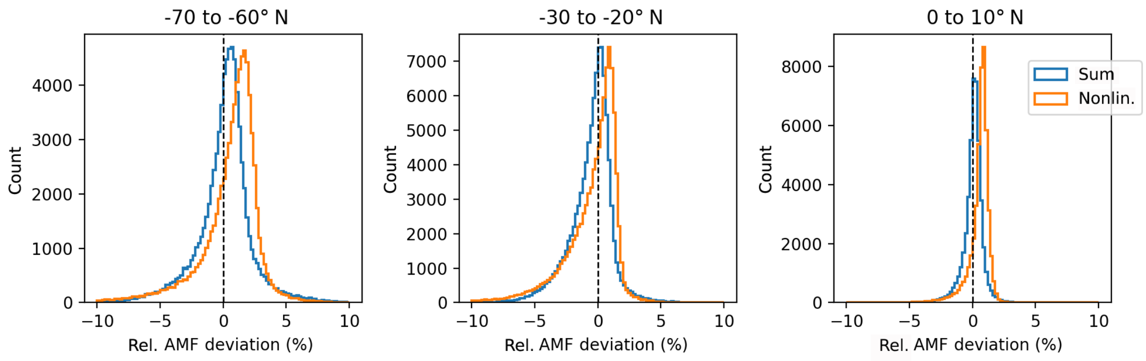

Figure 2.15: Histogram of the relative deviation of the calculated synthetic AMFs between the sum method (blue)/non-linear fit (orange) and the COSMIC profile for selected latitude bins (0 to 10, −30 to −20, and −70 to −60°N) assuming clear-sky conditions and nadir-viewing geometry.

In summary, the sum method is to be preferred because it provides more consistent results for clear-sky and cloudy-sky scenarios than the non-linear fit.

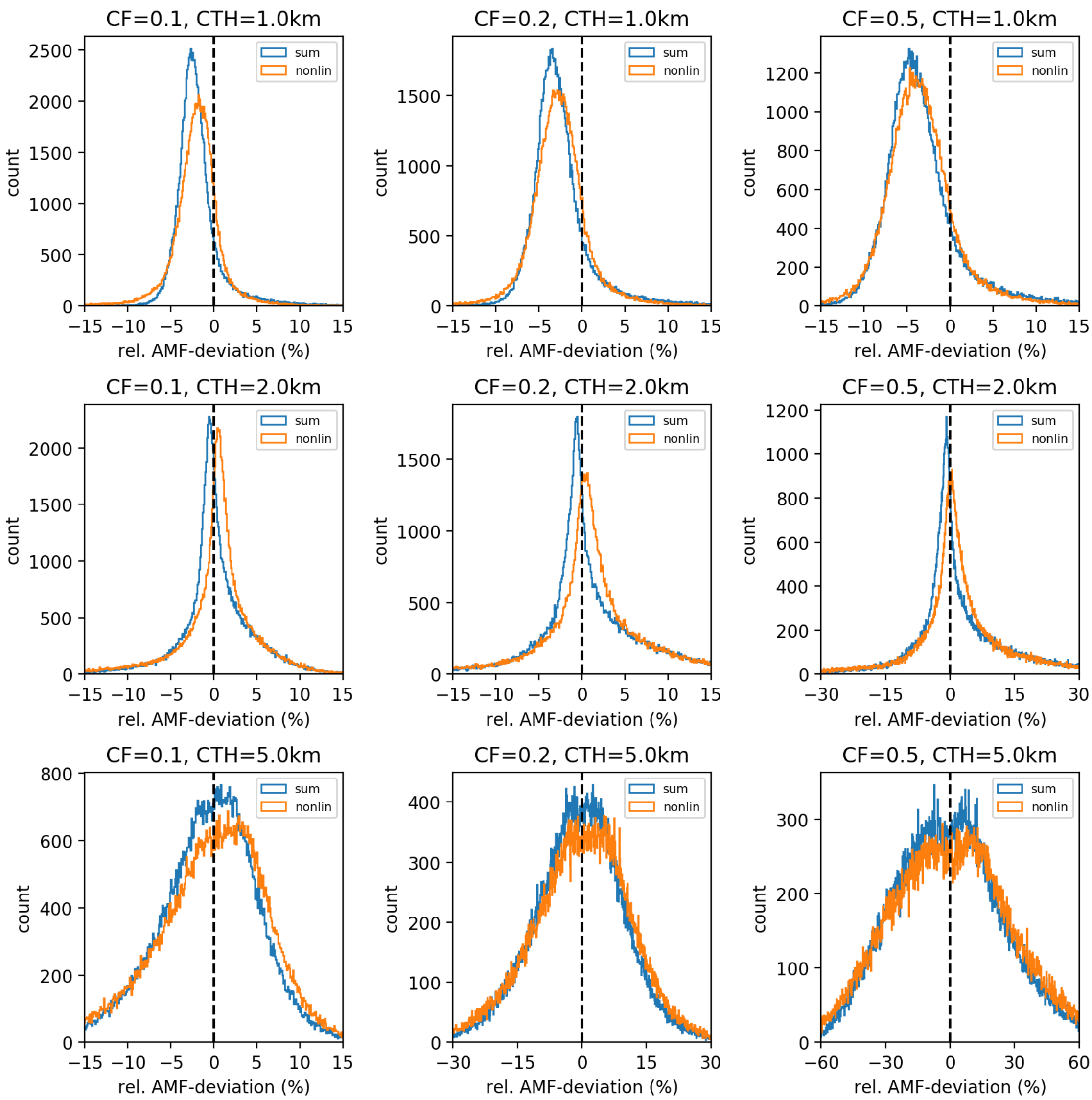

Figure 2.16: Histogram of the relative deviation of the calculated synthetic AMFs between sum method (blue)/non-linear fit (orange) and COSMIC profile for latitude bin from -30°N to -20°N assuming different cloudy-sky conditions (cloud fraction 10, 20 and 50% (left to right); cloud top height 1 km, 2 km and 5 km (top to bottom)) and nadir viewing geometry.

2.3.4 Parameterization of scale height

Figure 2.17 depicts the distribution of the calculated COSMIC scale height H_{sum} against the COSMIC TCWV for boreal summer over ocean for latitude bins of 10°. The regression fits (solid red lines) are based on orthogonal distance regression (ODR) using the "scipy.odr" package built on ODRPACK (Boggs et al., 1992). For low latitudes (tropics and subtropics) the scale height shows a high linear correlation with the H_2O VCD, with slopes around 0.04 and Pearson correlation coefficients R of 70% and above. In contrast, for high latitudes the slope increases up to 0.1, and the scatter also increases distinctively; i.e. the correlation coefficient only reaches values of around 0.3 in the polar regions. This decrease in linear agreement is likely caused by the higher atmospheric variability due to higher atmospheric dynamics in the midlatitudes. Also, the uncertainty is higher in the COSMIC profiles because a drier atmosphere leads to a smaller sensitivity of the COSMIC profile retrieval to water vapour concentrations (compare Kursinski et al., 1997).

Figure 2.18 illustrates the same panels as Fig. 2.17 but for data over land. In general, the scatter for all latitude bins has increased distinctively, resulting in an inferior linear agreement between the H_2O VCD and the scale height compared to the data over ocean, especially for latitude bins dominated by deserts and for the northern polar regions. Fortunately, the surface albedo of these regions is usually high, and thus the AMF is less dependent on the a priori profile shape. In addition, these regions are governed by an arid climate, and thus the retrieved H_2O VCDs are expected to be small. Correspondingly, the absolute H_2O VCD errors due to uncertainties in the AMF are still relatively small.

In the following sections a parameterization of the scale height with respect to H_2O VCD, latitude, and season is investigated separately for ocean and land. To distinguish between ocean and land surface, a land-sea mask derived from GSHHS coastline data (Wessel and Smith, 1996) is used.

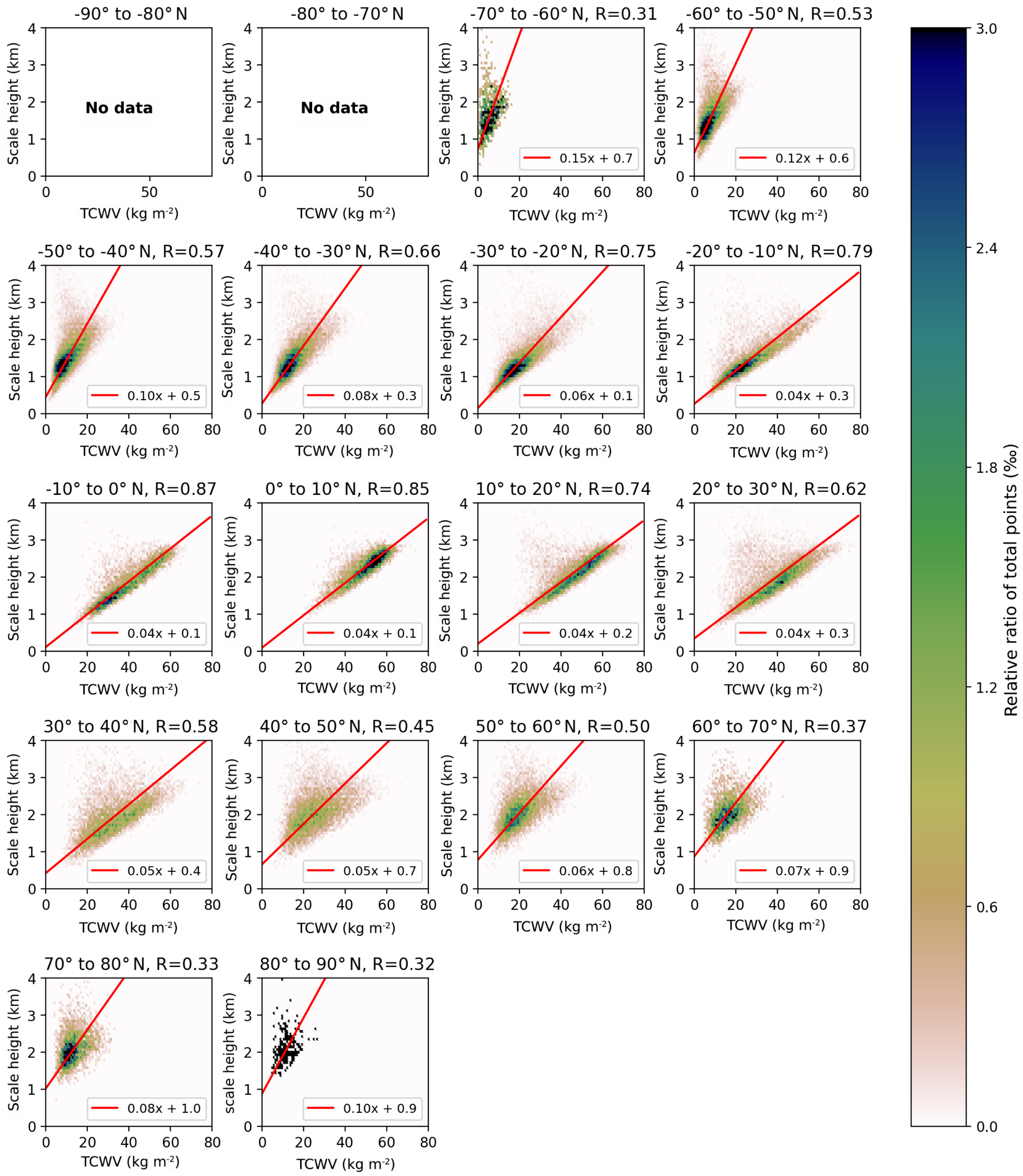

Figure 2.17: 2D histograms depicting the relation between calculated scale height and TCWV from COSMIC profiles for boreal summer (June, July, and August) only over ocean summarized in 10° latitude bins. Only latitude bins with a sample size of 1500 data points are illustrated. The colour indicates the relative share of total points within one bin of the histogram and the red line indicates the fit results of the orthogonal distance regression with detailed results in the legend of each subplot. In addition the Pearson correlation coefficient for each data set is given in the title of each subplot.

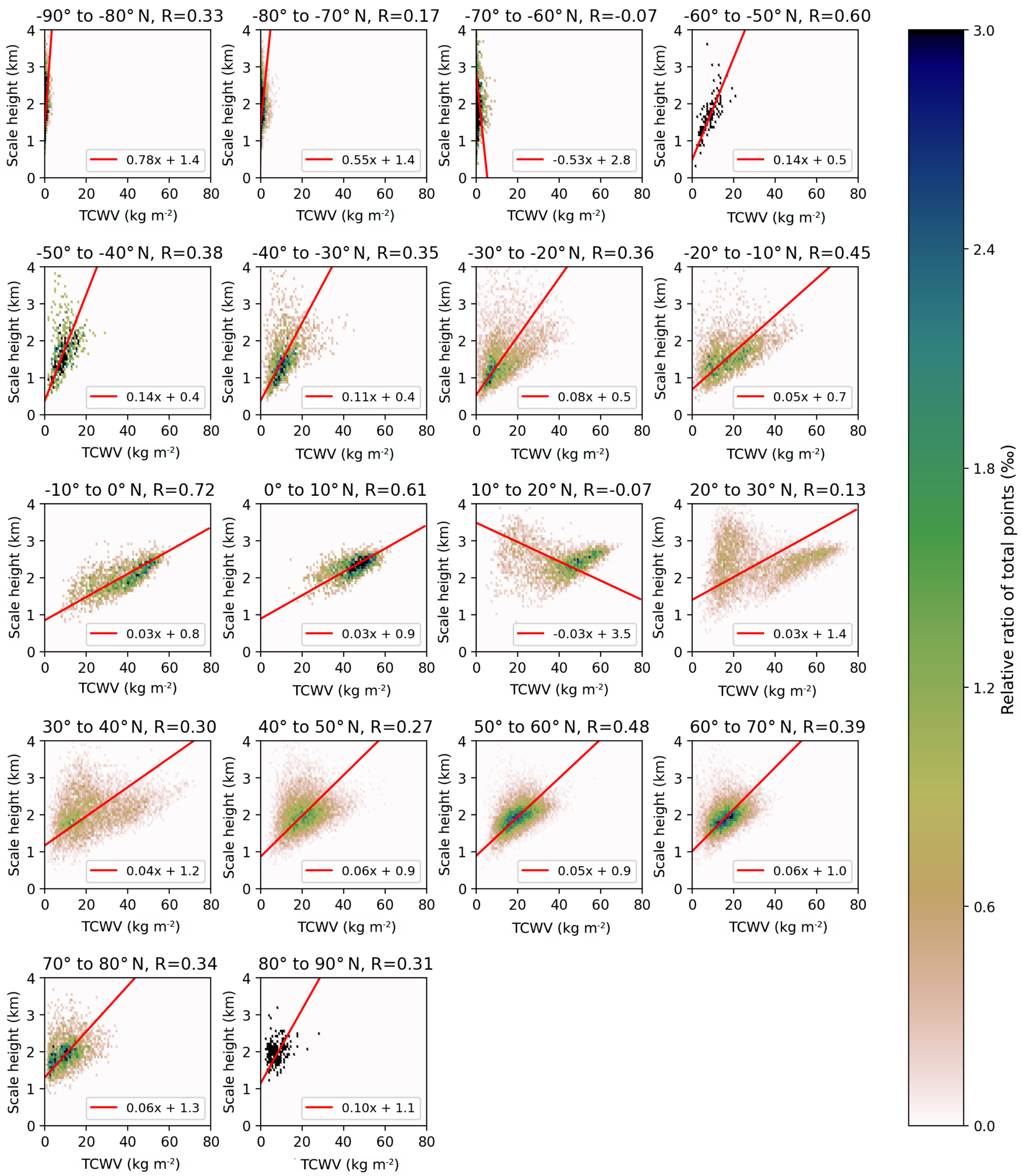

Figure 2.18: Same as Fig.2.17 but for data over land.

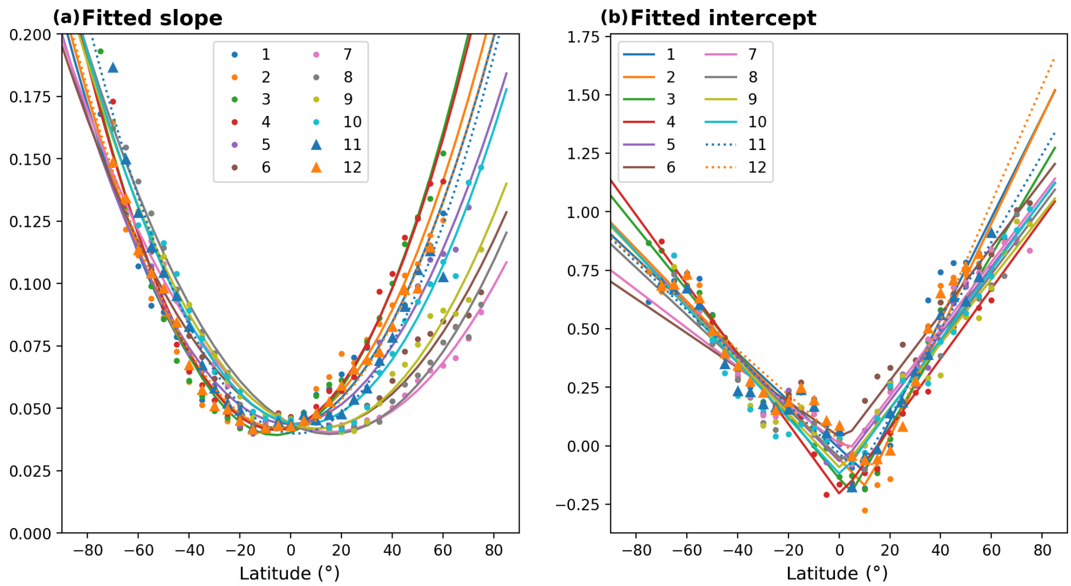

Figure 2.19: Summary of the results of the ODR fit between COSMIC scale height and COSMIC TCWV as a function of latitude and month for data over ocean. Panel **(a)** illustrates the fitted slopes and panel **(b)** the corresponding fitted intercepts whereby the coloured points represent the fit results and the lines represent the approximations for $\alpha(\theta, t)$ and $\beta(\theta, t)$ for each month.

2.3.4.1 Ocean

The regression line parameters of the ODR fit results between COSMIC TCWV and COSMIC scale height for each latitude bin for each month for data over ocean are illustrated in Fig. 2.19. The values for the fitted slopes (Fig. 2.19a) indicate a quadratic dependency with latitude and reveal a seasonal shift towards higher latitudes during July, August, and September. Also, the values for the fitted intercept vary with latitude and season.

Thus, the scale height over ocean H_{ocean} can be approximated as follows:

$$H_{\text{ocean}}(\text{VCD}, \theta, t) = \alpha(\theta, t) \cdot \text{VCD} + \beta(\theta, t) \tag{2.12}$$

with

$$\begin{aligned} \alpha(\theta, t) &= a_0(t) + a_1(t) \cdot \theta + a_2(t) \cdot \theta^2 \\ \beta(\theta, t) &= b_0(t) + b_1(t) \cdot \theta + b_2(t) \cdot |\theta - \theta_0(t)| \end{aligned} \tag{2.13}$$

with the latitude θ and the day of year t. The annual variation of the function parameters a_i, b_i, and θ_0 from Eq. (2.13) fitted for the monthly data sets (illustrated in Fig. 2.19) is depicted in Fig. 2.20.

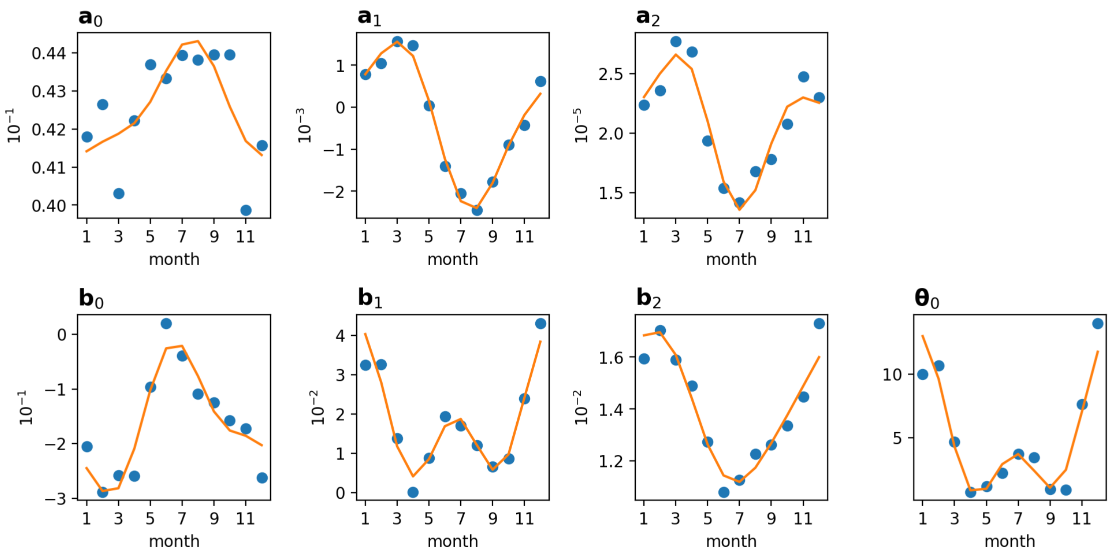

Figure 2.20: Monthly/seasonal dependence of the fit parameters (a_0, a_1, a_2) and $(b_0, b_1, b_2, \theta_0)$ for the functions $\alpha(\theta, t)$ and $\beta(\theta, t)$ in Eq. (2.13).

Most function parameters reveal an annual and semi-annual cycle over the year. Hence, these function parameters can be approximated by a superposition of two simple cosine functions with prescribed frequencies:

$$a_i(t) = a_{i1} \cdot \cos(a_{i2} + \omega t) + a_{i3} \cdot \cos(a_{i4} + 2\omega t) + a_{i5} \tag{2.14}$$

with t as the day of year and $\omega = \frac{2\pi}{365}$. Such functions have also been fitted and illustrated for the monthly data in Fig. 2.20 (solid orange lines), whereby it is assumed that the day of year representing the month is the first day of the month. For most function parameters the fits coincide well with the data points, and in the cases of suboptimal fit results the annual variation of the data is relatively small, indicating that our choice of parameterization is valid.

Altogether, 35 parameters have to be fitted to the complete data set of calculated COSMIC scale heights for the parameterization of the scale height over ocean. The goodness of the parameterization in approximating the scale height is illustrated in Fig. 2.21 for different latitude zones. For the latitude zones including the tropics (−15 to 15°N) and subtropics (−35 to 35°N) a good agreement between the parameterization and the calculated COSMIC scale height is obtained , with R^2 of 0.72 and 0.60 respectively. However, including higher latitudes in the evaluation, i.e. midlatitudes (−60 to 60°N) and polar regions (−90 to 90°N), leads to an increased scatter and a worsening of the parameterization (R^2 of 0.45 and 0.44 respectively). This inferior agreement is likely caused by the larger atmospheric variability in the midlatitudes (e.g. higher atmospheric dynamics) as well as an increased uncertainty in the COSMIC water vapour profile measurements due to lower water vapour concentrations.

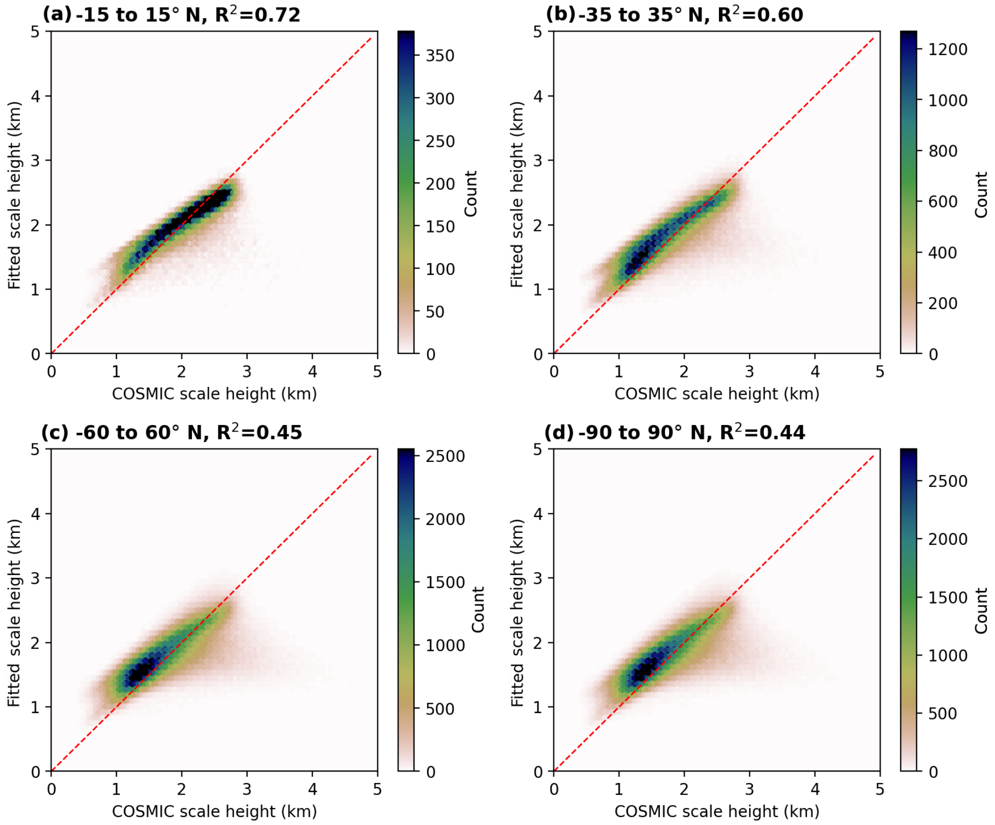

Figure 2.21: 2D histograms of the distribution between the parameterized scale height and the COSMIC scale height over ocean for selected global latitude zones.

2.3.4.2 Land

Figure 2.18 already revealed much larger scatter in the distribution of COSMIC TCWV and COSMIC scale height for data over land, indicating that the water vapour profile shape over land is less homogeneous than over ocean, likely due to further heterogeneously distributed water vapour sources, such as evapotranspiration by plants and soil. Thus, the H_2O VCD and scale height are likely to be dependent on the amount of vegetation; i.e. high vegetation is associated with high evapotranspiration and high water vapour concentrations near the ground, and thus the scale height should be close to the scale height over ocean. In contrast, low amounts of vegetation are associated with less evapotranspiration and a usually drier atmosphere, indicating that the scale height should be higher than over ocean.

To quantify the amount of vegetation, the Normalized Difference Vegetation Index (NDVI) is used, where a value of 1.0 indicates a high amount of vegetation and a value around 0.0 indicates no vegetation. As data source for the NDVI, data within the MODIS Aqua MYDC13C2 Version 6 product (Didan et al., 2015) is used. The following procedure is then applied: first, the parameterized scale height H_{ocean} is calculated assuming an ocean surface globally. Then

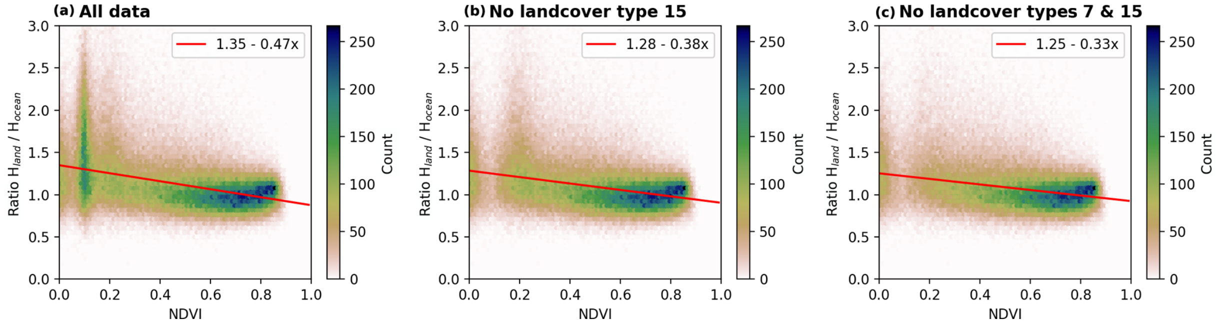

Figure 2.22: 2D histograms of the distribution between the ratio $H_{\mathrm{land}}/H_{\mathrm{ocean}}$ against the NDVI for different filtered data sets: panel **(a)** includes all data points, panel **(b)** includes all points except those with MODIS landcover type 15 (corresponding to deserts), and panel **(c)** includes all points except landcover types 7 (corresponding to open shrublands) and 15. The red solid line represents the linear fit result using the Siegel algorithm with details of the fit results in the legends of each panel.

Table 2.3: Fit results of the robust regression between the ratio of scale heights $H_{\mathrm{land}}/H_{\mathrm{sum}}$ and the NDVI for different filtered data sets.

Data set	slope	intercept
All data	–0.47	1.35
No landcover type 15	–0.38	1.28
No landcover type 7 & 15	–0.33	1.25

the ratio of the calculated COSMIC scale height over land H_{land} and the parameterized scale height H_{ocean} is determined.

Figure 2.22 shows the ratio $H_{\mathrm{land}}/H_{\mathrm{ocean}}$ as a function of the NDVI for data sets filtered by different landcover types and the solid red lines represent the robust regression results (summarized in Table 2.3) using the model from Siegel (1982). Panel (a) depicts the distribution for which no filter is applied. Except for low NDVI values, a linear relation between the ratio and the NDVI is observable with a gradual decrease in the ratio up to an NDVI value of 0.7 and a very weak increase from there on. However, for NDVI values around 0.1 the ratio varies strongly between 0.7 and 3.0. In Panel (b) the landcover classification from the MODIS Aqua MCD12C1 Version 6 product (Sulla-Menashe et al., 2019) is used to filter measurements for locations classified as landcover type 15 (corresponding to a desert). With this filter the ratio now only varies between 0.7 and 1.5, with a weak dependence on the NDVI. If, in addition, the locations of landcover type 7 (corresponding to open shrublands) are also filtered, the fit results of the robust regression change only slightly compared to the first filtered data set.

Hence, the scale height over land H_{land} can be approximated as the scale height over ocean H_{ocean} multiplied by a first-order polynomial of the NDVI:

$$H_{\mathrm{land}} = H_{\mathrm{ocean}}(\mathrm{VCD}, \theta, t) \cdot (\gamma_{\mathrm{land}} + \delta_{\mathrm{land}} \cdot \mathrm{NDVI}) \tag{2.15}$$

whereby in the following the results for the data set filtered for landcover types 7 and 15 globally are used. Since regions of landcover types 7 or 15 are usually arid, the retrieved H_2O VCD is small, and thus the error due to an inadequate parameterization of the AMF is much smaller than the fit error of the spectral analysis.

2.3.5 Iterative retrieval scheme

For the calculation of the H_2O VCD several AMF look-up tables (LUTs) have been precomputed for the different water vapour profile shapes with scale heights ranging from 0.5 to 5.0 km. These LUTs can then be used within a fixed-point iteration. In this case, the iterative retrieval scheme is based on a fixed-point iteration according to Steffensen's method (Steffensen, 1933; Wendland and Steinbach, 2005):

$$\mathrm{VCD}_{i+1} = \mathrm{VCD}_i - \frac{[f(\mathrm{VCD}_i) - \mathrm{VCD}_i]^2}{f\left(f(\mathrm{VCD}_i)\right) - 2 \cdot f(\mathrm{VCD}_i) + \mathrm{VCD}_i} \tag{2.16}$$

Here, f is a function which first estimates the scale height for a given VCD using Eqs. (2.12) and (2.15), then applies it to the precomputed AMF look-up tables and from that finally returns a new VCD. The advantage of Steffensen's method is that it does not need a derivative and is able to determine the fixed point even for the case of a non-contractive function (Wendland and Steinbach, 2005). For the first guess the initial VCD is derived from the SCD using a geometric AMF $\left(\mathrm{AMF}_{\mathrm{geo}} = \frac{1}{\cos(\mathrm{SZA})} + \frac{1}{\cos(\mathrm{VZA})}\right)$ and the iteration stops as soon as the logarithmic difference between two consecutive results is smaller than 5% (approximately 1 kg m^{-2} assuming an average H_2O VCD of 20 kg m^{-2}) or after six iteration steps. Also other values for the first guess have been checked and it could be confirmed that the convergence of the iterative scheme is independent of them.

Figure 2.23 illustrates a comparison of H_2O VCD distributions for the cases of using a global constant a priori water vapour profile shape (Fig. 2.23a) with a scale height of 2 km (in accordance with Weaver and Ramanathan, 1995) and using the iterative scale height approach (Fig. 2.23b) for all-sky conditions (i.e. no cloud filter applied) during an atmospheric river event at the western coast of the US on 13 February 2019. Figure 2.23c depicts the distribution of the water vapour scale height yielded during the iterative VCD conversion. The water vapour scale height varies a lot along the orbit and differs distinctively from 2 km, causing large deviations between the two approaches, particularly at pixels with high TCWV values and for

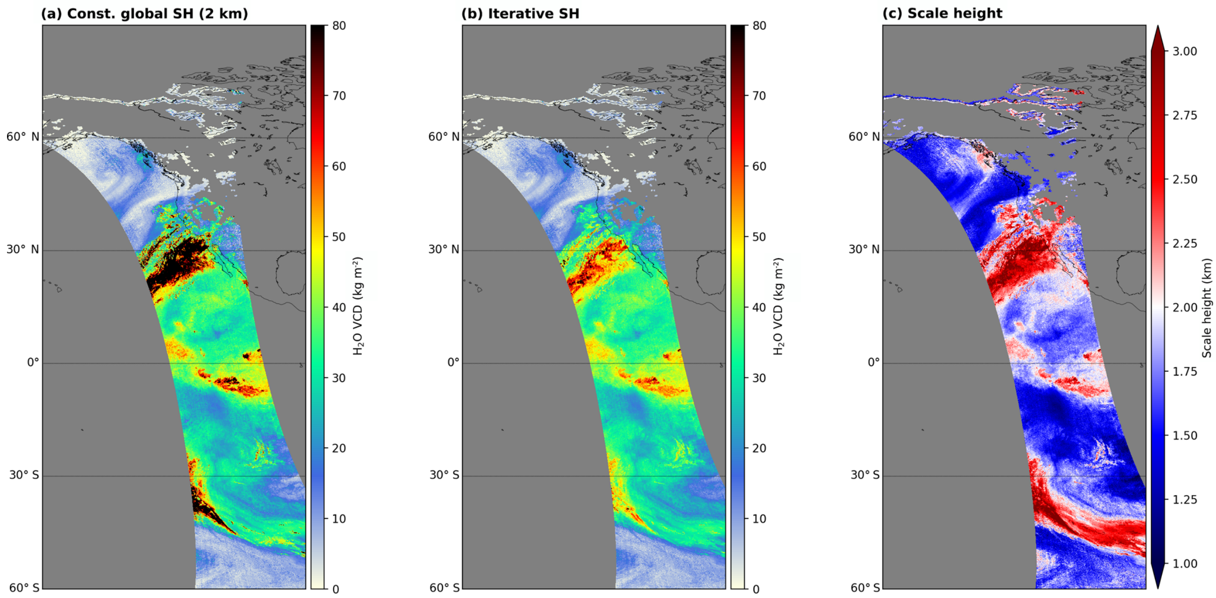

Figure 2.23: Comparison of the H_2O VCD calculated using a global constant a priori profile shape of 2 km **(a)** and the iterative scale height method **(b)** for all-sky conditions. Panel **(c)** illustrates the water vapour scale height estimated within the retrieval's VCD conversion. All panels show an atmospheric river hitting the eastern Pacific/western US coast on 13 February 2019. Invalid pixels are coloured grey.

clouded pixels. However, in contrast to the approach with a constant scale height, the iterative approach is still able to give reasonable TCWV results and does not exceed values higher than 80 kg m^{-2}.

Figure 2.24 illustrates the H_2O VCD distributions from calculations using constant, ERA5, and iterative profile shapes for the same scenario for clear-sky (effective cloud fraction CF $<$ 20%, top row) and all-sky (CF $\leq$ 100%, bottom row) conditions. The ERA5 data has been provided by the Copernicus Climate Data Store (Hersbach et al., 2018a, 2020) on a $0.25° \times 0.25°$ grid with a temporal resolution of 1 h and the model profile data have been interpolated to the TROPOMI pixel centre coordinates. In addition to the TROPOMI H_2O VCDs, Fig. 2.24 also depicts the TCWV distribution from microwave satellite sensor Special Sensor Microwave Imager/Sounder (SSMIS) f16, which has a temporal difference of around +2.3 h.

For the clear-sky case (top row) the VCD distributions between all profile approaches are almost identical, whereby for the constant scale height approach (first panel from the left) very high VCDs (exceeding values higher than 80 kg m^{-2}) can be observed at the edges of the cloudy regions in the northern subtropics. For the all-sky case (bottom row) the differences between all approaches are largest in cloudy regions: for instance, in the region of the atmospheric river, the VCDs from the constant and ERA5 profiles distinctively overestimate the VCD and exceed values higher than 80 kg m^{-2}. In contrast, even under these unfavourable observation conditions

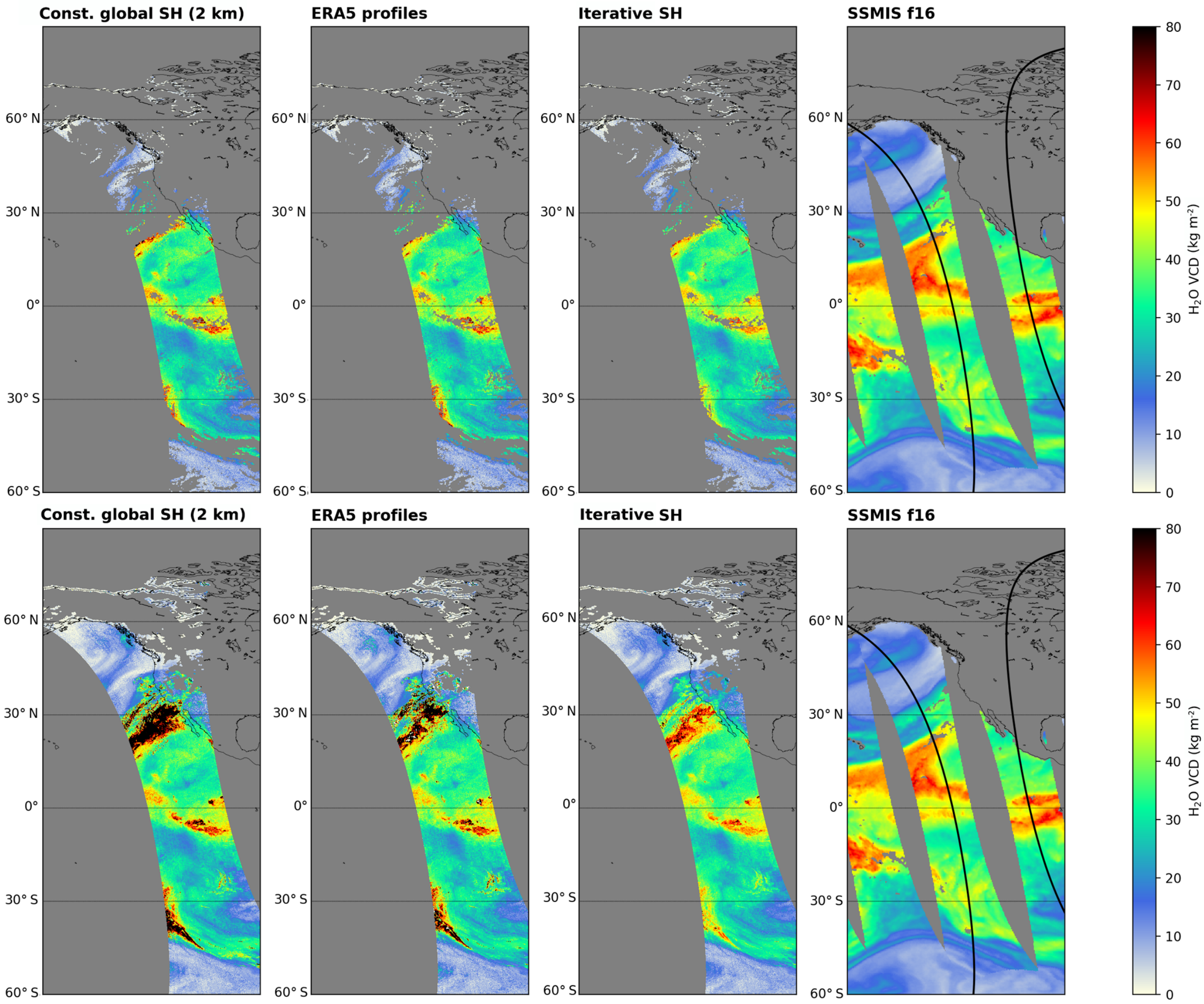

Figure 2.24: Comparison of the H_2O VCD calculated using a global constant a priori profile shape of 2 km (first from left), ERA5 profiles (second from left), and the iterative scale height method (third from left) for clear-sky (effective cloud fraction $< 20\%$; top row) and cloudy-sky conditions (effective cloud fraction $\leq 100\%$; bottom row) with TCWV from SSMIS f16 (right) for the same scenery as in Fig. 2.23. Invalid pixels are coloured grey. The solid black lines indicate the edges of the TROPOMI swath.

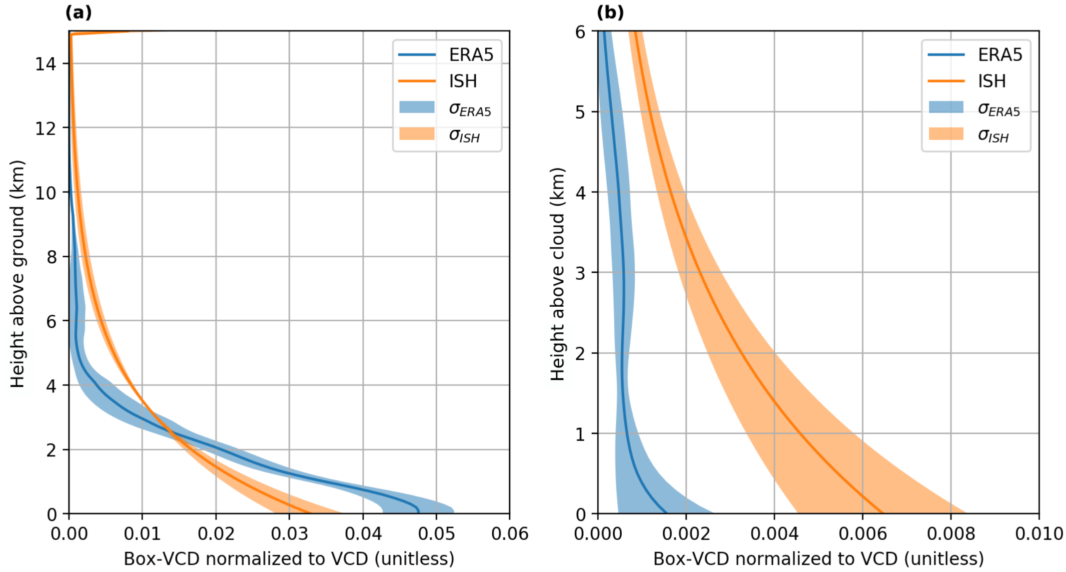

Figure 2.25: Mean normalized Box-VCD profiles of ERA5 and the iterative scale height approach for cases of distinctive VCD disagreement within the region of the atmospheric river. Panel **(a)** illustrates the mean of the selected profiles from the ground up to 15 km and panel **(b)** the mean of the same profiles, but from the cloud top up to 6 km above the cloud top. The solid lines indicate the mean profiles and the shaded areas the corresponding 1σ standard deviation.

the iterative approach is still able to give reasonable VCD values. Furthermore, the iterative approach shows an overall good agreement with the SSMIS observations.

Taking a closer a look at the reasons for the deviations of the results retrieved for the ERA5 profiles, Fig. 2.25 depicts the mean of the normalized water vapour profiles of ERA5 and the iterative scale height approach for the atmospheric river region (around 30° N). Figure 2.25a shows the water vapour profile from the ground up to 15 km. In comparison to the iterative approach, ERA5 is much drier above approximately 2.5 km for these particular cases, indicating that ERA5 might systematically underestimate the water vapour content above the cloud within the region of the atmospheric river. This finding is further supported by Fig. 2.25b, which illustrates the normalized water vapour profiles above the cloud top: ERA5 profiles are close to 0 and show only small variations, whereas the profiles of the iterative approach indicate higher water vapour concentrations along with a much higher variability. One potential reason for the discrepancies of ERA5 could be the missing observational input data for the reanalysis: without observations, the reanalysis model is dominated by its a priori information (e.g. a climatological mean), so that it can be systematically distorted from the real atmosphere. However, further investigations of possible ERA5 biases are beyond the scope of this study.

2.4 Evaluation of different surface albedo input data

The surface albedo has a strong impact on the radiative transfer and thus also on the AMF. Hence, the impact of different albedo products on the TCWV retrieval is investigated: the OMI monthly (a) mean and (b) minimum Lambertian equivalent reflectance (LER) at 442 nm from Kleipool et al. (2008) and (c) MODIS Aqua blue surface reflectance from the MODIS MYD13C2 Version 6 product (Didan et al., 2015). The MODIS reflectance covers a broad spectral window from 459 to 479 nm. Thus, to account for the different spectral windows of the albedo products, the MODIS albedo is scaled by factor of 0.9. This factor was estimated by calculating the ratio between 472 and 442 nm of the OMI yearly minimum LER over parts of Australia where cloud contamination is generally low and hence the OMI LER has reasonably accurate values. Moreover, Kleipool et al. (2008) also found a similar value of 0.88 for 440 nm in their comparative study between MODIS and OMI via RTM simulations.

Figure 2.26 illustrates the global mean H_2O VCD of boreal summer 2018 for the different albedo input data over land (top row: monthly mean OMI LER, middle row: monthly minimum OMI LER, bottom row: scaled monthly MODIS Aqua blue surface reflectance). In the tropical and subtropical regions the OMI albedos cause a distinctive separation of the VCDs between land and ocean, in particular at the coasts of South America, Africa, and Indonesia. These aforementioned regions are often affected by cloud cover, which might cause the OMI albedo statistics to be unable to filter cloudy cases correctly, so that cloud-contaminated observations are used within the albedo calculations. As a consequence, the values in the OMI albedo are too high and lead to an overestimation of the AMF, which in turn causes an underestimation of the H_2O VCD.

In contrast, MODIS pixels have a much higher spatial resolution and MODIS' NIR channels are more sensitive to cloud contamination, yielding a higher sample size and allowing for correct cloud filtering. Hence, the H_2O VCD distribution using the MODIS surface reflectance results in a much smoother transition from ocean to land and in general much higher VCD values over land along the Equator. Thus, in the following a combination of the MODIS and OMI albedos is used: the scaled MODIS Aqua blue surface reflectance over land and the monthly minimum OMI albedo over ocean.

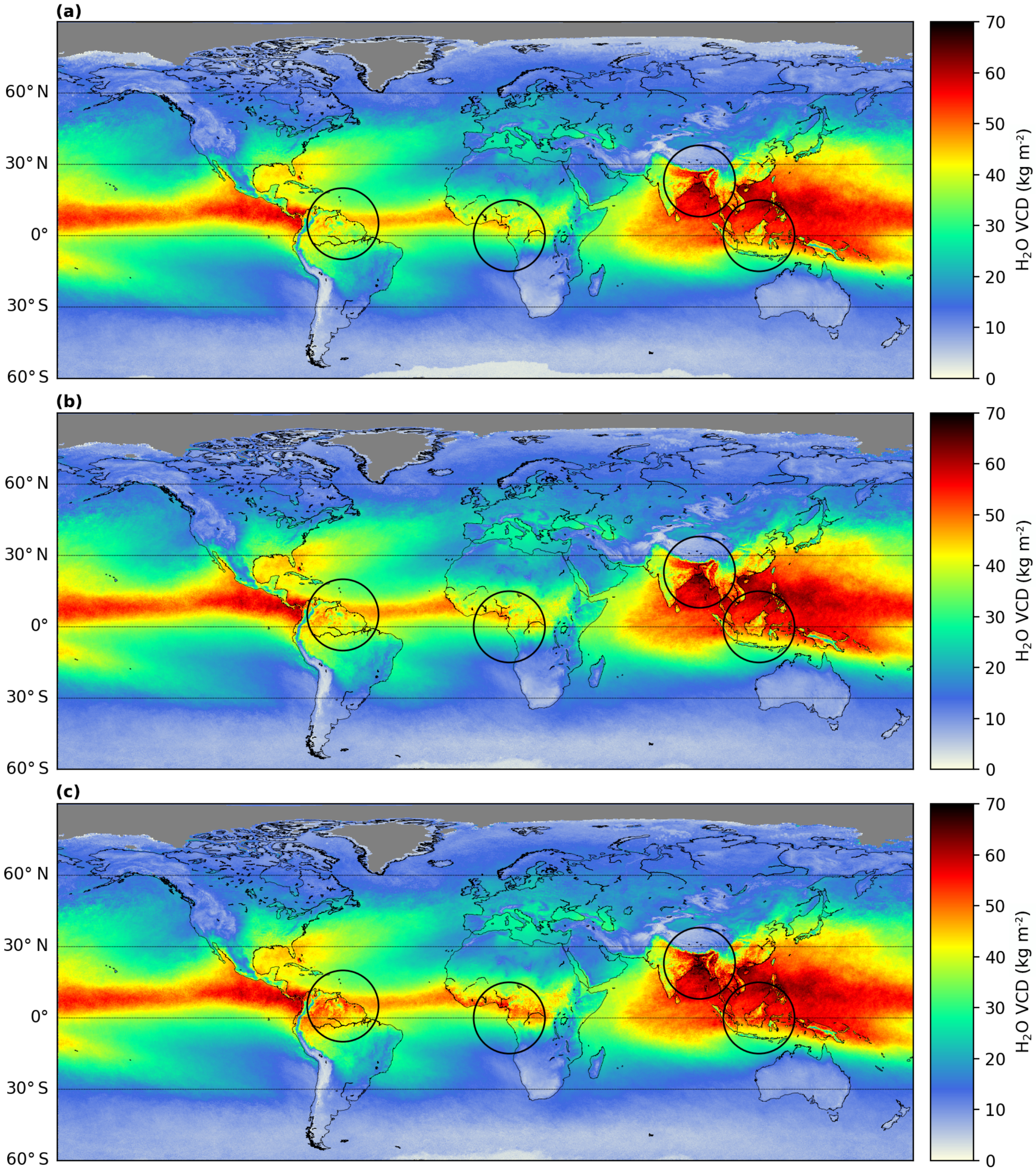

Figure 2.26: Comparison of the effect of different land albedo input data on the mean H_2O VCD for boreal summer 2018 (**a**: OMI monthly mean LER, **b**: OMI monthly minimum LER, **c**: scaled MODIS Aqua blue surface reflectance). Only pixels with an effective cloud fraction smaller than 20% are included.

2.5 Uncertainty estimation

The error budget of the H_2O VCD is determined by the propagation of the main error sources of the fitted SCD and the precalculated AMF. Errors in the SCD are mainly caused by random errors, like the photon noise, and systematic errors, e.g. the uncertainty of the absorption cross section, whereas errors in the AMF are mostly systematic with random contributions.

2.5.1 Uncertainties in the slant column density

Table 2.4 summarizes the different error sources for the H_2O SCD and the corresponding estimated uncertainties. As demonstrated in Sect. 2.2.1.2 the water vapour absorption cross section varies systematically between the different HITRAN versions. Hence, it is assumed that the uncertainty of the water vapour cross section is of the same order of magnitude as the changes between the different cross-section versions, i.e. approximately around 10%. Considering the LP-DOAS comparisons (see Sect. 2.2.1.2) these errors are estimated to be around 5% for this study.

The retrieval's spectral analysis directly yields the 1σ standard fit error of the H_2O SCD, which is usually dominated by noise. For a better understanding of these fit errors, they are separated into data for small/large solar zenith angles (SZA <20° and 70° $<$ SZA $\leq$ 90° respectively), low/high surface albedo ($<$ 3% and >15% respectively), and clear-/cloudy-sky observation conditions (CF $<$ 5% and CF $>$ 20% respectively). The distributions of the standard and relative fit errors of the spectral analysis are given in Figs. 2.27 and 2.28 respectively. The median values in Fig. 2.27 indicate that the standard errors for high SZA (around 0.3×10^{23} molec cm^{-2}) are twice as high as for small SZA (around 0.15×10^{23} molec cm^{-2}). Under clear-sky conditions the standard error for small surface albedo values is larger than for high surface albedo, but for cloudy conditions it does not depend on the surface albedo.

Figure 2.28 reveals that the relative fit errors for high SZAs are higher than for low SZAs. However, the locations of maximal probability density and the medians also indicate that the distributions are right-skewed, in particular for high SZA scenarios: for these scenarios the

Table 2.4: Summary of the different error sources considered in the H_2O SCD uncertainty.

Source	Type	Parameter uncertainty	Estimated uncertainty in SCD
Absorption cross section	Systematic	10%	10%
DOAS fit error	Random	–	SZA $<$ 20°: 0.15×10^{23} molec cm^{-2} ($\sim$ 10%)
	–	–	SZA $>$ 70°: 0.3×10^{23} molec cm^{-2} ($\sim$ 30%)

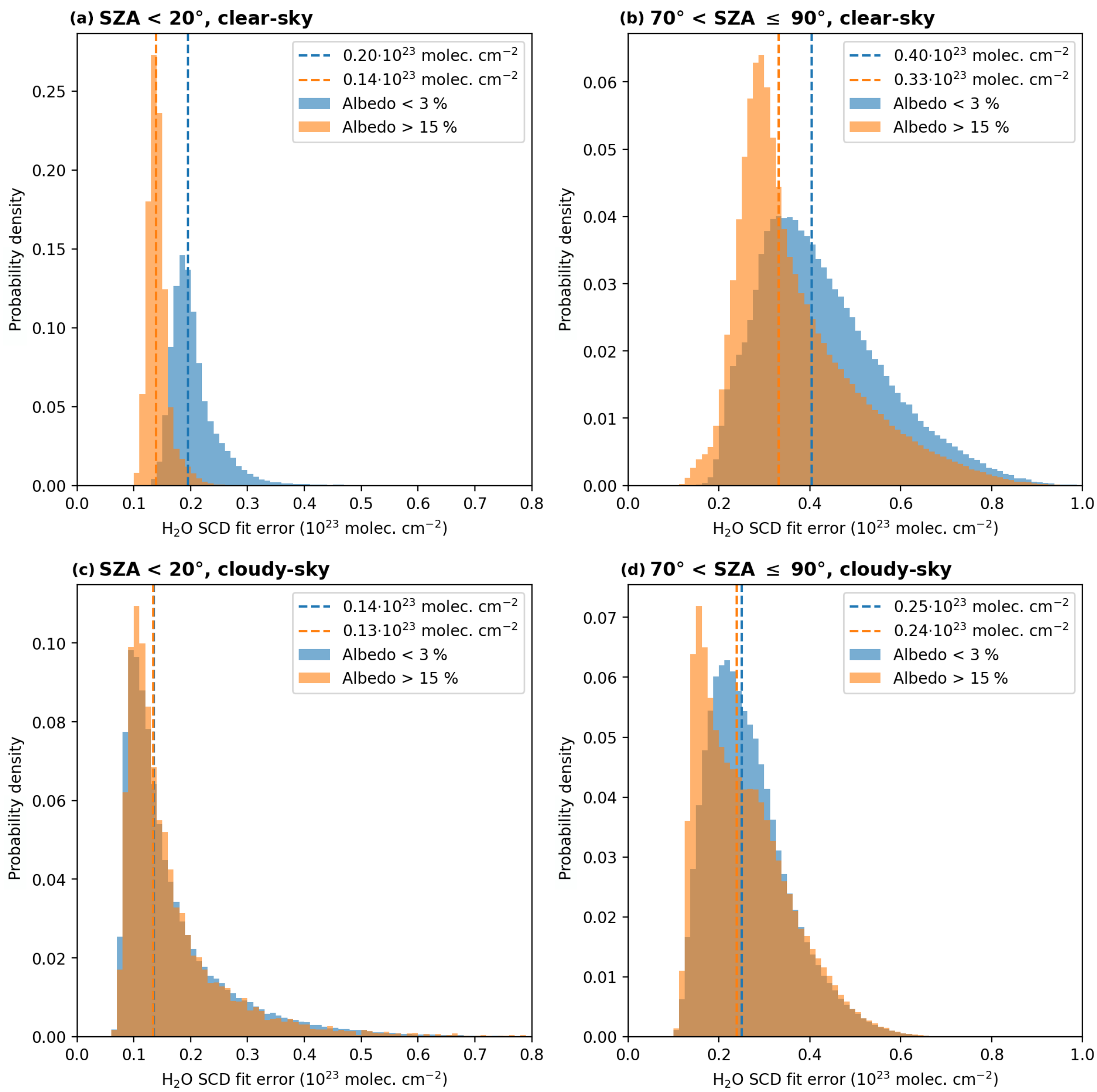

Figure 2.27: Histograms of the standard H_2O SCD fit error distribution for small (SZA<20°, **a, c**) and large (70° < SZA ≤ 90°, **b, d**) solar zenith angles for relatively small (< 3%, orange) and high (> 15%, blue) surface albedo values for clear-sky (cloud fraction < 5%, **a, b**) and cloudy-sky (cloud fraction > 20%, **c, d**) conditions. The coloured dashed lines represent the median of the respective distributions and their values are given in the legend of each panel.

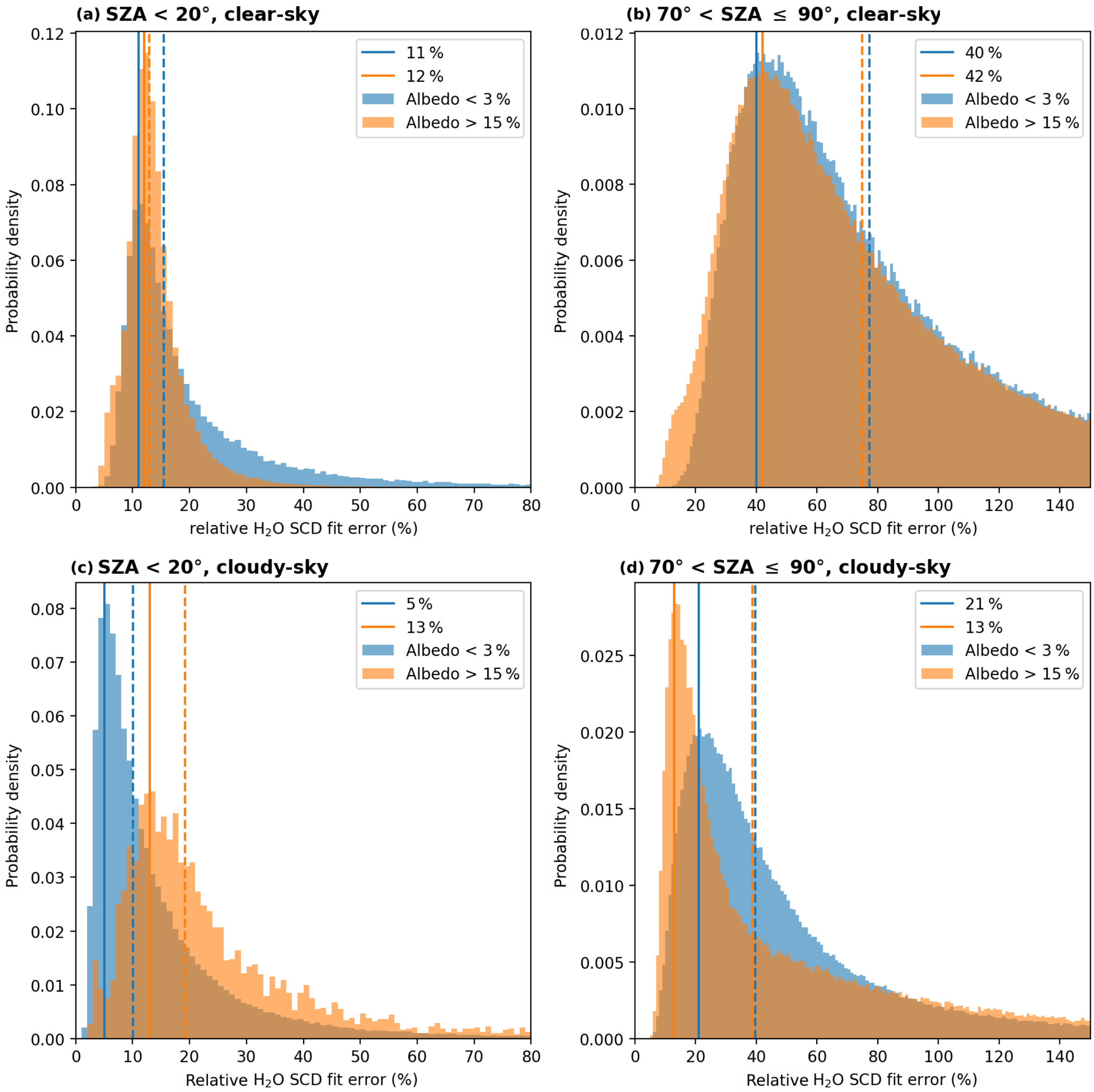

Figure 2.28: Histograms of the relative H_2O SCD fit error distribution for small (SZA $< 20°$, **a, c**) and large ($70° <$ SZA $\leq 90°$, **b, d**) solar zenith angles for relatively small ($< 3\%$, orange) and high ($>15\%$, blue) surface albedo values for clear-sky (cloud fraction $< 5\%$, **a, b**) and cloudy-sky (cloud fraction $> 20\%$, **c, d**) conditions. The coloured dashed lines represent the median of the respective distributions and the solid lines represent the location of maximal probability density (values given in the legend of each panel).

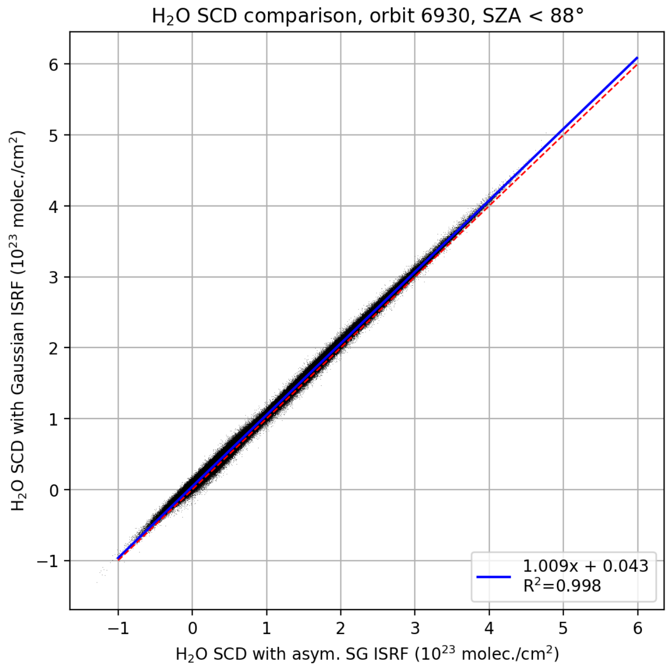

Figure 2.29: Comparison of H_2O SCDs fitted assuming a Gaussian and an asymmetric Super-Gaussian ISRF. Values are taken from orbit 6930 for a solar zenith angle $< 88°$. The blue solid line indicates the results of the linear regression and the red dashed line the 1-to-1 diagonal.

relative errors easily exceed values of 100%. Nevertheless, using the locations of maximal probability density as a rule-of-thumb estimate, relative fit errors have values around 10% for low SZAs and approximately 30% for high SZAs.

To estimate errors associated with uncertainties of the ISRF, the H_2O SCD has been calculated for orbit 6930 using a Gaussian ISRF (instead of an asymmetric Super-Gaussian) and compared to the SCDs from the "standard" retrieval setup for SZA $< 88°$. The comparison depicted in Fig. 2.29 reveals that the SCDs using the Gaussian ISRF highly correlate with the "standard" SCDs and only differ by approximately 1%. Considering the much higher fit errors, errors due to uncertainties in the ISRF are negligible.

2.5.2 Uncertainties in the AMF

The uncertainty in the AMF depends on the uncertainty of its input parameters. Because the parameters of the viewing geometry (i.e. solar zenith angle, line-of-sight angle, and solar relative azimuth angle) are known with high accuracy, the most important uncertainties are uncertainties of the surface albedo, cloud fraction, cloud top height, and water vapour profile shape. To estimate the contribution of each input parameter to the overall AMF uncertainty, standard scenarios have been defined (summarized in Table 2.5) for which the AMF are calculated from the precalculated LUT. Then the input parameter is varied for each scenario according to its uncer-

Table 2.5: Standard retrieval scenarios for the estimation of AMF error.

Parameter	Values
Surface albedo	2 %, 7 %, 20 %
Solar zenith angle	0°, 45°, 90°
Water vapour scale height	1 km, 2 km, 3 km
Cloud fraction	10 %, 20 %, 50 %
Cloud top height	1 km, 2 km, 5 km
Line-of-sight angle	–90°

Table 2.6: Summary of different error sources considered in the AMF uncertainty.

Parameter	Type	Parameter uncertainty	Source	Estimated uncertainty in AMF	
				clear-sky	cloudy-sky
Surface albedo	Random+systematic	0.02	Kleipool et al. (2008)	5 %–25 %	5 %–10 %
Scale height (ocean)	Random	0.45 km	–	2 %–10 %	5 %–20 %
Scale height (NDVI, low)	Random	0.73 km	–	5 %–25 %	20 %–50 %
Scale height (NDVI, high)	Random	0.34 km	–	2 %–7 %	5 %–15 %
Cloud fraction	Random+systematic	0.05	Veefkind et al. (2016)	–	2 %–10 %
Cloud top height	Random+systematic	0.5 km	–	–	5 %–15 %

tainty assumption listed in Table 2.6. The uncertainties of the water vapour scale height have been derived from the fit results of the intercomparisons between the measured COSMIC scale height and the parameterized scale height over ocean (see Fig. 2.21) and land (see Fig. 2.22).

Figure 2.30 depicts box-whisker plots of the relative AMF errors due to uncertainties in surface albedo and scale height for the standard clear-sky scenarios of surface albedo, solar zenith angle, and scale height. It reveals that uncertainties in surface albedo and scale height over areas with low amounts of vegetation have the strongest impact on the AMF and can cause AMF errors larger than 30%, in particular for scenarios with low surface albedo or high solar zenith angle. On average the median values of the AMF errors typically vary around approximately 10%.

Figure 2.31 illustrates box-whisker plots of the relative AMF errors due to uncertainties in surface albedo, scale height, cloud fraction, and cloud top height for all standard scenarios listed in Table 2.5. In contrast to the clear-sky scenarios, the impact of the surface albedo uncertainties has strongly decreased, but in general the contributions of all AMF errors have increased distinctively. The main source of the AMF errors is still the uncertainty of the scale height over low vegetation, whose median values vary between 20 % and 50 % but can also cause AMF errors larger than 60 %.

Table 2.6 summarizes the results of the different error sources considered in the AMF uncertainty for clear- and cloudy-sky conditions. For clear-sky conditions one can typically assume a relative AMF error around 10–15 % and for cloudy-sky conditions around 10–25 %.

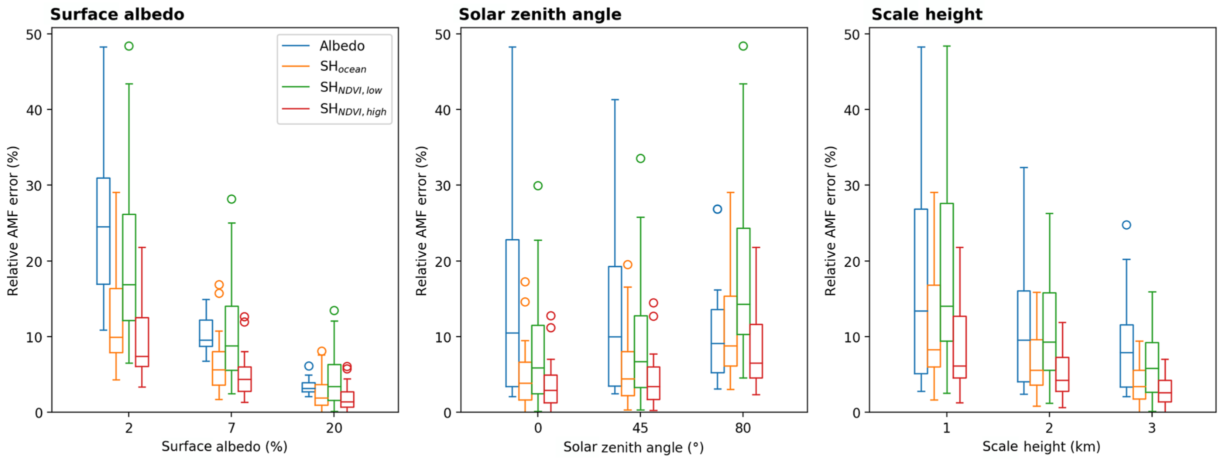

Figure 2.30: Box-whisker plots of the relative AMF errors for clear-sky conditions due to uncertainties within the retrieval's input parameters (blue: surface albedo, orange: scale height over high vegetation, green: scale height over low vegetation, red: scale height over ocean) according to the uncertainty assumptions in Table 2.6 and simulated for the standard scenarios of the surface albedo, solar zenith angle, and scale height given in Table 2.5.

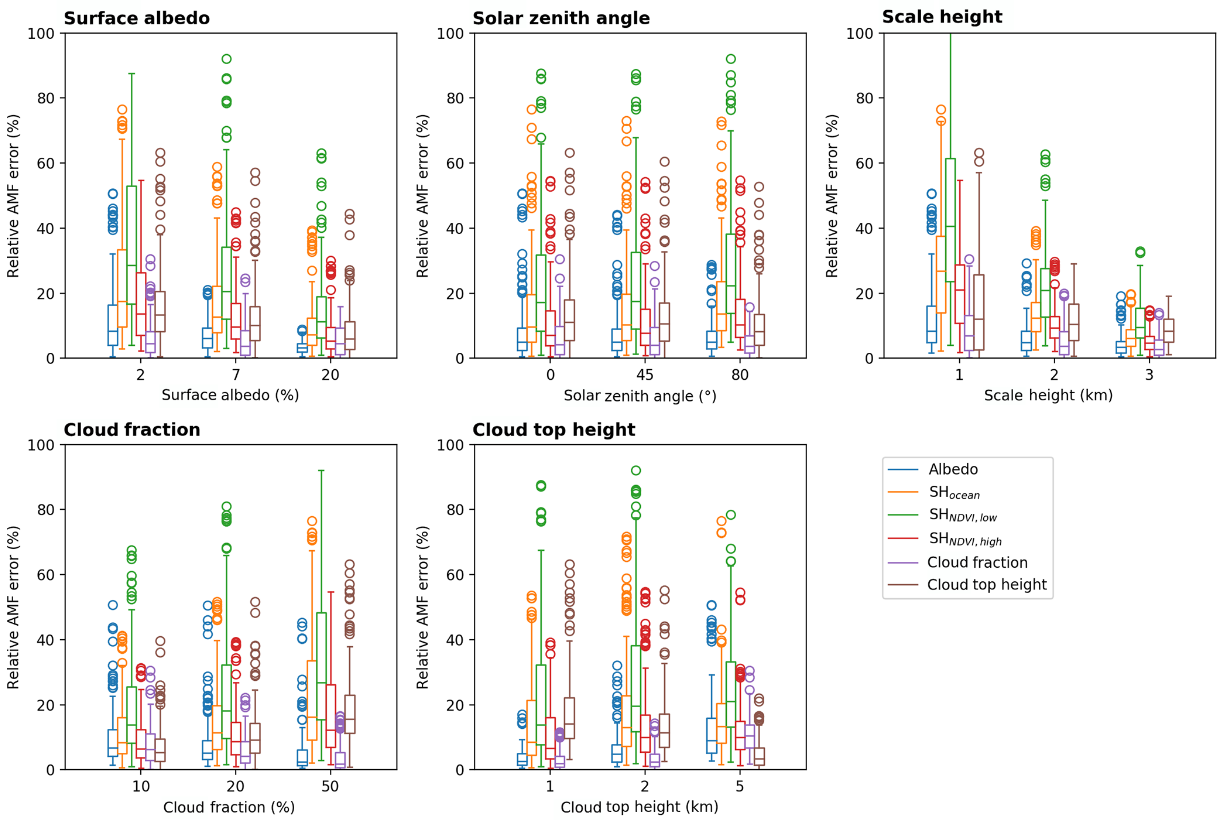

Figure 2.31: Box-whisker plots of the relative AMF errors for cloudy-sky conditions due to uncertainties within the retrieval's input parameters according to the uncertainty assumptions in Table 2.6 and simulated for the standard scenarios given in Table 2.5.

2.5.3 Total H_2O VCD uncertainty

The total relative H_2O VCD uncertainty can be approximated by

$$\frac{\Delta \mathrm{VCD}}{\mathrm{VCD}} = \sqrt{\left(\frac{\Delta \mathrm{AMF}}{\mathrm{AMF}}\right)^2 + \left(\frac{\Delta \mathrm{SCD}}{\mathrm{SCD}}\right)^2} \tag{2.17}$$

With our findings of typical relative AMF and H_2O SCD uncertainties, the total relative VCD uncertainty is typically around 10–20 % for observations during clear-sky conditions, over ocean surface, and at low solar zenith angles. During partly cloudy-sky conditions, over land surface, and at high solar zenith angles the error reaches values of approximately 20–50 %.

2.6 Validation study

In order to evaluate the retrieval's performance, a validation study has been conducted for the time ranges of boreal summer (June, July, and August) 2018 and boreal winter (December, January, and February) 2018/2019 whereby only clear-sky observations (i.e. pixels with an effective cloud fraction smaller than 20 %) and ice- and snow-free pixels are included. To avoid extreme outliers, only observations with an AMF > 0.1 are considered. As reference data for the validation TCWV from the Special Sensor Microwave Imager/Sounder (SSMIS), from the reanalysis model ERA5, and from the ground-based GPS network SuomiNet are used. For the sake of completeness, also higher cloud fractions have been briefly investigated at the end of each subsection.

As cloud input data the cloud information (effective cloud fraction at 440 nm and cloud top height) as well as the surface altitude from the TROPOMI L2 NO_2 product (Van Geffen et al., 2019) are used. As surface albedo input data the combination of the modified MODIS and OMI albedo described in Sect. 2.4 is used. Here, it is important to mention that the calculation of the effective cloud fraction is based on the OMI LER from Kleipool et al. (2008). However, for the calculation of the cloud top height the FRESCO algorithm (Wang et al., 2008) is applied, which uses the GOME-2 LER from Tilstra et al. (2017). Because of the different overpass time of GOME-2 (around 10:00 LT) this LER is not fully representative for TROPOMI observations, so these inconsistencies could cause additional uncertainties.

To distinguish between ocean and land surface, a land-sea mask has been derived from GSHHS coastline data (Wessel and Smith, 1996), in which the pixel centre coordinates are used for the separation into land and ocean. As the NDVI is not available over lakes, they are treated as ocean.

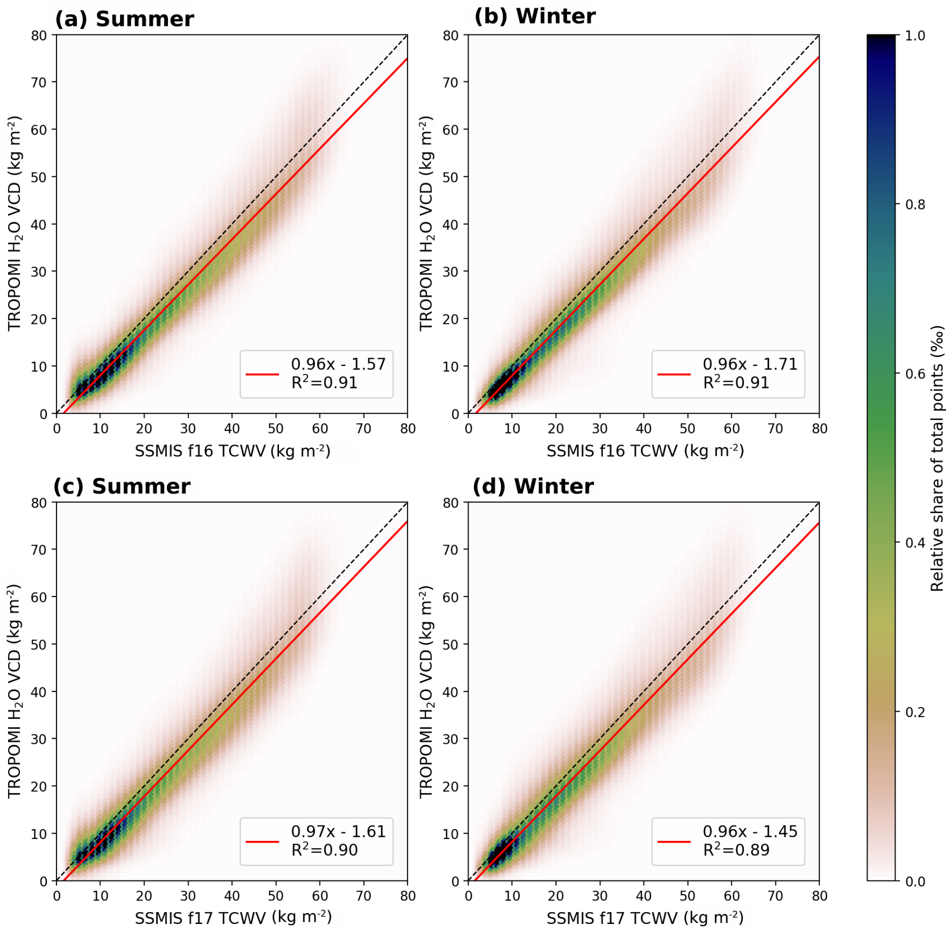

Figure 2.32: 2D histograms for the comparison between TROPOMI and SSMIS f16 **(a, b)** and f17 **(c, d)** for clear-sky conditions (CF $<$ 20%) for boreal summer **(a, c)** and boreal winter **(b, d)**, where the colour indicates the relative share of total data points. The black dotted line indicates the 1-to-1 diagonal and the red solid line represents the results of the linear regression. The parameters of the linear regression and the coefficient of determination are given in the box in each panel.

2.6.1 SSMIS comparison

For the evaluation measurements from SSMIS onboard NOAA's f16 and f17 satellites processed by Remote Sensing Systems (RSS) and provided by the NASA Global Hydrology Resource Center on a daily 0.25° × 0.25° grid are used. SSMIS can observe the TCWV distribution under all-sky conditions over ocean with an accuracy of around 1 kg m^{-2} (Wentz, 1997; Mears et al., 2015). Since SSMIS changes its Equator crossing time (ECT), only SSMIS observations are included whose ECT is within 3 h (and 5 h for f17 respectively) with respect to TROPOMI's ECT of 13:30 LT. For the intercomparison only SSMIS measurements are considered that are not affected by rain.

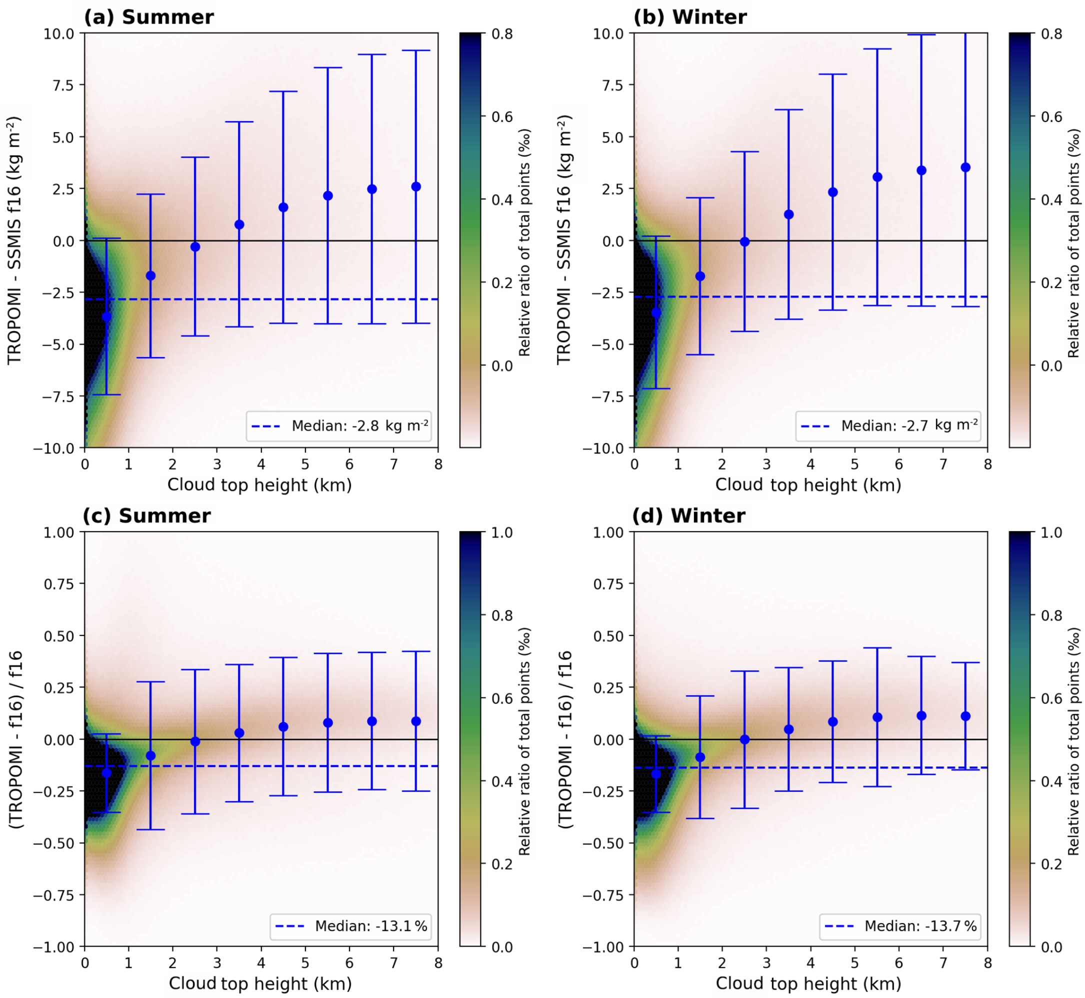

Figure 2.33: 2D histograms of the difference (TROPOMI – SSMIS f16, **a, b**) and relative difference $(\text{TROPOMI} - \text{f16})/\text{f16}$ **(c, d)** as a function of the input cloud top height (CTH) for clear-sky conditions (CF $<$ 20%) for summer **(a, c)** and winter **(b, d)**. The blue dashed line represents the median over the whole CTH range. The blue dots represent the median within a 1 km CTH and the error bars represent their respective 1σ standard deviation.

Figure 2.32 depicts the comparison between SSMIS (f16, top row, and f17, bottom row) and TROPOMI for boreal summer (left column) and winter (right column). For f16 (top row) the scatter is distributed closely along the 1-to-1 diagonal (dashed lines) for both seasons and the fitted regression lines (red solid lines) indicate a very good agreement between both data, with slopes around 0.96, intercepts around $-1.6\,\text{kg}\,\text{m}^{-2}$ for summer and $-1.7\,\text{kg}\,\text{m}^{-2}$ for winter, and coefficients of determination of $R^2 = 0.91$. For f17 the comparison reveals similar agreement, with slopes around 0.97 and intercepts around $-1.5\,\text{kg}\,\text{m}^{-2}$ with R^2 =0.89 for both seasons. Overall, considering the differences in collocation time (3 h and 5 h for f16 and f17 respectively), the comparison shows that the TROPOMI TCWV retrieval can well capture the water vapour distribution over ocean.

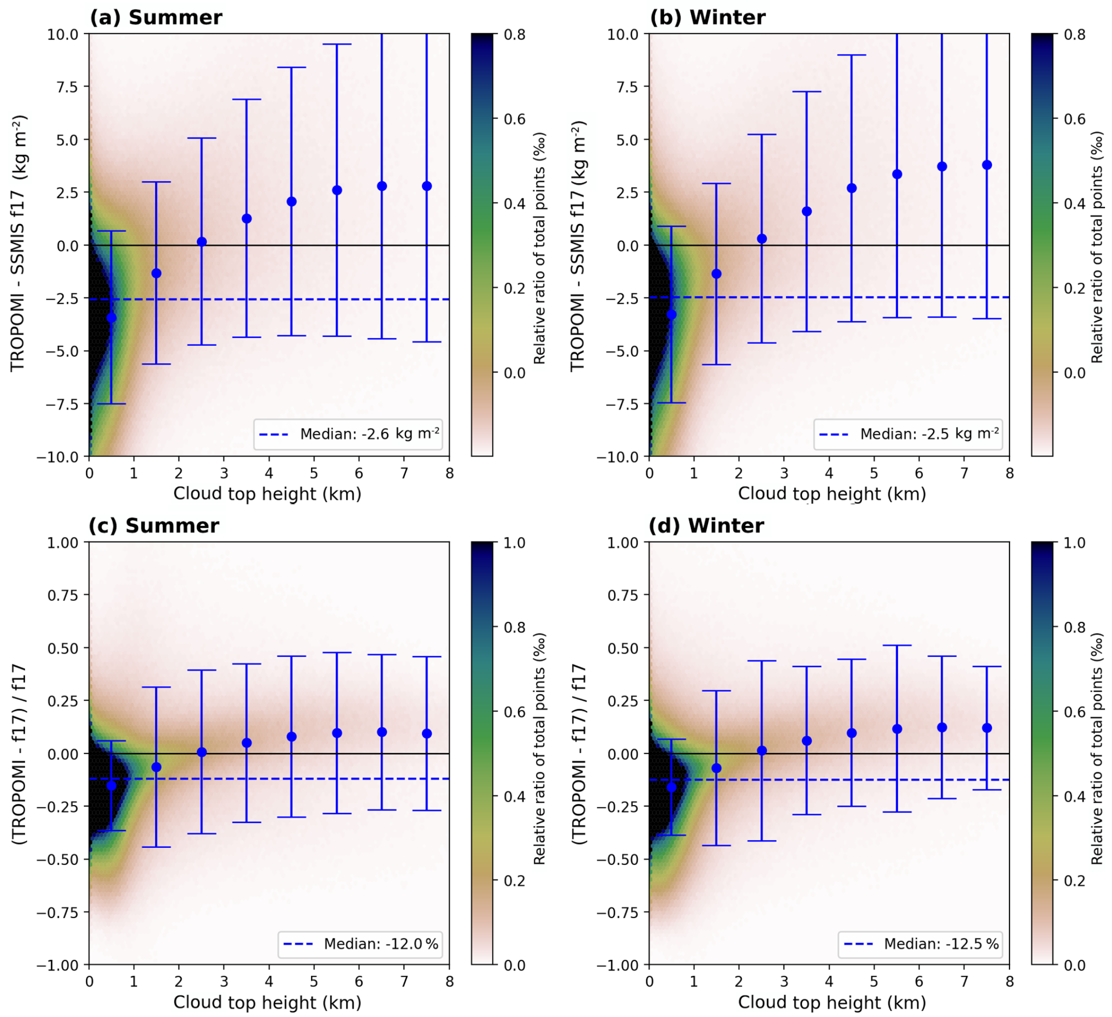

Figure 2.34: Same as Fig. 2.33 but for SSMIS f17.

To investigate the influence of clouds on the retrieval, Figs. 2.33 and 2.34 depict the difference (top row) and relative difference (bottom row) between TROPOMI and SSMIS as a function of the input cloud top height (CTH) for f16 and f17 respectively. The median over the whole CTH range (blue dashed line) indicates an underestimation of the TROPOMI H_2O VCD of approximately 12–13 % (2.6 kg m^{-2}). However, the large majority of data points is distributed within the CTH bin between 0 and 1 km, revealing that the underestimation of the TROPOMI TCWV is mainly caused by low clouds. For mid-level clouds the median difference almost cancels out, whereas for high clouds it first increases and then remains almost constant with cloud top height.

Further validation results for SSMIS f16 and f17 separated into different cloud fraction and cloud top height bins for July 2018 are given in Figs. 2.35 and 2.36 respectively. The results indicate that there is no dependency with cloud fraction but a distinctive dependency with cloud top height: the TROPOMI retrieval underestimates for clouds below 1 km, is in very good agreement for mid-level clouds (1–4 km), and overestimates for higher clouds.

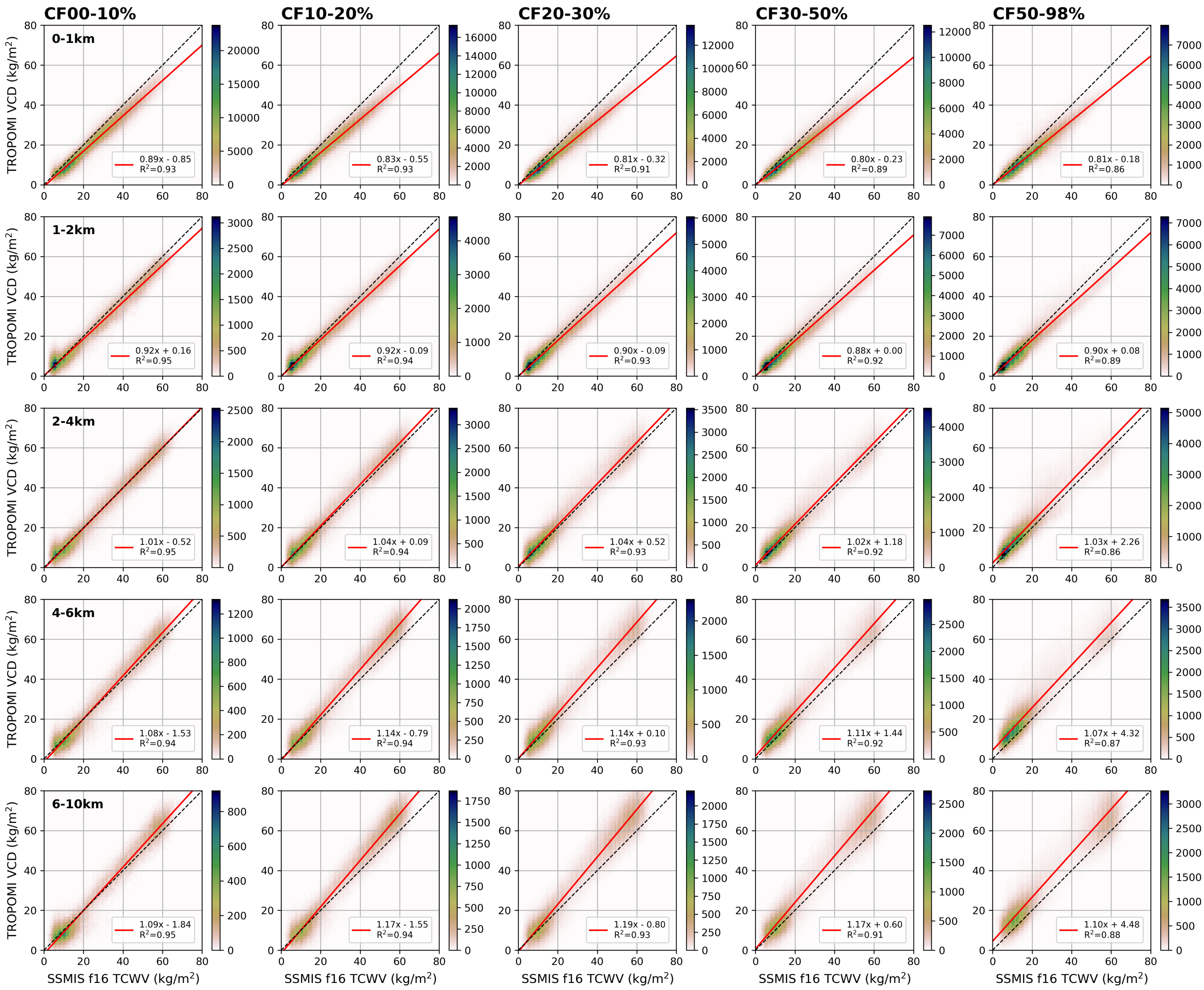

Figure 2.35: 2D histograms for the comparison between TROPOMI and SSMIS f16 for July 2018 for different cloud fraction bins (left to right column) and cloud top height bins (top to bottom row). The color indicates the amount of points within one bin of each panel. The black dotted line indicates the 1-to-1 diagonal and the red solid line represents the results of the linear regression. The parameters of the linear regression and the coefficient of determination are given in the box in each panel.

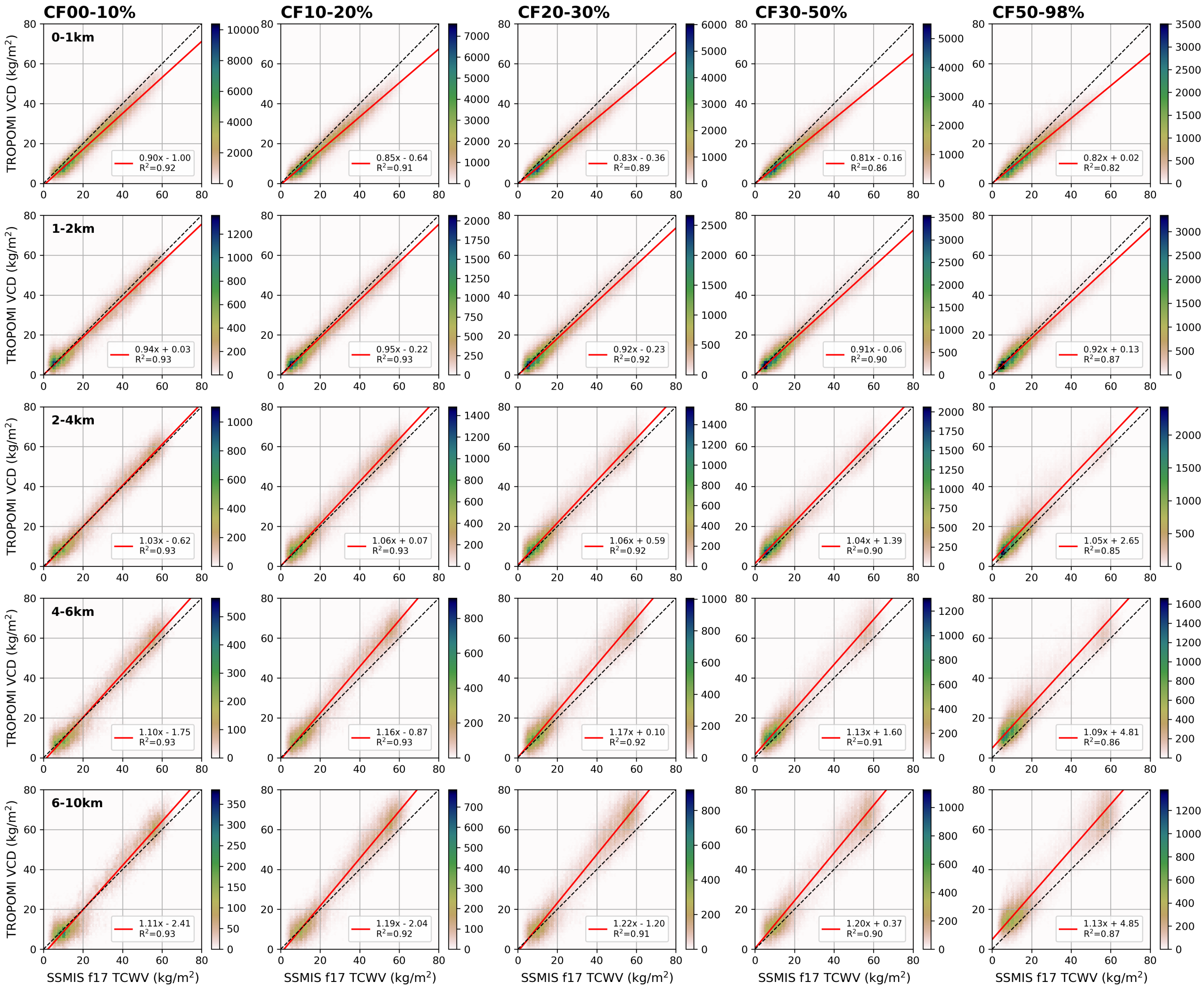

Figure 2.36: Same as Fig. 2.35, but for SSMIS f17.

2.6.2 ERA5 comparison

For the intercomparison between the reanalysis model ERA5 and TROPOMI, ERA5 TCWV data provided by Hersbach et al. (2018b) on a 0.25° × 0.25° grid are used. Only values which are within +1 h with respect to the starting sensing time of the TROPOMI orbit are taken into account. Moreover, the data are separated into data over ocean and data over land.

The results of the intercomparison are summarized in Fig. 2.37. Over ocean (top row in Fig. 2.37) the results are similar to the results from the comparison between TROPOMI and SSMIS: apart from slopes close to 0.95 and intercepts close to zero, the linear regression yields R^2 of 94% for summer and 95 % for winter respectively. Over land the linear regression still yields high values of the coefficient of determination R^2, but the TROPOMI retrieval generally

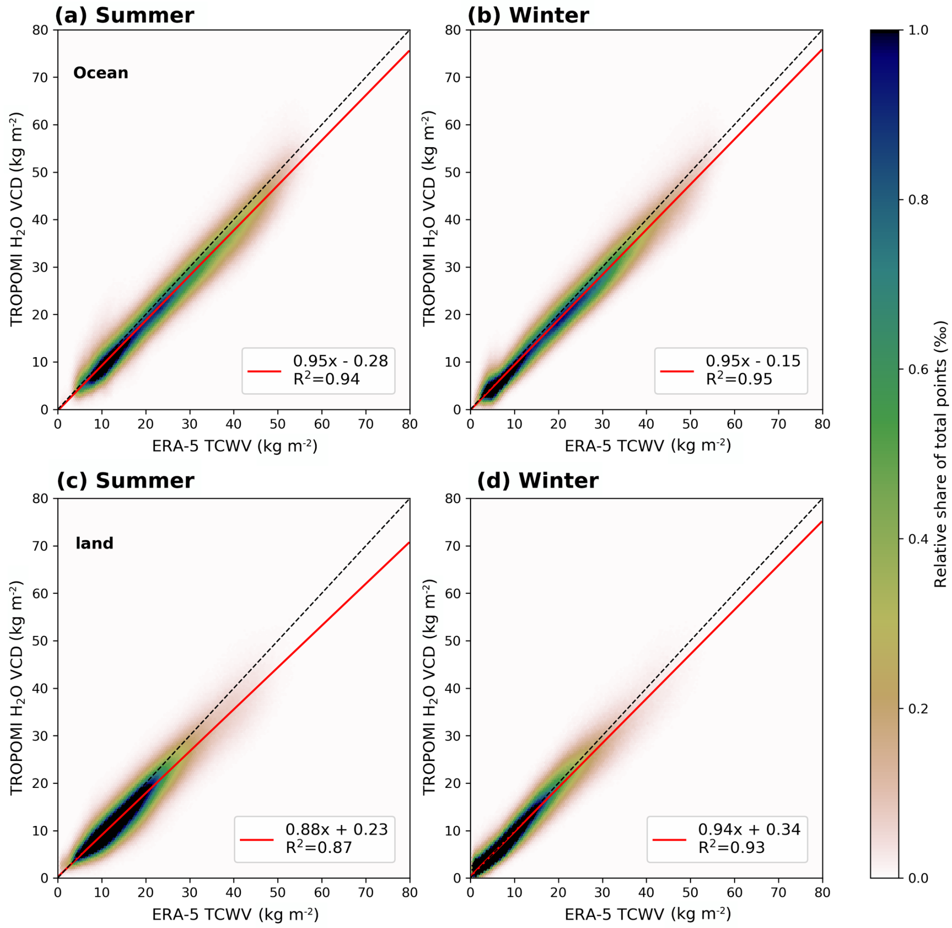

Figure 2.37: 2D histograms for the comparison between TROPOMI and ERA5 for data over ocean **(a, b)** and over land **(c, d)** for clear-sky conditions (CF $<$ 20%) for boreal summer **(a, c)** and boreal winter **(b, d)**, where the colour indicates the relative share of total data points. The black dotted line indicates the 1-to-1 diagonal and the red solid line represents the results of the linear regression. The parameters of the linear regression and the coefficient of determination are given in the box in each panel.

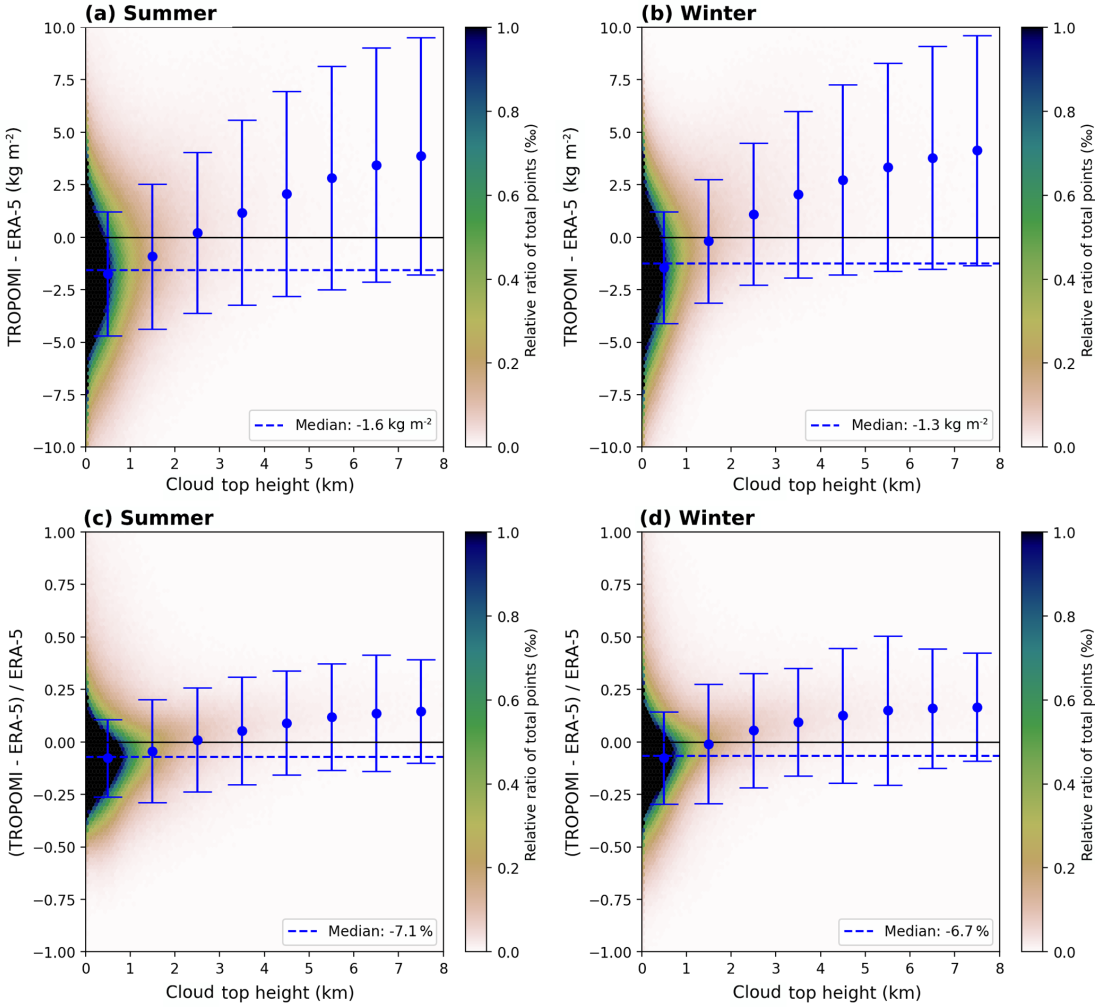

Figure 2.38: 2D histograms of the difference (TROPOMI – ERA5, **a, b**) and relative difference (TROPOMI – ERA5)/ERA5 **(c, d)** as a function of the input cloud top height (CTH) for clear-sky conditions (CF < 20%) for summer **(a, c)** and winter **(b, d)** for data over ocean. The blue dashed line represents the median over the whole CTH range. The blue dots represent the median within a 1 km CTH and the error bars represent their respective 1σ standard deviation.

underestimates the H_2O VCD by approximately 12% during summer (and 7% during winter). Since the values of the correlation coefficient are still high and the values over ocean coincide very well with the reference data sets, one can assume that this underestimation has to be caused by a systematic uncertainty within the input parameters for our retrieval.

The influence of the cloud top height input is illustrated in Fig. 2.38 for data over ocean. The median is around $-1.6\,\mathrm{kg\,m^{-2}}$ (–7.1%) and $-1.3\,\mathrm{kg\,m^{-2}}$ (–6.7%) during summer and winter respectively, whereby similar to SSMIS, these underestimations are caused by the majority of data points within the 0–1 km CTH bin. For increasing CTH the deviation from the reference increases and leads to an overestimation. For data over land (Fig. 2.39) the CTH variability is much larger than over ocean; i.e. most data points are now distributed between 0 and 3 km and

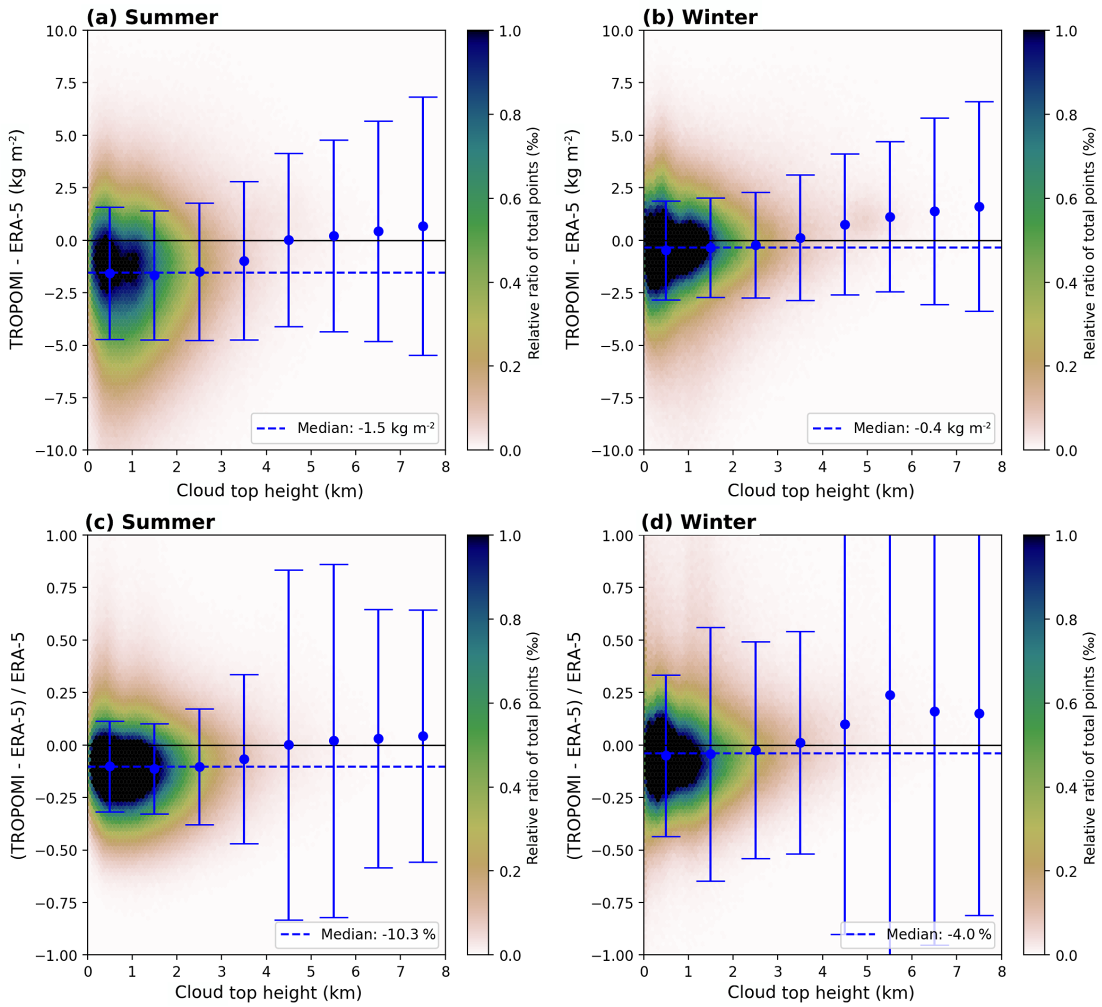

Figure 2.39: Same as Fig. 2.38 but for data over land.

the median is around values of $-1.5\,\mathrm{kg\,m^{-2}}$ (−10.3%) and $-0.4\,\mathrm{kg\,m^{-2}}$ (−4.0%) during summer and winter respectively. Furthermore, low clouds still cause an underestimation, and for mid- to high-level clouds the deviations almost cancel out, but one can also observe an increasing scatter for winter data.

All these findings reveal that the combination of albedo uncertainties and uncertainties in the cloud properties (cloud fraction and cloud top height) as well as in the scale height parameterization have a distinctive influence on the AMF. The cloud products from TROPOMI rely on the OMI albedo which, as was demonstrated in Sect. 2.4, has several problems over land surface. In addition, the uncertainty of the OMI albedo over land surface is higher than over ocean due to a highly spatiotemporal variability of the scenery, and the differences between the monthly minimum and the monthly mean albedo are higher over land than over ocean. Furthermore, the cloud top height is calculated via the cloud top pressure and has to be combined with the surface pressure. Thus, the uncertainty of the cloud top height over land is higher than over ocean, since over ocean the topography is much simpler.

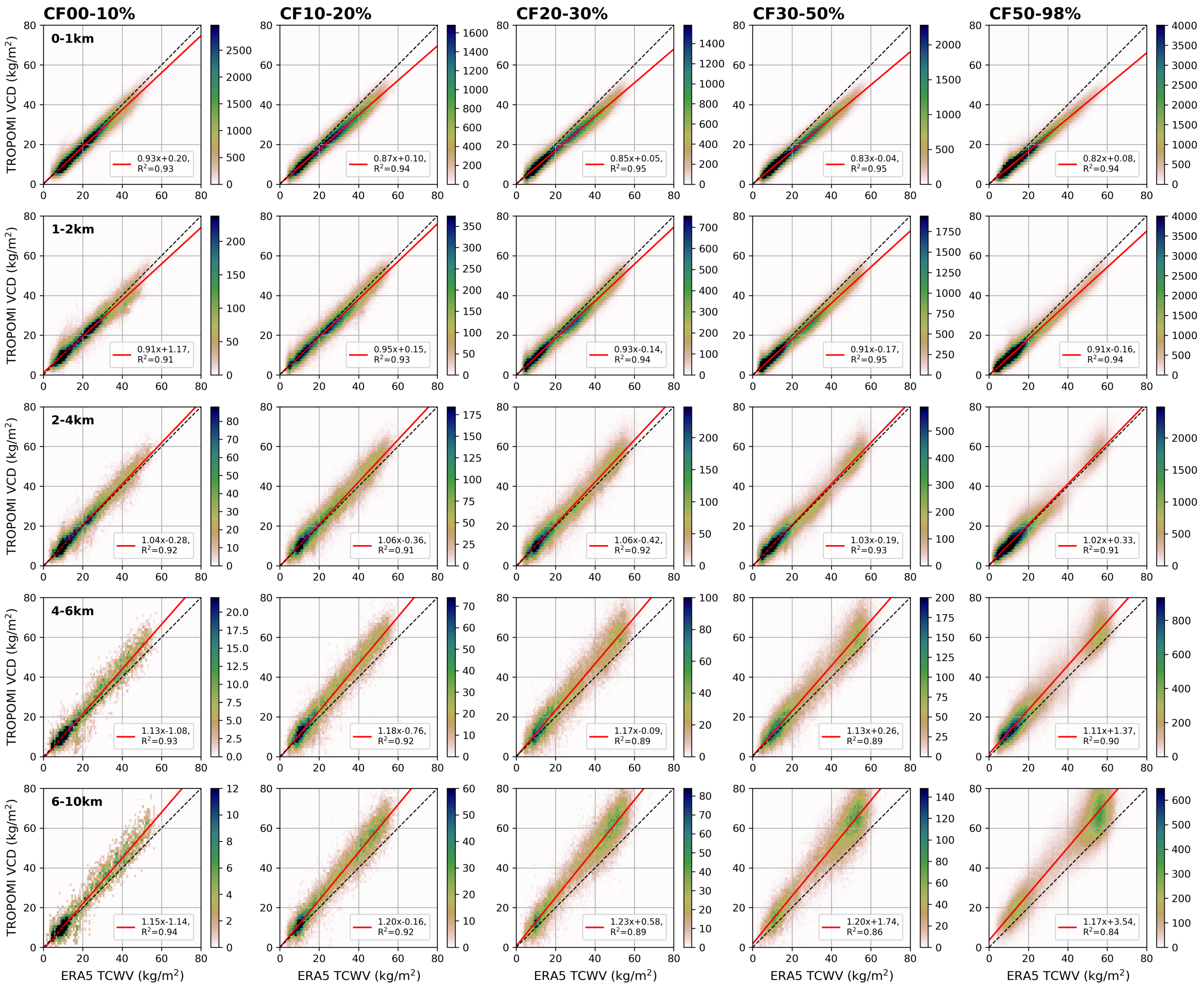

Figure 2.40: Same as Fig. 2.35, but for ERA5 TCWV data over ocean.

Nevertheless, the complex interactions between effects of albedo and clouds might amplify or cancel out these deviations and thus make it difficult to draw clear conclusions.

As for the SSMIS comparison, further validation results for ERA5 over ocean and land separated into different cloud fraction and cloud top height bins for July 2018 are given in Figs. 2.40 and 2.41.

Similar to SSMIS, the results over ocean reveal an underestimation for low clouds and an overestimation for high clouds and that there is almost no dependency with cloud fraction. Over land low clouds still cause an underestimation; however, for cloud top heights above 2 km the retrieval shows very good agreement with ERA5, indicating that the input cloud top height for our retrieval is too low.

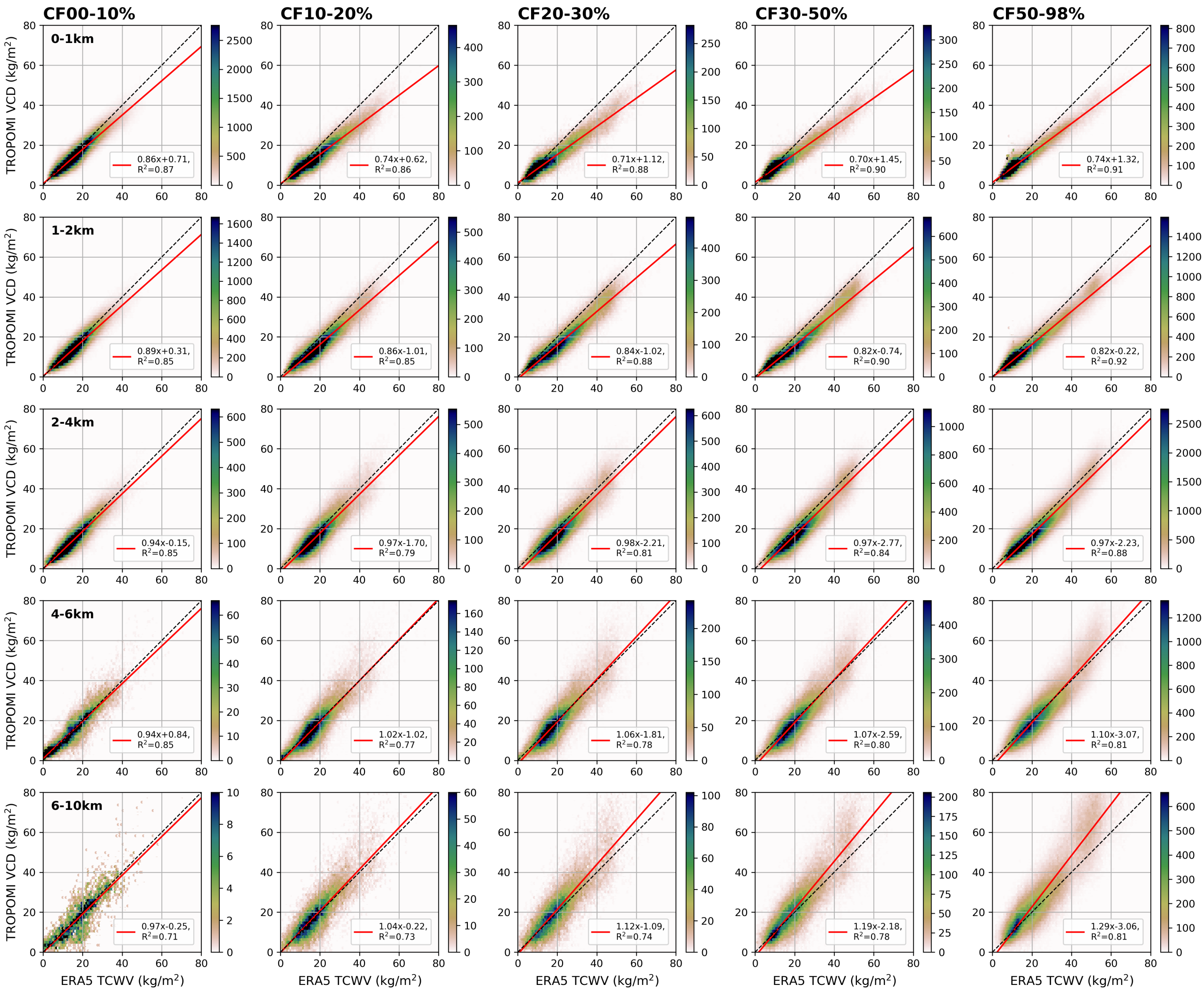

Figure 2.41: Same as Fig. 2.35, but for ERA5 TCWV data over land.

2.6.3 SuomiNet/GPS comparison

For further comparisons, TCWV data from ground-based GPS data are used. These data use the path delay due to atmospheric water vapour in the GPS or GNSS signal and enable the detection of TCWV with high temporal resolution at very high accuracy (Bevis et al., 1992). Here, GPS TCWV data from the SuomiNet network (Ware et al., 2000) is used. SuomiNet stations are distributed over North and Central America and provide data every 30 min with a typical accuracy of 2 kg m^{-2} (Duan et al., 1996; Fang et al., 1998). Thus, only TROPOMI pixels within a distance of 0.1° to the GPS station and within 2 h with respect to the GPS measurement are taken into account.

Figure 2.42 illustrates scatter plots of the intercomparison between TROPOMI and SuomiNet for boreal summer and winter. For both seasons the robust regression indicates an underestimation of around 20 % (i.e. slopes of 0.82 and 0.84) with high Pearson correlation coefficients

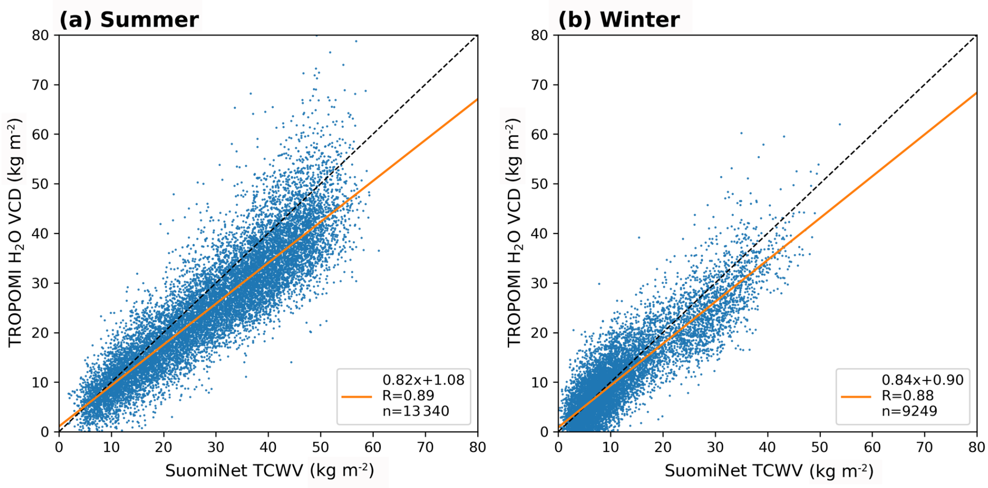

Figure 2.42: Scatter plots of the intercomparisons between TROPOMI and SuomiNet for clear-sky conditions (CF $<$ 20%) for boreal summer **(a)** and boreal winter **(b)**. The black dashed line indicates the 1-to-1 diagonal and the orange solid line represents the results of the robust regression based on Siegel (1982). The parameters of the regression and the coefficient of correlation are given in the box in each panel.

of 88%. To investigate the influence of clouds on the TCWV retrieval, Fig. 2.43 depicts the difference (top row) and the relative difference (bottom row) between TROPOMI and Suominet as a function of the input cloud top height (CTH). The median over the whole CTH range (blue dashed line) indicates an underestimation of the TROPOMI H_2O VCD of approximately 14 % (3.5 kg m^{-2}) during summer and of 8% (0.8 kg m^{-2}) during winter. However, during summer the median values for each 1 km CTH bin (blue dots) reveal that the underestimation is mainly caused by low clouds, whereas for mid- and high-level clouds the median difference almost cancels out. During winter this pattern is not clearly observable due to much larger scatter, but also here low clouds mainly cause the underestimation in TCWV, whereby the difference is generally within the range of accuracy of the SuomiNet retrieval.

Figure 2.44 depicts further validation results separated into different cloud fraction and cloud top height bins for boreal summer 2018. Though the sample size is much smaller, similar results to SSMIS and ERA5 are obtained: independent of the cloud fraction, low clouds cause an underestimation of around 15–20%, whereas for mid-level clouds the TROPOMI H_2O VCDs show much better agreement with the SuomiNet TCWV, and for high clouds TROPOMI overestimates by around 10%.

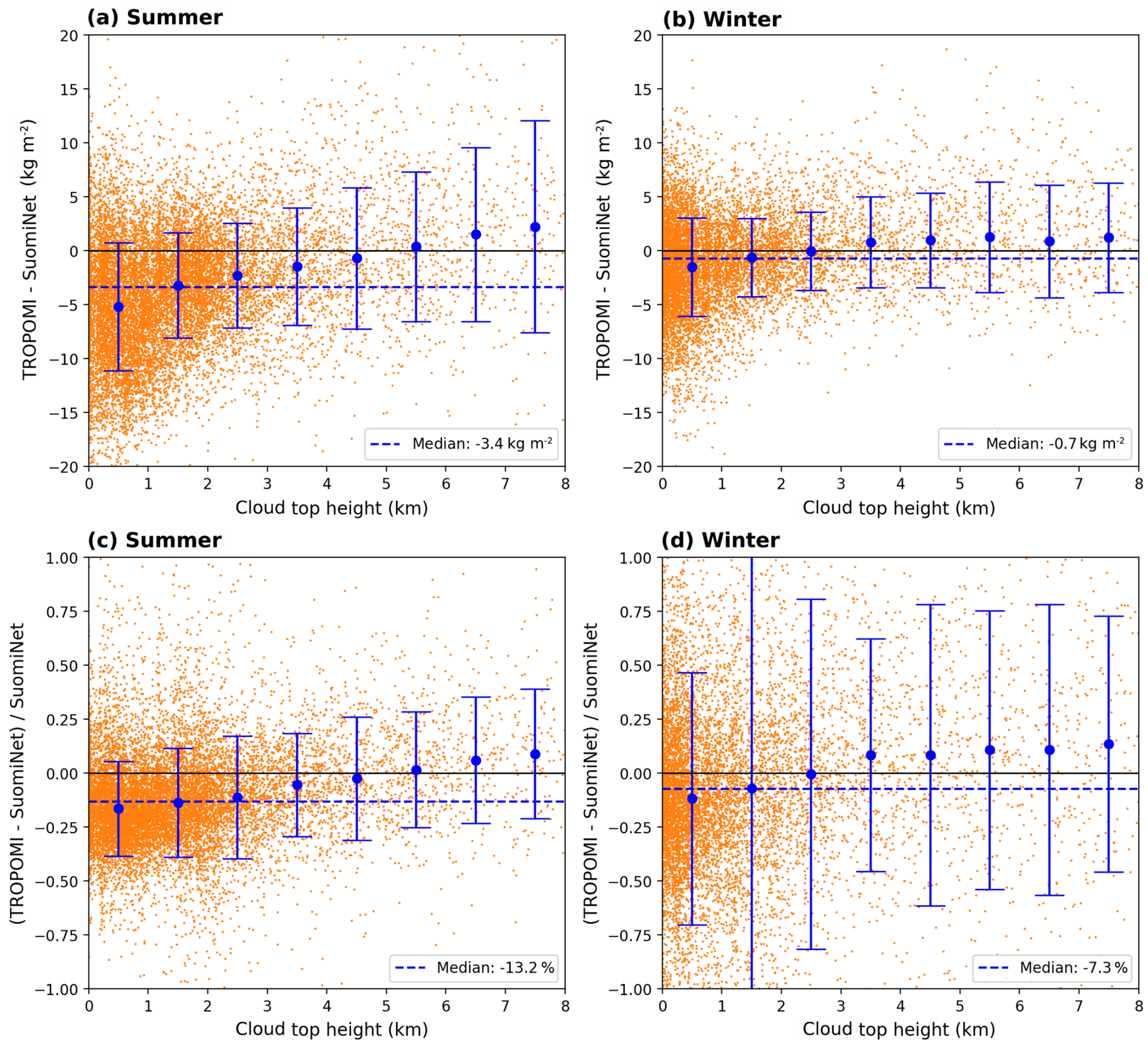

Figure 2.43: Scatter plot of the difference (TROPOMI − SuomiNet, **a, b**) and relative difference (TROPOMI−SuomiNet)/SuomiNet **(c, d)** as a function of the input cloud top height (CTH) for clear-sky conditions (CF $<$ 20%) for summer **(a, c)** and winter **(b, d)**. The blue dashed line represents the median over the whole CTH range. The blue dots represent the median within a 1 km CTH and the error bars represent their respective 1σ standard deviation.

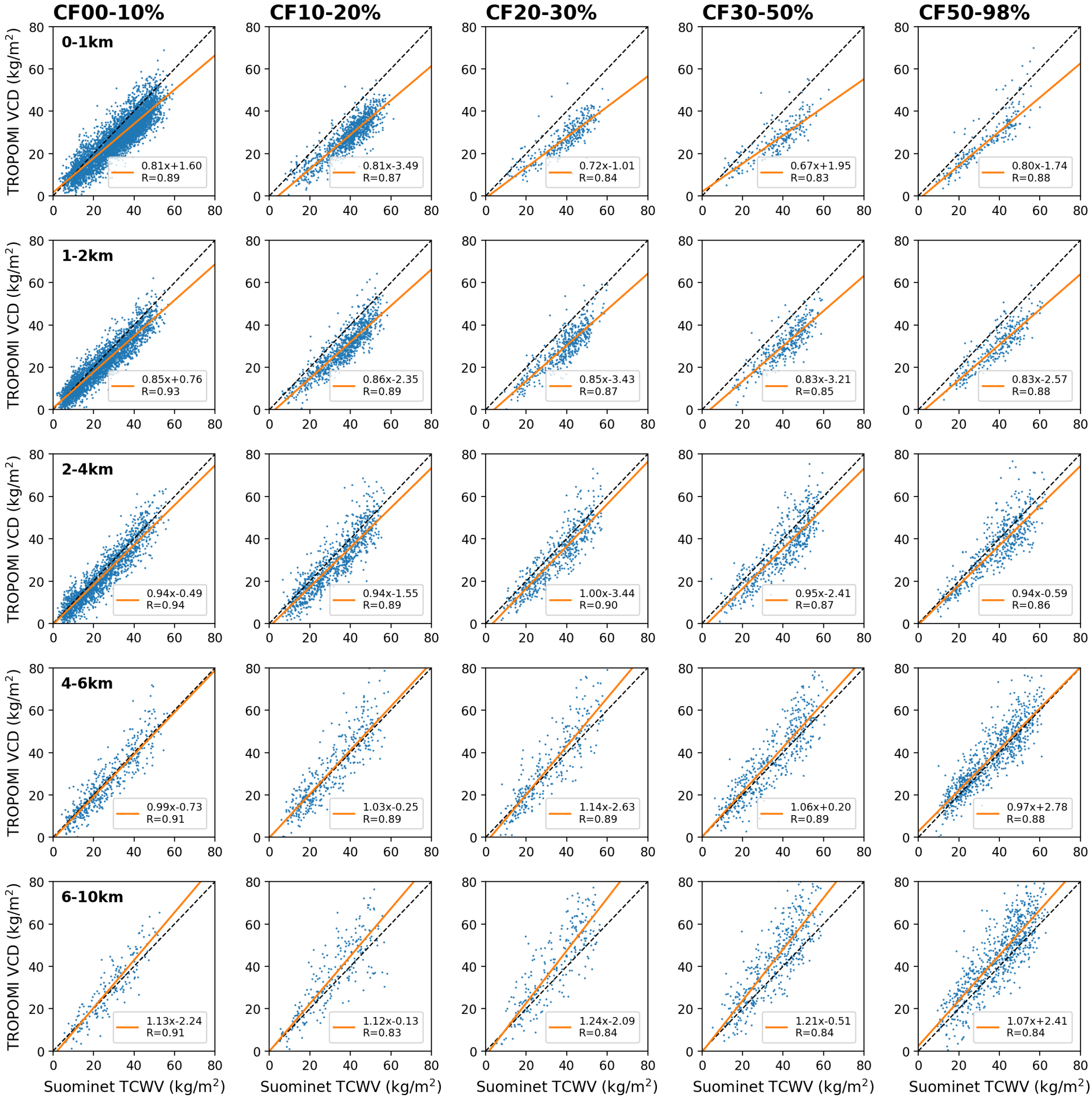

Figure 2.44: Scatterplots for the comparison between TROPOMI and SuomiNet for boreal summer 2018 for different cloud fraction bins (left to right column) and cloud top height bins (top to bottom row). The black dashed line indicates the 1-to-1 diagonal and the orange solid line represents the results of the robust regression. The parameters of the regression and the correlation coefficient are given in the box in each panel.

2.7 Summary, conclusions and outlook

This study introduces a total column water vapour retrieval from TROPOMI spectra in the visible blue spectral range using an iterative vertical column conversion scheme and provides a detailed characterization of the retrieved H_2O VCD by performing a comprehensive uncertainty analysis and intercomparisons to reference data sets from the microwave sensor SSMIS, from the reanalysis model ERA5, and from the ground-based GPS network SuomiNet.

For the iterative scheme the a priori water vapour profile is described as an exponential decay with a scale height H and an empirical parameterization for this scale height has been developed. This parameterization is based on COSMIC water vapour profile data and relates the a priori water vapour profile shape to the H_2O VCD, the seasonal cycle, the latitude, and the density of vegetation. It is demonstrated that the scale heights can be correctly reproduced, in particular for data at low latitudes (tropics and subtropics). However, also an increasing scatter is observed if higher latitudes are included in the comparison, likely because of the higher variability in H_2O VCD due to midlatitudinal cyclone dynamics and a general higher uncertainty in the COSMIC profile data for drier atmospheric conditions. Overall, the retrieved profile heights are very reasonable, and a substantial improvement is obtained by using the new parameterization compared to the use of a prescribed constant (relative) water vapour profile.

For the uncertainty analysis the impact of several error sources on the H_2O SCD and AMF, like clouds, surface albedo, profile shape, and instrument properties, has been investigated. The error estimation reveals that the main SCD uncertainty is the fit error of the spectral analysis and that the main AMF uncertainties are caused by uncertainties in the surface albedo, cloud properties, and water vapour profile shape. For the H_2O VCD a typical total relative error of around 10–20% is estimated for observations during clear-sky conditions, over ocean surface, and at low solar zenith angles. For observations during cloudy-sky conditions, over land surface, and high solar zenith angles the error reaches values of approximately 20–50%. Thus, the theoretically estimated errors are of the same order of magnitude as the deviations found during the retrieval's evaluation. However, uncertainties in the absorption cross section of water vapour are a further systematic error source that can additionally contribute up to 10%. Based on the LP-DOAS comparisons these errors are estimated to be around 5% for this study, so that they are negligible compared to the other error sources.

The validation study demonstrates that for clear-sky conditions the retrieved TROPOMI H_2O VCDs over ocean are in very good agreement with the reference data sets and can correctly capture the global water vapour distribution. Likewise, the TROPOMI retrieval can reproduce the TCWV distribution over land; however, also a distinctive underestimation of around 10% is observed, in particular during boreal summer.

These underestimations might be caused by the uncertainties of the external input data for the retrieval: for instance, the OMI LERs from Kleipool et al. (2008) are too high over tropical land masses, likely due to incorrect cloud filtering which causes too high AMFs, leading to too low H_2O VCDs. Although it has been tried to overcome this issue by using a surface reflectance product from MODIS Aqua, the cloud products from the TROPOMI L2 NO_2 product still rely on the OMI and GOME-2 LER to calculate the effective cloud fraction and cloud top height, respectively, and thus also have a large uncertainty. The intercomparisons to the reference data sets show that these uncertainties in the cloud products have a substantial impact on the H_2O VCD: the investigations reveal that the input cloud top height is probably too low, which in turn leads to higher AMFs and consequently to an underestimation in TCWV. However, one has to consider that a complex interaction of the effects of the cloud and albedo products exists, so that a clear explanation or suggestion on how to overcome these issues is beyond the scope of this study. For general purposes it is recommended to only use VCDs with an effective cloud fraction $< 20\%$ and AMF > 0.1, which represents a good compromise between spatial coverage and retrieval accuracy.

Overall, the successful application of the TCWV retrieval in the visible blue spectral range to TROPOMI measurements is very promising for further investigations, including the application to further satellite sensors such as OMI, SCIAMACHY, GOME-1/2, GEMS or the upcoming Sentinel-4 and Sentinel-5 instruments and expanding the retrieval to measurements contaminated by higher cloud fractions. As the retrieval allows for a fast execution of large data sets and enables the creation of a consistent TCWV data set over ocean and land surface, investigations of long-term trends using a TCWV data set of merged time series of different satellite sensors are easily possible. However, since these data sets have to be uniform, they require consistent input data across the different satellite sensors, in particular for cloud products.

In addition, there are several opportunities to further optimise the retrieval in the near future. Concerning the determination of the a priori water vapour profile, using machine learning and deep learning one could not only refine the existing routine, but possibly also directly determine a profile shape instead of a scale height for an exponential profile. Furthermore, improving the quality of cloud information is of great importance to reduce the uncertainty in the TCWV retrievals in the UV-vis spectral range. The application of cloud height algorithms in the same spectral range as the fit window (e.g. by means of the O_4 VCD or the Ring effect) in combination with geometry-dependent cloud fraction algorithms (e.g. MICRU; Sihler et al., 2021) could make important contributions to this.

With regard to TROPOMI, the introduction of a TROPOMI-specific directional LER can be expected to lead to further improvements in the retrieval input parameters: in addition to a higher spatial resolution (which is particularly important for coastlines) and the consideration of viewing the geometry dependence, first results indicate striking changes in the cloud information. Moreover, recent updates in the algorithm of the NO_2 product have resulted in an increase in cloud height and thus a better agreement to reference measurements (van Geffen et al., 2022).

Thus, all these changes should then also have a direct impact on the TCWV retrieval presented here.

3 A 16-year global climate data record of total column water vapour generated from OMI observations in the visible blue spectral range

The following chapter is based largely verbatim on the publication by Borger et al. (2021) and has only been restructured in a few places compared to this publication.

3.1 Introduction

For studies of climate change or global warming, respectively, continuous long-term observations on the global scale are necessary, making observations from satellite instruments indispensable. While observations and retrievals of atmospheric water vapour in the microwave and infrared spectral range are well established and thus also make up a large part of climate or reanalysis data sets, the use of such combined data sets for trend studies over several decades is not straightforward due to jumps in the availability of observational data (e.g. additional new observations due to new instruments; Bengtsson et al., 2004).

Meanwhile, substantial progress has been made within the past decade in retrieving total column water vapour (TCWV) in the visible blue spectral range (e.g. Wagner et al., 2013; Wang et al., 2019; Borger et al., 2020; Chan et al., 2020). This allowed to make use of measurements from satellite instruments like TROPOMI (Veefkind et al., 2012) and even GOME-2 (Munro et al., 2016) for which so far only retrievals in the visible red and near-infrared spectral range have been available.

Building on the TCWV algorithm developed in Chapter 2 on basis of TROPOMI measurements, this retrieval is now applied to TROPOMI's predecessor model, the so-called Ozone Monitoring Instrument (OMI; Levelt et al., 2006, 2018) onboard NASA's Aura satellite. However, in order to adapt the TCWV retrieval to OMI measurements, some adjustments have to be made to the retrieval algorithm.

The OMI instrument is of particular interest for climate investigations: launched in July 2004 it offers an almost continuous measurement data record of more than 18 years up until today, making it possible to create a unique long-term climate data set based on measurements from only one single instrument (in contrast to combined data sets for instance from reanalysis models).

This study documents how OMI's long-term observation data record is utilized to retrieve total column water vapour from its measurements in the visible blue spectral range in order to generate a climate data set.

To this end, the study is structured as follows: First, the data set generation is described and the retrieval methodology and the applied modifications in comparison to the TCWV retrieval from Borger et al. (2020) are briefly explained. Then, potential sampling errors are analyzed, and the impact of the limitation to clear-sky satellite observations on the representativeness of the TCWV values of the data set is investigated. Furthermore, the generated data set is characterized via intercomparisons to various different reference TCWV data sets. Moreover, its temporal stability is analyzed with regard to the aforementioned reference data sets. Finally, the results are summarized and conclusions are drawn.

3.2 Ozone Monitoring Instrument

The Ozone Monitoring Instrument OMI (Levelt et al., 2006, 2018) onboard NASA's Aura satellite is a nadir-looking UV-vis pushbroom spectrometer that measures the Earth's radiance spectrum from 270–500 nm with a spectral resolution of approximately 0.5 nm following a sun-synchronous orbit with an equator crossing time around 13:30 LT. The instrument employs a 2D CCD consisting of 60 across-track rows which in total cover a swath width of approximately 2600 km with a spatial resolution of 24 km $\times$ 13 km at nadir increasing to 24 km $\times$ 160 km towards the edges of the swath. Launched in July 2004, OMI provides an almost continuous measurement record until today with more than 95000 orbits.

However, since July 2007 OMI has suffered from the so-called "row-anomaly" (RA), a dynamic artefact causing abnormally low radiance readings in the across-track rows, i.e. several rows of the CCD detector receive less light from the Earth, and some other rows appear to receive sunlight scattered off a peeling piece of spacecraft insulation. One plausible explanation for these effects is a partial obscuration of the entrance port by insulating layer material that may have come loose on the outside of the instrument (Schenkeveld et al., 2017; Boersma et al., 2018). Thus, in this study, the affected measurements are excluded for the entire period of the data set.

3.3 Modifications of the spectral analysis

For the application of the algorithm to OMI measurements several modifications had to be applied to the algorithm of Borger et al. (2020) (see also Chapter 2). For climate studies such as trend analyses it is evident to provide a consistent data record. Thus, all rows that have ever been affected by the so called "row-anomaly" (i.e. rows 22 to 54) are excluded from the data set for the complete time series, which corresponds to approximately half of the OMI swath. Also, instead of a daily solar irradiance, an Earthshine radiance is used as reference spectrum within the DOAS analysis.

3.3.1 Removing of across-track biases: irradiance based vs. Earthshine based SCD

A major disadvantage of pushbroom spectrometers is the varying sensitivity of the rows of the 2D CCD detector, which can lead to jump-like structures from row to row across-track of the retrieved SCD.

To reduce the across-track biases of the retrieved H_2O SCDs based on a solar reference spectrum, a destriping algorithm can be performed during post-processing. For instance, one way to destripe the swath of an OMI orbit is to

1. calculate the median SCD for each OMI row along-track,
2. calculate the across-track median SCD from the along-track median SCDs,
3. calculate the deviation of the along-track median SCDs from this across-track median SCD,
4. subtract the deviation from the SCDs of the respective OMI row.

Another way to reduce across-track stripes is to use so-called Earthshine spectra as reference spectra. In the case of OMI, the rationale for using an Earthshine radiance over a solar irradiance is as follows:

- The daily OMI solar irradiance spectra (OML1BIRR version 3) are very noisy and have several gaps causing high H_2O SCD fit errors and thus leading to an overall poor quality of the H_2O VCD data set.
- By using an annual mean solar irradiance spectrum from the year 2005 (also used during the QA4ECV project; Boersma et al., 2018) a good fit quality can be obtained, however, OMI is also suffering from degradation effects (Schenkeveld et al., 2017). Thus, for the case of climate trend analyses it will be almost impossible to disentangle if a trend signal

originates from the spectral degradation of OMI or indeed from a geophysical trend (see also Fig. 3.3). By the use an Earthshine radiance as reference spectrum these degradation effects will largely cancel out.

- By using an Earthshine radiance spectrum as reference spectrum for each detector row, also the across-track biases within the OMI swath are strongly reduced (see Panel (c) in Fig. 3.1) and consequently no destriping is necessary during post-processing (see also Anand et al., 2015).

- However, as a disadvantage of the use of Earthshine spectra, the retrieved H_2O slant columns do not represent absolute slant columns because the Earthshine reference spectra also contain H_2O absorptions. Hence, a slant column representative for the chosen reference sector has to be added to the retrieved values.

3.3.2 Generation and application of Earthshine spectra

For the creation of annual Earthshine reference spectra, the Antarctic continent was selected as reference sector (high surface albedo due to snow and ice cover) and the month of December as reference period (i.e. during austral summer) yielding a relatively high signal-to-noise ratio for the radiance measurements despite large solar zenith angles. Furthermore, only pixels above an altitude of 2000 m above sea level are selected: as the air temperatures are very low there, the water vapour concentrations are very low as well, thus representing a reference atmosphere that is as dry as possible (i.e. the reference SCD or better saying the absolute value of its uncertainty has to be as minimal as possible). Also, to avoid the inclusion of noisy measurements (in particular from the descending part of the OMI orbit), only pixels with a solar zenith angle (SZA) $< 80°$ are considered. From these measurements the monthly-mean radiance for December for each year for every OMI row is calculated and then the resulting reference spectra are used for the retrievals of the upcoming year.

Figure 3.1 (and 3.2) illustrate the effect of different reference spectra on the H_2O SCD distribution for an examplary orbit. Distinctive stripe patterns are prominent in particular when using the daily solar irradiance as reference spectrum (Fig. 3.1a). Although the usage of the annual-mean solar irradiance (Fig. 3.1b) can reduce the strength of the stripes, they are still clearly visible. In contrast, no across-track stripes are detectable for the case of the Earthshine reference and overall the SCDs are also lower due to the H_2O absorption in the Earthshine reference (Fig. 3.1c).

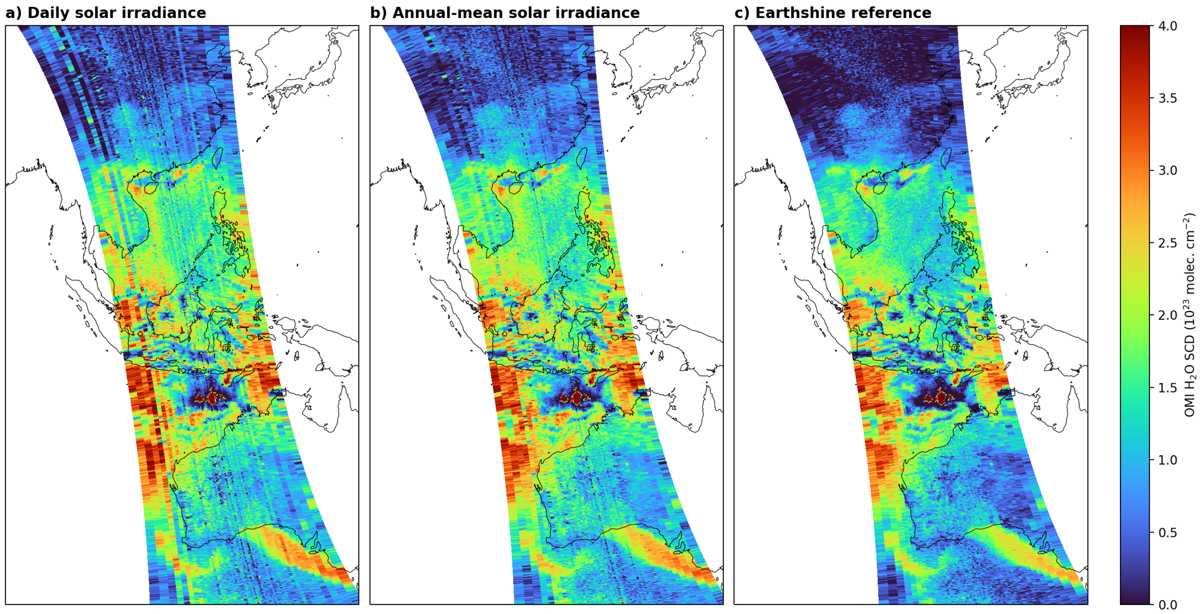

Figure 3.1: Examplary orbit showing the impact of different reference spectra on the OMI H_2O SCDs: **(a)** daily solar irradiance, **(b)** annual-mean solar irradiance, and **(c)** monthly mean Earthshine reference. Orbit 8693, date: 3 April 2006.

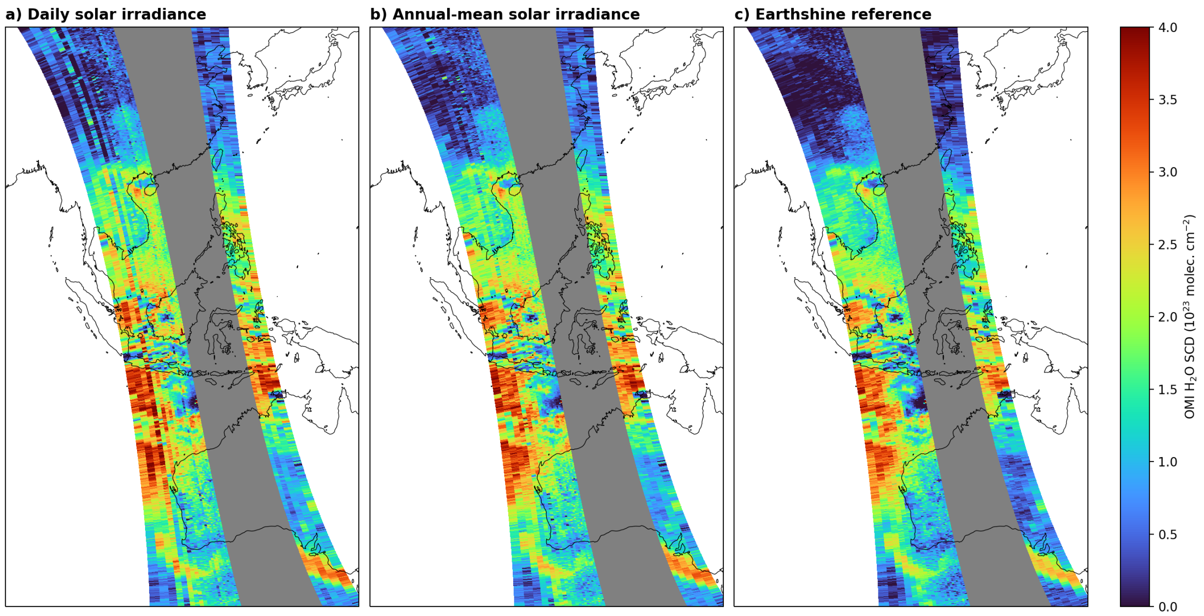

Figure 3.2: Same as Fig. 3.1, but now with RA-affected rows marked as grey.

3.3.3 Offset correction

Although the usage of the Earthshine spectrum significantly reduces the across-track stripes, one still has to consider that the Earthshine reference spectrum is not perfectly pristine of the trace gas of interest. Thus, although the water vapour concentrations in Antarctica are very low, the Earthshine reference might still be contaminated because of the long light path at such high solar zenith angles. Therefore, the retrieved H_2O SCD from the Earthshine fit (eSCD) must be corrected by means of an offset ΔSCD.

Figure 3.3 illustrates the time series of the global monthly mean H_2O SCDs derived from the annual-mean solar irradiance (and destriped following the aforementioned destriping process) and the Earthshine reference for SZA $< 80°$. Until 2009 the offset between both SCDs remains constant at values around 0.2×10^{23} molec cm^{-2}. Between 2009 and 2015 the irradiance based SCDs first decrease and then increase distinctively compared to the Earthshine based SCDs and from 2015 onwards a strong increase in the irradiance based SCDs can be observed. In contrast, the Earthshine SCDs show no jumps or steps and remain at the same magnitude after 2015 and over the complete time range in general.

To get an overview of how the SCD difference (i.e. solar irradiance based minus Earthshine SCD) behaves with time over the complete OMI swath, Fig. 3.4 depicts the monthly mean SCD difference for each OMI row. Between 2005 and 2009 the SCD differences remain fairly constant for each row, however, after 2009 artefacts arise first at rows 55-60 and then start to

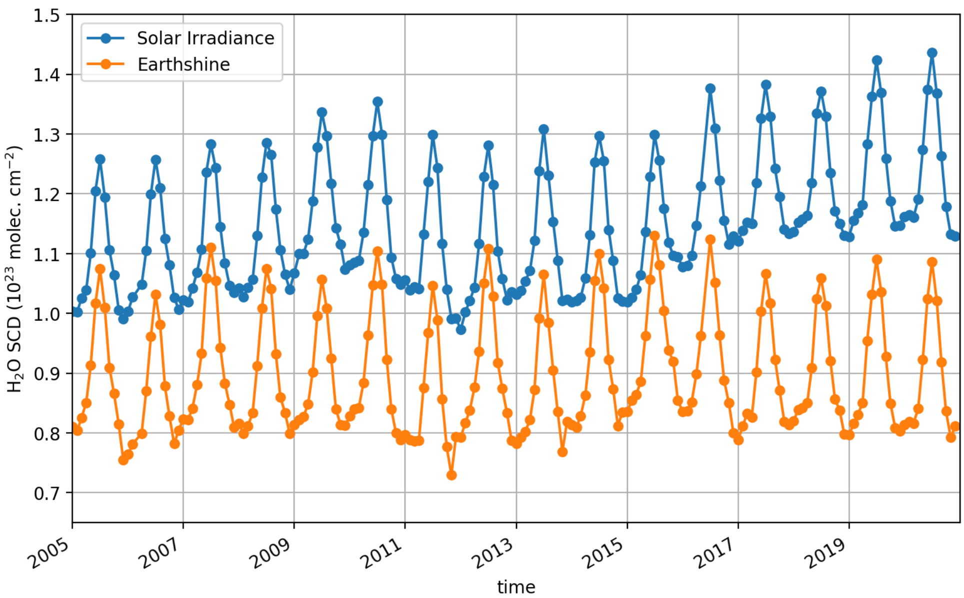

Figure 3.3: Globally averaged monthly-mean of the destriped H_2O SCDs derived from the annual-mean solar irradiance and H_2O SCDs derived using the annual Earthshine reference from 2005 until 2020.

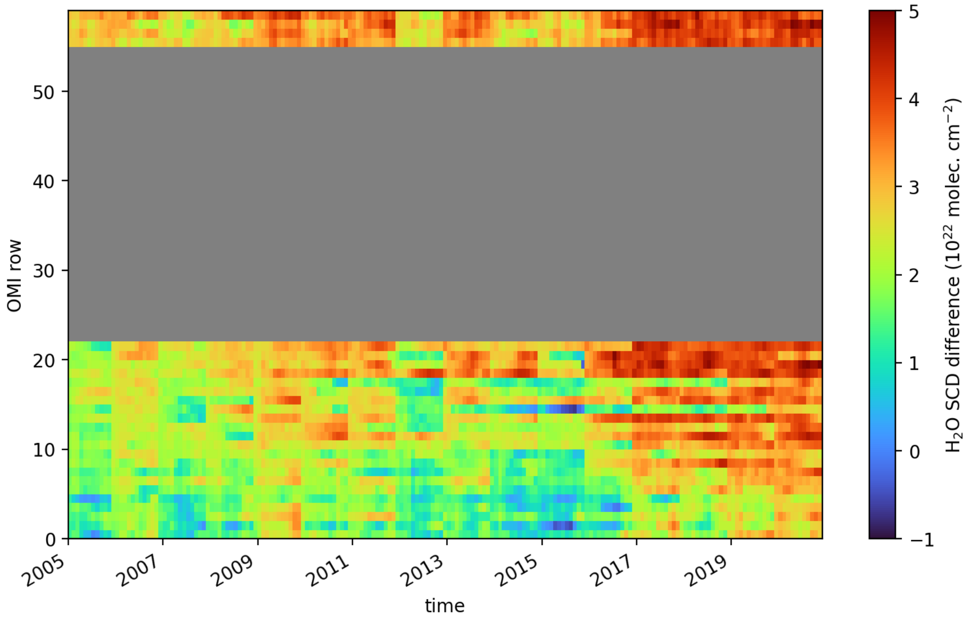

Figure 3.4: Global mean monthly averaged difference between annual-mean irradiance and Earthshine H_2O SCD for each OMI row separately. Only observations with a solar zenith angle $< 80°$ and which are snow- and ice-free are included. Rows affected by the "row-anomaly" (coloured in grey) are excluded for the complete time series.

expand to other rows and become even stronger. This clearly illustrates that a OMI TCWV product based on a solar irradiance fit cannot be used for trend analyses.

Consequently, the offset ΔSCD is determined for each row based on the difference of the Earthshine based SCDs and solar irradiance based SCDs for the first 5 years of OMI operation.

3.4 VCD conversion and data set generation

To account for the water vapour absorption within the Earthshine reference spectra, the SCDs based on the Earthshine reference have to be corrected for the corresponding offset. Taking into account the determined offset ΔSCD for each row (see Sect. 3.3.3), the retrieved SCDs based on the Earthshine reference (eSCD) can be corrected, and Eq. (2.4) can then be rewritten as:

$$\mathrm{VCD} = \frac{\mathrm{eSCD} + \Delta\mathrm{SCD}}{\mathrm{AMF}} \tag{3.1}$$

where eSCD denotes the SCD derived using the Earthshine reference.

The AMFs are calculated as described in Borger et al. (2020). For the determination of the AMF, additional information about the retrieval scenario like cloud cover and surface properties is necessary. Here, the cloud information from the OMI L2 NO_2 product (OMNO2, Lamsal et al., 2021) and the modified OMI surface albedo version of Kleipool et al. (2008) as described in Borger et al. (2020) are used. Also the surface albedo information from the OMNO2 product has been tested, however, within the framework of a trend analysis study (Borger et al., 2022) spatial artefacts in the surface albedo trends were observed which likely arise from the use of an older version of the MODIS data for the albedo calculation (Lok Lamsal, personal communication).

The distribution of TCWV trends is mainly determined by the trends in the SCD (see Chapter 4 and Borger et al. (2022)). The albedo or AMF trends usually only determine whether the trend signal becomes stronger or weaker, but this only affects trends over land, since a static albedo climatology from Kleipool et al. (2008) is used over ocean. As the ice flags from the OMI processor sometimes indicate snow/ice-free surfaces over Antarctica or Greenland, the monthly mean sea ice cover information from ERA5 (Hersbach et al., 2019, 2020) and the annual mean land cover information from MODIS Aqua (Sulla-Menashe et al., 2019) are used in addition.

To create the OMI TCWV data set, the time range from January 2005 to December 2020 has been chosen and only observations are included with an effective cloud fraction $< 20\%$ and AMF > 0.1. Furthermore, the pixels have to be free of snow and ice and must not be affected by the row anomaly. So while about 50% of the orbit is missing because of the RA-filter, the remaining data still covers an "effective" swath of about 1300 km which is still larger than the swaths of GOME-1, SCIAMACHY, or GOME-2A (all about 1000 km) or of the order of SSM/I (about 1394 km). Thus, OMI still achieves complete coverage of the Earth about every 2 to 3 days, which should provide enough observational data for good representativeness in case of a monthly mean (see also Sect. 3.5.3 and the good agreement to the reference data in Sect. 3.6). In total, after all these filters, about 30% of TCWV data remain from an RA-filtered orbit and about 12% of data from a complete orbit. The results of every orbit are then gridded to a $1° \times 1°$ lattice for every day. From these daily grids, the monthly mean H_2O VCD distributions are then calculated ensuring that a continuous TCWV time series is available for as many grid cells as possible.

Figure 3.5 shows the global mean OMI H_2O VCD averaged over the complete time range of the TCWV data set. The resulting distribution demonstrates that the retrieval is capable to capture the macroscale water vapour patterns like high VCD values in the tropics and low values towards the polar regions, but also characteristic regional patterns like the South Pacific convergence zone.

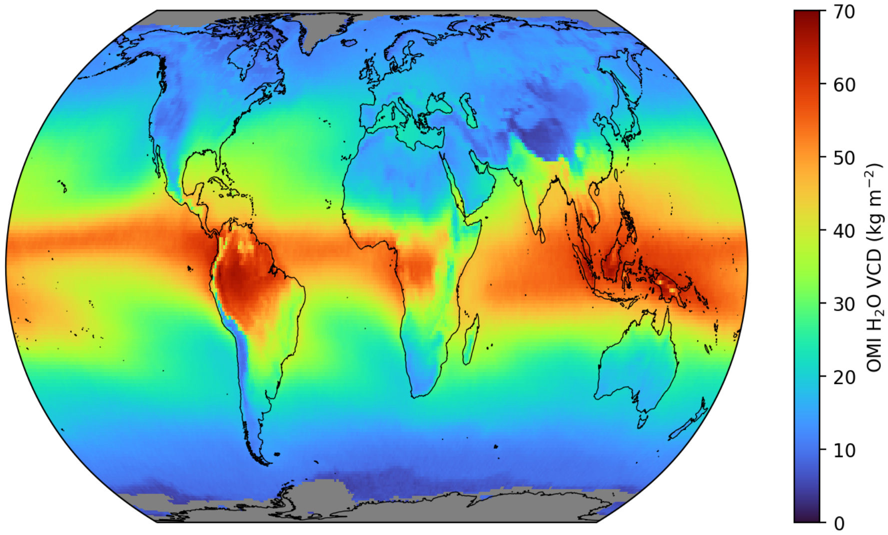

Figure 3.5: Global mean OMI H_2O VCD distribution from January 2005 until December 2020 based on the OMI analysis using Earthshine reference spectra and corrected for the H_2O SCD bias. Areas with no valid values are coloured grey.

3.5 Assessment of the sampling error and its relationship to the clear-sky bias

Although satellite observations enable the analysis of trace gas concentrations on a global scale, a fundamental problem is that typically a satellite measurement is only taken once a day for one location. Furthermore, satellite measurements are usually only available under cloud-free conditions in the visible or infrared spectral range and thus no continuous time series is guaranteed. Consequently, they cannot provide a complete picture of the geophysical variability, which leads to sampling biases in the calculation of averaged values (e.g. monthly means).

Moreover, the question arises to what extent the limitation to cloud-free pixels influences the monthly averages determined from the OMI satellite measurements, i.e. whether a so-called "clear-sky bias" exists in the OMI TCWV data set. Gaffen and Elliott (1993) investigated this bias using radiosonde ascents and found that the TCWV is about 0-15% lower under cloud-free conditions than under cloudy conditions. Similarly, Sohn and Bennartz (2008) found a clear-sky bias between MERIS and AMSR-E of about 10%.

Since this section examines many different TCWV data sets, Table 3.1 summarises them for the sake of an overview.

Table 3.1: Overview of properties of TCWV data sets created for the investigation of sampling errors and clear-sky bias.

Data set	Spatiotemporal collocation	Cloud filter	RA filter
$\text{TCWV}_{sampled}$	yes	yes	yes
TCWV_{true}	no	no	no
$\text{TCWV}_{all-sky}$	yes	no	yes
TCWV_{RA}	yes	yes	no

3.5.1 Sampling error

To estimate the sampling errors, the methods of Xue et al. (2019) and Gleisner et al. (2020) are followed:

1. Hourly-resolved ERA5 data with a spatial resolution of $0.25° \times 0.25°$ are chosen as reference data and are then collocated spatially and temporally with OMI observations also following the filter criteria in Sect. 3.4. These data are then resampled to the $1° \times 1°$ resolution of the OMI TCWV data set and the monthly averages are calculated, yielding $\text{TCWV}_{sampled}$. To put it simply, the reference data set is used to try to mimic the data set under investigation as closely as possible.

2. Then the complete, original ERA5 data is resampled to the same spatial resolution and monthly means from this data are calculated as well (TCWV_{true}).

The difference between the two resampled data sets then represents the total sampling error:

$$\varepsilon_{sampling} = \text{TCWV}_{sampled} - \text{TCWV}_{true} \tag{3.2}$$

With this definition, the sampling error summarises the bias due to gaps in the swath, temporal differences or missing data (e.g. due to clouds) (Xue et al., 2019).

Figure 3.6 shows the mean absolute and relative sampling errors for the complete time range of the OMI TCWV data set (January 2005 to December 2020). Overall, it can be seen that most deviations are negative, i.e. the actual TCWV is underestimated. Regarding the absolute deviations, the strongest deviations can be seen in the area of storm-tracks in the mid-latitudes (e.g. North Atlantic) and the polar regions with values around $-5\,\text{kg}\,\text{m}^{-2}$. The smallest deviations are found in the quasi-permanent cloud-free regions in the subtropics. Since the absolute deviations in the cloudy regions are about the same magnitude globally, the relative differences increase from the equator towards the poles due to the decreasing TCWV values and reach values stronger than $-30\,\%$.

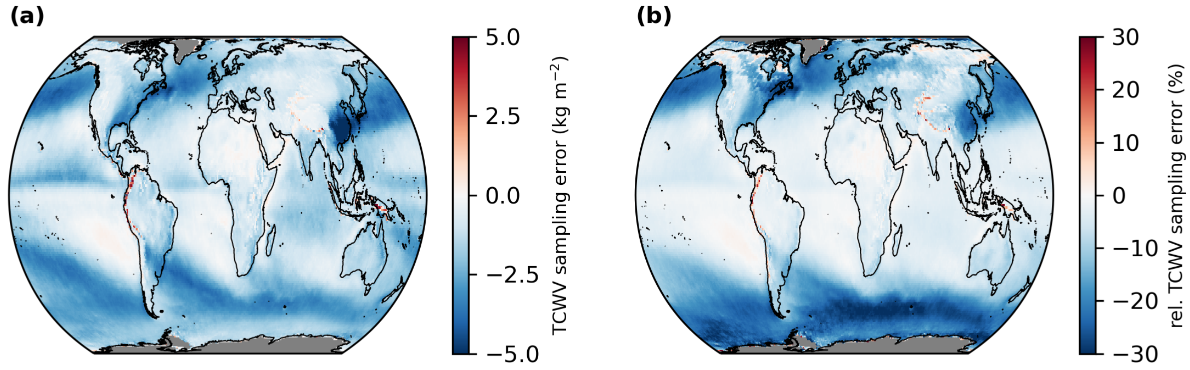

Figure 3.6: Global distributions of the mean sampling errors derived from monthly mean sampling differences for the time range January 2005 to December 2020 based on ERA5 reanalysis data. Panel **(a)** depicts absolute sampling error (i.e. $\varepsilon_{sampling}$) and Panel **(b)** relative sampling error (i.e. $\varepsilon_{sampling}/\mathrm{TCWV}_{true}$). Grid cells for which no data is available are coloured grey.

For further investigation, Fig. 3.7 shows the global distributions of the sampling error grouped into the different seasons. On the whole, it can be seen that the global structures remain almost constant for all seasons. Only the magnitude of the deviations seems to change, most prominently in the deep tropics and also in the northern mid-latitudes and Southeast Asia.

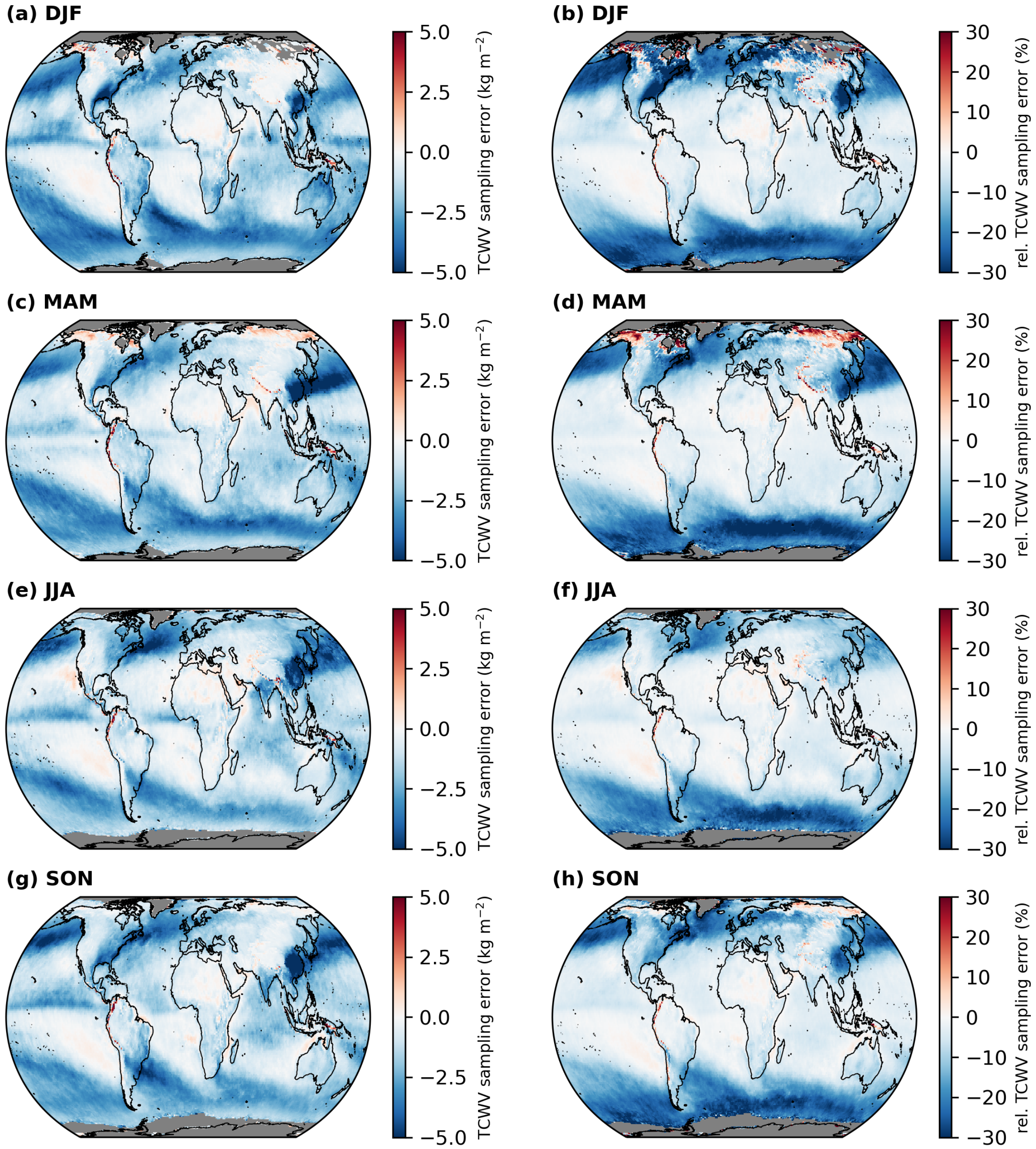

Figure 3.7: Global distributions of the absolute differences ($\varepsilon_{sampling}$; left column) and relative differences ($\varepsilon_{sampling}/\mathrm{TCWV}_{true}$; right column) of the mean differences due to sampling errors for winter (DJF; **(a)** & **(b)**), spring (MAM, **(c)** & **(d)**), summer (JJA, **(e)** & **(f)**), and autumn (SON, **(g)** & **(h)**) for the time range January 2005 to December 2020. Grid cells for which no data is available are coloured grey.

3.5.2 Clear-sky bias

To investigate to what extent these deviations are related to the clear-sky bias, a similar procedure is followed as for the calculation of the sampling error: Similar to the calculation of $\mathrm{TCWV}_{sampled}$, the ERA5 data are collocated spatially and temporally to the OMI orbit, however, now a cloud filter is not applied. The remaining TCWV data are then resampled to a $1° \times 1°$ grid and the monthly means are calculated, yielding $\mathrm{TCWV}_{all-sky}$. The difference of both sampled data sets then represents the clear-sky bias:

$$\varepsilon_{clear} = \mathrm{TCWV}_{sampled} - \mathrm{TCWV}_{all-sky} \tag{3.3}$$

To investigate seasonal structures, the global distributions of the absolute and relative clear-sky bias for the different seasons were determined from the monthly differences (see Fig. 3.8). Overall, the distributions of the clear-sky bias correspond very closely to the distributions of the sampling error, both in strength and in pattern. Moreover, the absolute and relative deviations show only slight changes between the different seasons.

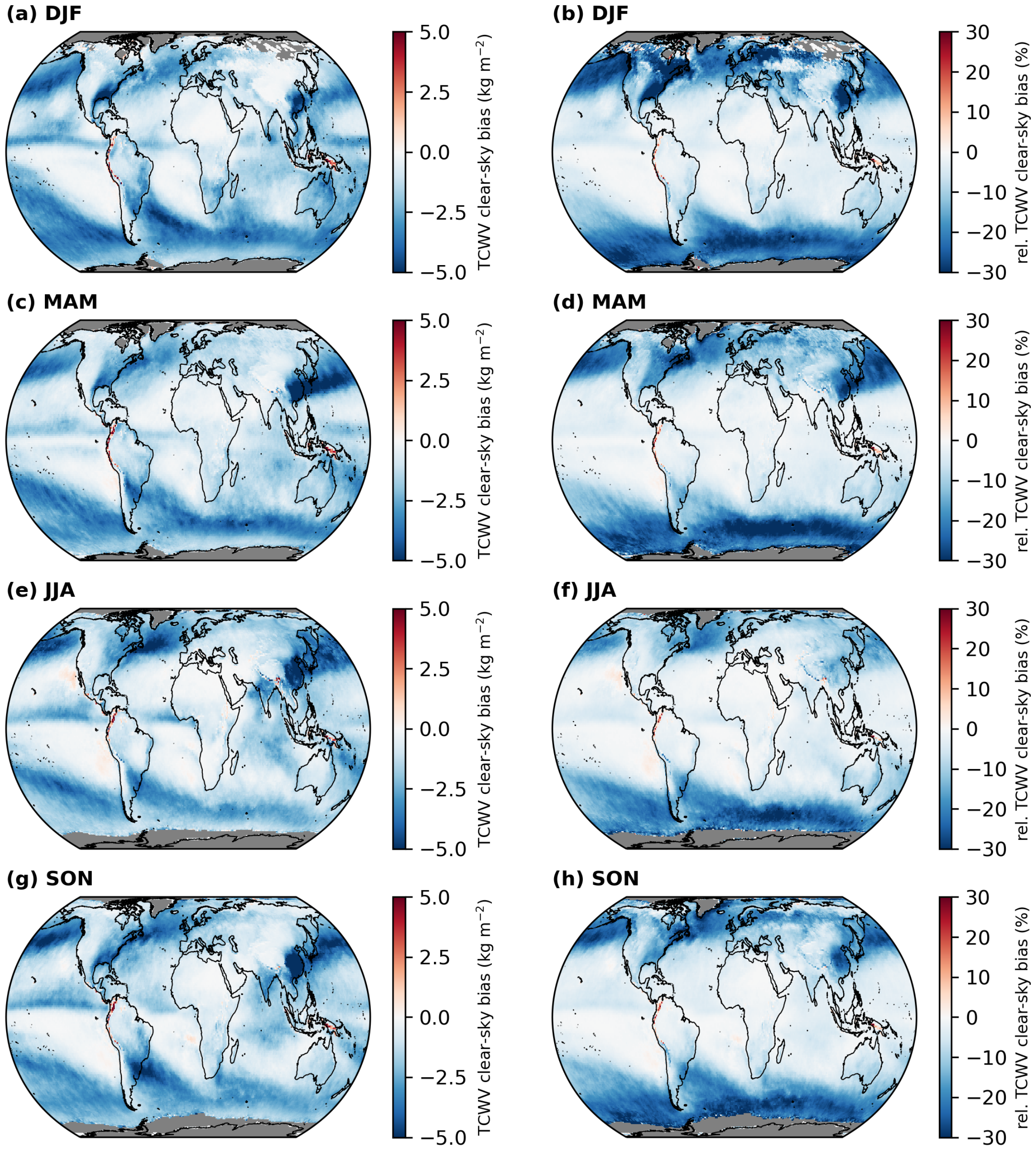

Figure 3.8: Global distributions of the absolute differences (ε_{clear}; left column) and relative differences (ε_{clear}/TCWV$_{all-sky}$; right column) of the mean differences between clear-sky and all-sky ERA5 based on the OMI cloud information for winter (DJF; **(a)** & **(b)**), spring (MAM, **(c)** & **(d)**), summer (JJA, **(e)** & **(f)**), and autumn (SON, **(g)** & **(h)**) for the time range January 2005 to December 2020. Grid cells for which no data is available are coloured grey.

3.5.3 Representativeness of row-anomaly filtered data in comparison to full swath

Due to the row anomaly filter, approximately 50% of the complete satellite swath of OMI is not considered in the TCWV data set. This raises the question of how much the monthly mean values would differ if the data of the complete swath were available. To investigate this, the same scheme as in the previous sections is applied with the same ERA5 data as a reference. The ERA5 data are selected to match the OMI overpass, once applying the row-anomaly filter and once not. However, in both cases the clear-sky filter based on the OMI cloud information is applied (effective cloud fraction $< 20\%$). The error due to the RA filter is then given by:

$$\varepsilon_{RA} = \mathrm{TCWV}_{sampled} - \mathrm{TCWV}_{RA} \tag{3.4}$$

Compared to the clear-sky bias, the deviations ε_{RA} are much weaker and no particular spatial patterns are discernible in the global distributions except in the deep Pacific tropics and parts of Southeast Asia (see Fig. 3.9a). Considering the much larger uncertainties of the OMI TCWV retrievals of typically 20% and more and that the clear-sky bias is almost one order of magnitude larger, the obtained deviations are negligible and thus the monthly means from the RA-filtered data are a good representation compared to the monthly means from the data for a full swath, even though only half of the satellite data is actually used.

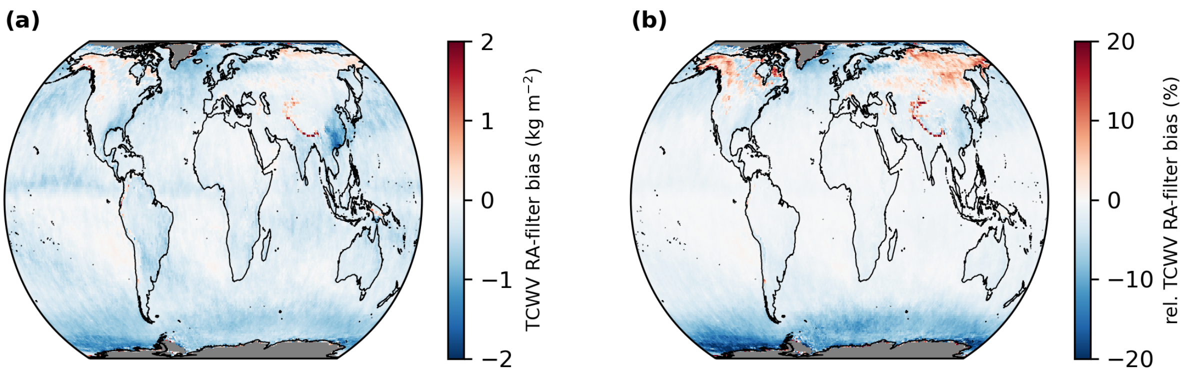

Figure 3.9: Global distributions of the mean differences between row-anomaly (RA) filtered and full swath ERA5 based on the OMI cloud information for the time range January 2005 to December 2020. Panel **(a)** depicts the absolute differences (ε_{RA}) and Panel **(b)** relative differences (i.e. $\varepsilon_{RA}/\mathrm{TCWV}_{RA}$). Grid cells for which no data is available are coloured grey.

3.5.4 Overview

The histograms of the sampling error, the clear-sky bias, and the representative error are summarized in Figs. 3.10, 3.11, and 3.12, respectively. For the sampling error a mean absolute deviation of $-1.6\,\mathrm{kg\,m^{-2}}$ (median $-1.4\,\mathrm{kg\,m^{-2}}$) and a mean relative deviation of -9.5% (-6.2%) are obtained and for the clear-sky bias a mean absolute deviation of $-1.7\,\mathrm{kg\,m^{-2}}$ (median $-1.3\,\mathrm{kg\,m^{-2}}$) and a mean relative deviation of -10.0% (-5.9%) are calculated. However, the distributions of the absolute and relative deviations for the sampling error and the clear-sky bias are highly left-skewed and thus the mean value in particular is influenced by the long tails of the distributions. Nevertheless, the obtained values for the clear-sky bias agree well with the findings of Gaffen and Elliott (1993) and Sohn and Bennartz (2008).

Since the effect of the clear-sky bias is already included in the sampling error and the results for both errors are very similar, it can be assumed that the spatial and temporal sampling errors play only a minor or negligible role compared to the clear-sky bias.

In contrast to the histograms of the sampling error and clear-sky bias the distributions of the representative error follow normal or Gaussian shapes with mean values of $-0.30\,\mathrm{kg\,m^{-2}}$ and -2.1% (and for the median $-0.23\,\mathrm{kg\,m^{-2}}$ and -1.1%). So although deviations arise due to the RA-filter, these deviations are almost an order of magnitude smaller than those of, for instance, the clear-sky bias and hence can be neglected.

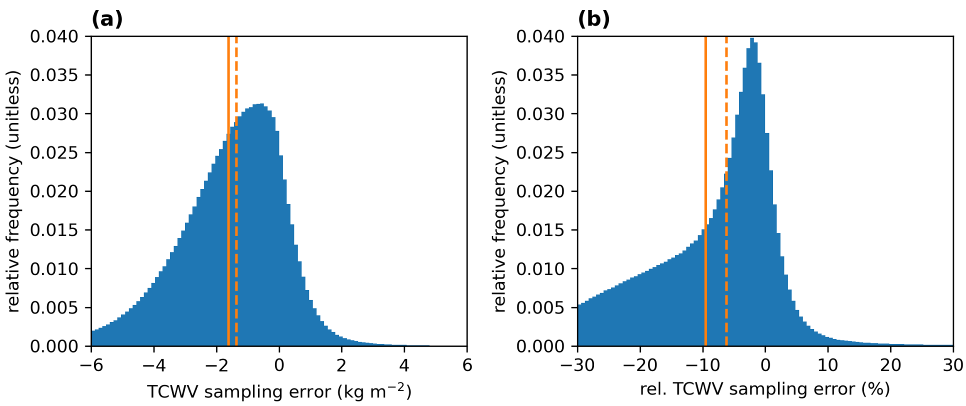

Figure 3.10: Distributions of the absolute differences ($\varepsilon_{sampling}$; Panel **(a)**) and relative differences ($\varepsilon_{sampling}/\mathrm{TCWV}_{true}$; Panel **(b)**) of the monthly mean differences between clear-sky and all-sky ERA5 data based on the OMI cloud information. The solid and dashed oranges line indicate the mean and the median of the distributions, respectively.

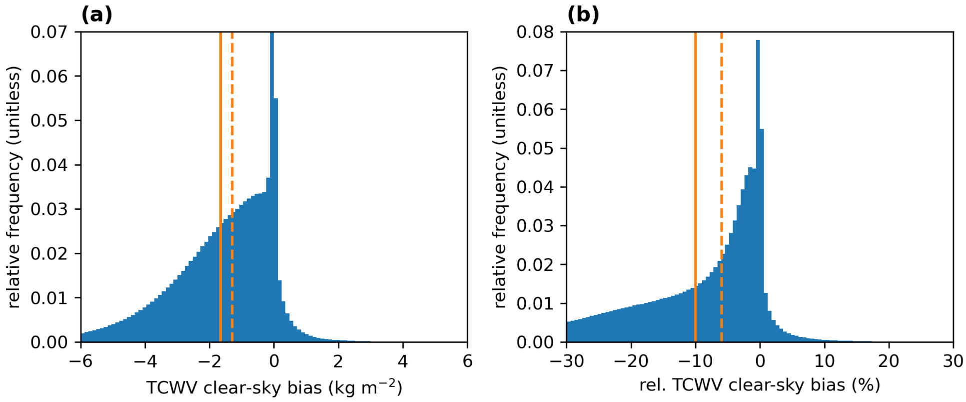

Figure 3.11: Distributions of the absolute differences (ε_{clear}; Panel **(a)**) and relative differences ($\varepsilon_{clear}/\mathrm{TCWV}_{all-sky}$; Panel **(b)**) of the monthly mean differences between clear-sky and all-sky ERA5 data based on the OMI cloud information. The solid and dashed orange lines indicate the mean and the median of the distributions, respectively.

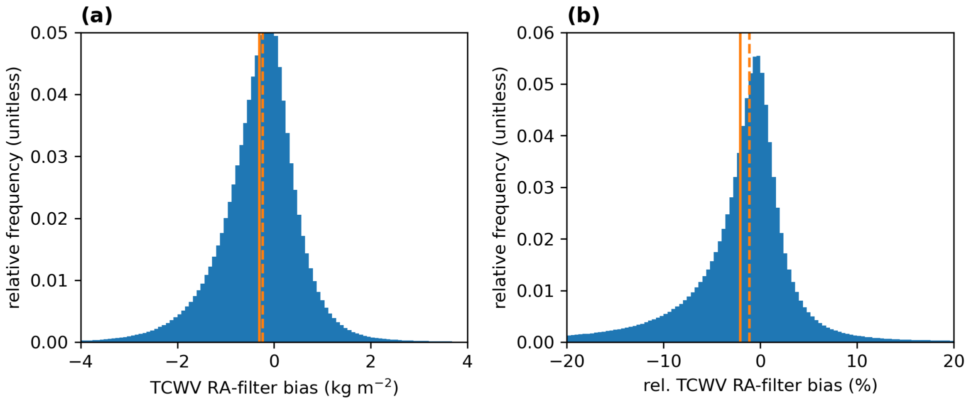

Figure 3.12: Distributions of the absolute differences (ε_{RA}; Panel **(a)**) and relative differences ($\varepsilon_{RA}/\mathrm{TCWV}_{RA}$; Panel **(b)**) of the monthly mean differences between RA-filtered and full swath ERA5 data based on the OMI cloud information. The solid and dashred orange lines indicate the mean and the median of the distributions, respectively.

3.6 Intercomparison to existing water vapour climate data records

To evaluate the overall quality of the OMI TCWV data set, an intercomparison study is conducted for which the merged, 1-degree total precipitable water (TPW) data set version 7 from Remote Sensing Systems (RSS) (Mears et al., 2015; Wentz, 2015), TCWV data from the reanalysis model ERA5 (Hersbach et al., 2019, 2020), and from the ESA Water_Vapour_CCI (WV_cci) climate data record CDR-2 are used as reference.

The RSS data set consists of merged geophysical ocean products whereby the values are retrieved from various passive satellite microwave radiometers. These microwave radiometers have been intercalibrated at the brightness temperature level and the ocean products have been produced using a consistent processing methodology for all sensors (more details in Wentz, 2015; Mears et al., 2015). The major advantages of microwave TCWV retrievals are their high precision and accuracy and that they are insensitive to clouds, so that TCWV values can also be retrieved even under cloudy-sky conditions. A disadvantage, however, is that these retrievals are (mostly) only available over the ocean surface.

Thus, the OMI TCWV data are also compared to the ESA WV_cci CDR-2. At the moment of preparation of this thesis, the CDR-2 is a beta-version of the combined microwave and near-infrared imager based TCWV data record (COMBI). The CDR combines microwave and near-infrared imager based TCWV over the ice-free ocean as well as over land, coastal ocean and sea-ice, respectively. The data record relies on microwave observations from SSM/I, SSMIS, AMSR-E and TMI, partly based on a fundamental climate data record (Fennig et al., 2020) and on near-infrared observations from MERIS, MODIS-Terra and OLCI (Danne et al., 2022).

Within comparisons between different satellite data sets a major drawback is the influence of sampling errors due to different observation times, pixel footprint sizes or orbit patterns. To minimise this source of error, data from reanalysis models are useful. ERA5 is the fifth generation ECMWF reanalysis (Hersbach et al., 2020) and combines model data with in situ and remote sensing observations from various different measurement platforms. For this comparison study, the "monthly averaged reanalysis by hour of day" from the Copernicus Climate Data Store on a $1° \times 1°$ grid are used. To account for OMI's observation time (around 13:30 LT), first the local time is calculated for each longitude in the ERA5 data set, then the TCWV data are selected for the time period between 13:00-14:00 LT and finally the selected data are merged.

For the intercomparison, it is also important to consider that the reference data sets are not perfect or error-free and that the comparisons across the different TCWV regimes are not consistent. Thus, an orthogonal distance regression (ODR; Cantrell, 2008) and a piece-wise linear regression (PWL) are performed. In the case of the ODR it is necessary to use reasonable ratios of the relative errors of the compared data sets instead of using absolute errors in order to obtain meaningful results. In a comprehensive uncertainty analysis, Wentz (1997) determined a typical error of 1.22 kg m^{-2} for SSM/I observations. Mears et al. (2015) found that the uncertainty of daily microwave TCWV observations for TCWV = 10 kg m^{-2} was around 1 kg m^{-2} and for TCWV = 60 kg m^{-2} around 2–4 kg m^{-2}. Hence, it is assumed that the uncertainty of the RSS data set is 5% or at least 1 kg m^{-2}. The minimum (absolute) error is intended to prevent VCDs close to 0 from being considered completely error-free and thus forcing the ODR fit through them.

For ERA5 and the ESA CDR-2 one can assume similar uncertainties over ocean, since the TCWV values there are also mainly based on microwave observations. Unfortunately, no uncertainties are provided for TCWV over land. Thus, for the sake of simplicity, it is assumed that the relative errors of the reference data sets over land are twice as high as over ocean, i.e. 10% or at least 2 kg m^{-2}. For the OMI TCWV data set an uncertainty of 20% is assumed (Borger et al., 2020), but at least 2 kg m^{-2}. Also other error assumptions have been tested and it turned out that the exact choice of errors is negligible for the regression results as long as the ratio of uncertainties remains similar.

3.6.1 Intercomparison to RSS SSM/I

The results of the intercomparison between OMI and the RSS TCWV data set are summarized in Figs. 3.13 and 3.14. Figure 3.13 depicts the 2D histogram from the comparison between the monthly mean values from RSS and the OMI TCWV data set. The data is distributed closely along the 1-to-1 diagonal (black dashed line) and the results of the orthogonal distance regression (ODR, red solid line) indicate an overall very good agreement with slopes of around 1.01 and a coefficient of determination of $R^2 = 0.96$. For the PWL regression, similar results with a slope around 1.04 are obtained for TCWV values > 9.5 kg m^{-2}, which represents the vast majority of the comparison data set (approximately 90%).

Figure 3.14 illustrates the zonally averaged monthly mean absolute and relative difference of OMI minus RSS TCWV within the latitude-time space. In general, the deviations between OMI and RSS in Fig. 3.14a are quite low with a positive bias of +1.0±1.5 kg m^{-2}. Within the tropics (i.e. between −20 to 20°N) a mean deviation of +2.0±1.6 kg m^{-2} is obtained and in the extratropics values of +0.7±1.3 kg m^{-2}. However, within the tropics, also distinctive periodic patterns of positive deviations are observable. In terms of relative deviations (Fig. 3.14b), the seasonal pattern is slightly weaker with an overall mean relative deviation of +6.8% (median: +4.7%).

Figure 3.15 shows the global mean absolute and relative TCWV difference between OMI and RSS SSM/I over the complete time period of the OMI TCWV data set. Consistent with the findings from Fig. 3.14 highest positive absolute deviations can be found in the tropical Pacific ocean and near the coastlines of South America, Africa, and Indonesia whereas strongest

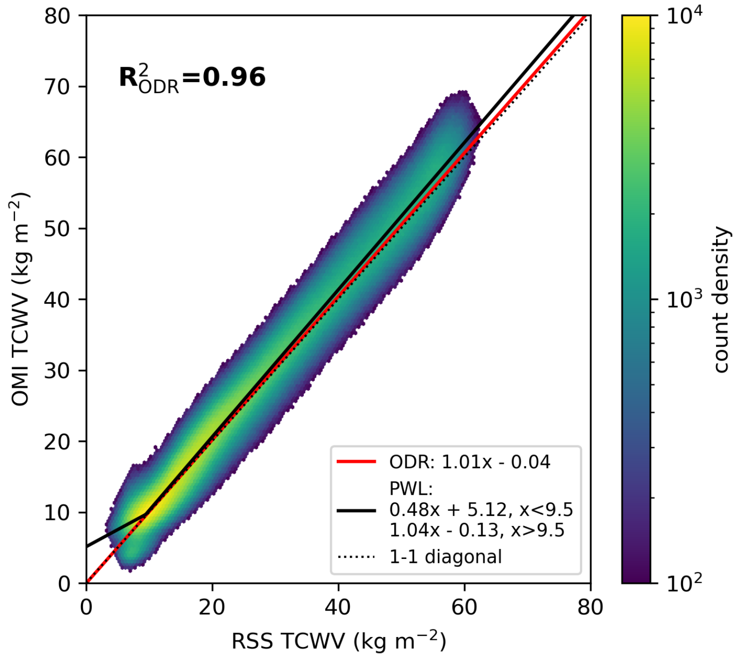

Figure 3.13: Intercomparison between monthly mean TCWV from OMI and Remote Sensing Systems (RSS) merged SSM/I data set for data over ocean. In the 2D histogram the colour indicates the count density; the red solid line represents the results of the orthogonal distance regression (ODR) and the solid black line the results of the piecewise linear regression (PWL). The results of the respective fits are given in the bottom right box and the correlation coefficient in the top left corner. The dashed black line indicates the 1-to-1 diagonal.

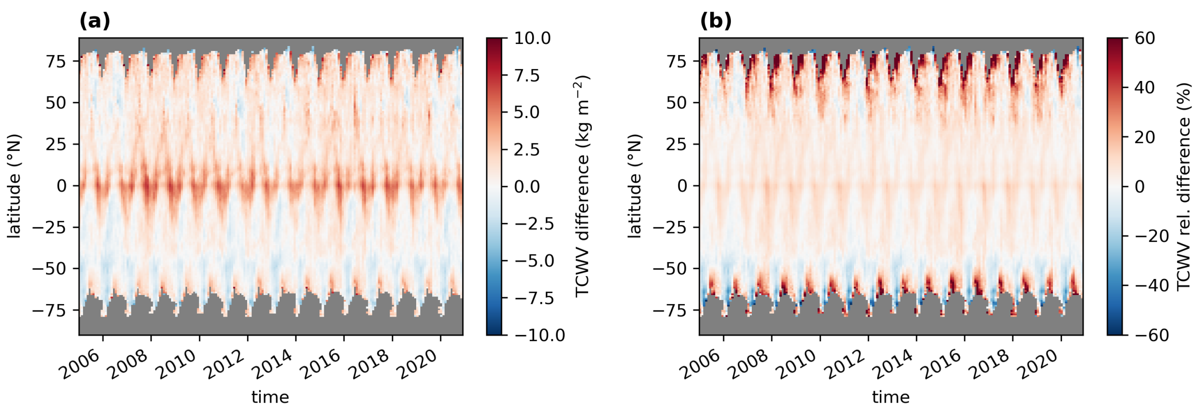

Figure 3.14: Intercomparison between monthly mean TCWV from OMI and Remote Sensing Systems (RSS) merged SSM/I data set for data over ocean. Absolute (**a**) and relative TCWV difference (**b**) of OMI minus RSS within the latitude-time space; reddish colours indicate an overestimation, blueish colours an underestimation of the OMI TCWV data set.

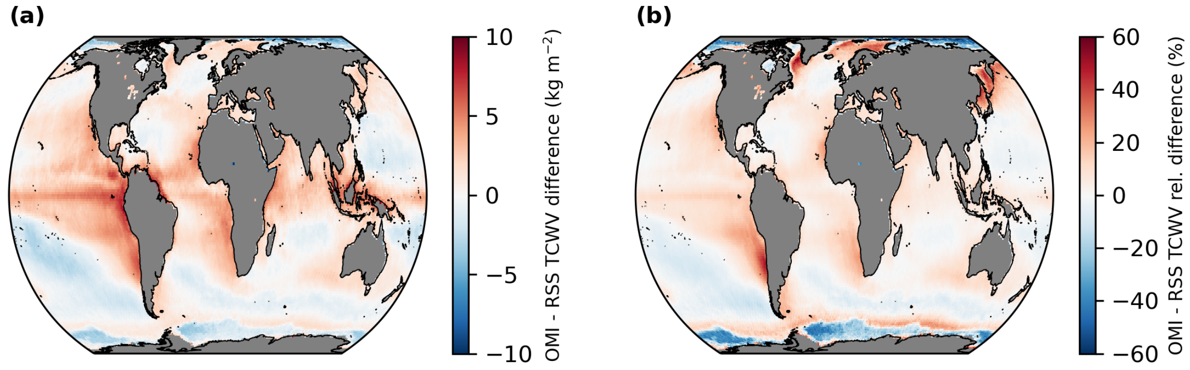

Figure 3.15: Global mean TCWV absolute (**a**) and relative difference (**b**) of OMI minus RSS SSM/I for the time range January 2005 until December 2020. Areas with no valid values are coloured grey.

negative absolute deviations are obtained around the South Pacific convergence zone and the East Siberian Sea. For the relative differences (Fig. 3.15b), the patterns of the deviations are less concise, except around the western coast of South America.

In the case of the (tropical) Pacific ocean the distribution of the systematic positive absolute deviations matches quite well regions of cold water or of the so called "cold tongue". Likewise, the prominent positive deviation on the west coast of South America matches well with the Humboldt Current. These regions are frequently affected by low clouds. Since the highest water vapour concentrations occur in the lower troposphere, small deviations of a few 100 m in cloud top height can have relatively large effects on the AMF (and thus on the retrieved TCWV). In the case of Central America or the Atlantic ocean, a too low albedo due to additional absorption by phytoplankton (Kleipool et al., 2008) could explain the systematic positive deviations.

Additional comparisons taking into account only valid grid cells according to the "common-mask" from ESA WV_cci are presented in Sect. 3.6.4. This mask filters regions where no continuous time series of data is available or where the data are affected by high uncertainties e.g. due to frequent cloud cover. Therefore only high quality measurements are compared to each other. However, since mainly regions over land surface are affected, the comparisons with the filtered data are almost identical to the unfiltered data.

3.6.2 Intercomparison to ERA5

The results of the intercomparison to ERA5 are depicted in Figure 3.16. To investigate potential dependencies on the surface type, the data is separated into data over ocean and data over land (Fig. 3.16a & b, respectively). The intercomparison for data over ocean (Fig. 3.16a) reveals similar results as the intercomparison between OMI and RSS: the ODR results indicate a slight

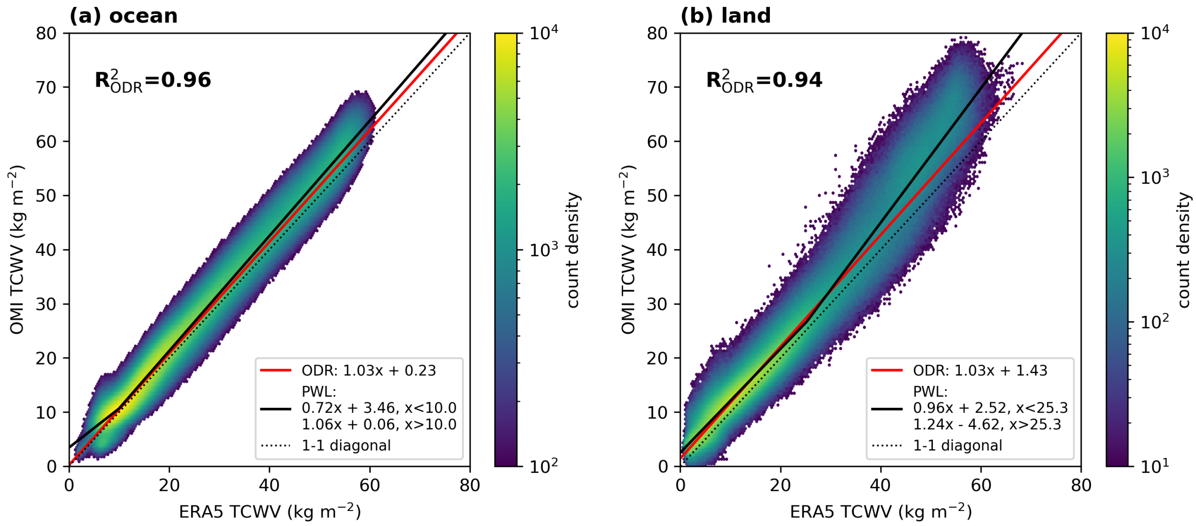

Figure 3.16: Same as Fig. 3.13, but now with ERA5 data for data over ocean (**a**) and for data over land (**b**).

overestimation (slopes of around 1.03) together with a coefficient of determination close to unity (R^2 of around 0.96).

For data over land, the picture is different: although the ODR gives similar results for the slope as for data over ocean, the distribution in the 2D histogram (Fig. 3.16b) shows particularly strong positive deviations of approximately +10 kg m^{-2} at high TCWV values and an overall systematic offset of around +1.43 kg m^{-2}. Within the PWL analysis a good agreement to the reference data is obtained for TCWV values up to about 25 kg m^{-2} (which represents approximately 74% of all data points) with slopes of around 0.96. However, for higher TCWV values distinctive positive overestimations of up to 24% are observed. Nevertheless, even for low TCWV values a systematic offset of approximately +2.52 kg m^{-2} is obtained.

The zonal averages of the monthly mean differences are depicted in Fig. 3.17. For data over ocean (Fig. 3.17a & b) the periodic pattern of positive deviations in the tropics occurs again, with an overall small positive bias of +1.7±1.7 kg m^{-2}, which increases to +3.4±1.7 kg m^{-2} in the tropics (−20 to 20 °N) but is around +1.1±1.3 kg m^{-2} in the extratropics. Over land, in the corresponding latitude-time difference plot (Fig. 3.17), the systematic positive deviation in the tropics is now much stronger with values around +6.2±3.4 kg m^{-2} (for latitudes $<$ 20°). However, in the extratropics the positive deviation is around +1.7±1.2 kg m^{-2} on average and thus of similar magnitude as for the ocean comparisons.

Closer inspection of the mean TCWV difference between OMI and ERA5 (see Fig. 3.18) reveals that the strong deviations over the tropical landmasses mainly occur in the regions that are affected by frequent cloud cover such as the Amazon basin, Central Africa and the maritime continent.

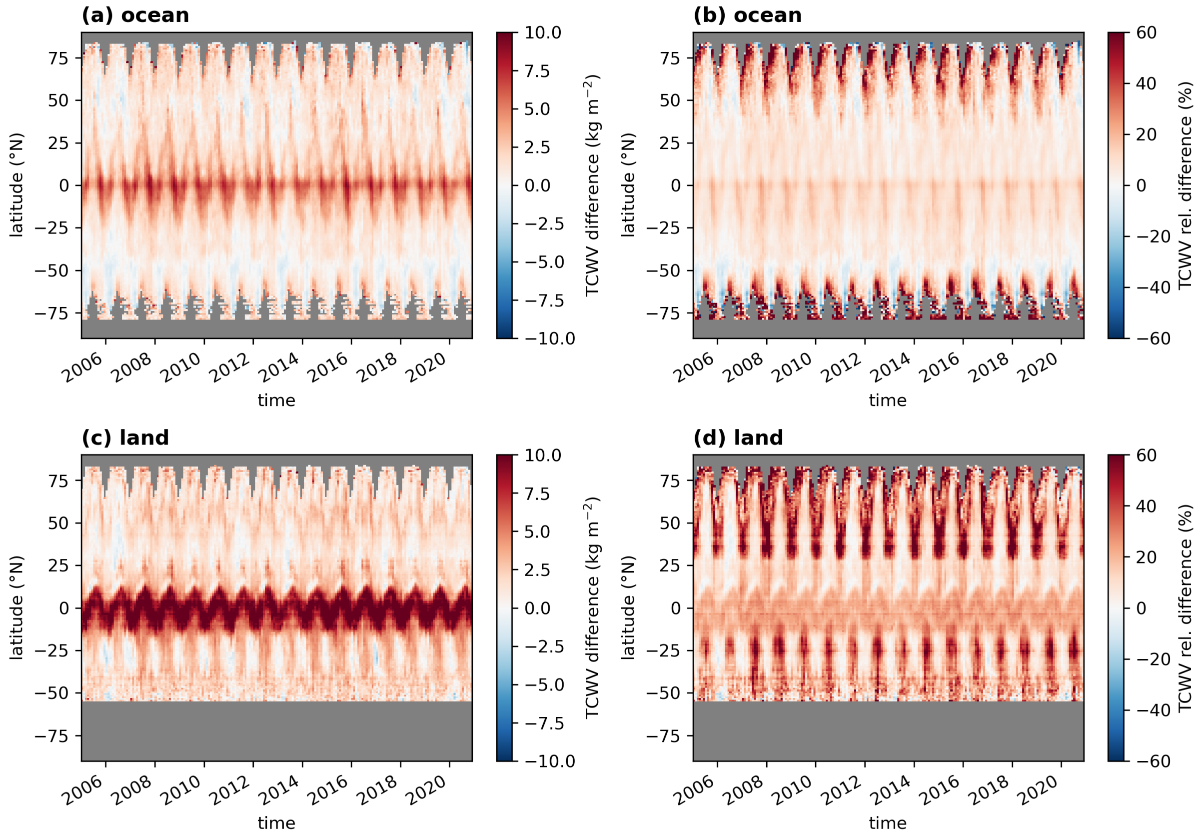

Figure 3.17: Same as Fig. 3.13, but now with ERA5 data for data over ocean (top row; **a** & **b**) and for data over land (bottom row; **c** & **d**).

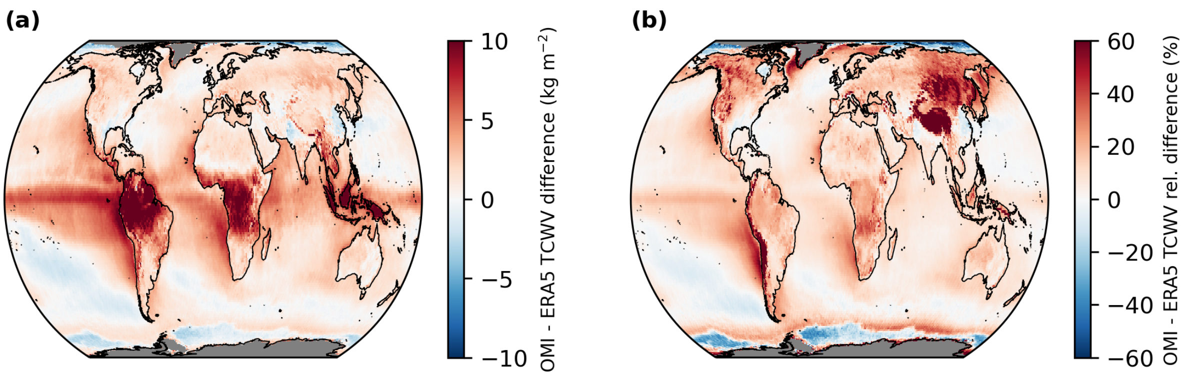

Figure 3.18: Same as Fig.3.15, but for ERA5.

Hence, the reasons for the distinctive positive deviations with respect to ERA5 may arise from different causes. For the case of the OMI TCWV retrieval two main uncertainty sources may cause strong, systematic positive deviations: First, there is the possibility that the used land surface albedo from Borger et al. (2020) is too low, leading to an underestimation of the AMF and consequently to an overestimation of the H_2O VCD. However, Borger et al. (2020) also showed that their modified albedo map led to overall better results in comparison to the static albedo climatology from Kleipool et al. (2008) for the case of the TROPOMI TCWV retrieval. On the other hand, there may also be uncertainties in the retrieval input data of the cloud information from the L2 NO_2 product: For example, if the surface albedo is underestimated in the input of the cloud algorithm, this leads to an overestimation of the cloud top height and thus to an underestimation of the AMF, and finally to an overestimation of the H_2O VCD. For the case of ERA5, the frequent cloud cover can be also major source of uncertainty, as only few satellite measurements (or none at all in the thermal infrared) are available due to the frequent cloud contamination. This might lead to clear-sky dry biases in the cloud-affected regions and increased uncertainties within the assimilation process due to the complex radiative transfer in cloudy scenarios (e.g. Li et al., 2016). Likewise, these remote regions are affected by an overall sparseness in the observation density of in situ measurements, so the ERA5 TCWV values are likely to be based mainly on modelled data. Overall, the strong positive deviation of the OMI TCWV data set thus likely results from a combination of an overestimation of the OMI TCWV retrieval and an underestimation of the ERA5 data.

Hence, considering these large uncertainties in the OMI retrieval and that the uncertainties in ERA5 for data over tropical landmasses are not negligible anymore, it is concluded that the OMI TCWV data set can well represent the global distribution of the atmospheric water vapour content at least over ocean. Over land, however, the data set should be treated with caution due to the systematic positive deviations from the reference data sets, especially in areas of high TCWV values (i.e. above $25\,\mathrm{kg\,m^{-2}}$). Regarding the possible impact on trend analyses, it can be assumed that the influence of a false albedo is likely not strong, as the TCWV trends mainly depend on the trends in the H_2O SCD but only in second order on changes in the AMF and its input parameters (see e.g. Borger et al. (2022) or Chapter 4).

An additional comparison in which particularly critical regions were filtered using the ESA WV_cci "common mask" (see Fig. 3.25) is given in the Sect. 3.6.4. When this mask is applied, only high quality measurements are taken into account for the intercomparison. As a result, the extreme overestimations are filtered out and the distribution in the 2D histogram for the comparison over land improves considerably (see Fig. 3.27a). The slope of the ODR is now around 0.97, which is closer to the results of the PWL regression for TCWV $< 25\,\mathrm{kg\,m^{-2}}$.

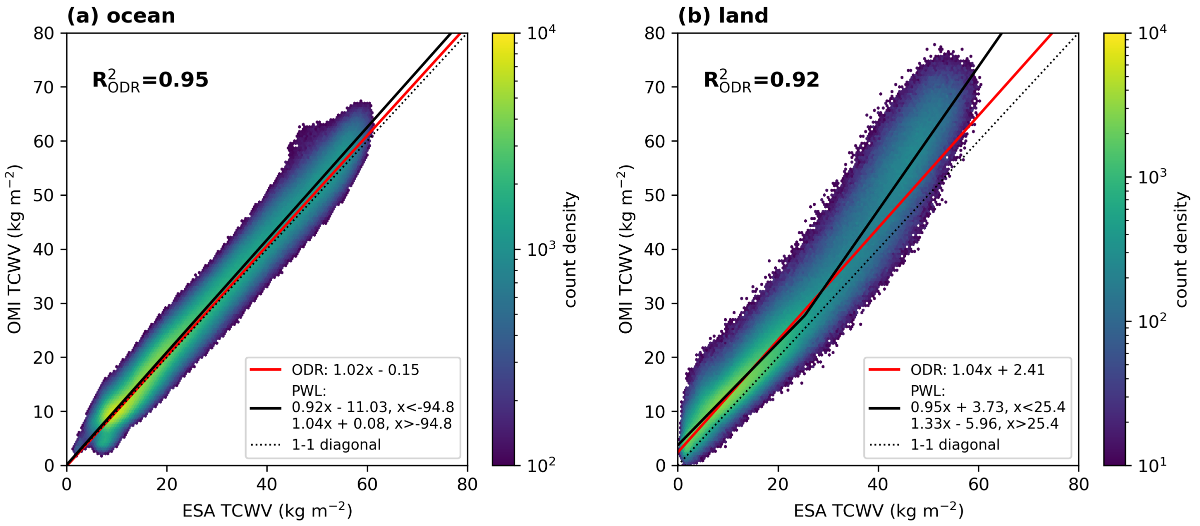

Figure 3.19: Same as Fig. 3.13, but now with ESA WV CCI CDR-2 data for data over ocean (**a**) and for data over land (**b**).

3.6.3 Intercomparison to ESA Water Vapour CCI climate data record

For the intercomparison with the ESA WV_cci climate data record CDR-2 the CDR is resampled from its native spatial resolution (0.5° × 0.5°) to the lattice of the OMI TCWV data set. Furthermore, though the CDR covers a time span from July 2002 to December 2017, the focus is on the time period January 2005 to March 2016, as the CDR's difference relative to ERA5 over land is only stable over the MERIS and MODIS period, i.e., from 2002 until March 2016 if looking at clear-sky data.

Figure 3.19 summarizes the results of the intercomparison. Not surprisingly, the results for data over ocean (Fig. 3.19a) are similar to the findings of the RSS SSM/I and ERA5 comparison as measurements from the same (or similar) sensors have been considered: the ODR results indicate slight overestimations of around 2% with a coefficient of determination of around 0.95.

As in the intercomparison of ERA5, the intercomparison over land (Fig. 3.19b) shows roughly similar ODR fit results as over ocean, but also striking positive deviations for high TCWV values and an overall positive offset of 2.41 kg m^{-2}. Again, when applying a piecewise linear regression analysis a good agreement is obtained with slopes of around 0.95 for TCWV values to about 25 kg m^{-2} but still a distinctive positive offset of 3.73 kg m^{-2} for low TCWV values and distinctive overestimations of up to 33% for higher TCWV values are present, which is even higher than for the comparison to ERA5.

Regarding zonal averages, the time-latitude diagrams for data over ocean (Fig. 3.20a & b) indicate an average deviation of +1.3±1.8 kg m^{-2} (+2.5±1.9 kg m^{-2} in the tropics, +0.8±1.5 kg m^{-2} in the extratropics). As expected from the 2D histograms, the systematic deviations for data over land are also much stronger (see. Fig. 3.19c) and reach values of around +7.3±3.6 kg m^{-2} in the

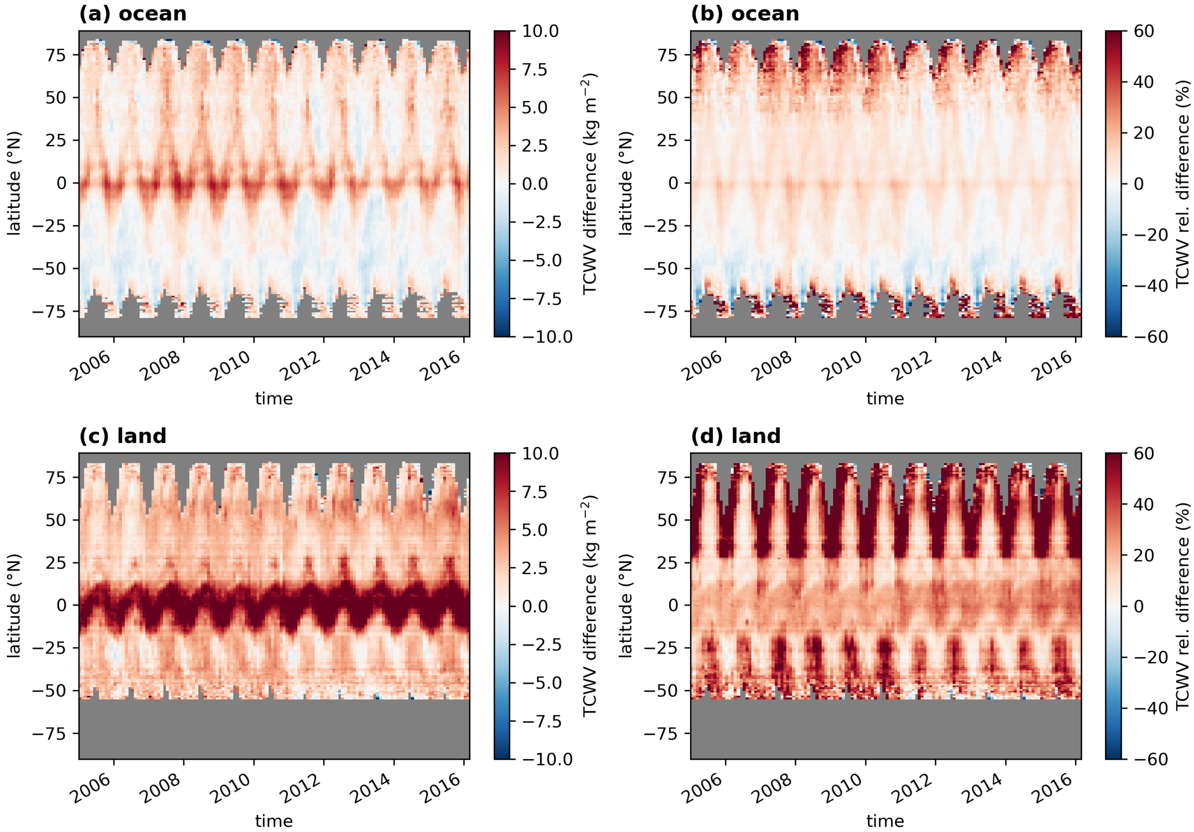

Figure 3.20: Same as Fig.3.15, but for ESA WV CCI CDR-2.

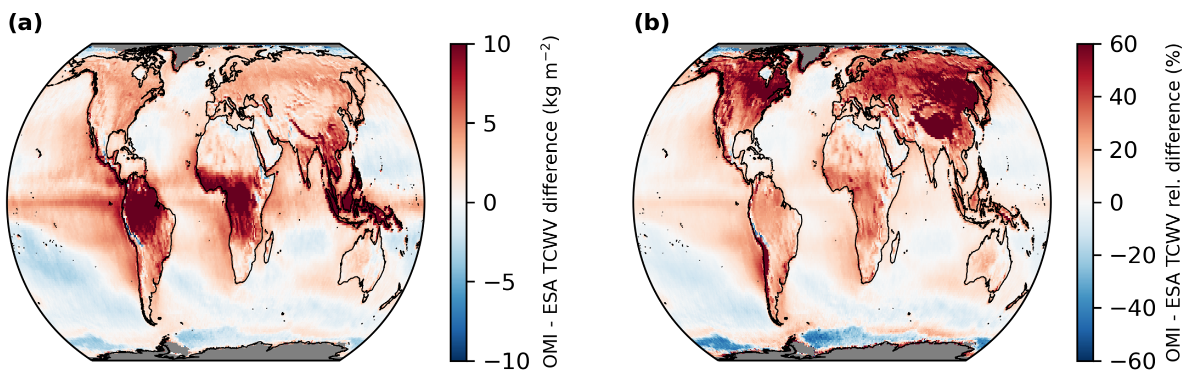

Figure 3.21: Same as Fig.3.15, but for ESA WV CCI CDR-2.

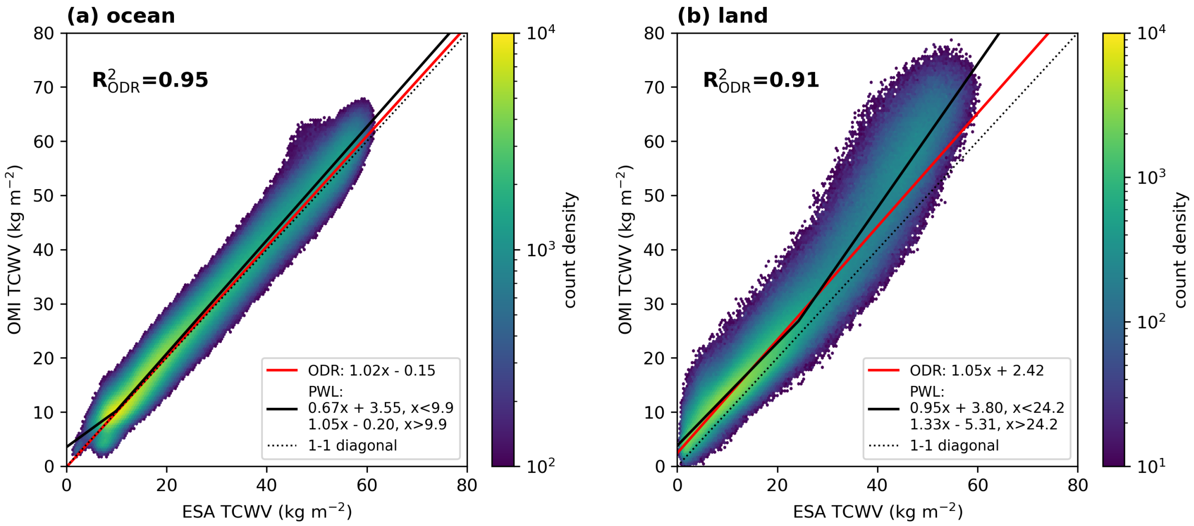

Figure 3.22: Same as Fig. 3.19, but now with ESA WV CCI CDR-2 data for data over ocean (top row; **a** & **b**) and for data over land (bottom row; **c** & **d**) for the complete time range.

tropics, around +2.8±1.4 kg m^{-2} in the extratropics, and a global average of +4.2±3.2 kg m^{-2}. These even higher deviations compared to the analysis with ERA5 could be due to the different observation times of the data sets: MERIS on Envisat and MODIS on Terra have an overpass time of 10:00 LT and 10:30 LT, respectively, and follow a descending orbit, whereas OMI measures at 13:30 LT in an ascending orbit.

Overall, similar to the comparison to ERA5 the strongest positive deviations occur again over the tropical landmasses that are mostly affected by frequent cloud cover (see Fig. 3.21). However, also systematic overestimations are observable along coastlines (e.g. Central America) and in some mountain regions (e.g. in the Himalayas) which eventually arise from sampling issues of the different satellite products.

Sect. 3.6.4 presents a comparison in which critical regions were filtered using the "common mask" from the ESA WV CCI CDR. When this mask is applied, there are clear improvements for the comparison over land: the prominent overestimates at high TCWV values are filtered out and the distribution is now closer to the 1-1 diagonal (see Fig. 3.27b). For the ODR, the slope is around 0.97, which agrees quite well with the slopes obtained for the PWL regression for TCWV < 25 kg m^{-2}.

For the sake of completeness, the results for the comparison over the complete time range are depicted in the Figs. 3.22, 3.23, and 3.24.

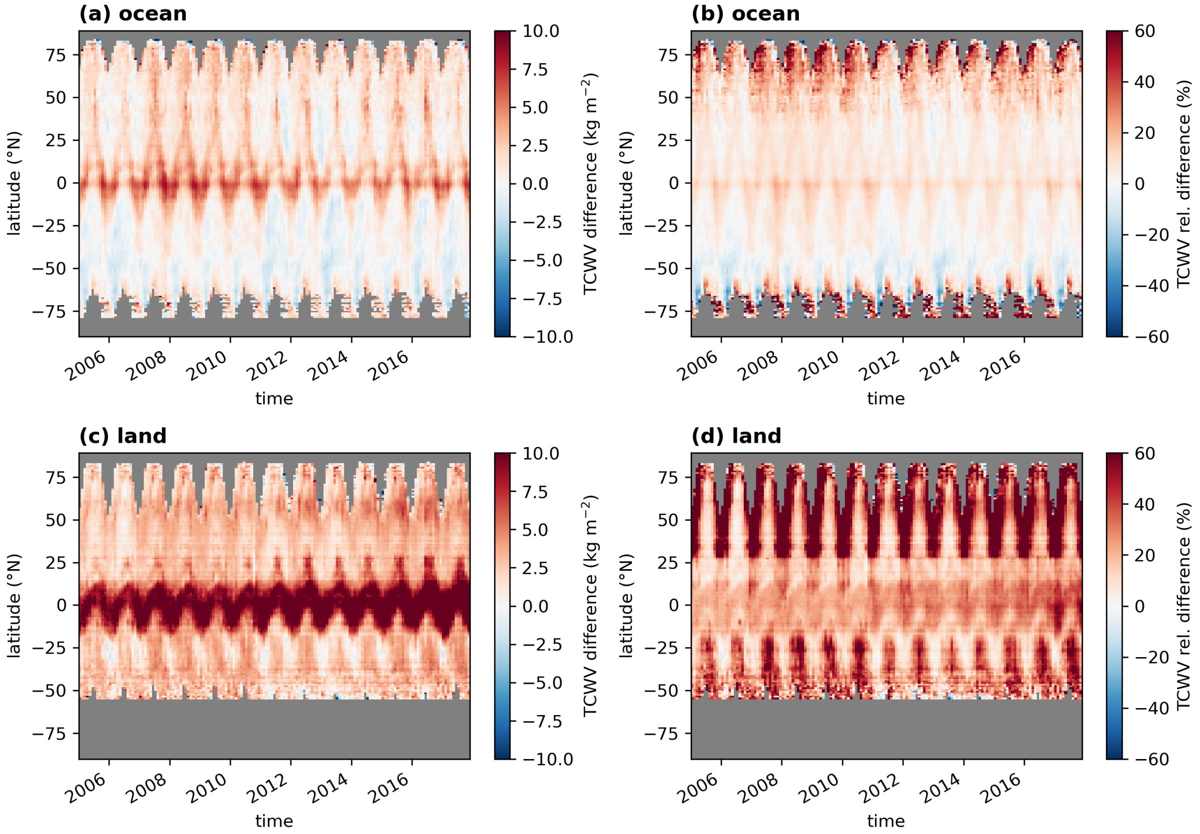

Figure 3.23: Same as Fig. 3.19, but now with ESA WV CCI CDR-2 data for data over ocean (top row; **a** & **b**) and for data over land (bottom row; **c** & **d**) for the complete time range.

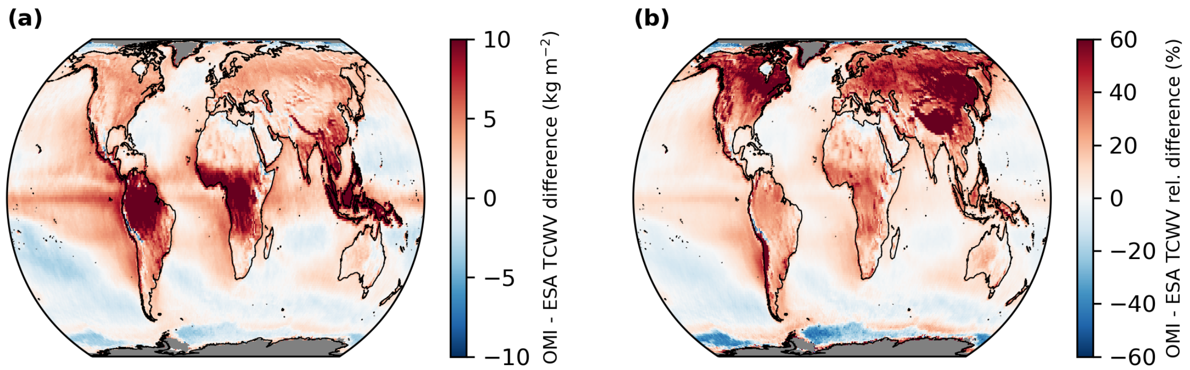

Figure 3.24: Same as Fig.3.21, but now for ESA WV CCI CDR data over the complete time range.

3.6.4 Intercomparisons considering the common mask from ESA WV_cci

The intercomparison in Sect. 3.6 also considers regions for which only a small number of measurements are available, for example due to frequent cloud cover or seasonality of the solar zenith angle. On the one hand, the small sample size of measurements leads to a higher statistical uncertainty with regard to the monthly mean, and on the other hand also to a non-continuous time series when data are missing for the complete month. Moreover, the errors of the individual measurements are also significantly larger in these regions. With the help of the "common-mask" of the ESA WV_cci CDR-2 (see Fig. 3.25), these regions can be identified and filtered for additional intercomparisons.

The results of the intercomparisons with the "filtered" data are shown in Fig. 3.26 for data over ocean and in Fig. 3.27 for data over land. For all comparisons, the coefficients of determination for the ODR regression remain at approximately a similar level (i.e. R^2 above 0.90) as for the non-"filtered" comparisons. For the comparisons over ocean hardly any changes are obtained, as the filter is mainly applied over land surfaces. However, there is a remarkable improvement for the comparison over land: although the fit results of the ODR change only slightly, the extreme overestimates at high TCWV values are now filtered out and the distributions are now closer to the 1-1 diagonal. Overall, the results for the "filtered" comparison over land also agree very well with the results of the piecewise linear regression, for which similar slope regression results were found for TCWV $< 25\,\mathrm{kg\,m^{-2}}$.

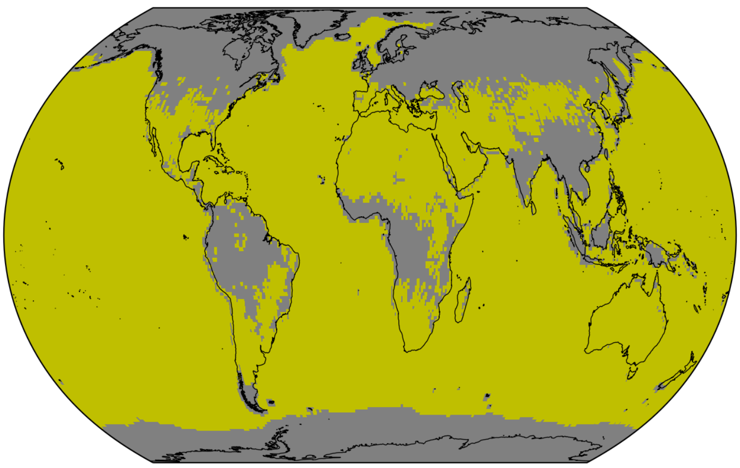

Figure 3.25: "Common mask" of the ESA WV CCI CDR-2. Yellow grid cells indicate data points which are accounted for within a temporal stability analysis. Invalid grid cells are coloured grey.

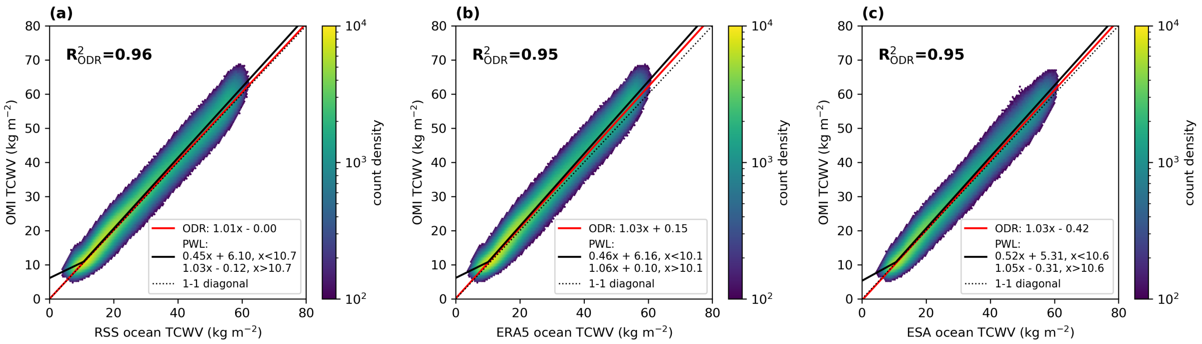

Figure 3.26: Correlation analysis of the OMI TCWV data set and **(a)** RSS SSM/I, **(b)** ERA5, and **(c)** the ESA WV CCI CDR-2 for data over ocean taking into account only valid grid cells according to "common mask" in Figure 3.25.

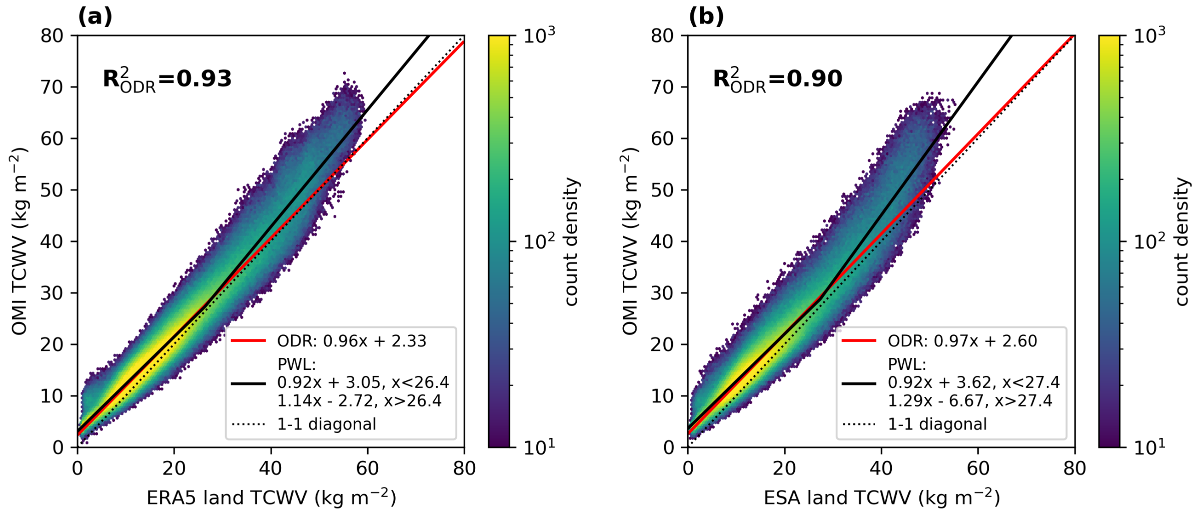

Figure 3.27: Same as Fig. 3.26, but for data over land.

3.7 Intercomparison to IGRA2 radiosonde observations

For further comparisons besides reanalysis and satellite data, in situ measurements from radiosondes are invaluable, as these measurements can provide information on the vertical water vapour distribution with high accuracy (Dirksen et al., 2014). Here, the Integrated Global Radiosonde Archive (IGRA) is particularly well-suited for global intercomparisons: IGRA is a collection of historical and near-real-time radiosonde and pilot balloon observations from around the globe (Durre et al., 2006, 2018) provided by the National Centers for Environmental Information (NCEI) of the National Oceanic and Atmospheric Administration (NOAA). For IGRA version 2 (IGRA2; Durre et al., 2016, 2018), 40 data sources were converted into a common data format and merged into one coherent data set which then went through a quality-assurance system.

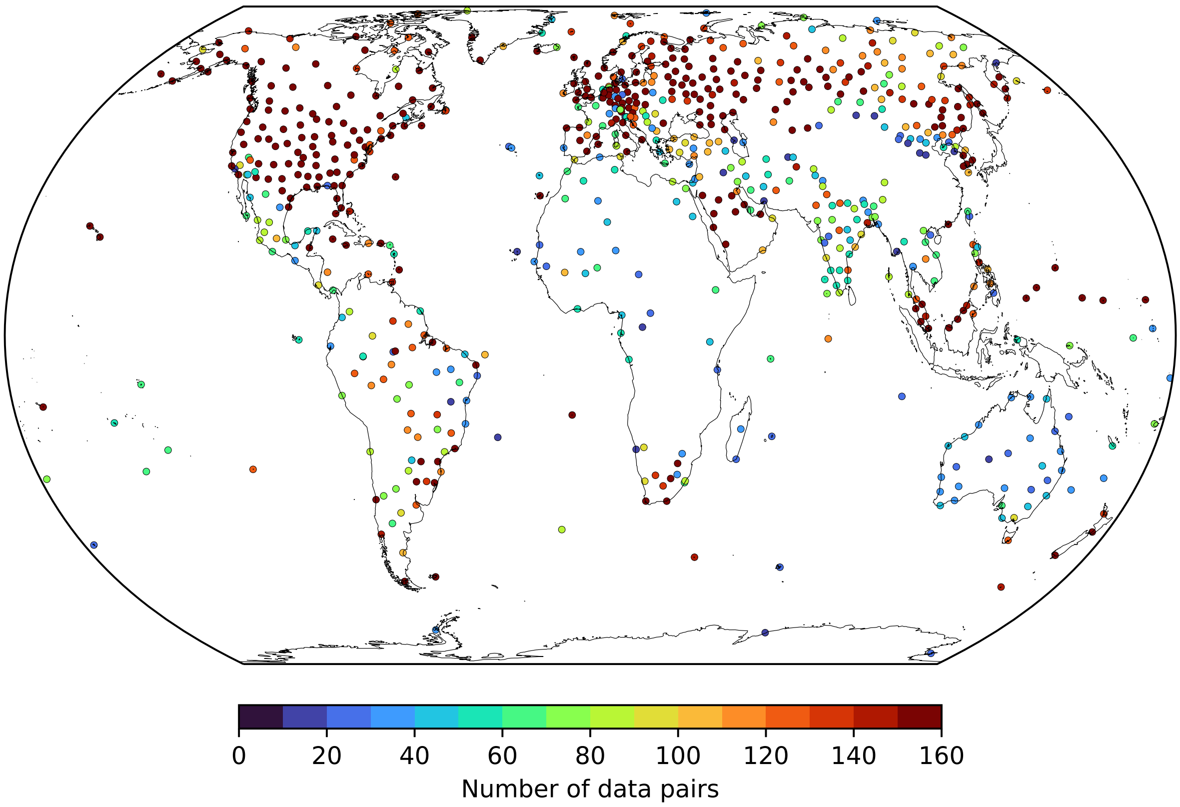

Figure 3.28: Global distribution of radiosonde stations used for the TCWV intercomparison to the MPIC OMI data set. Colours indicate the amount of data pairs for the intercomparison.

Although IGRA2 also provides TCWV data, these are calculated from the surface only up to 500 hPa. Typically, this pressure level is at about 5 km above mean sea level, so if one assumes a typical scale height of the water vapour of 2.1 km (Weaver and Ramanathan, 1995), a low-bias of 10% could be introduced. Thus, to ensure a consistent calculation of the TCWV monthly means from the IGRA2 data, the following criteria were applied to the individual radiosonde ascents:

1. Only radiosonde ascents that have reached an altitude of at least 300 hPa were considered for the calculation of the TCWV. This pressure level corresponds to a typical geometric altitude of around 9 km. This ensures that the radiosondes covered a large part of the troposphere and thus captured the majority of the TCWV without introducing non-negligible low biases.

2. For the calculation of the monthly means, valid radiosonde ascents of at least 10 different days in the month must have taken place in order to achieve a good temporal coverage of the month.

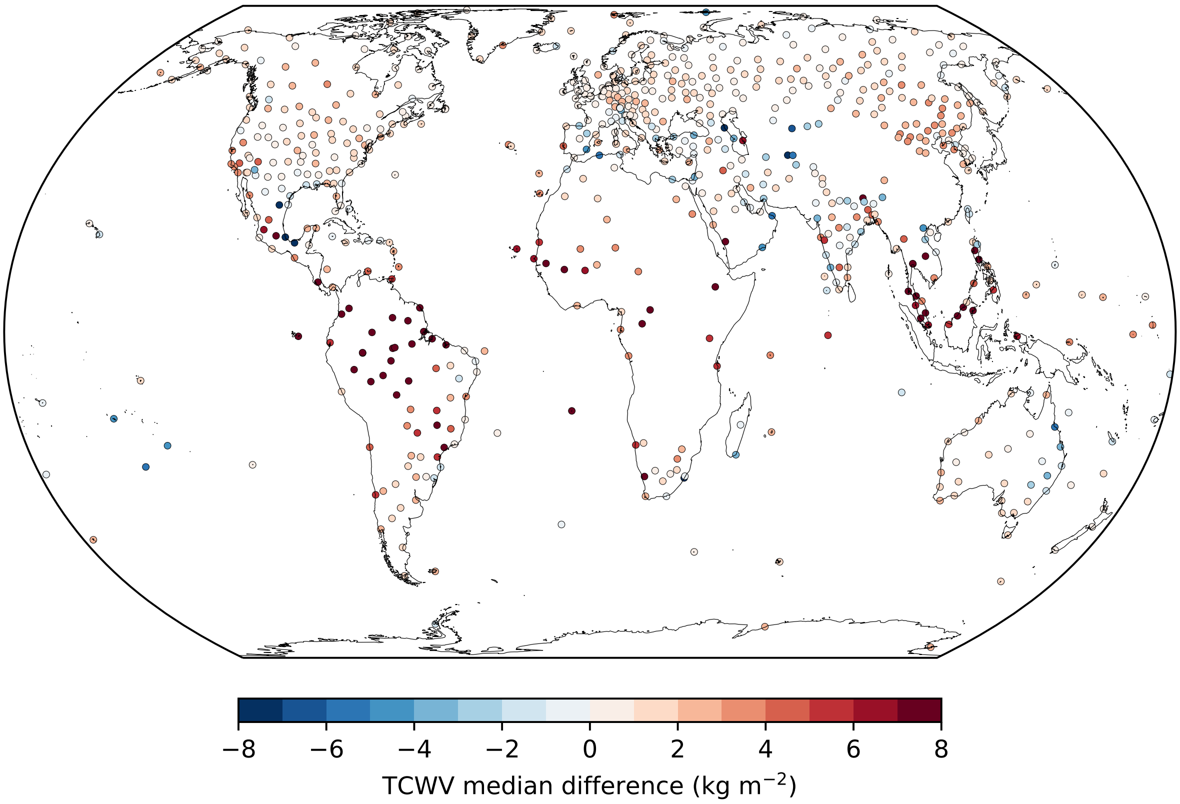

Figure 3.29: Global distribution of the median TCWV difference between the monthly means of the MPIC OMI TCWV data set and those derived from the IGRA2 radiosoundings.

3. Only stations with at least 12 valid data pairs between the monthly means of IGRA2 and MPIC OMI were considered for the statistical analysis.

Figure 3.28 shows the global distribution of the locations of the radio sounding stations as well as the number of valid data pairs used for the comparison. Altogether, 731 different radiosonde stations are considered for this comparison study. In addition to a high density of measurement stations, there is a general good temporal coverage in the northern mid latitudes (especially in North America and Europe) and thus good temporal collocation between MPIC OMI and IGRA2 data. For the other parts of the world, however, the measurement network is much less dense and hence the number of temporal collocations of the two data sets do not reach the values from the Northern mid latitudes. Thus, due to the limited sample size at many stations the median of the deviation is now used instead of the mean deviation for the comparisons.

The distribution of these median deviations is given in Fig. 3.29. Overall, the results are consistent with the findings from the previous comparisons with the global satellite and reanalysis data sets (see Sect. 3.6), in which a good to very good agreement was found for extratropics and an overestimation for the tropics. On average, the median deviation is about $+1.6 \pm 3.4\,\mathrm{kg\,m^{-2}}$,

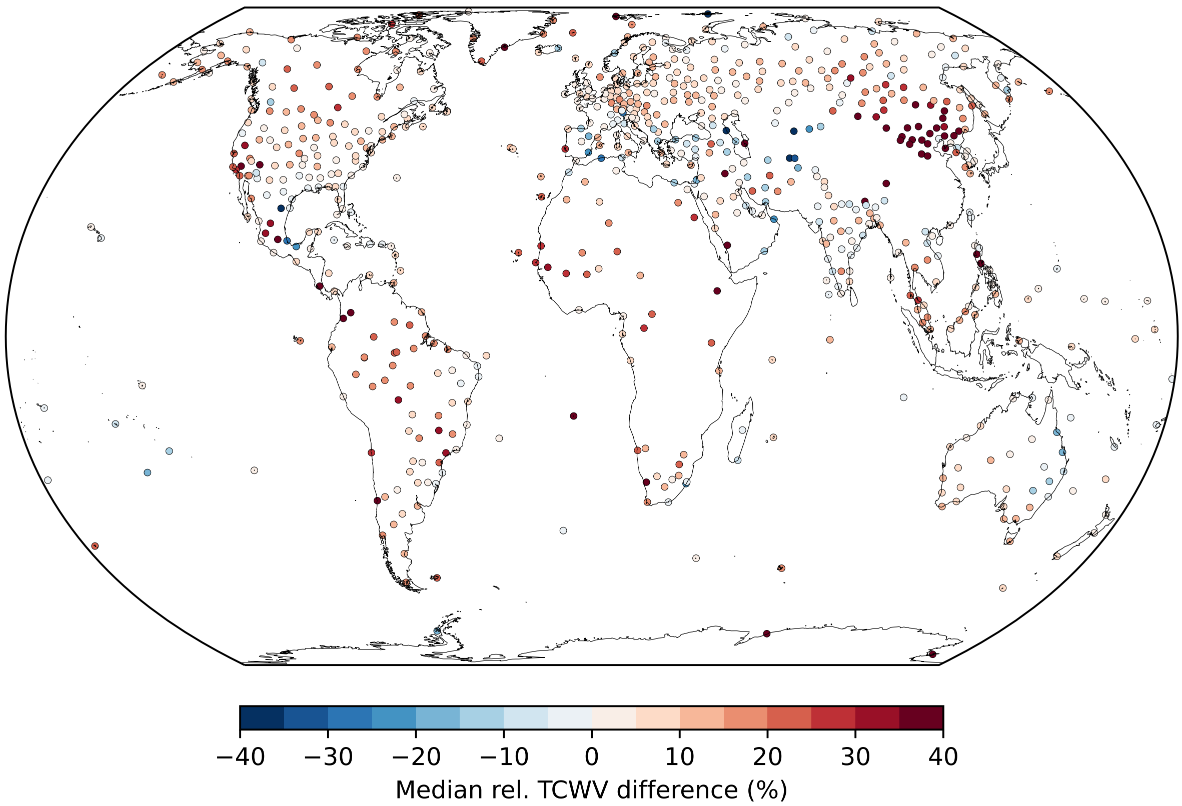

Figure 3.30: Global distribution of the median relative TCWV difference between the monthly means of the MPIC OMI TCWV data set and those derived from the IGRA2 radiosoundings.

with about +0.9±2.0 kg m^{-2} in the extratropics and +4.3±5.5 kg m^{-2} in the tropics in which these high deviations mainly occur in the Amazon region and Indonesia.

Similar to the comparisons with the global data sets, the median values of the relative deviations are typically around +9 % (Fig. 3.30), however in the area of northeast China an agglomeration of distinctive positive deviations can be observed. This region is characterised by arid to semi-arid steppes and therefore TCWV values are usually very low which means that the normalization might lead to exaggerations of the deviations. Interestingly, such high relative deviations do not occur in other desert regions (e.g. Sahara or Australia).

Nevertheless, this comparison to radiosonde measurements demonstrates that the MPIC OMI TCWV data set is also in good to very good agreement to in situ reference data sets, but tends to be systematically overestimated in the tropical landmass regions which is in line with the previous findings from the comparisons with reanalysis and satellite data (Sect. 3.6).

3.8 Temporal stability

In addition to a good agreement to existing reference data sets, the temporal stability is an important property of a climate data record. As the ESA WV_cci CDR data set only covers the time range up to December 2017, the focus is on the comparison to the RSS SSM/I and ERA5 data sets as these two cover the complete time range of OMI TCWV data set. For the sake of completeness, however, also the results for ESA WV_cci CDR are shown.

To assess the stability of the OMI TCWV data set, first the global mean relative deviation $\langle\epsilon\rangle$ is derived for every time step:

$$\langle\epsilon\rangle = \frac{\langle \text{OMI} - \text{TCWV}_{ref}\rangle}{\langle \text{TCWV}_{ref}\rangle} \tag{3.5}$$

For the calculation of global means only data points or grid cells are taken into account for which for every time step data from the OMI TCWV and reference data set are available. In the case of the ESA WV_cci CDR a "common mask" has been provided (see also Fig. 3.25). Then, temporal linear trends of these deviations are calculated using a generalized least-squares (GLS) regression. To account for the temporal autocorrelation of the fit residuals of the GLS, it is assumed that the residuals follow an autoregressive process. When examining the autocorrelation function (ACF) of the fit residuals, it was found that the ACF is smaller than 0.5 only from a lag of 3. Thus, the GLS system is transformed by means of a 3$^{\text{rd}}$ order autoregressive process and the trends are determined from this transformed system. The results and their uncertainties then already include the effect of the temporal autocorrelation. More details about the transformation and the trend calculation can be found in Section 4.2.

Figure 3.31 illustrates the temporal variability of the relative differences of the OMI TCWV data set and RSS SSM/I, ERA5, and ESA WV_cci CDR for the time range January 2005 to March 2016 (blue dashed lines) and January 2005 to the end of the respective data set (blue solid lines). For the time series until March 2016 one finds trends of +0.21 % per decade for the comparison to RSS SSM/I, +0.20 % per decade for the comparison to ERA5, and −1.73 % per decade for the comparison to the ESA data.

For the time series until the end of the reference data set one finds trends of 0.02 % per decade for the comparison to RSS SSM/I and −0.09 % per decade for the comparison to ERA5. Moreover, the statistical analyses reveal that these trends are not significantly different from 0 % per decade. For the comparison to the ESA data there is a stronger trend (around −0.42 % per decade) than for the other two data sets, however also the time range is much shorter and does not cover the complete time range of the OMI TCWV data set. Altogether, the obtained trends of the relative deviations are in line with typical stability requirements for climate data products of ±1 % per decade (see e.g. Beirle et al. (2018) and references therein or the ESA WV_cci user requirements; https://climate.esa.int/media/documents/Water_Vapour_cci_D1.1_URD_v3.0.pdf;

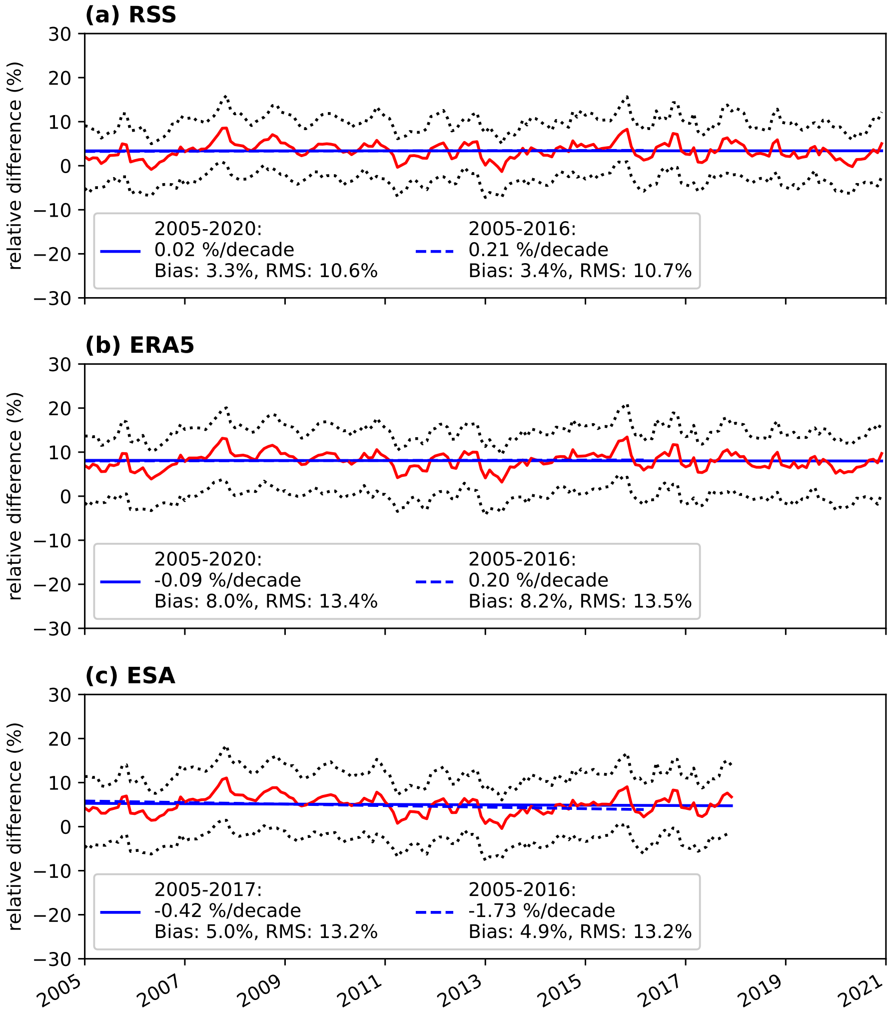

Figure 3.31: Stability analyses of the global mean relative deviations of the OMI TCWV data set with respect to **(a)** RSS SSM/I, **(b)** ERA5, and **(c)** ESA WV CCI CDR-2. Red line: global mean relative deviation; blue line: results of the linear regression; dotted black line: 25th and 75th percentiles, respectively. Dashed lines represent data for the time range from January 2005 to March 2016 and solid lines represent data for the time range from January 2005 to the end of the respective data set. The bias and RMS provided in the legends correspond to the time seriues of the global mean deviation for the respective time range.

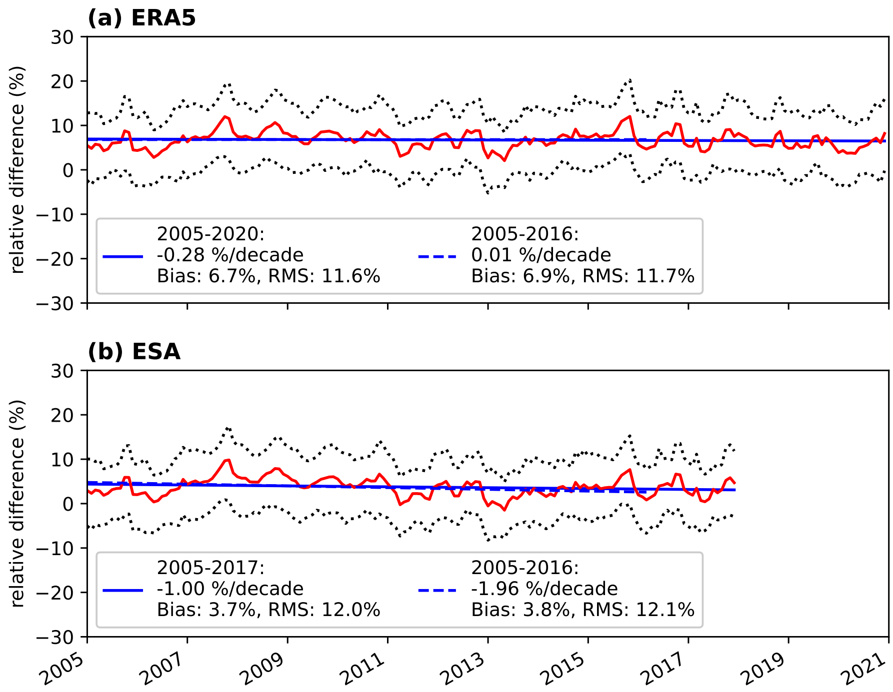

Figure 3.32: Same as Fig. 3.31, but only for (**a**) ERA5 and (**b**) ESA WV CCI CDR-2 and only for data over ocean.

last access: 28 October 2022). Moreover, these trends are also in line with the recently published stability requirements for Essential Climate Variables (ECV) according to the Global Climate Observing System (GCOS) implementation plan with stabilities of ±0.1 % per decade as "goal", ±0.2 % per decade as "breakthrough", and ±0.5 % per decade as "target" stability (see GCOS-245; https://library.wmo.int/doc_num.php?explnum_id=11318; last access: 28 October 2022).

To understand to what extent the temporal stability differs over land and over ocean, the data were separated and analysed. The results of this separate analyses are shown in Fig. 3.32 (over ocean) and Fig. 3.33 (over land). The RSS data set was not investigated again as it is only available over ocean and therefore redundant to re-examine.

Over ocean, the OMI data set also meets the 1 % per decade stability criterion (and also various GCOS stability criteria) for both the long and short periods for the case with ERA5 as reference (+0.01 % and –0.28 % per decade, respectively). In contrast, no stability criterion for the comparison with the ESA data set is fulfilled for both time periods any more (−1.00 % per decade for the longer and −1.96 % per decade for the shorter time period). This is surprising, since both reference data sets should consist largely of similar measurement data from mainly microwave satellites. ERA5 is possibly better constrained again due to its larger volume of observation data.

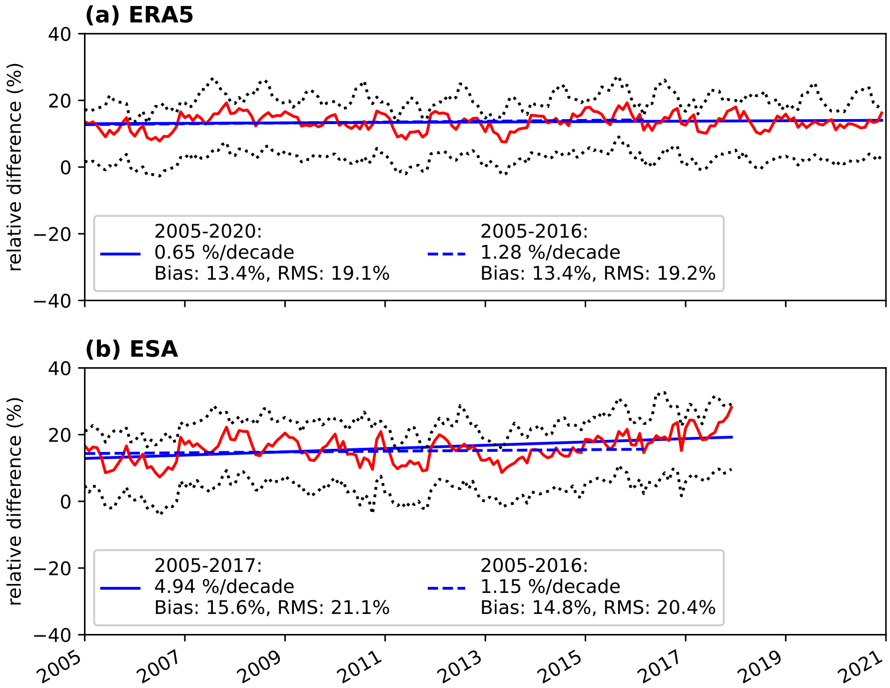

Figure 3.33: Same as Fig. 3.31, but only for (**a**) ERA5 and (**b**) ESA WV CCI CDR-2 and only for data over land.

Over land, the situation is even more complicated: while for ERA5 the 1 % stability criterion is still met at +0.65 % per decade for the period from 2005 to 2020, this is no longer the case for the shorter period at +1.28 % per decade. In the case of the ESA data set, the stability criterion is not even close to being fulfilled either for the period 2005-2017 (+4.94 % per decade) or for the period 2005-2016 (+1.15 % per decade).

Considering the obtained results, it seems that both stability trends over land and ocean largely cancel each other. However, one reason for the high relative deviations over land could be that mainly desert-like regions are used in the analysis due to the aforementioned filter criterion. Thus, rather low TCWV values are used in the normalisation, which means that extreme relative deviations can occur even with rather small, absolute deviations.

In addition to the global data sets, a stability analysis was also carried out with the IGRA2 radiosonde data. Due to the criterion of temporal coverage, only 62 of the more than 700 IGRA2 stations are left for the analysis. Since almost all of these are located in the northern mid-latitudes, the stability analysis is not globally representative, but the comparison can provide further important independent information.

The course of the temporal stability and the results of the analysis are depicted in Fig. 3.34. To calculate the temporal stability, a second order autoregressive process was assumed for the GLS regression which yielded a stability of +1.33 % per decade. Although this does not fulfill any stability criterion, these results are considerably better than the findings for the ESA TCWV

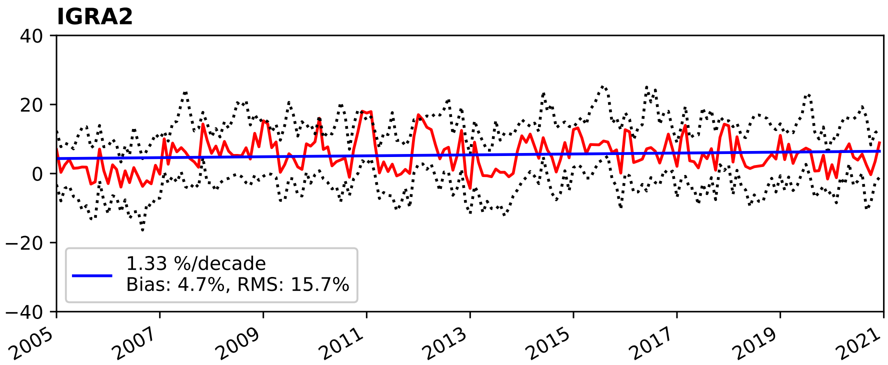

Figure 3.34: Stability analysis of the mean relative deviations of the OMI TCWV data set with respect to IGRA2 radiosonde data for the time range January 2005 to December 2020. Red line: global mean relative deviation; blue line: results of the linear regression; dotted black line: 25th and 75th percentiles, respectively. The bias and RMS provided in the legends correspond to the time seriues of the global mean deviation for the respective time range.

data set over land (see Fig. 3.33). Furthermore, it is difficult to determine whether the trend may come from the radiosondes themselves, as it is not clear how regularly the radiosondes are calibrated (e.g. according to the standard of the GCOS Reference Upper Air Network GRUAN (Dirksen et al., 2014)).

3.9 Summary

This chapter presents a long-term 16-year data record of total column water vapour (TCWV) retrieved from multiple years of OMI observations in the visible blue spectral range by means of Differential Optical Absorption Spectroscopy. To derive TCWV from OMI measurements, the TCWV retrieval developed for TROPOMI (Borger et al., 2020) is applied and the spectral analysis is modified to account for the degradation of OMI's daily solar irradiance. Thus, annual Earthshine reference spectra were calculated from radiance measurements over Antarctica during December (austral summer).

The estimation of the sampling errors in the OMI TCWV data set results in average errors of about -10% (and -6% for the median) and that the largest deviations occur mainly in the mid-latitude storm tracks and polar regions, as these are very often affected by cloud cover. Further investigations show that the large deviations of the sampling error correlate well with the deviations of the clear-sky bias. However, the investigation of a seasonal effect of the clear-sky bias did not show any seasonal dependence. Considering the dominant role of the clear-sky bias on the sampling error, one concludes that the spatiotemporal sampling errors are rather negligible.

Within an intercomparison study, the OMI TCWV data set proves to be in good agreement to the reference data sets of RSS SSM/I, ERA5, and the ESA WV_cci CDR-2 in particular over ocean surface. Moreover, it is also in good agreement to in situ measurements from IGRA2 radiosonde observations. However, over land surface the OMI data set tends to systematically overestimate TCWV values. While this overestimation is relatively small in large parts of the extratropics, high TCWV values are overestimated by more than 24% especially in the tropical regions affected by frequent cloud cover. The reasons for these overestimations are manifold, but likely due to an overestimation of the OMI TCWV retrieval due to uncertainties in the retrieval input data (surface albedo, cloud information) on the one hand and an underestimation of the reference data due to missing or uncertain observations on the other hand. Nevertheless, the validation also shows that for TCWV $< 25\,\mathrm{kg\,m^{-2}}$ good agreement to the reference data can be obtained and also for the case when regions of large uncertainty are filtered.

Considering the temporal stability analysis no significant deviation trends could be obtained with respect to ERA5 and RSS SSM/I which demonstrates that the OMI TCWV data set is well suited for climate studies.

Regarding the effects of the clear-sky bias and the sampling error, it can be assumed that these should not have such a large impact on trend analyses, as it appears to be a quasi-constant offset. Thus, effects should occur, if at all, in the absolute trends.

Altogether, the MPIC OMI TCWV climate data record provides a promising basis for investigations of climate change: on the one hand, it covers a long time series (more than 16 years and with measurements still in operation), and on the other hand, these measurements are based on a single instrument, so that no bias corrections between different sensors need to be taken into account (e.g. in trend analysis studies). Although OMI is affected by degradation effects, these effects could be suppressed successfully by using Earthshine reference spectra. Furthermore, the data set is based on a retrieval in the visible blue spectral range, where a similar sensitivity for the near-surface layers over ocean and land is given and thus a consistent global data set can be obtained from measurements of only one sensor.

In the future, it might be interesting to complement the data set with TCWV measurements from TROPOMI to ensure the continuation of the data set after the end of the OMI mission. Since the TCWV retrieval can be easily applied to other UV-vis satellite instruments, additional data sets from other instruments from past and present missions such as GOME-1/2 and SCIAMACHY, but also to future instruments such as Sentinel-5 on MetOp-SG can be created and eventually combined with the OMI TCWV data set taking into account the different instrumental properties (e.g. observation times). This would allow the construction of a data record that extends from 1995 to today. Similarly, a combination of data from low-earth orbit satellites and geostationary satellite instruments such as GEMS, TEMPO or Sentinel-4 (Kim et al., 2020;

Zoogman et al., 2017; Ingmann et al., 2012) could be a promising option to fill temporal gaps in daily observations, but also to investigate (semi-) diurnal cycles of the water vapour distribution.

Currently, or since July 2021, the OMI L1B data are processed with the TROPOMI processor, which no longer includes the stringent filtering of spectral pixels in the solar irradiance and thus these reference spectra are less noisy compared to the former processor. Thus, it might be possible to return from an Earthshine-based to a solar-based reference retrieval and thereby ensure a fully consistent OMI-TROPOMI retrieval. However, it is planned to reprocess the complete OMI data set only after the end of the mission, which, depending on the available budget, could probably not be the case until mid-2023 at the earliest.

The created OMI TCWV climate data set is now used in the following chapter to determine climatological trends in the given period.

4 Analysis of global trends of total column water vapour from multiple years of OMI observations

The following chapter is based largely verbatim on the publication by Borger et al. (2022) and has only been restructured in a few places compared to this publication.

4.1 Introduction

Building on the previously established results and algorithms in Chapters 2 and 3, in Chapter 4 TCWV trends in the MPIC OMI TCWV climate data record will be analyzed. In addition to its good agreement with other climate reference data sets and its proven temporal stability (see Chapter 3 or Borger et al. (2021)), the major advantages of this TCWV data set in comparison to others are that, on the one hand, the data set provides a consistent time series since it is based on measurements from only one satellite instrument. Thus, inter-instrumental offsets do not have to be corrected when merging the data time series of the different instruments. On the other hand, in contrast to other spectral ranges, TCWV retrievals in the visible blue spectral range have a similar sensitivity over ocean and land surfaces and thus allow for consistent global analyses.

In addition to trend analyses, in Chapter 4 it is not only investigated how strong the trends in water vapour are at the local scale, but also to what extent the assumption of constant relative humidity is fulfilled there. Moreover, by combining precipitation and TCWV data for calculating the water vapour residence time (WVRT), it is investigated to which extent the global atmospheric water cycle is changing or whether it is continuing to slow down (Douville et al., 2002; Bosilovich et al., 2005; Stephens and Ellis, 2008; Li et al., 2011) and how sensitive these changes are to changes in near-surface temperature.

To this end, the chapter is structured as follows: Sect. 4.2 describes the scheme for the trend analysis in detail and Sect. 4.3 addresses the multiple testing problem. Then, Sect. 4.4 presents the trend results from the OMI TCWV data set and puts these results in context to the trend results from other data sets. Sect. 4.5 analyses local trends in relative humidity derived from the OMI TCWV trends and Sect. 4.6 investigates how these are related to changes in precipitation. Moreover, Sect. 4.7 analyses the responses of the water vapour residence time to global warming. Finally, Sect. 4.8 will briefly summarise the results and draw conclusions.

4.2 Trend analysis scheme

The trend analysis is based on the approaches of Weatherhead et al. (1998), Mieruch et al. (2008), and Schröder et al. (2016), in which the fit function is given as follows:

$$Y_t = m + b \cdot X_t + S_t + \Theta_t + N_t = \mathbf{M}_t x + N_t \tag{4.1}$$

with the intercept m, the slope or trend b, respectively, the increasing time index X_t (in months), the seasonal components S_t, and components accounting for the influence of geophysical teleconnections (e.g. the El Niño-Southern Oscillation, ENSO), Θ_t, which can all be summarised in a matrix $\mathbf{M}_t$. The term N_t stands for the fit residuals with respect to the measurement time series.

The seasonal components are modelled as a sum of sine and cosine functions with up to four frequencies, as follows:

$$S_t = \sum_{i=1}^{4} \left[c_i \sin(i \cdot \omega X_t) + d_i \cos(i \cdot \omega X_t)\right] \tag{4.2}$$

with $\omega = \frac{2\pi}{12}$.

To account for the influence of teleconnections, several teleconnection indices Ω_i are considered in the trend analysis. For the case of ENSO, the NOAA Oceanic Niño Index (ONI) is included, which, according to Wagner et al. (2021), has the strongest impact on the TCWV time series distribution. Moreover, following the recommendations from Trenberth and Stepaniak (2001), a second ENSO index is included. In this case, the Trans-Niño Index (TNI; Trenberth and Stepaniak, 2001) is applied. Furthermore, the influence of several other teleconnection indices has been investigated and it was found that the Pacific Meridional Mode (PMM) sea surface temperature index (Chiang and Vimont, 2004) has a particularly strong influence on the autocorrelation of the fit residuals in the Pacific Ocean.

Typically, trends are already removed from teleconnection indices. However, since the time series of the indices cover several decades, the detrending is optimised for this large time period. Accordingly, the indices have been detrended again for the investigated time period (2005–

2020). Apart from the three detrended index time series themselves, their time derivatives are also considered within the trend analysis, as follows:

$$\Theta_t = \sum_{i=1}^{3} \theta_{1,i} \cdot \Omega_i + \theta_{2,i} \cdot \frac{\partial \Omega_i}{\partial t} \tag{4.3}$$

For the fit residuals N_t, it is assumed that they follow a first-order autoregressive process AR(1), which can be described as follows:

$$N_t = \phi N_{t-1} + \varepsilon_t \tag{4.4}$$

with the autocorrelation ϕ. In classical statistical methods it is often assumed that data are independent. However, this is not always the case in environmental data, in particular for time series analysis, in which data are likely temporally autocorrelated. Thus, not accounting for autocorrelation can give misleading results when these classical statistical test methods are applied to strongly persistent time series (von Storch, 1999; Wilks, 2019). For instance, Weatherhead et al. (1998) showed that, in the presence of temporal autocorrelation, the uncertainty of a linear trend is linked to the level of autocorrelation as follows:

$$\sigma^2_{\text{trend}} \propto \sigma^2_N \cdot \frac{1+\phi}{1-\phi} \propto \frac{\sigma^2_\varepsilon}{1-\phi^2} \cdot \frac{1+\phi}{1-\phi} \tag{4.5}$$

with the fit error σ^2_N influenced by the autocorrelation and the "true" fit error σ^2_ε. Consequently, positive (negative) autocorrelation can lead to an underestimation (overestimation) of the uncertainty of the trend which, in turn, can cause misleading results when classical statistical test methods (e.g. Z test) are used to classify if a trend is significant or not. Moreover, as the presence of an autocorrelation violates the Gauss-Markov conditions for linear regression, the fit results do not represent the best linear unbiased estimator and are not statistically efficient (i.e. do not have the smallest possible variance) (Mudelsee, 2014; Wilks, 2019). As a consequence, the fit results can also deviate from the "truth" (see also Sect. 4.4.1.2).

Thus, to account for the effect of autocorrelation, the Prais-Winsten transformation (Prais and Winsten, 1954) is used and the following procedure is applied. First, to calculate the autocorrelation ϕ of the residuals, a linear least squares fit of Eq. (4.1) is performed to the time series of the TCWV data set as the first guess for each grid cell which yields the time series of N_t. Then, the autocorrelation function is estimated using the Gaussian-kernel-based cross-correlation function algorithm, as described in Rehfeld et al. (2011), via the NEST package (http://tocsy.pik-potsdam.de/nest.php, last access: 7 June 2022). The advantage of this algorithm is that it takes into account the complete data of an irregular spaced time series. From the autocorrelation function, the lag 1 autocorrelation ϕ can then be derived by simple linear algebra.

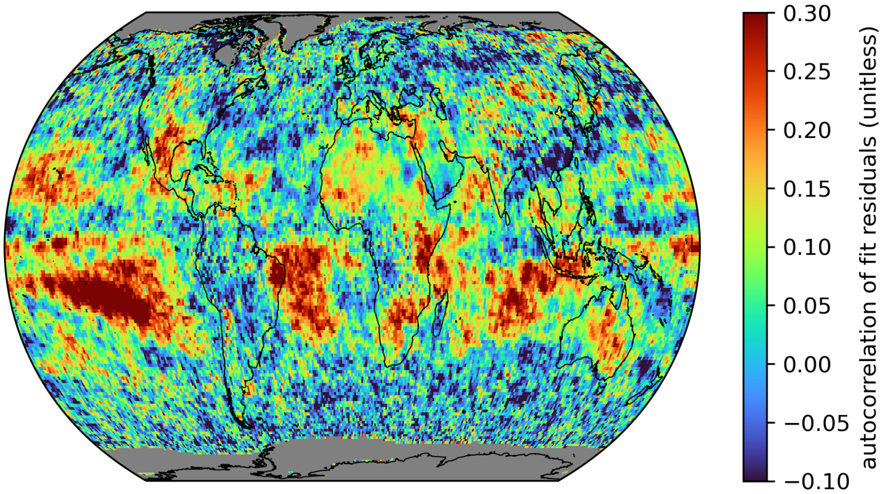

Figure 4.1: Global distribution of the lag 1 autocorrelation coefficients of the fit residuals (or fit noise) of the trend analysis for the MPIC OMI TCWV data set.

Figure 4.1 illustrates the global distribution of the lag 1 autocorrelation coefficients of the fit residuals from the trend analysis of the OMI TCWV data set. Distinctive patterns of enhanced autocorrelation are observable within the tropics and subtropics, in particular in the southern Pacific Ocean, with values reaching up to about 0.5. Towards higher latitudes, the distribution of the autocorrelation becomes spottier, and the values decrease to about 0.

After the calculation of the autocorrelation for each grid cell, the AR(1) model can be prepared via the transformation matrix $\mathbf{P}$, as follows:

$$\mathbf{P} = \begin{bmatrix} \sqrt{1-\phi^2} & 0 & \cdots & 0 & 0 \\ -\phi & 1 & 0 & \vdots & 0 \\ 0 & -\phi & 1 & \ddots & \vdots \\ \vdots & \ddots & \ddots & \ddots & \vdots \\ 0 & \cdots & 0 & -\phi & 1 \end{bmatrix} \tag{4.6}$$

For the case of the first element in the matrix, the AR(1) model cannot be constructed. Thus, the influence of the autocorrelation is approximated by $\sqrt{1-\phi^2}$. If the time series has a gap between index t and $t-1$ (i.e. $X_t - X_{t-1} > 1$), then the autocorrelation ϕ in Eq. (4.6) is set to 0 for this element.

Finally, the matrix $\mathbf{P}$ is then used to transform the fit function of Eq. (4.1) into the autocorrelation space as follows:

$$\mathbf{P}Y_t = Y_t' = \mathbf{P}(\mathbf{M}_t x + N_t) = \mathbf{M}_\mathbf{t}' x + \varepsilon_t \tag{4.7}$$

The system of linear equations in Eq. (4.7) can then be solved by simple linear algebra in which the fit errors of the estimators already include the contribution from the autocorrelation of the fit residuals.

One limitation of the AR model is the assumption of stationarity of the variance. Although this limitation can be overcome by using ARMA (autoregressive moving average) or ARIMA (autoregressive moving integrated moving average) processes, the determination and application of these models (for example, in the transformation of the linear equation system of the fit function) is highly nontrivial, especially for the case of unevenly spaced time series. Although an ARMA(1,1) process would be possible in the case that the lag 1 and lag 2 coefficients of the autocorrelation function have the same sign (e.g. Foster and Rahmstorf, 2011), this condition is not always given in this study. Thus, it was decided to stay with the AR(1) process.

4.3 Multiple-Testing problem

4.3.1 False discovery rate and spatial correlation[1]

Special problems occur when the results of multiple statistical tests are evaluated simultaneously, which is known as the problem of test multiplicity. The multiplicity problem arises in many settings, but in meteorology and climatology it is most usually confronted when analyses involving atmospheric fields must be performed.

An example of this is statistical tests performed on N grid points of an (atmospheric) field at a significance level of α (e.g. at 5%). If the local null hypothesis is true on one grid point, then the probability of falsely rejecting it is equal to α. However, insofar as mulitple N tests are carried out at the same time, so-called Type 1 error inflation occurs. This means that although N local null hypotheses are true, on average $N\alpha$ of them are falsely rejected (Wilks, 2006). Various techniques and methods have been developed in order to account for this problem, for example the Bonferroni correction or, in the atmospheric sciences, the so-called Walker test or the "field significance approach" according to Livezey and Chen (1983). However, all these test methods have their advantages and disadvantages. For example, the Livezey-Chen approach does not weight how strongly the local null hypotheses are rejected and is also sensitive to the effects of positive correlation among the data underlying the different tests. Thus, Wilks (2006) proposed using the false discovery rate, or FDR (Benjamini and Hochberg, 1995; Ventura et al., 2004), which is the expected fraction of nominally significant tests whose null hypotheses are actually valid.

The FDR approach to evaluating multiple hypothesis tests begins with the order statistics for the p values of the N tests, $p(1)$, $p(2)$, $p(3)$, ..., $p(N)$. The smallest (nominally most signifi-

[1]Large parts of this section are based verbatim on the papers of Wilks (2006, 2016) and the textbook of Wilks (2019).

cant) of these is $p(1)$, and the largest (least significant) is $p(N)$. Results of individual tests are regarded as significant if the corresponding p value is no greater than

$$p_{\text{FDR}} = \max_{j=1,..,N} \left\{ p_{(j)} : p_{(j)} \leq \frac{j}{N} \alpha_{\text{FDR}} \right\} \tag{4.8}$$

That is, the sorted p values are evaluated with respect to a sliding scale, so that if the largest of them, $p(N)$, is no greater than a global $\alpha = \alpha_{\text{FDR}}$, then all N tests are regarded as statistically significant at that level.

Another problem with statistical analyses is that it is typically assumed that the tests are independent of each other. When a collection of multiple tests is performed using data from spatial fields, the positive spatial correlation of the underlying data induces statistical dependence among the local tests. Hence, the positive correlation between data at two locations could result in the probability of a Type I error (falsely rejecting the null hypothesis) at one location being larger if a Type I error had occurred at the other location. This is because a hypothesis test statistic is a statistic like any other - a function of the data - and, to the extent that the underlying data are correlated, the statistics calculated from them will be also. Thus false rejections of the null hypothesis tend to cluster in space, possibly leading to the erroneous impression that a spatially coherent and physically meaningful feature may exist.

Wilks (2016) demonstrated that the FDR approach shows only modest sensitivity to correlation among the multiple tests and that this sensitivity actually results in more conservative tests. Thus, Wilks (2016) propose that in the case of high spatial correlation the FDR should be adjusted by choosing $\alpha_{\text{FDR}} = 2\alpha$.

4.3.2 Spatial autocorrelation of meteorological data sets

The significance level at which the FDR approach is performed depends on the degree of spatial autocorrelation. Thus, for every timestamp within the MPIC OMI TCWV data set, the spatial autocorrelation is calculated from the global TCWV distribution for grid point separations up to 7000 km.

Figure 4.2a illustrates the spatial autocorrelation of the OMI TCWV data set as a function of grid point separation. The red solid line is the fit result of $f(x) = e^{-a|x|^b}$, with the grid point separation distance x. For the OMI TCWV data set, one calculates a value of $a \approx 0.098$ and $b \approx 1.88$, which equals an e-folding distance of approximately 3.43×10^3 km. According to Wilks (2016), this e-folding distance indicates a strong spatial dependency. Consequently, the recommendations of Wilks (2016) are followed and the significance level for the FDR test is set to 10% instead of 5%.

For comparison and later purpose, the same procedure was also applied to the precipitation data set from the GPCP (Global Precipitation Climatology Project) Version 3.2 Satellite-Gauge

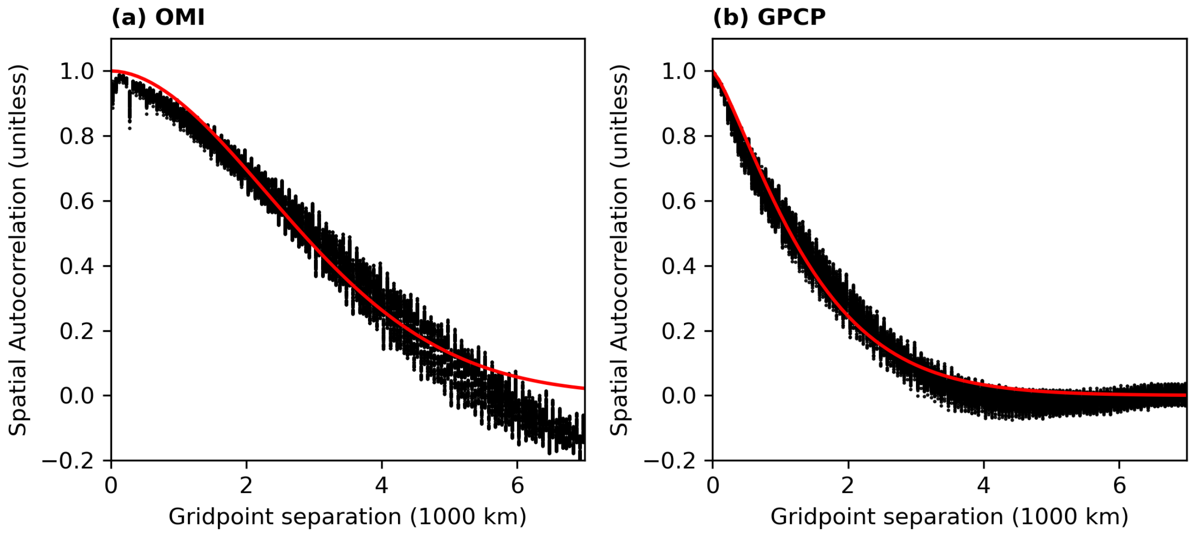

Figure 4.2: Spatial autocorrelation as function of the great circle distance of the MPIC OMI TCWV **(a)** and the GPCP data set **(b)**. The black dots represent the results of the analysis of the spatial distribution for each time step in the respective data set. The solid red lines illustrate the fit result of $f(x) = e^{-a|x|^b}$.

(SG) Combined Precipitation Data Set (Huffman et al., 2020), the results of which are shown in Fig. 4.2b. For the fit results, one obtains $a \approx 0.58$ and $b \approx 1.28$, which correspond to an e-folding distance of 1.53×10^3 km, which is thus less than half as large as that of TCWV. Accordingly, the spatial dependence is not so strong, and the significance level for the FDR test can remain at 5% for the GPCP data set.

4.4 Trend results

At this point, it must be mentioned that, especially in the high latitudes, complete temporal coverage within the MPIC OMI TCWV data set is not always given. For example, the winter months are often missing because no satellite measurements are available due to the seasonal solar cycle or ice cover. Thus, the trends shown are not representative for the entire year, but only for part of it, and should be interpreted with caution. However, the results are still presented in this work, as these regions are of great interest in climate research. A map depicting the fractional temporal coverage (i.e. the number of months with valid data divided by the total number of months) is provided in Fig. 4.3.

Moreover, when investigating climatological trends of TCWV on a local scale, these are also influenced by changes in atmospheric dynamics and should therefore be judged with caution. Nevertheless, they can still provide us with information about changes in the large-scale TCWV distribution.

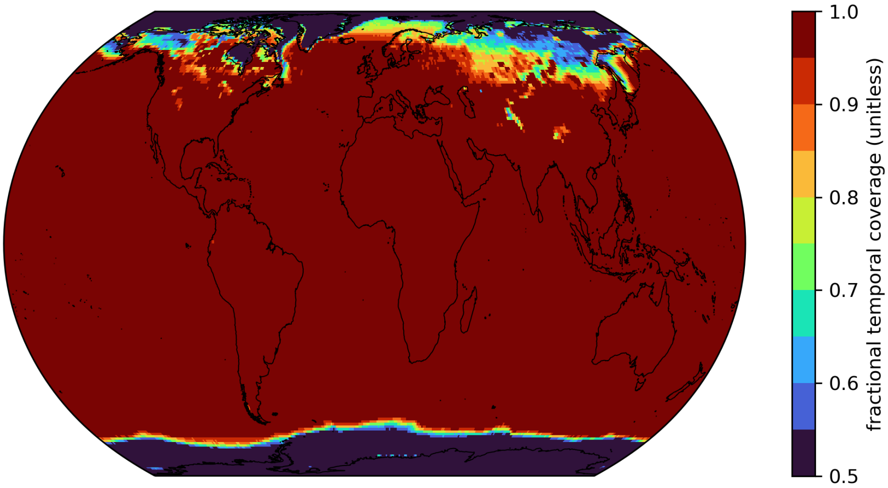

Figure 4.3: Fractional temporal coverage of the MPIC OMI TCWV data set for the time range January 2005 to December 2020.

4.4.1 OMI TCWV trends

To obtain reliable results, the trend analysis is performed only for grid cells whose time series cover at least half of the complete time period of interest. The results of the trend analysis of the OMI TCWV data set for the time range from January 2005 until December 2020 are illustrated in Fig. 4.4.

The top row shows the absolute trends b (Fig. 4.4a) and the relative trends $\frac{b}{m}$ (Fig. 4.4b), respectively. Overall, increasing TCWV amounts are obtained. The absolute trends show high values in the equatorial Pacific and Southeast Asia, and the relative trends reveal high values in North America, the northern Pacific, and Southeast Asia. However, negative values in the TCWV trends can also be observed, e.g. in the region of the South Pacific convergence zone, southern Africa, Brazil, and the equatorial Atlantic. Altogether, one obtains a global area-weighted (i.e. weighted by the cosine of the latitude) mean absolute TCWV trend of $+0.054\,\mathrm{kg\,m^{-2}\,yr^{-1}}$ and a relative TCWV trend of approximately +0.21 % yr^{-1}. Also, distinctively high trend values over mountains such as the Himalayas and Andes have been obtained. However, these high values are likely artefacts due to uncertainties of the satellite retrieval, for example, in the input data for the ground elevation. Thus, it was decided to filter these artefacts and only show grid cells for which the mean ground elevation is lower than 3000 m above mean sea level, based on the GMTED2010 elevation data set (Danielson and Gesch, 2011).

The linear least squares fit assumes that errors of the estimators are normally distributed. Thus, one can perform a Z test from the fit results and determine which trends are statistically significant or not. For this purpose, a significance level of 5 % has been chosen, for which the Z test requires that $|b| \geq 1.96\sigma_b$ (see Fig. 4.4c and d). Furthermore, to account for test multiplicity and field significance, a false discovery rate (FDR) test (Benjamini and Hochberg, 1995; Wilks,

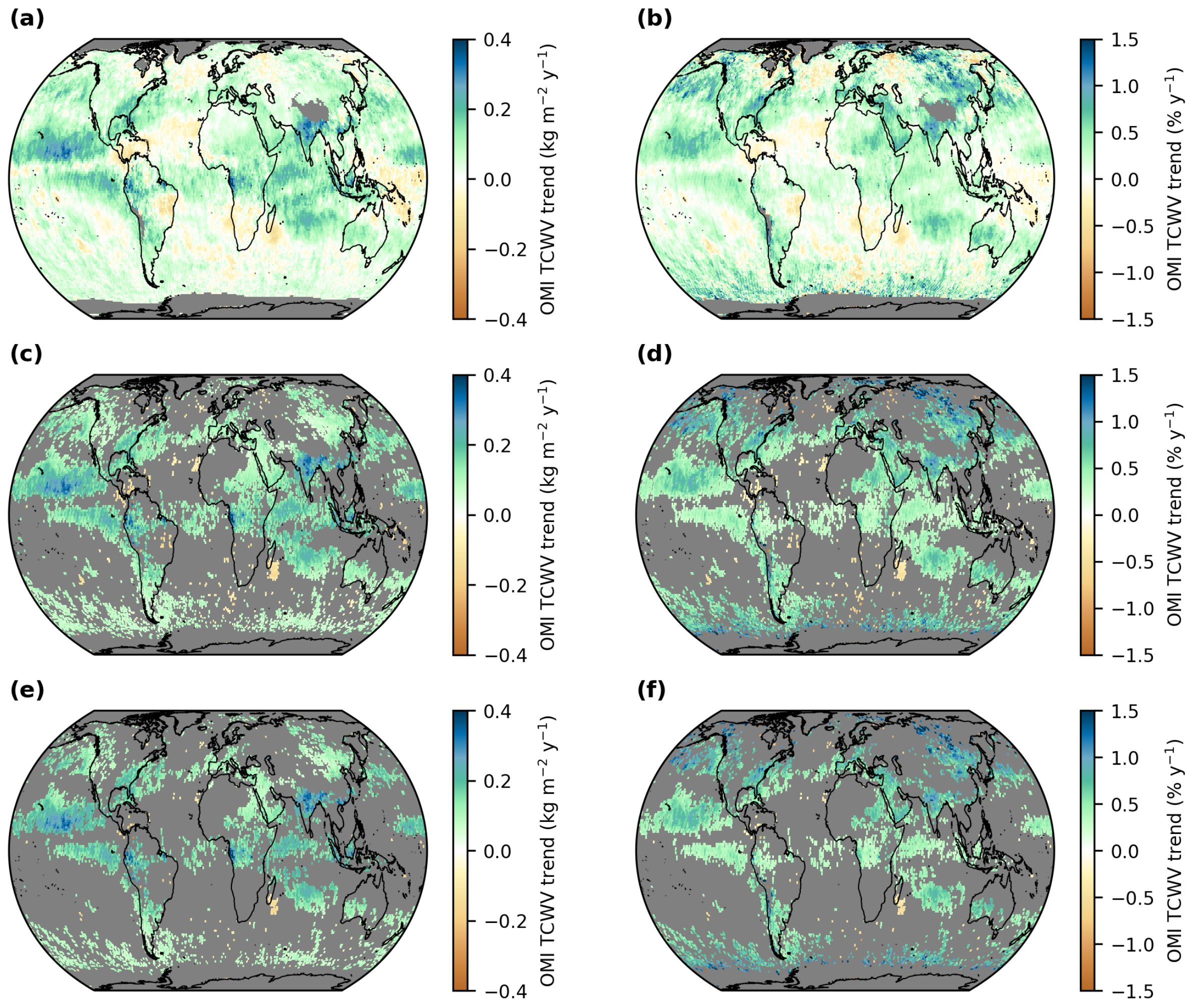

Figure 4.4: Global distributions of TCWV trends (2005–2020) derived from the MPIC OMI TCWV data set. Panels **(a)** and **(b)** depict the calculated absolute and relative TCWV trends, respectively. Panels **(c)** and **(d)** depict significant absolute and relative trends, respectively, after the application of the Z test. Panels **(e)** and **(f)** depict significant absolute and relative trends, respectively, after the application of the Z test and the false discovery rate (FDR) test. Grid cells for which no trend could be calculated **(a, b)** and/or for which the trends do not fulfil the significance criteria **(c–f)** are coloured grey.

2006, 2016) is additionally performed. Because the OMI TCWV data set also shows a high spatial autocorrelation (see Sect. 4.3), the recommendations in Wilks (2016) are followed and a significance level of 10 % was chosen for the FDR test.

The remaining trends are given in the bottom row of Fig. 4.4, with the absolute and relative trends in panels (e) and (f), respectively. From about 12 500 trends for individual grid cells originally classified as significant according to the Z test, approximately 7900 grid cells still remain significant after the application of the FDR test, and almost all of them reveal a positive TCWV trend, in particular over the Pacific Ocean, East Asia, and parts of the U.S. East Coast.

In addition to the TCWV trends, also the trends of the individual components of the DOAS retrieval, i.e. the slant column density (SCD) and the air mass factor (AMF), where TCWV = SCD/AMF, have been analysed. These additional analyses reveal that the TCWV trends are mainly determined by trends in the SCD, i.e. by increasing or decreasing H_2O absorption due to changing atmospheric water vapour content, respectively. The trends of the inverse AMF (i.e. 1/AMF) are generally negative but also distinctively weaker (about 3 to 4 times) than the SCD trends and thus have only a moderate influence on the overall TCWV trends. More details on these analyses are given in Sect. 4.4.2.

4.4.1.1 Trend results for higher order AR models

In addition to the AR(1) model, also other AR models with lag = 2, 3, 6, and 12 have been tested and it was found that the trend results and the distributions of the significant trends differ only slightly from those using an AR(1) model. The corresponding trend results can be found in Fig. 4.5.

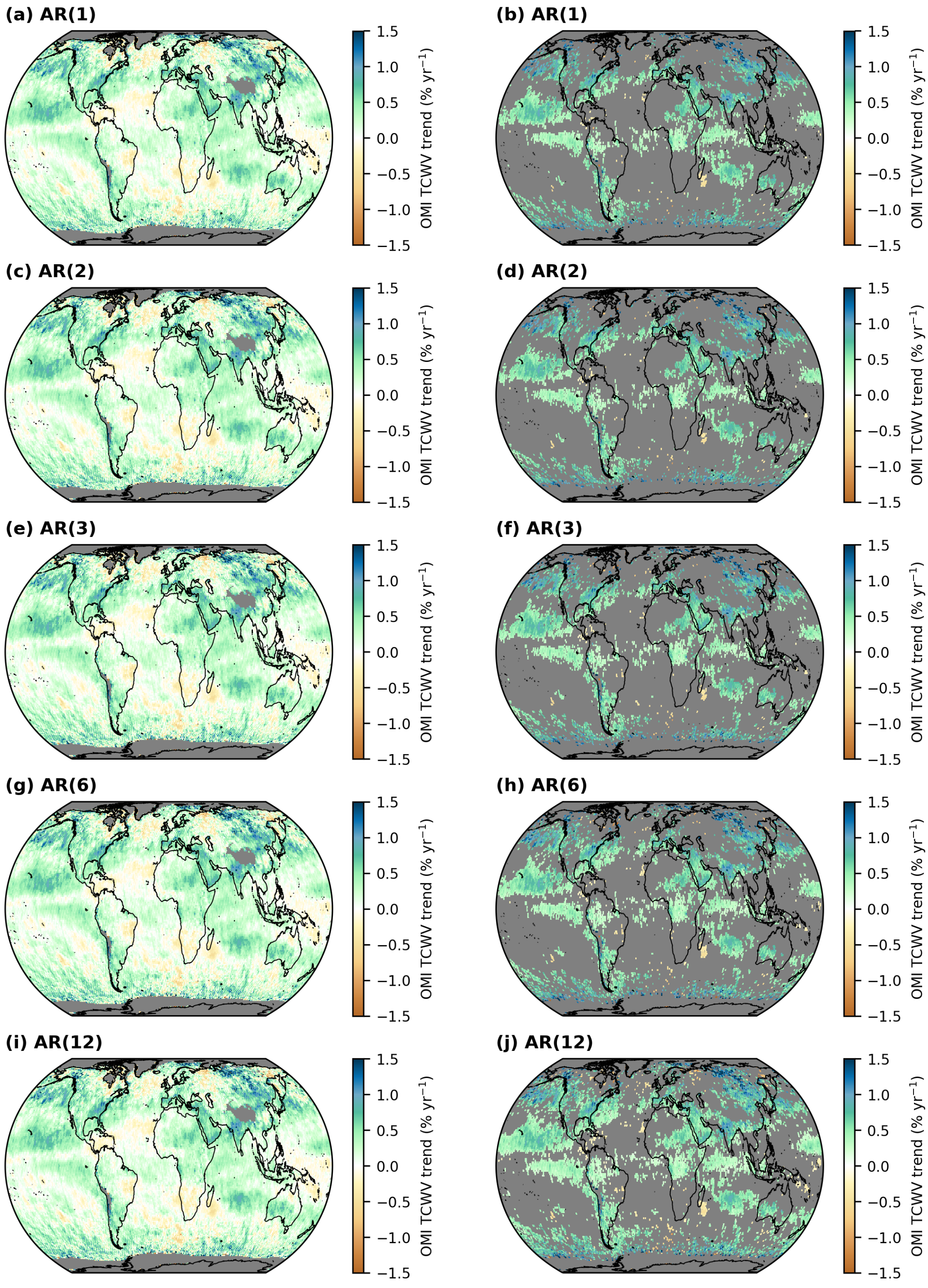

Figure 4.5: Global distributions of relative TCWV trends (2005-2020) derived from the MPIC OMI TCWV data set using different AR-models. Panels **(a)**, **(c)**, **(e)**, **(g)**, and **(i)** depict the calculated relative TCWV trends assuming a AR(1), AR(2), AR(3), and AR(6) process for the fit residuals, respectively. Panels **(b)**, **(d)**, **(f)**, **(h)**, and **(j)** depict significant relative trends, respectively, after the application of the Z-test and FDR test. Grid cells for which no trend could be calculated and/or for which the trends do not fulfill the significance criteria are coloured grey.

4.4.1.2 Influence of autocorrelation and ENSO on trend results

To address the influence of the autocorrelation, as well as teleconnection indices like ENSO, on the trend results for the OMI TCWV data set, the trend analysis is also performed not accounting for these effects.

The panels in Fig. 4.6 illustrate the difference in the absolute (Fig. 4.6a) and relative (Fig. 4.6b) trend results for the case in which the autocorrelation is not considered (i.e. the difference of the results with accounting minus the results without accounting for the influence of the temporal autocorrelation). For high and mid latitudes, the differences are close to zero, indicating that the influence of the autocorrelation on the trend results is negligible. However, within the subtropics and tropics, distinctive deviations are observable, especially in the regions where the autocorrelation is high (e.g. the Pacific Ocean; see also Fig. 4.1). For the case of the relative trends (Fig. 4.6b), the deviations can reach up to 0.05 % yr^{-1} and eventually can cause wrong signs in the trend estimation (i.e. indicating a negative instead of a positive trend).

To highlight the influence of teleconnections on the trend results for the OMI TCWV data set, the trend analysis is also performed not accounting for them. The resulting trends and their difference are shown in Fig. 4.7. While overall the spatial distributions of the relative trends (Fig. 4.7a and b) look quite similar, distinct patterns emerge when looking at the trend differences (Fig. 4.7c). For instance, the typical PMM and ENSO teleconnection patterns are clearly visible (e.g. dipole structure over the maritime continent in the case of ENSO). Consequently, the resulting deviations are particularly strong in the tropical and subtropical Pacific and can reach values as high as the relative trends themselves.

For the OMI time series, it can therefore be stated that a trend objectively exists. It is merely a matter of perspective whether these trends are assigned to a teleconnection index or interpreted with their absolute value.

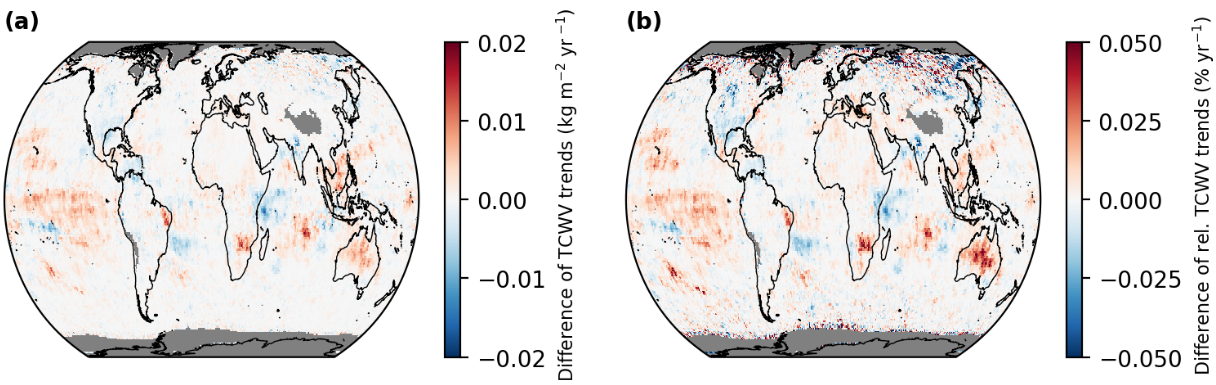

Figure 4.6: Difference between trends of the MPIC OMI TCWV data set (2005–2020) with accounting minus not accounting for the influence of autocorrelation, where panel **(a)** shows the absolute trends and panel **(b)** the relative trends.

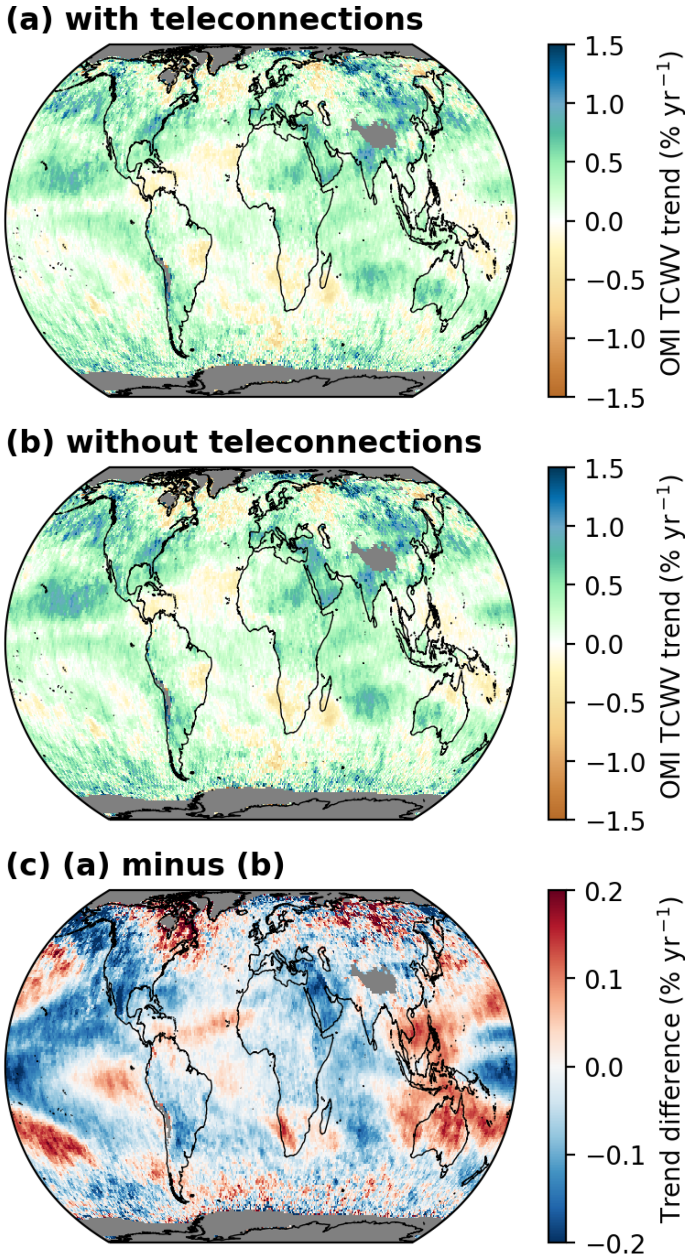

Figure 4.7: Global distributions of TCWV trends (2005–2020) derived from the MPIC OMI TCWV data set. Panels **(a)** and **(b)** depict the calculated relative TCWV trends with and without teleconnection indices, respectively, in the trend analyses. Panel **(c)** depicts the differences between the trend results with teleconnections in the analysis minus the trend results without teleconnections in the analysis. Grid cells for which no trend could be calculated are coloured grey.

4.4.2 Trends of individual retrieval parameters

Here, it is investigated to what extent the relative TCWV trends are due to geophysical changes in the water vapour content or due to changes in the retrieval input parameters. For DOAS retrievals, the TCWV amount is derived via the quotient of the integrated concentration along the light path (so-called slant column density, SCD) and the so-called air mass factor, AMF, i.e. TCWV $= {}^{\text{SCD}}/_{\text{AMF}}$. Thus, the relative trends of these two quantities were calculated following the analysis scheme in Sect. 4.2. For the case of the SCD, the geometrical VCD (vertical column density, VCDgeo) is used, which is simply the SCD divided by the geometrical air mass factor (which remains constant over time). By using the geometrical VCD, the influence of the seasonal cycle of the solar zenith angle and the varying viewing zenith angle can be compensated for a better illustrative representation.

The global distributions of the relative trends of both quantities are illustrated in Fig. 4.8b and Fig. 4.8c and the relative TCWV trends (in Fig. 4.8a). The distribution and strength of the geometrical VCD (Fig. 4.8b) largely coincide with the distribution of the relative TCWV trends (Fig. 4.8a). The trends of the inverse AMF (1/AMF, Fig. 4.8c), on the other hand, are, in general, much weaker than the SCD trends (approx. 3 to 4 times weaker) and do not follow the TCWV trend distribution. However, it occasionally happens that the relative inverse AMF trends either weaken or cancel the SCD trends (e.g. North America or northeastern Asia) or even strengthen them (e.g. around the Arabian Peninsula). Overall, one concludes that the relative TCWV trends are mainly determined by the SCD trends, which consequently means that TCWV trends are mainly due to an increase in atmospheric water vapour concentration.

In addition to the trends of the SCD and AMF, also the trends of the AMF input parameters, i.e. the effective cloud fraction (CF), the cloud-top height (CTH), and the surface albedo, are analysed. The corresponding global distributions are depicted in Fig. 4.9. Here, it is important to mention that the MPIC OMI TCWV data set only includes mostly clear-sky observations (i.e. $\text{CF} < 20\%$), so the calculated trends of the cloud input parameters for this selection of CF are very likely not representative for the actual cloud trends of the atmosphere. For CF (Fig. 4.9a), one obtains, in general, decreasing trends around $-0.1\,\%\,\text{yr}^{-1}$ globally, except for the Indian subcontinent and some individual locations. For the input CTH (Fig. 4.9b), no clear trend pattern is observable, except for slightly increasing trends over the tropical landmasses with values around $+0.03\,\text{km}\,\text{yr}^{-1}$. As expected for the surface albedo (Fig. 4.9c), no trends are observable over ocean, as a static monthly albedo map has been used here. Over land, however, strong varying trends can be found in the high latitudes of the northern hemisphere, with absolute values higher than $0.2\,\%\,\text{yr}^{-1}$. Nevertheless, these strong albedo trends in the northern hemisphere are typically not significant.

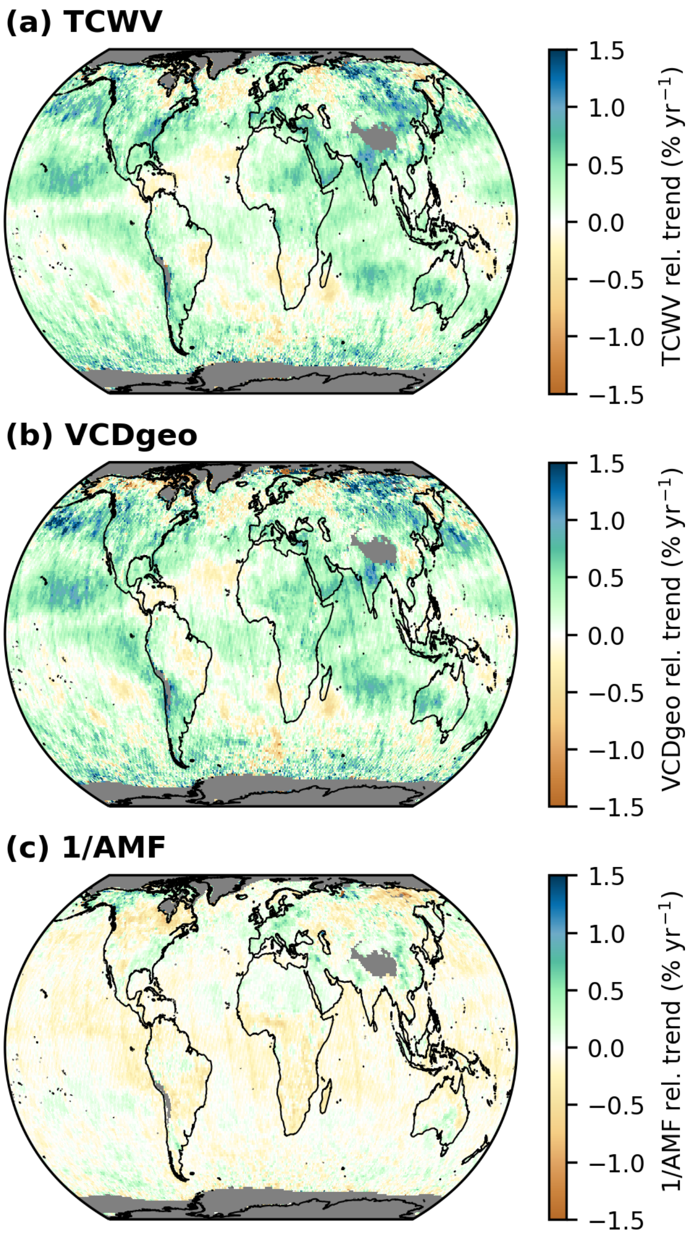

Figure 4.8: Global distributions of relative trends of the TCWV **(a)**, geometrical vertical column density (VCDgeo; **b**), and the inverse of the air mass factor (1/AMF; **c**) for the time period from January 2005 to December 2020. Grid cells for which no trend has been calculated are coloured grey.

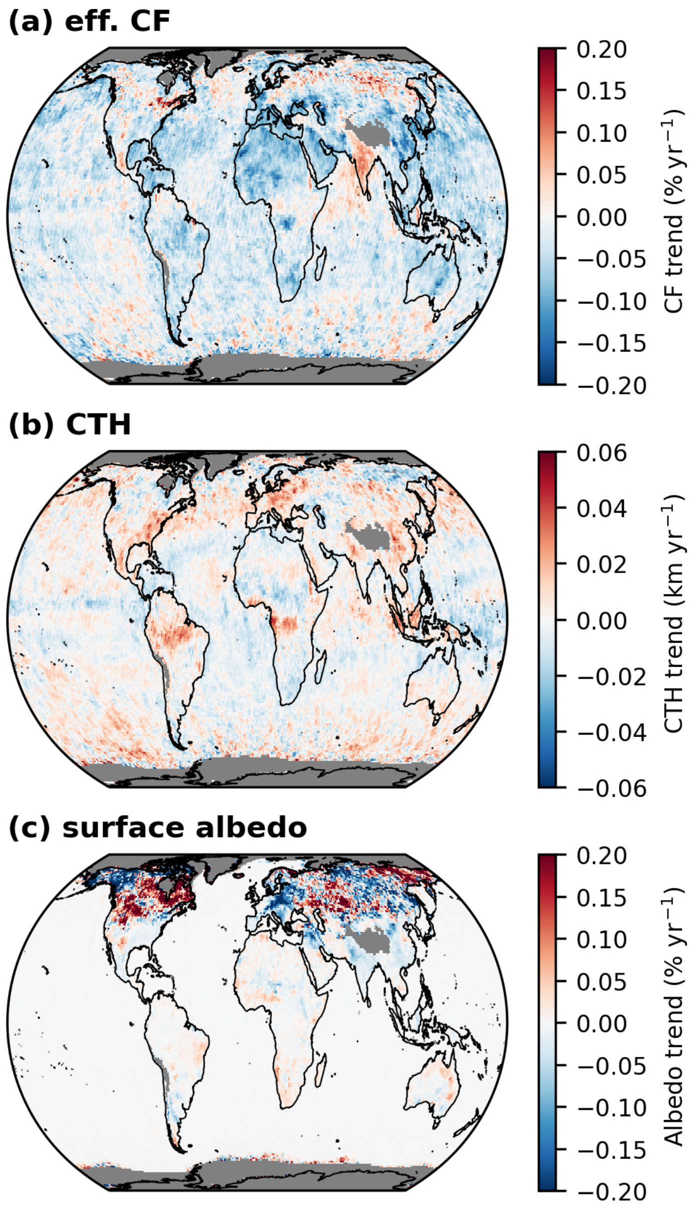

Figure 4.9: Absolute trends of the retrieval input parameters for the calculation of the air mass factor for the time period from January 2005 to December 2020. **(a)** Effective cloud fraction. **(b)** Cloud-top height. **(c)** Surface albedo. Grid cells for which no trend has been calculated are coloured grey. It is particularly important to consider that the illustrated trend distributions are based on clear-sky observations with CF<20%.

4.4.3 Intercomparison to trends of other TCWV data sets

To verify the OMI TCWV trends and to detect potential shortcomings within the MPIC OMI TCWV data set, the analyses are also performed for monthly mean TCWV data from the re-analysis model ERA5 (Hersbach et al., 2019, 2020). For this purpose, the ERA5 TCWV data set is gridded on a $1^\circ \times 1^\circ$ lattice. Moreover, to account for OMI's observation time (13:30 LT), only ERA5 monthly mean values between 13:00–14:00 LT are taken into account.

The resulting maps of the relative trends are given in Fig. 4.10. Overall, the trend results of OMI and ERA5 agree well to each other, as both all and only significant relative trend results (top and bottom rows in Fig. 4.10, respectively) have similar strengths and also show similar global distributions. Nevertheless, the OMI TCWV trends reveal slightly stronger increases over parts of East Asia (which are also classified as significant) and South America and are in general less smooth than the ERA5 results. Similar findings can be obtained for the absolute trends, which are available in Fig. 4.11.

In addition, the trend results are also compared to trends from the TCWV satellite product GOME-Evolution (Beirle et al., 2018). Since the GOME-Evolution product is only available until 2015, the time range for the calculation of the trends is adapted accordingly, i.e. the results for the relative trends shown in Fig. 4.12 (and for the absolute trends in Fig. 4.13) correspond

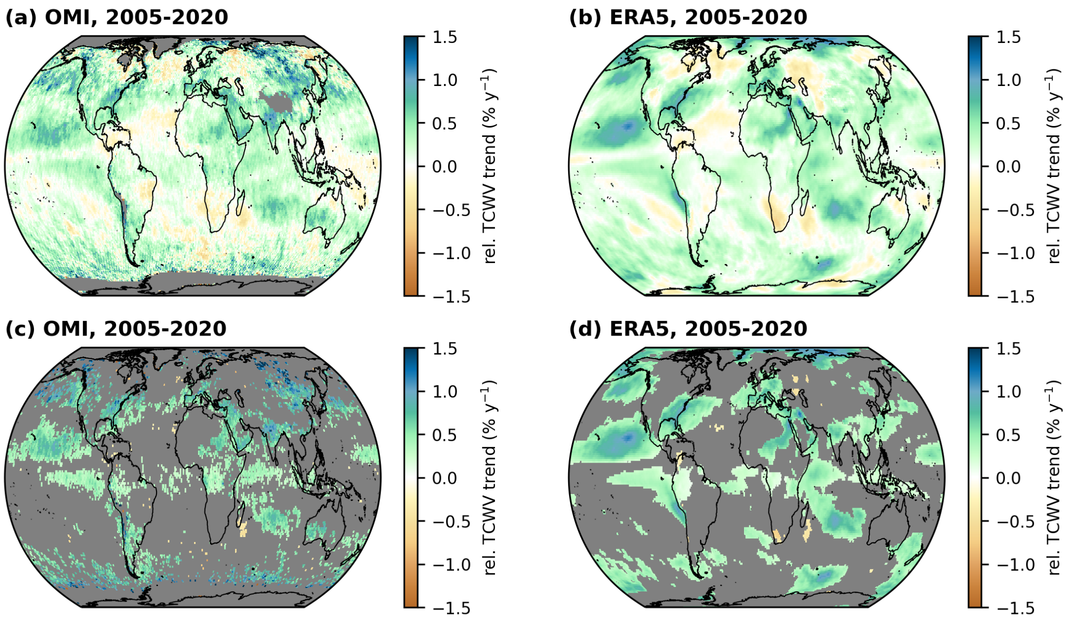

Figure 4.10: Global distributions of relative TCWV trends derived from the OMI TCWV data set **(a, c)** and ERA5 **(b, d)**. Panels **(a)** and **(b)** depict all calculated relative TCWV trends, and panels **(c)** and **(d)** show the corresponding significant trends remaining after the application of the Z test and FDR test. Grid cells for which no valid trend could be calculated are coloured grey.

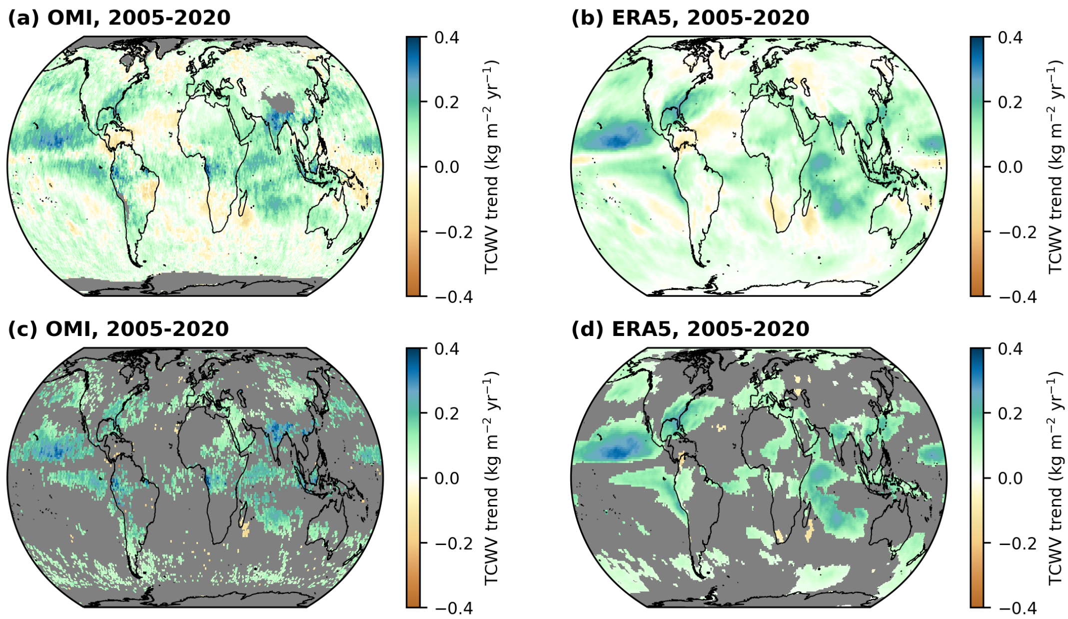

Figure 4.11: Same as Fig. 4.10, but for absolute trends.

to a time range from January 2005 to December 2015. Due to the shorter time period, resulting trends are generally larger and differ strongly from the trend maps shown so far. While the distributions of the relative trends have quite similar patterns and partly similar magnitudes, striking differences can be seen in some regions. For example, the OMI trends in the tropical Pacific, North America or the Arabian Peninsula are much higher than the GOME-Evolution trends. Also, overall, many more trends are classified as significant for OMI than for GOME-Evolution.

Nevertheless, considering that the GOME-Evolution product retrieves total column water vapour in the visible red spectral range, uses a different vertical column density (VCD) conversion scheme (see also Wagner et al., 2003, 2007; Grossi et al., 2015), and observes the atmosphere at an earlier overpass time (around 10:00 LT), the good agreement in the trend results further confirms the reliability of the findings of the OMI TCWV trend analysis.

To find out how strong the influence of different observation times on the trend results is, the trends for 10:00LT as well as for the whole day were determined by means of ERA5 and compared with the results for 13:30LT. The results of the relative trends and the differences to 13:30LT are shown in Fig 4.14. The distribution of the relative trends for 10:00LT and the whole day are almost identical. The differences to the relative trends for 13:30LT range between ±0.1 % yr^{-1}, with no clear structures discernible in the global distributions (except east of Europe). However, the patterns seem to follow waves, which could possibly be due to the fact that ERA5 is based on a global spectral numerical weather prediction model. Overall, these results are consistent with findings of the sampling error in Sect. 3.5 in that the largest uncertainties or

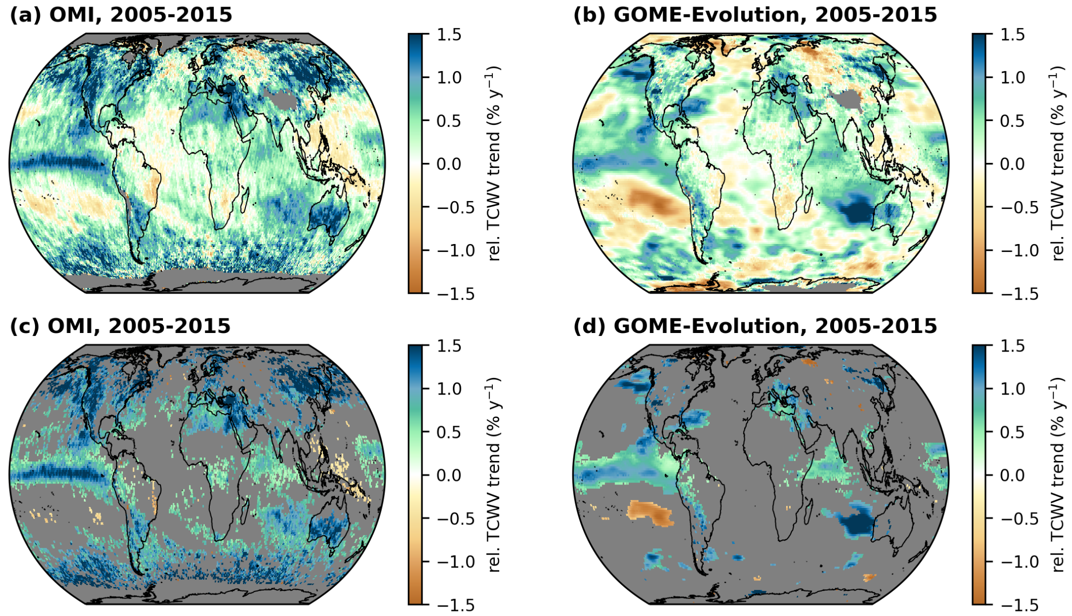

Figure 4.12: Global distributions of relative TCWV trends derived from the OMI TCWV data set **(a, c)** and GOME-Evolution **(b, d)** for the time range from January 2005 to December 2015. Panels **(a)** and **(b)** depict all calculated relative TCWV trends, and panels **(c)** and **(d)** show the corresponding significant trends remaining after the application of the Z test and FDR test. Grid cells for which no valid trend could be calculated are coloured grey.

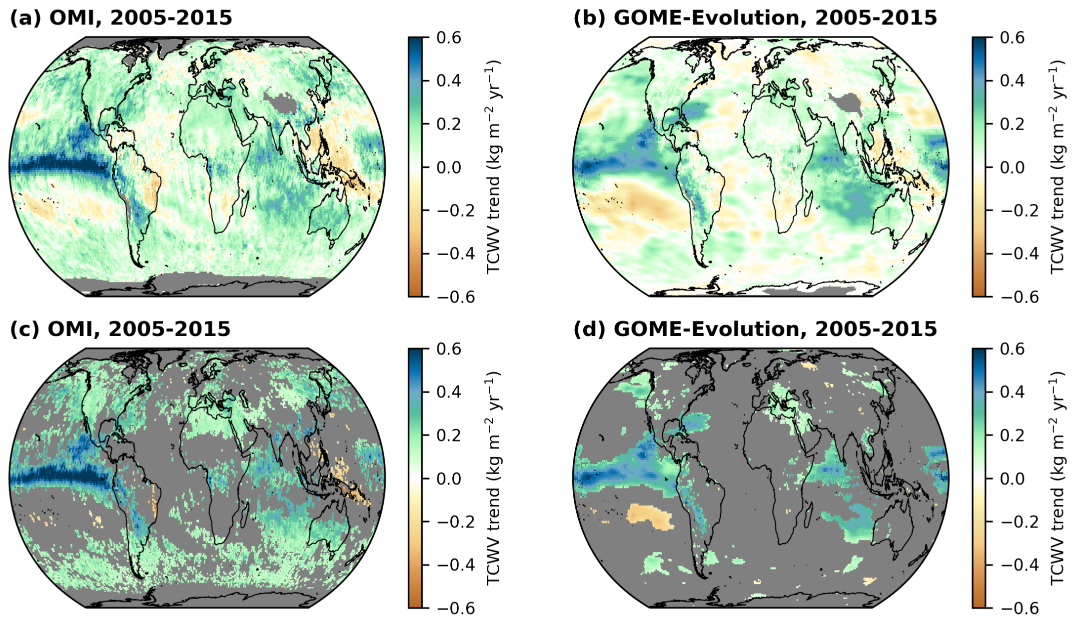

Figure 4.13: Same as Fig. 4.12, but for absolute trends.

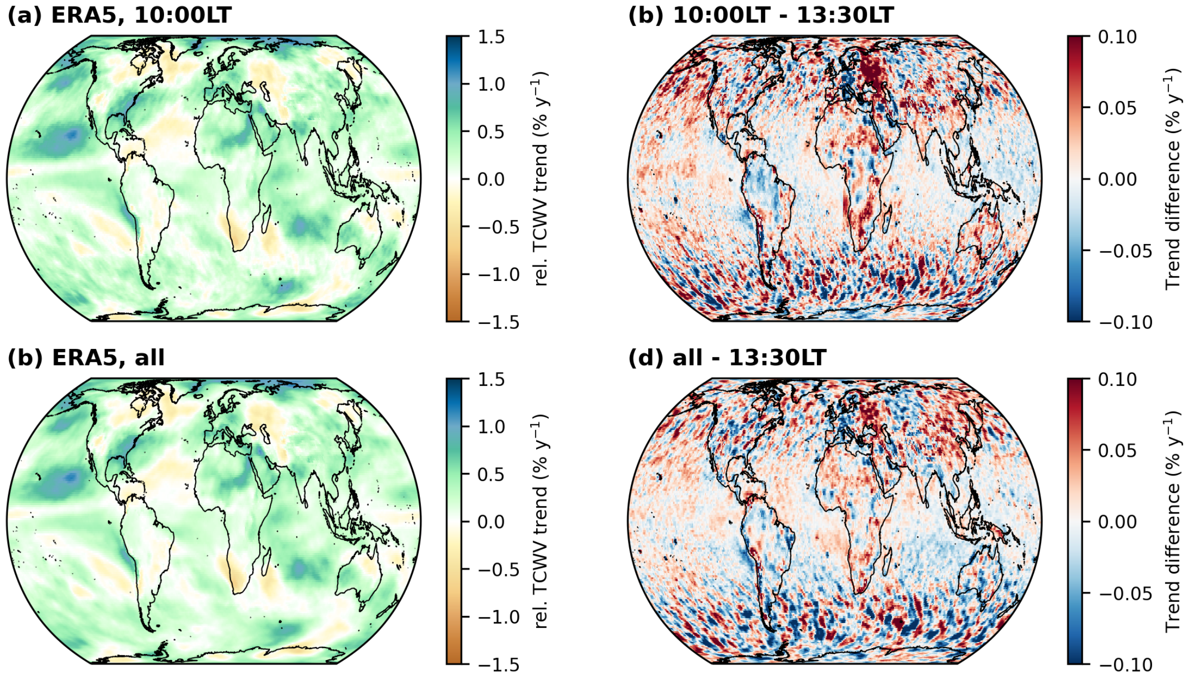

Figure 4.14: Global distributions of relative TCWV trends for different local times derived from the ERA5 for the time range from January 2005 to December 2020. Panels **(a)** and **(c)** depict the relative TCWV trends for 10:00LT and averaged over the whole day, respectively. Panels **(b)** and **(d)** show the corresponding difference to the relative trends for 13:30LT.

deviations arise due to the clear-sky bias and that other error sources (e.g. representative error) tend to be second-order errors.

Furthermore, additional comparisons are made to the results of past studies. From these comparisons, several differences in the strength and spatial distribution of TCWV trends emerge. The reasons for these differences are, on the one hand, the consideration of different time periods and, on the other hand, also different methods of analysis. Further details about these comparisons can be found in Sect. 4.4.5.

4.4.4 Trends in sampling error

Based on the results for the assessment of the sampling error of the MPIC OMI TCWV data set in Sect. 3.5, the question now arises as to what extent the sampling error itself is also subject to trends. Figure 4.15 illustrates the calculated absolute trends of the sampling error as well as these trends normalised with the mean TCWV distribution, determined from the trend analysis for the ERA5 TCWV data set for all times in Sect. 4.4.3 (see also Fig 4.14).

The distribution of absolute trends is largely spotty. However, areas with particularly strong amplitudes (both positive or negative) can be seen in the North Atlantic, east of Australia and

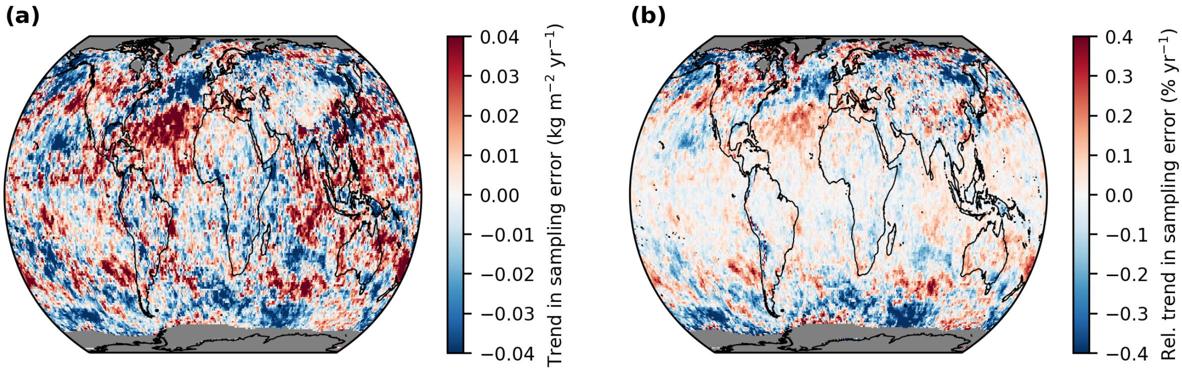

Figure 4.15: Global distribution of the trends of the sampling error of the MPIC OMI TCWV data set. Panel (**a**) depicts the absolute trends and Panel (**b**) illustrates the trends normalized by the mean TCWV distribution derived from the trend analysis of the ERA5 data set.

in the southern mid-latitudes. These particularly prominent areas are also clearly recognisable after the normalisation.

It should be noted, however, that the trends of the sampling error are about an order of magnitude smaller than the TCWV trends and should therefore not be relevant, which is probably also a reason for the good agreement of the OMI trends with the trends from ERA5. The results found for the low trends in the sampling error thus confirm once again that the MPIC OMI TCWV data set is a suitable data set for trend analyses.

4.4.5 Intercomparison to trends from other studies

In the following, the results of relative OMI TCWV trends for the time range 2005–2020 are compared to trends presented in previous studies and it will be investigated which TCWV trends are significant within the respective time range of the previous studies. It is particularly important to note that TCWV trends from different time periods have been investigated.

Trenberth et al. (2005) analysed trends from the RSS SSM/I data for the time period of 1988 to 2003. While the patterns generally match quite well, the trends often have opposite signs. In the time period of the OMI TCWV data set (2005–2020), the trends are mainly positive, whereas in the period of this study (1988–2003), the trends are mainly negative. This is particularly visible in the eastern Pacific. However, no trends have been identified as significant for this period (see Fig. 4.16f). Overall, however, the trends of Trenberth et al. (2005) are in very good agreement with the trends that have been determined for this period using the analysis scheme from Sect. 4.2 (compare Fig. 4.16e to Fig. 11 in their paper).

Mieruch et al. (2008) investigated TCWV trends from 1996 to 2006, using a TCWV data set created from measurements of GOME and SCIAMACHY, using the AMC-DOAS method (Air Mass Corrected Differential Optical Absorption Spectroscopy; Noël et al., 2004). In contrast

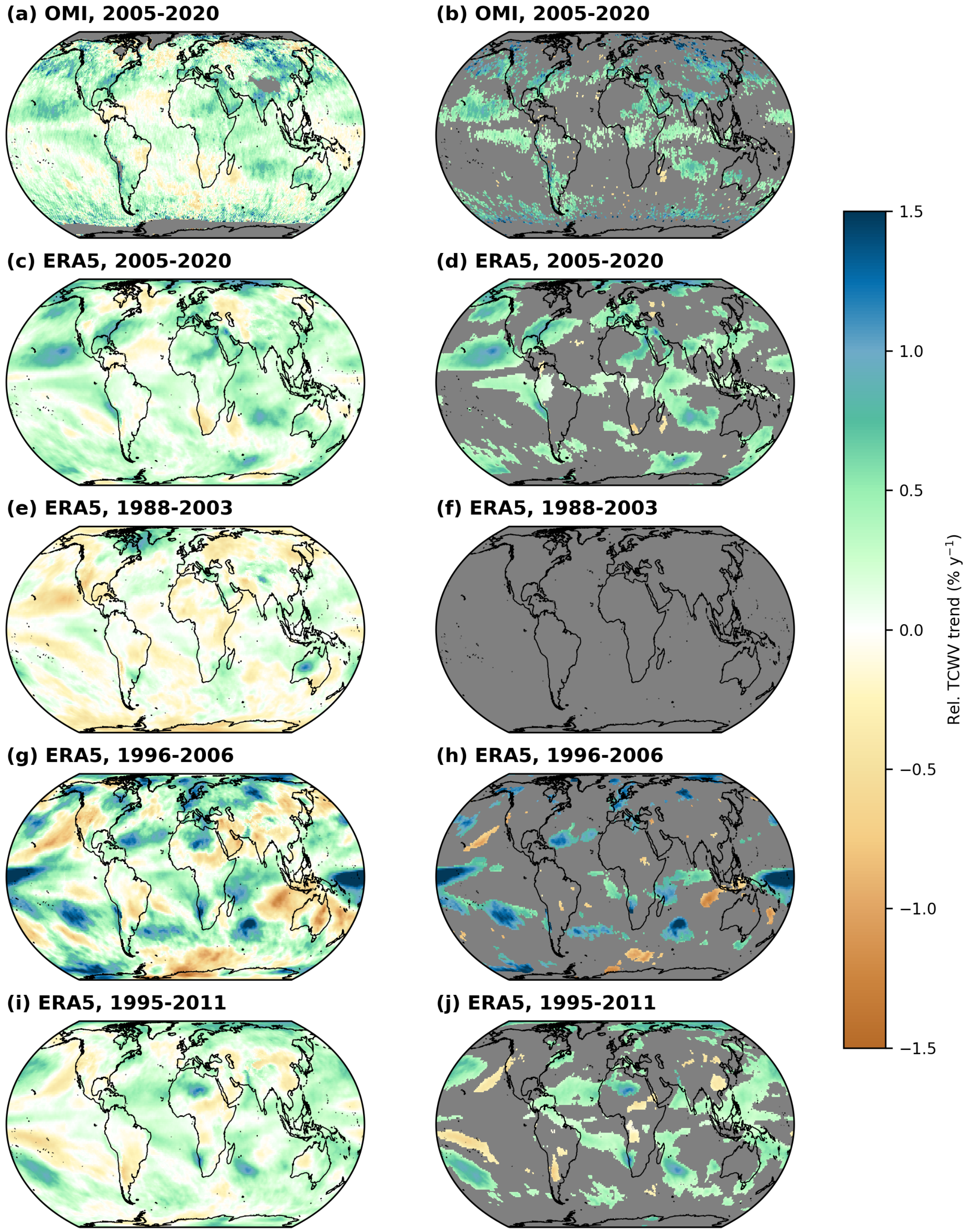

Figure 4.16: Global distributions of relative TCWV trends of OMI (2005–2020; **a**, **b**) and ERA5 for the following different time periods: **(c, d)** 2005–2020, **(e, f)** 1988–2003, **(g, h)** 1996–2006, and **(i, j)** 1995–2011. Panels in the left column illustrate all calculated trends, and panels in the right column illustrate statistically significant trends after the application of a Z test and a FDR test. Grid cells for which no valid trend has been calculated are coloured grey.

to the comparison with Trenberth et al. (2005), almost no similarities are discernible neither in the spatial patterns nor in the strength of the trends. Overall, the spatial distribution is not as smooth as in the other periods studied and is distinctively spottier. This is probably due to the fact that the period studied in Mieruch et al. (2008) is quite short and that there was also a strong El Niño event in 1997/1998, i.e. at the beginning of the considered period. Compared to the results in Mieruch et al. (2008, Fig. 5 in their paper), the results based on the trend analysis scheme from Sect. 4.2 for the same period find only few similarities, even for the case of the significant trends. For example, the trends of Mieruch et al. (2008) are sometimes 4 to 6 times higher than the ones obtained via the trend analysis scheme from Sect. 4.2 for the same period. One reason might be that Mieruch et al. (2008) do not explicitly consider the time series of teleconnection indices (such as from El Niño) or even remove the affected months from the trend analysis for the strong event in 1997/1998.

More recently, Wang et al. (2016) also investigated TCWV trends for the time period from 1995 to 2011 for a TCWV data set combining measurements from radiosondes, GPS radio occultation, and microwave satellite instruments. As for the comparison to Trenberth et al. (2005), the findings for the OMI TCWV data set and the findings from Wang et al. (2016) share many similarities but also several discrepancies. Wang et al. (2016) find a "sandwich" shape in the tropical and subtropical Pacific, with positive trends in the region of the Intertropical Convergence Zone bounded by two bands of negative trends. In contrast, the OMI TCWV trends also suggest a sandwich shape but with opposite signs to Wang et al. (2016), i.e. negative trends bounded by positive trends. Such opposite findings also occur over parts of the Indian subcontinent, the Arabian Peninsula, and South America. However, for central Europe and parts of Asia, good agreement for the trend patterns is found.

For the comparisons of the OMI TCWV trend results to the findings of Trenberth et al. (2005), Mieruch et al. (2008), and Wang et al. (2016), one explanation for the differences may be the different time periods of investigations (1988 to 2003, 1996 to 2006, and 1995 to 2011 vs. 2005 to 2020). Figure 4.16e–j illustrate the relative TCWV trends derived from the ERA5 data set for the aforementioned time periods. For the sake of completeness, Panels (c) and (d) in Fig. 4.16 illustrate the relative TCWV trends from ERA5 for the time period of the OMI TCWV trends, i.e. 2005 to 2020. Although only the time periods have been changed, clear differences can indeed be identified in both the distribution and the strength of the trends. Furthermore, these trend distributions agree very well with the results of the three previously mentioned studies. Nevertheless, different methodologies of observations or different methods for the trend calculation may also be a cause for the discrepancies. For instance, the trend analysis scheme in Sect. 4.2 explicitly accounts for the influence of ENSO by including the ONI and TNI index (see also Sect. 4.4.1), whereas Mieruch et al. (2008) explicitly filtered the time around the strongest ENSO signal.

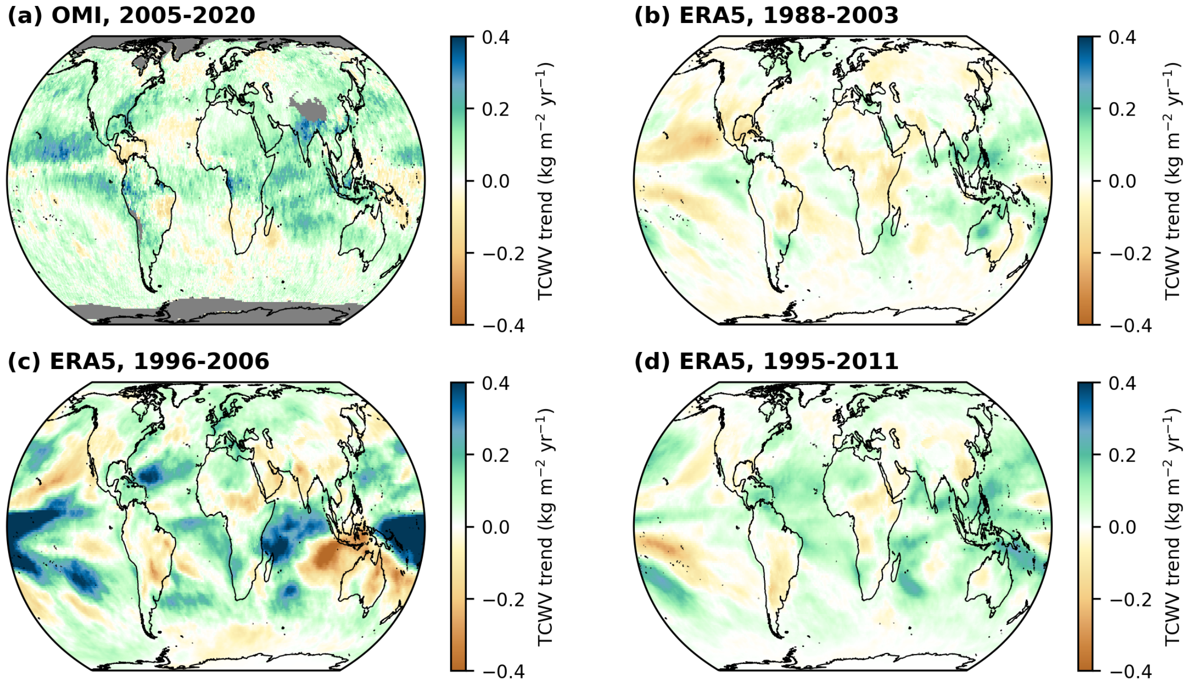

Figure 4.17: Global distributions of absolute TCWV trends of OMI (2005-2020; Panel **(a)**) and ERA5 for different time periods: **(b)** 1988-2003; **(c)** 1996-2006; and **(d)** 1995-2011. Grid cells for which no valid trend has been calculated are coloured grey.

Combining that the detected trends for ERA5 and the GOME-Evolution data set agree well to the findings from the OMI TCWV data set (see Sect. 4.4.3) but that the comparisons to the results from other trend analysis studies show systematic differences, it is evident to not only compare trends for the same time periods but also to ensure that the same methodology for the trend analysis is used. As a lot of different methods exist for estimating trends in environmental data sets, it would be particularly interesting to evaluate which trend analysis scheme performs best and should be recommended for future studies. For example, one could run simulations of climate models with predefined trend patterns and then compare the determined trends of the different methods with the predefined ones. However, such an evaluation study is beyond the scope of this thesis.

For the sake of completeness, the global distributions of the absolute trends for the same data sets and time ranges are available in Fig. 4.17.

4.5 Trends in relative humidity

In various trend studies on TCWV changes on a global scale, it is assumed or determined that relative humidity remains constant over time. In this section, it is investigated to what extent the assumption of constant relative humidity is given at the local scale. For this purpose, the following assumptions are made. First, it is assumed that the relative changes in TCWV correspond to those in near-surface specific humidity q_s, i.e. $\frac{d\text{TCWV}}{\text{TCWV}} \approx \frac{dq_s}{q_s}$. This assumption should be fulfilled, since TCWV is directly connected to the specific humidity via its vertical integral, and approximately 60 % of the TCWV is located within the planetary boundary layer. Second, it is also assumed that relative changes in specific humidity correspond to changes in water vapour pressure e, i.e. $\frac{dq}{q} \approx \frac{de}{e}$ (assuming that relative changes in surface air pressure are negligible, i.e. $\frac{dp_s}{p_s} \ll \frac{de}{e}$). Given the aforementioned assumptions and that the water vapour pressure e can be described as $e = \text{RH} \cdot E$ (with the saturation water vapour pressure E), the relative changes in relative humidity (RH) can be derived by combining the relative TCWV trends with trends in surface air temperature T, as follows:

$$\frac{dq_s}{q_s} \approx \frac{de}{e} = \frac{d\text{RH}}{\text{RH}} + \frac{dE}{E} \tag{4.9}$$

$$\rightarrow \frac{d\text{RH}}{\text{RH}} = \frac{dq_s}{q_s} - \frac{L_v(T)}{R_v}\frac{dT}{T^2} \approx \frac{d\text{TCWV}}{\text{TCWV}} - \frac{L_v(T)}{R_v}\frac{dT}{T^2} \tag{4.10}$$

Thus, if RH is 50 %, a relative increase of 1 % indicates an absolute RH increase of 0.5 %. However, it should be noted that the largest uncertainties lie in the first assumption, i.e. slight under- or overestimations of the actual relative q_s changes will cause corresponding deviations in the relative RH changes.

Figure 4.18 depicts the resulting relative RH trends derived from the OMI TCWV trends in combination with the temperature trends from the Berkeley Earth temperature data record (Rohde and Hausfather, 2020), from ERA5, and from the relative RH trends from the HadISDH (Hadley Centre Integrated Surface Dataset of Humidity) surface relative humidity data set (Willett et al., 2014, 2020). In general, the results for OMI and ERA5 reveal a global (relative) increase in RH, in particular that the trends over ocean are widely positive. However, in all three data sets, distinctive decreasing trends are observable over land, for instance over Russia or southern Africa. Considering the differences in the selected time period and measurement source, the RH trends from OMI over land surface coincide well with the results from Dunn et al. (2017). The reduction in relative RH over land is likely related to a marked land-ocean contrast in warming (Simmons et al., 2010; Fasullo, 2012), besides various local factors such as changes in vegetation cover (Simmons et al., 2010). Over ocean, due to the direct link with sea surface temperature, the water vapour content can increase adequately to keep RH constant. Over land, this is usually only possible with a delay due to limited water availability, as water must first be transported there from ocean. Since the temperature also increases much more over land than over ocean, the decrease in RH might be due to the lack of an increased water supply from the ocean (Simmons et al., 2010).

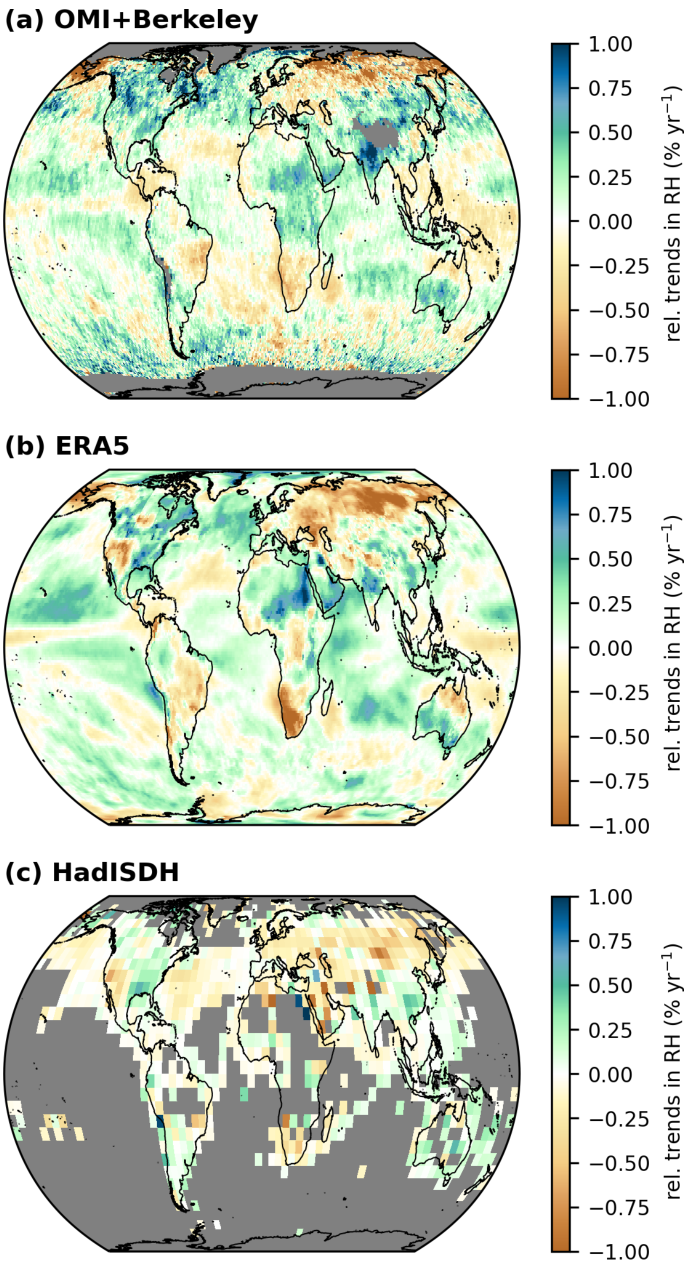

Figure 4.18: Relative trends in relative humidity (RH) derived from the relative TCWV trends and the temperature trends from OMI and Berkeley Earth **(a)**, from ERA5 **(b)**, and from the data set HadISDH (Hadley Centre Integrated Surface Dataset of Humidity) **(c)** for the time range from January 2005 to December 2020. Grid cells for which no trend has been calculated are coloured grey.

Interestingly, one also finds distinctive increases in RH in arid regions (e.g. over the Sahara) and distinctive decreases in humid regions (e.g. the tropical Pacific Ocean) within the OMI and the ERA5 results. Recently, Bourdin et al. (2021) investigated RH trends from the reanalysis models ERA5 and JRA-55 (Japanese 55-year Reanalysis) over the past 40 years and also found significant negative trends in the tropical lower troposphere.

Several studies have shown that global warming will lead to a further drying of dry regions (e.g. Sherwood and Fu, 2014), and wet regions will become even wetter (e.g. Held and Soden, 2006; Chou et al., 2013; Allan et al., 2010), leading to the simple paradigm of “dry gets drier, wet gets wetter” (DDWW; Chou et al., 2009). In addition, other studies show that changes in precipitation correlate very well with changes in ocean salinity, suggesting a “fresh gets fresher, salty gets saltier” pattern (Cheng et al., 2020, and references therein). Though most of these studies focus on changes in precipitation, the results for RH support the findings from Greve et al. (2014) and Byrne and O’Gorman (2018) in that the DDWW paradigm is not always fulfilled over land. Surprisingly, according to the obtained RH results, this paradigm is not even fulfilled over the tropical Pacific Ocean, the region on which most of the concepts of the studies are based (e.g. Held and Soden, 2006). However, it is important to stress here that the time period studied is probably too short to question the paradigm.

4.6 Relationship between TCWV and precipitation

According to Bretherton et al. (2004) and Rushley et al. (2018), a nonlinear relationship between TCWV (or column relative humidity, respectively) and precipitation exists for the tropical ocean. Thus, given the TCWV and RH trend results, one can expect to observe a decline or negative trend of precipitation, in particular over the Pacific Ocean along the Intertropical Convergence Zone. For the analysis of trends in precipitation, the monthly mean rain rates from the GPCP (Global Precipitation Climatology Project) Version 3.2 Satellite-Gauge (SG) Combined Precipitation Data Set (Huffman et al., 2020) are used. For the sake of consistency, the GPCP data, provided on a $0.5° \times 0.5°$ grid, was re-gridded on a $1° \times 1°$ lattice.

Although precipitation climate data records (CDRs) allow a global analysis, they are subject to large uncertainties, as satellite and rain gauge observations do not have good spatiotemporal coverage, weak and short rain events are not well detected or even missed, and satellite retrievals can determine the rain rate only indirectly. Thus, deviations of about 50 % in the daily rain rate can occur, compared to in situ measurements (e.g. Prat et al., 2021). Nevertheless, Prat et al. (2021) show that, over accumulation periods of month or years, precipitation CDRs perform satisfactorily. Moreover, Prat et al. (2021) used an older GPCP version (v2) than the one that is used here in their evaluation study.

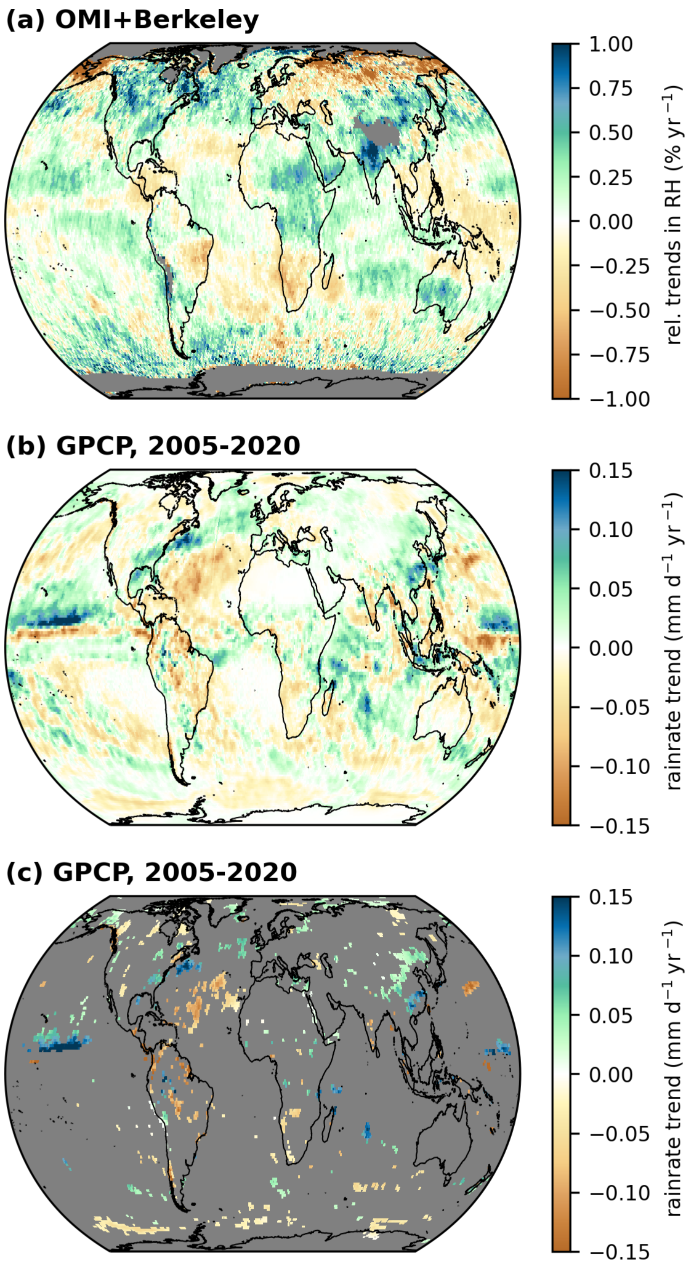

Figure 4.19: Global distribution of relative RH trends derived from the OMI TCWV data set (time range from 2005 to 2020; (**a**); same as in Fig. 4.18a) and of trends in precipitation derived from the GPCP v3.2 monthly mean data set for the time range from January 2005 to December 2020. Panel **(b)** depicts all rain rate trends, and panel **(c)** shows only those that are considered significant after applying the Z test (to the significance level of 5 %) and a FDR test (see also Sect. 4.3). Grid cells for which no valid trends have been calculated are coloured grey.

Figure 4.19 depicts the obtained trends in precipitation and the relative RH trends from OMI. Comparing the trend distributions of the monthly mean rain rates to the relative RH trends, negative and positive trends in precipitation and RH match quite well over the tropical and subtropical ocean, especially over the tropical Pacific and the northern subtropical Atlantic. While over land within the subtropics an acceptable match can be determined in some regions (e.g. southern Africa and Brazil), the patterns of the relative RH and rain rate trends no longer match well towards mid and high latitudes (e.g. in North America), likely because, in these regions, the rain rate is mainly determined by atmospheric dynamics (cyclone or storm tracks) rather than thermodynamics.

Trenberth (2011) and Trenberth and Shea (2005) analysed local correlations between precipitation and surface temperature for cold and warm seasons and reported mainly positive correlations over ocean and negative correlations year round over land throughout the tropics. However, over ocean, the correlations also depend on whether the (sea) surface temperature is driven by the ocean or by the atmosphere (Trenberth and Shea, 2005). While in some regions of the subtropics one can also find this high correlation in the trend patterns of precipitation and surface temperature (e.g. increase in the precipitation in the northern subtropics in the eastern Pacific or decrease in the subtropical Atlantic over ocean; decrease in Brazil or southern Africa over land), there is no direct link for the striking negative precipitation trends in the equatorial Pacific. However, it should also be taken into account that a large part of the precipitation trends are not statistically significant.

The DDWW paradigm was mostly based on simulations of climate models (e.g. Chou et al., 2009; Held and Soden, 2006), whereas the relationship between TCWV and rain rate determined by Bretherton et al. (2004) and Rushley et al. (2018) is based on a parameterisation of mainly observational data (and reanalysis data). So while the relative obtained RH trends mostly follow the rain rate trends and thus the parameterisations of Bretherton et al. (2004) or Rushley et al. (2018) are more or less confirmed, it remains to be noted that in addition to the findings of the relative RH trends the patterns in the rain rate trends also do not agree with the expectations of the DDWW paradigm (also over the tropical Pacific). Thus, to reduce the inconsistencies between observations and expected or modelled changes in the hydrological cycle, further systematic investigations or comparison studies are essential. For this purpose, however, an expansion of accurate, long-term observations of the Earth's hydrological cycle on a global scale is required, both from remote sensing and in situ platforms.

4.7 Changes in the atmospheric water vapour residence time

Another key diagnostic of the hydrological cycle is the atmospheric water vapour residence time (WVRT). The WVRT can contribute to a better understanding of changes in dynamic and thermodynamic processes within a changing climate (Trenberth, 1998; Gimeno et al., 2021). For instance, an increase in WVRT suggests that the length of the atmospheric moisture transport increases, i.e. the distance between moisture sink and source regions (Singh et al., 2016). Thus, the WVRT is useful for studying changes in dynamical processes of the atmospheric hydrological cycle due to climate change (Läderach and Sodemann, 2016) and has implications for the expansion of the Hadley circulation, for example, due to its relationship to the distance between evaporation and precipitation (Singh et al., 2016).

Several different metrics exist for quantifying the WVRT (van der Ent and Tuinenburg, 2017; Gimeno et al., 2021), bearing in mind that the WVRT distribution or the lifetime distribution (LTD) is exponential on the local scale, and thus, the mean value is strongly influenced by a few high values (van der Ent and Tuinenburg, 2017; Sodemann, 2020). Ideally, one would determine the LTD for each grid cell for each month from backward trajectories and then examine their changes or trends. However, this would be well beyond the scope of this study.

Thus, for this purpose, and for the sake of simplicity, focus of this study lies on the so-called depletion time constant (DTC) and the turnover time (TUT). The TUT describes the global average mean age of precipitation and can be calculated as the ratio of TCWV to precipitation P, as follows:

$$\mathrm{TUT} = \frac{\overline{\mathrm{TCWV}}}{\overline{P}} \tag{4.11}$$

where the bar indicates global average. Typically, the TUT varies between values of 8 to 10 d and is expected to increase by 3–6 % K^{-1} (Gimeno et al., 2021, and references therein). Analogously, the DTC is defined as the local ratio of TCWV to precipitation, as follows (e.g. Trenberth, 1998):

$$\mathrm{DTC} = \frac{\mathrm{TCWV}}{P} \tag{4.12}$$

The DTC values might vary substantially from the TUT, but the global precipitation weighted average is equal to TUT (Gimeno et al., 2021).

For the investigations of trends in DTC, the regridded GPCP data set from Sect. 4.5 and the OMI TCWV data set are combined and the trend analysis scheme from Sect. 4.2 is applied to the monthly DTC values for the time range 2005 to 2020. To ensure numerical stability, only monthly rain rates greater than 0.25 mm d^{-1} are considered. As a result, large parts of the subtropical oceans and deserts are excluded from the analysis.

The results of the DTC trend analyses are depicted in Fig. 4.20. On average, one typically obtains mean DTC values between 5–10 d in the areas where rain occurs (Fig. 4.20a). In the subtropical dry zones, values of around 30 d and well above are found. In terms of absolute DTC trends, the most striking patterns are in the northern subtropical Atlantic, with strong

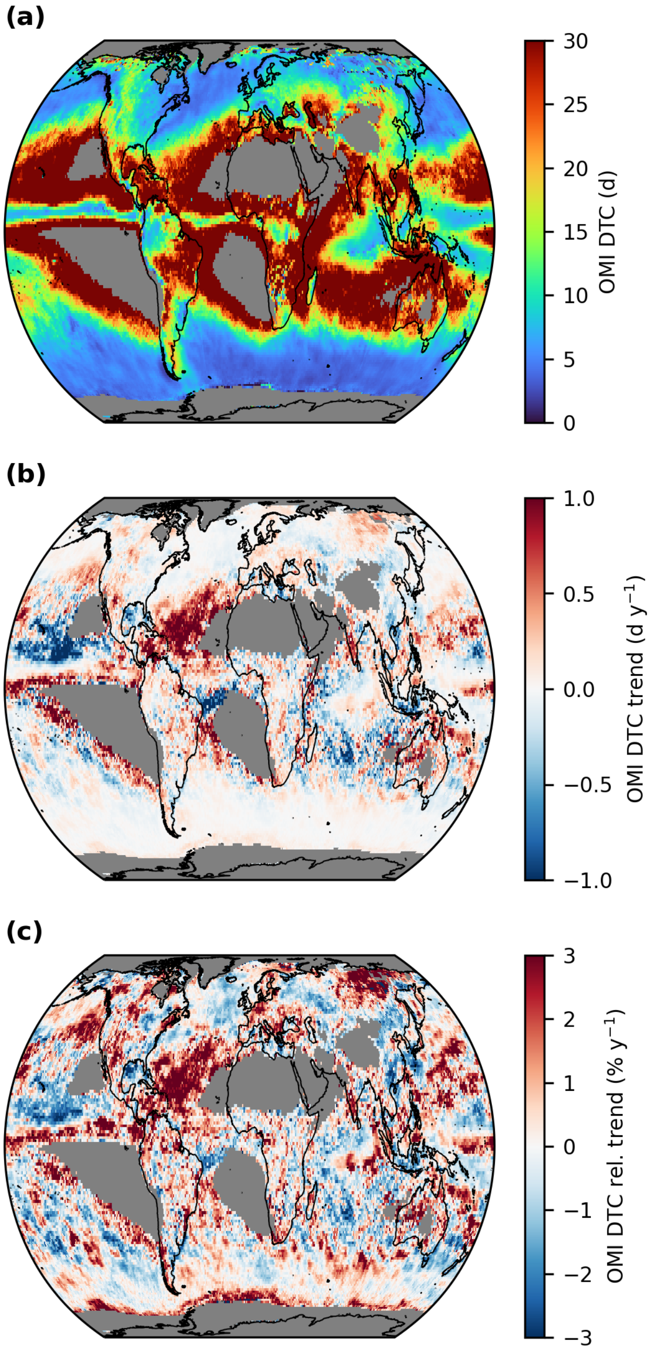

Figure 4.20: Global distribution of DTC trends for the time range of January 2005 to December 2020. Panel **(a)** depicts the distribution of the mean DTC. Panels **(b)** and **(c)** depict the absolute and relative DTC trends. Grid cells for which no valid trend has been calculated are coloured grey.

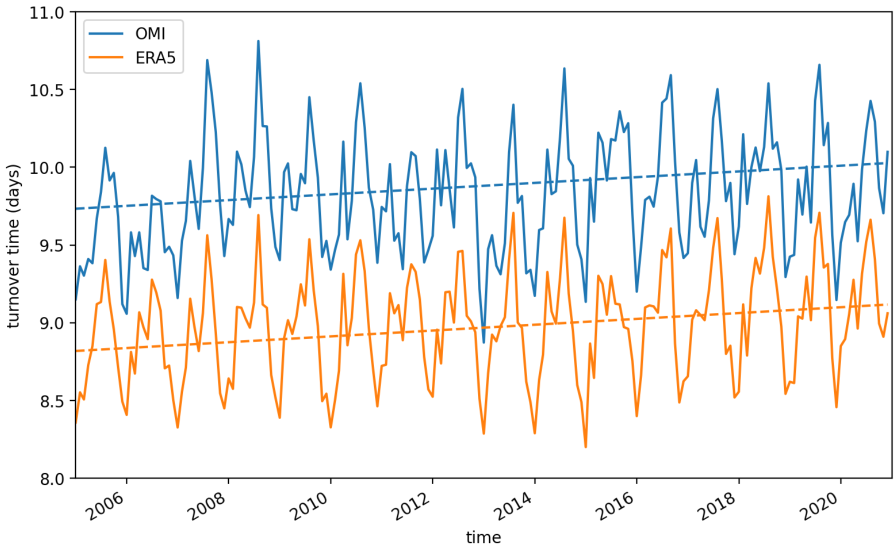

Figure 4.21: Timeseries of TUT determined for OMI (blue line) and ERA5 (orange line) for the time range of January 2005 to December 2020. Dashed lines represent the obtained respective trend results.

increases, and in the northern subtropical western Pacific, with strong decreases. In comparison, the distribution of relative DTC trends is much spottier, but overall, in addition to the patterns already mentioned, distinctive increases in DTC are obtained on the U.S. West coast, in Europe, Russia, and in the eastern Pacific.

Li et al. (2011) and Kao et al. (2018) examined the spatial patterns of trends in the inverse of the DTC, the so-called "recycling rate", for the years 1988 to 2009 and 1988 to 2008 from measurements and model simulations, respectively. Interestingly, similar spatial patterns and also similar magnitudes of the trends are found for all studies, but the DTC trends from the OMI and GPCP data have a different sign than the trends of the recycling rate. This is in line with the differences found for the TCWV trends from different time periods in Sect. 4.4.5.

For the investigations of trends in TUT, first global averages of the regridded GPCP data set from Sect. 4.5 and the OMI and ERA5 TCWV data sets between 60° S and 60° N are calculated for each month, then the time series of global averages are combined, and, finally, the trend analysis for the TUT time series is performed for the time range from 2005 to 2020.

Figure 4.21 depicts the TUT time series of OMI and ERA5 as well as the determined trend results. Altogether, one finds an increase in the global TUT of approximately 0.18 d per decade (relative trend of 1.9 % per decade) for OMI and 0.19 d per decade (2.1 % per decade) for ERA5 (both trend results statistically significant to 5% level), with TUT mean values of around 9.7 d and 8.8 d for OMI and ERA5, respectively. Hence, the TUT mean values found are consistent with those from previous literature (see for instance van der Ent and Tuinenburg (2017) and references therein). Kao et al. (2018) investigated the recycling rate (i.e. the inverse of the

TUT) from 13 CMIP5 models for the time range 1988 to 2009 and found strong negative trends varying between −0.5 and −1.7 % per decade, which is in line with the obtained results here despite different time periods of investigation. Moreover, the obtained TUT trends are of the same order of magnitude as the changes found by Hodnebrog et al. (2019). In their study, the TUT from 1986-2005 (approx. 8.2 d) increased across 25 CMIP5 models for a climate simulation assuming the high-emission scenario RCP8.5 to values of 9.9 d for the period 2081-2100. Thus, the obtained results here together with the results from the aforementioned studies consistently show that the global hydrological cycle is slowing down and will slow down, respectively.

Combining the long-term relative trends in TUT and trends in surface air temperature, one can estimate the sensitivity of TUT to global warming r, i.e. $r = \frac{\Delta \mathrm{TUT}}{\mathrm{TUT}}/\Delta T$. For the case of OMI and Berkeley Earth, a TUT sensitivity of around 8.4 % K^{-1} is found and for ERA5 of around 8.8 % K^{-1}, which is higher than the results of 3–6 % K^{-1} pooled in Gimeno et al. (2021).

4.8 Summary

In this chapter, global trends are analysed from a long-term data set of total column water vapour (TCWV) retrieved from multiple years of OMI observations for the time period January 2005 until December 2020. Within the trend analyses, the effects of autocorrelation of the residuals have been considered. The results of the analyses were then put into context with trends from additional TCWV data sets, like from the GOME-Evolution project or from the reanalysis model ERA5, and overall good agreement was found. In a next step, based on the relative OMI TCWV trends, trends in relative humidity were derived and put into the context of the assumption of invariant relative humidity. Moreover, under consideration of the relationship between (column) relative humidity and precipitation, the patterns of the relative RH trends have been compared to rain rate trends. Also, the changes in the water vapour residence time and its response to changes in surface air temperature were investigated. The corresponding results are discussed below.

The trend analysis reveals an increase in TCWV of approximately $+0.054$ $\mathrm{kg\,m^{-2}\,yr^{-1}}$ or $+0.21$ % yr^{-1} globally for the time period of January 2005 until the end of 2020. To determine if trends are significant or not, a Z test and a false discovery rate test are applied to the trend results. After application of these significance criteria, almost all remaining trends are positive and distributed across the globe. However, particular spatial patterns remain, for instance within the region of the northern subtropics of the eastern Pacific. Overall, the relative OMI TCWV trends agree well to the corresponding trends from ERA5 and from the GOME- Evolution data set.

To analyse if the assumption of temporally invariant relative humidity is fulfilled on the local scale, relative trends in relative humidity (RH) are derived from the TCWV trends. All in all, one obtains that RH increases distinctively over large areas of the ocean and land surface. However, over both surface types relative decreases can also be well identified in some areas. Interestingly, relative decreases and increases in RH are not limited to arid and humid regions, respectively. For instance, the present analysis reveals relative increases in RH over the (arid) Sahara desert and decreases in RH over the (humid) tropical Pacific Ocean. Within the tropics, it is also found that the patterns of decreasing RH trends match those of decreasing precipitation quite well, especially within the tropical Pacific Ocean. Thus, these results show that on the one hand the assumption of temporally constant relative humidity is not always fulfilled over land and sometimes not even over ocean. On the other hand, they also demonstrate that the expected predictions of the "dry-gets- drier, wet-gets-wetter" paradigm do not agree with the direct and indirect trends in precipitation or that these observed trends occasionally even contradict the paradigm.

Combining the TCWV and precipitation data sets, changes in the water vapour residence time (WVRT) have been investigated. Overall, an increase in the turnover time of about 0.18 d per decade or 1.9 % per decade, respectively, has been observed which is in line with previous studies based on CMIP5 model simulations. This indicates that the global atmospheric branch of the hydrological cycle is slowing down. Moreover, it is expected to continue to slow down under future (high emission) greenhouse gas scenarios which will have implications for future precipitation patterns. Together with the long-term trends in surface temperature, a TUT sensitivity to global warming was estimated to be around 8.4 % K^{-1}, which is 2 to 3 times higher than the values provided in Gimeno et al. (2021).

The presented results also show that several challenges still remain for a better understanding of the atmospheric hydrological cycle and even new questions arise regarding the complex interactions between air temperature, water vapour, precipitation, and atmospheric dynamics. The differences between observed and expected changes in the hydrological cycle show that simplified assumptions are not always valid (e.g. invariant relative humidity). Also, the observed, much higher global sensitivities of individual parameters of the hydrological cycle (i.e. TUT) to changes in surface temperature compared to previous studies raise the question of what effects can be expected at the local scale (e.g. precipitation) with further increasing temperatures, especially with regard to changes in the global circulation such as the expansion of the Hadley cell or the tropics towards higher latitudes (e.g. Staten et al., 2018).

With regard to TCWV retrievals in the visible blue spectral range, there is great potential for extending the OMI TCWV data set with further satellite data (e.g. from TROPOMI or GOME-2) and combining it with future missions from geostationary satellites, such as GEMS or Sentinel-4, which will also allow for investigations of (semi-) diurnal TCWV cycles.

5 Determining the tropical expansion directly from satellite observations of water vapour

This chapter is largely based on a planned publication by Borger et al. (2022a) which is still to be submitted to a peer-reviewed journal.

5.1 Motivation

In addition to the global rise in temperature of the Earth's atmosphere and oceans, numerous studies also reveal that the Earth's general atmospheric circulation is changing (Hartmann et al., 2013). A particularly important circulation pattern is the so-called Hadley circulation (HC; Hadley, 1735), which, simply put, consists of a branch with rising air in the tropics and a branch with descending air in the subtropics. Several studies showed that over the last decades, the descending branches of the Hadley circulation are expanding polewards (Lu et al., 2007; Seidel et al., 2008; Hartmann et al., 2013; Hu et al., 2018), which in turn also corresponds to an expansion of the tropical belt. As the Hadley circulation is one of the largest overturning circulation patterns in the atmosphere, changes of its location and strength directly impact the distribution of dynamical structures in the atmosphere (such as storm tracks; Studholme and Gulev, 2018; Sharmila and Walsh, 2018; Staten et al., 2020), subtropical dry zones (such as deserts; Feng and Fu, 2013; Staten et al., 2020), the precipitation distribution (Scheff and Frierson, 2012), and the hydrological cycle (Seager et al., 2010; Collins et al., 2013) as a whole, and can thus have a serious impact on the daily lives of billions of people.

The mechanisms of the tropical expansion are still not fully understood, but there is evidence that the expansion is related to increases in greenhouse gas concentrations, ozone depletion, volcanic aerosol and air pollution (Bindoff et al., 2013; Staten et al., 2018, 2020), and is thus also influenced by humans. Moreover, climate simulations indicate that an expansion of the tropical belt is likely in near-term and long-term climate projections (Collins et al., 2013; Kirtman et al., 2013; Hu et al., 2018).

However, quantifying the tropical expansion is challenging because the descending branches of the Hadley circulation are not sharp edges but rather cover broad bands of several degrees of latitude. Hence, various studies used different proxies for the determination of the expansion of the tropical width and derived different trends ranging over more than one order of magnitude from 0.1–3.0° latitude per decade (Seidel et al., 2008; Lucas et al., 2014). One reason for this wide range of values is the large variety of different metrics and proxies used to determine the expansion trends: for instance, it has been demonstrated that the trends of proxies calculated from variables of the lower troposphere rarely coincide with the trends from proxies of the upper troposphere and thus only weakly correlate with each other (Davis and Rosenlof, 2012; Solomon et al., 2016; Davis and Birner, 2017; Waugh et al., 2018). Moreover, the proxies from observational data are inconsistent with each other and are sometimes based on arbitrary threshold values (e.g. the outgoing longwave radiation or the tropopause height) (Birner, 2010; Davis and Rosenlof, 2012). And those that are consistent with each other and with lower tropospheric metrics (e.g. the stream function) can only be determined from (reanalysis) model data, which are themselves subject to large uncertainties (Davis and Rosenlof, 2012; Staten et al., 2018, 2020).

In the context of the atmospheric hydrological cycle the descending branch of the Hadley circulation can be understood as a boundary separating the warm humid tropics and the (relatively) cool dry extratropics. Furthermore, within the tropics there is a direct relationship between water vapour and atmospheric dynamics. More specifically, there is a link between tropical tropospheric humidity and vertical velocity in which ascending/subsiding motion is associated with high/low free tropospheric relative humidity (Brogniez and Pierrehumbert, 2007). In addition, observations and the trend analysis in Chapter 4 indicate an increase in the atmospheric lifetime of water vapour (i.e. the time between evaporation and precipitation; Gimeno et al., 2021), which implies an expansion of the subsiding regions of the Hadley circulation (Singh et al., 2016).

Commonly, the Hadley *circulation* or *cell* describes the zonal mean of the meridional overturning circulation in the tropics. While the zonal mean allows for a compact representation of the circulation, important information about the spatial variability of these circulations on local and regional scales is lost by averaging (Schwendike et al., 2015). For example, the local meridional overturning circulation in the tropics differs from continent to continent and from ocean to ocean (e.g. Schwendike et al. (2014) and Schwendike et al. (2015) and references therein).

The approach presented here takes advantage of the relationship between the water vapour distribution and atmospheric dynamics as well as the accurate long-term data basis from satellite measurements and thus represents a robust approach for determining the changes in the tropical width. For this purpose, the chapter is structured as follows: First, the new metrics for the characterisation of the Hadley cell or the tropical width, respectively, are introduced. Then, these are applied to the zonal mean of the TCWV distribution to obtain a time series of changes in width of the Hadley cell, which is thereupon compared with the time series of tropical widths from other established metrics. Based on this, first trends of the tropical expansion are estimated using the analysis scheme presented in Chapter 4 and Borger et al. (2022). After that, the different width metrics are applied on a regional scale to determine changes in the regional overturning circulation, from which then also temporal trends are estimated. Finally, conclusions will be drawn.

5.2 Parameters for characterizing the tropical width

To characterize the tropical width or the Hadley cell, respectively, 3 parameters are defined which are schematically illustrated in Fig. 5.1: first, the location of the center is calculated via the center of mass μ of the TCWV distribution between 60°S and 60°N:

$$\mu = \frac{\int_{60°\mathrm{S}}^{60°\mathrm{N}} \mathrm{TCWV}(\theta) \cdot \theta \, d\theta}{\int_{60°\mathrm{S}}^{60°\mathrm{N}} \mathrm{TCWV}(\theta) \, d\theta} = \int\limits_{60°\mathrm{S}}^{60°\mathrm{N}} \theta \cdot f(\theta) \, d\theta \tag{5.1}$$

with the latitude θ and the function f given as follows:

$$f(\theta) = \frac{\mathrm{TCWV}(\theta)}{\int_{60°\mathrm{S}}^{60°\mathrm{N}} \mathrm{TCWV}(\theta) \, d\theta} \tag{5.2}$$

Next, the 2nd centered moment is used to estimate the width. To investigate potential asymmetric expansion trends of the width on the northern and southern hemisphere, μ is used to calculate the 2nd moments for each hemisphere separately:

$$\sigma^2_{south} = \int\limits_{60°\mathrm{S}}^{\mu} (\theta - \mu)^2 \cdot f(\theta) \, d\theta \tag{5.3}$$

$$\sigma^2_{north} = \int\limits_{\mu}^{60°\mathrm{N}} (\theta - \mu)^2 \cdot f(\theta) \, d\theta \tag{5.4}$$

Here and in the following, the monthly mean TCWV data provided by the MPIC OMI TCWV data set (Borger et al., 2021) and the reanalysis model ERA5 (Hersbach et al., 2019, 2020) with a spatial resolution of $1° \times 1°$ are used for determining the tropical width and location for the time range of January 2005 to December 2020.

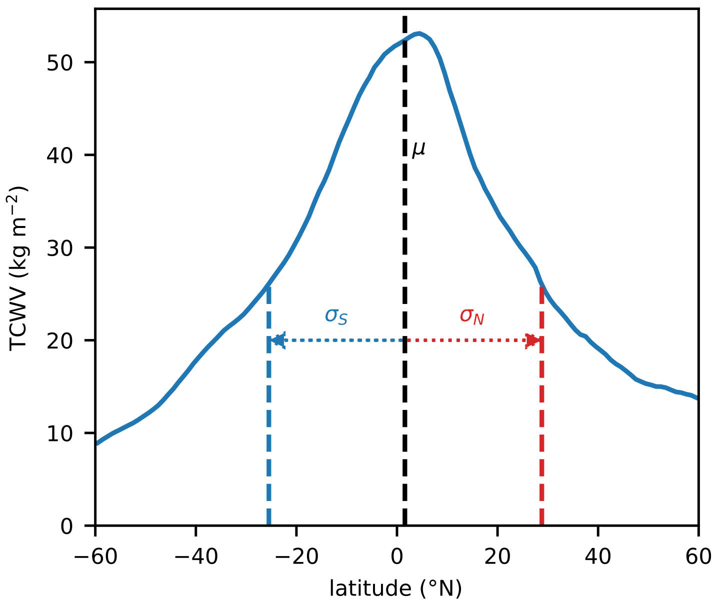

Figure 5.1: Schematic illustration of the three parameters used for the characterization of the tropical width.

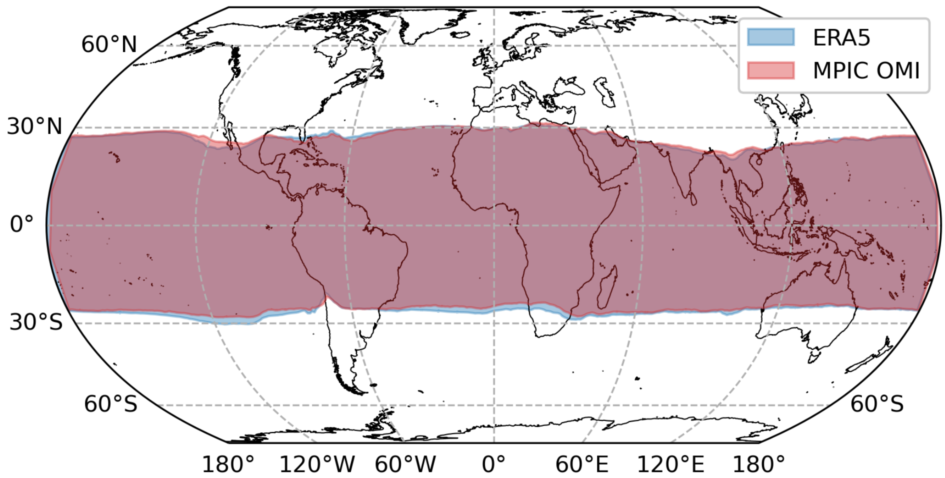

Figure 5.2: Mean global coverage of the tropical belt (or Hadley cell, respectively), as obtained from the MPIC OMI and ERA5 TCWV data sets.

Figure 5.2 depicts the mean global coverage of the tropical belt as obtained via the parametrization of the TCWV distribution from the MPIC OMI and ERA5 data sets. Overall, the obtained distributions for both data sets agree well to each other. With a latitudinal spread into the northern and southern subtropics, the determined distributions correspond to the expected extent of the Hadley circulation (or the tropics, respectively) of about 27-29° latitude (Held and Hou, 1980; Schneider, 2006) to the north and south of the equator.

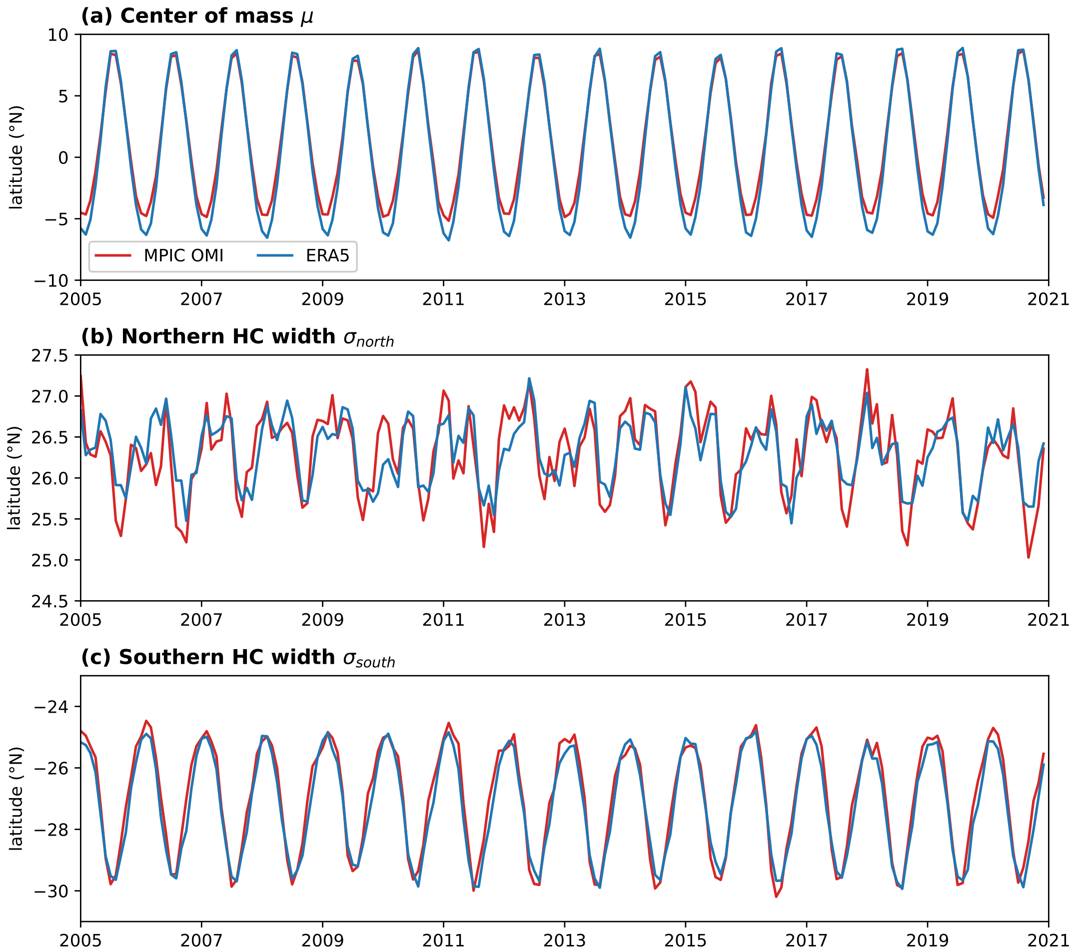

Figure 5.3: Time series of monthly values of the parameters μ (**a**), σ_{north} (**b**), and σ_{south} (**c**) for characterizing the tropics derived from the zonal mean TCWV distribution of MPIC OMI and ERA5.

5.3 Changes in zonal means

5.3.1 Time series of tropical width derived from TCWV distribution

To assess whether the approach of determining the tropical expansion via the meridional water vapour distribution is useful, zonal means are first considered. Figure 5.3 shows the time series of the monthly values of the parameters μ, σ_{north}, and σ_{south} calculated from the zonally averaged TCWV distribution of the MPIC OMI and ERA5 data sets. For the center of mass parameter μ a seasonal cycle around 2°N with an amplitude of 6° latitude is obtained (Fig. 5.3a) and for the σ_{south} parameter, a smooth seasonal cycle around –27°N and an amplitude of 4° can be observed (Fig. 5.3c).

In contrast, the amplitude of the seasonal cycle of the σ_{north} parameter (Fig. 5.3b) is distinctively lower than that of the other two parameters with a value of about 1.5° latitude. This could

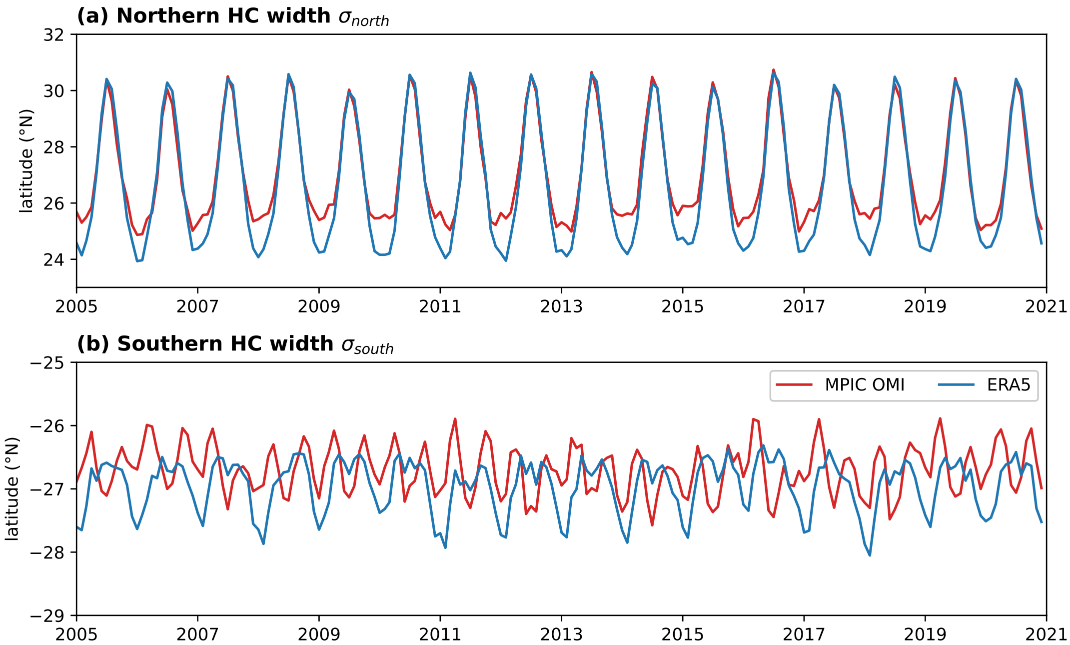

Figure 5.4: Time series of monthly values of the parameters σ_{north} (**a**), and σ_{south} (**b**) for characterizing the tropics derived from the zonal mean TCWV distribution of MPIC OMI and ERA5. Here the parameter μ is explicitly set to 0.

possibly be due to the fact that there are strong dependencies or interferences between the 3 parameters, especially between σ_{north} and μ. As a result, the seasonal cycle of σ_{north} seems to have been incorporated by the μ parameter. Consequently, due to the removal of the seasonal cycle from σ_{north} only the weak temporal variations are now clearly visible.

To estimate the influence of the μ parameter, it was explicitly set to 0 and the two width parameters were calculated again. The resulting time series are shown in Fig. 5.4. Overall, the results of the HC widths are in the same order of magnitude as before. In contrast to the previous results, there is now a clear seasonal cycle with a large amplitude for the σ_{north} parameter. For σ_{south}, however, as before for σ_{north}, this seasonal cycle seems to have been subtracted, which again illustrates the strong interdependencies between the parameters.

For the analysis of expansion trends, however, these cross-interferences or issues with the seasonal cycle, respectively, should play only a minor role at all, since the time series are de-seasonalised anyway when calculating the trends.

5.3.2 Correlation analysis

To see to what extent the width parameters from the TCWV distribution are representative, they are compared to results from widely accepted metrics based on other geophysical variables besides the TCWV distribution. For this, the following metrics are used:

- the zero-crossing (polewards of the ITCZ) of the meridional overturning stream function at 500 hPa (abbreviated PSI),
- the latitude of the maximum of the mean sea level pressure (MSL),
- the latitude of the maximum of the zonal wind averaged between the 100 and 400 hPa levels minus the zonal wind at the 850 hPa level (STJ),
- the latitude of the zero-crossing of the difference evaporation minus precipitation (E-P),
- and the isoline of the outgoing longwave radiation at a threshold of 250 W m^{-2} (OLR).

All these metrics were calculated from the zonally averaged monthly mean values of the reanalysis model ERA5 using the TropD software package (Adam et al., 2018).

Figure 5.5 illustrates the time series of the monthly mean tropical width derived from aforementioned metrics and from TCWV metric based on the MPIC OMI (MPIC_WV) and ERA5 TCWV data set (ERA_WV) for the northern hemisphere. For a better overview, the metrics have been separated according to the variables from which they have been determined, i.e. atmospheric dynamics (PSI, STJ, and MSL; Panel a), other geophysical variables (E-P and OLR; Panel b) and water vapour (ERA_WV and MPIC_WV; Panel c). In the time series for the northern hemisphere a seasonal cycle is observable for all metrics, however, this seasonal cycle is often overlayed by a high variability, in particular for the PSI, E-P, and MSL metrics. Moreover, the time series do not all oscillate around the same mean value, instead, small differences can be seen for instance between the MSL and PSI metrics (Fig. 5.5a). Overall, however, the latitude of the northern width derived from the TCWV metric is clearly lower than that of the other metrics. This is probably due to the fact that in the TCWV metric the center of mass μ was also fitted in addition to the northern expansion parameter (see also Fig. 5.3). It should also be noted that the MSL metric seems to contain outliers here and there and that the PSI metric systematically cannot determine a latitude for some specific months.

In contrast to the northern hemisphere, the time series for the southern hemisphere (Fig. 5.6) are much smoother for almost all metrics (except for the STJ metric), which is probably due to the much simpler topography of the southern hemisphere. Nevertheless, it can also be seen here that the time series oscillate around distinctively different mean values. For instance the mean latitude of the TCWV metric is around approximately 27°S, the PSI and MSL metrics around 32°S, the OLR metric around 35°S, and the E-P metric around 40°S. Overall, however, it also shows that the HC width of the TCWV metric is strongly anti-correlated to all other metrics.

The correlations between all width time series for the northern and southern hemisphere are summarised in the correlation matrix in Fig. 5.7. As already mentioned, the width from the TCWV metric is anti-correlated with all other metrics. However, it can also be seen that in the northern hemisphere (NH; upper right triangle of the matrix) the TCWV metric correlates

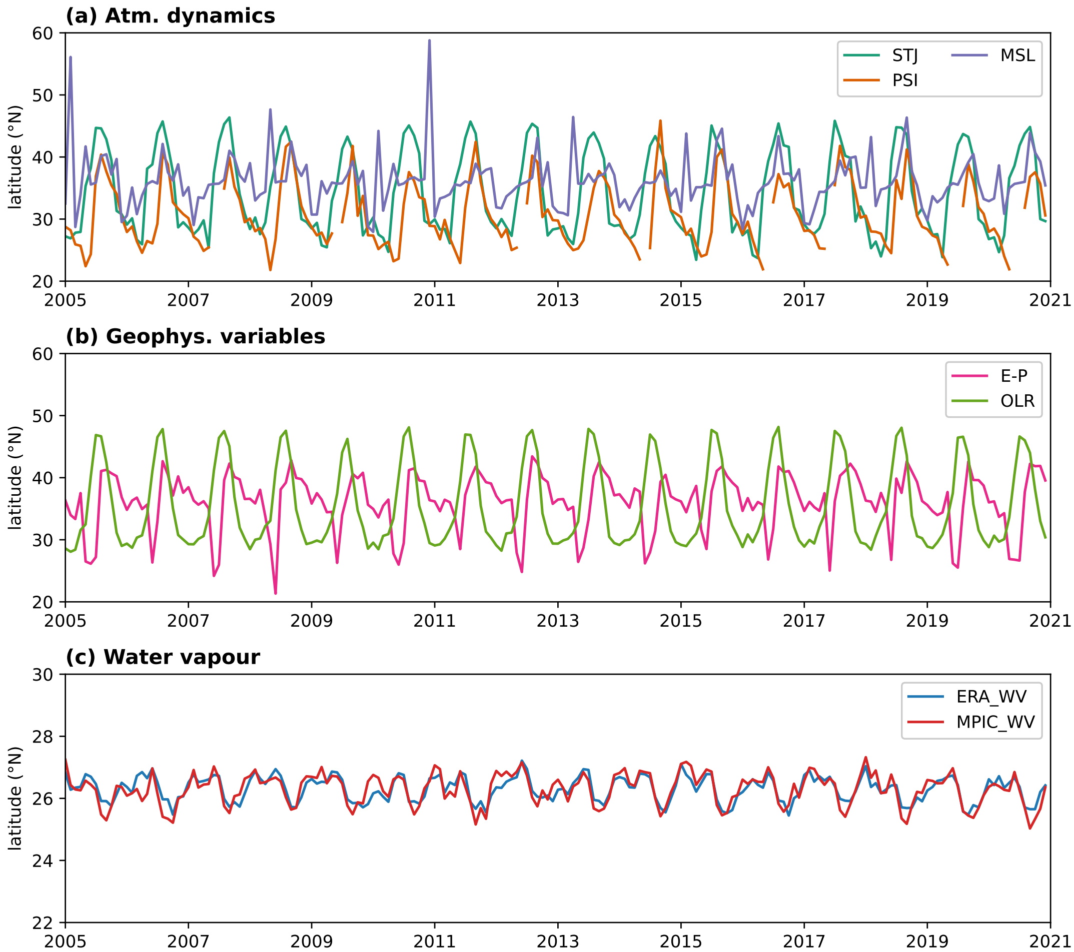

Figure 5.5: Time series of monthly means the northern tropical width derived from the water vapour distribution of MPIC OMI and ERA5 along with the HC width derived from different methodologies using the ERA5 data set and separated into different categories: (**a**) atmospheric dynamics (STJ, PSI, and MSL), (**b**) geophysical variables (E-P and OLR), and (**c**) water vapour.

well with the results of the E-P and PSI metrics (−0.60 and −0.71 for MPIC OMI and −0.66 and −0.65 for ERA5, respectively), but only weakly with the OLR, STJ, and MSL metrics. In general, however, correlations are only moderately high for the northern hemisphere (except for the correlation between OLR and STJ).

In contrast, for the southern hemisphere (SH; lower left triangle) high absolute correlation values are found across almost all metrics, which are typically greater than 0.8 in magnitude (except for the STJ metric). For the TCWV metric, for example, there are correlations of −0.89 for the MPIC data set with the MSL metric (or −0.9 for ERA5) or −0.82 with the OLR metric (−0.86 for ERA5).

Thus, the correlation results demonstrate that the TCWV distribution is another adequate proxy for determining the tropical expansion. The major advantages of this proxy are that it is based exclusively on measurement data from direct observations and does not require model

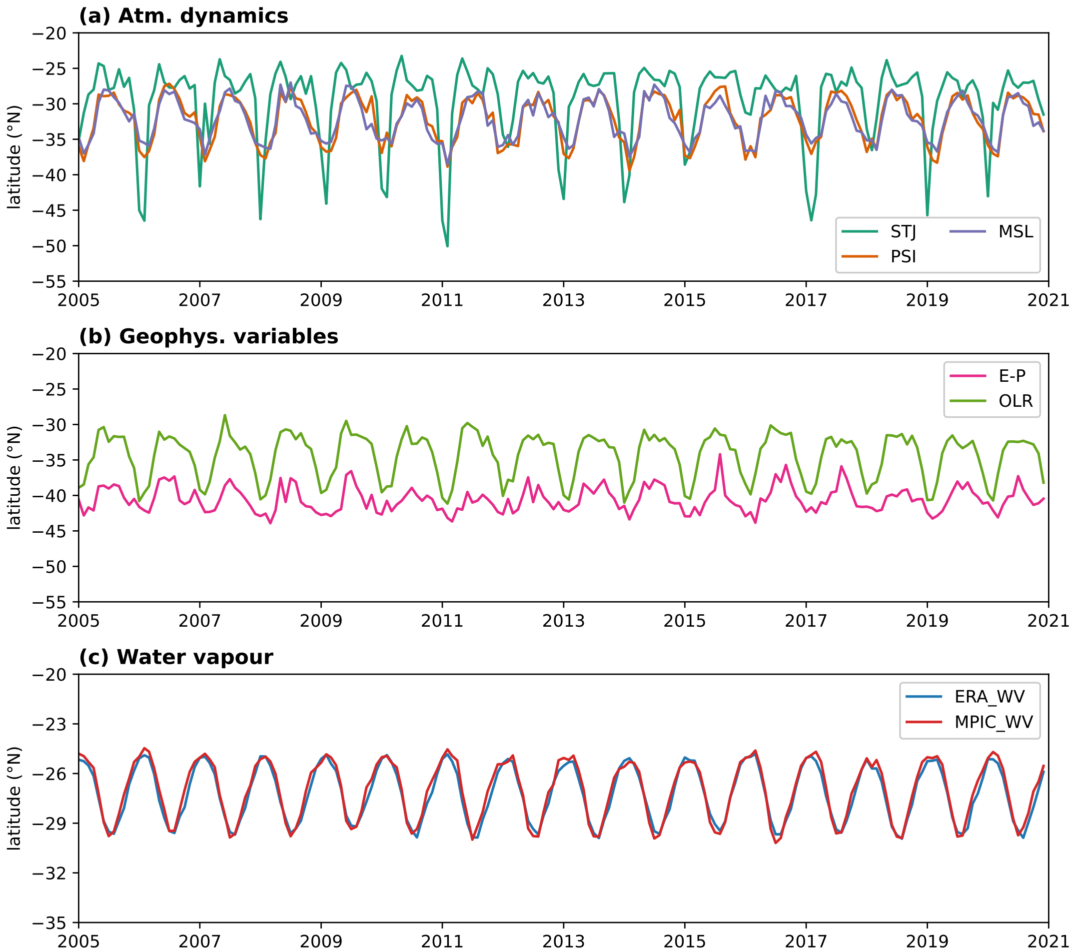

Figure 5.6: Time series of monthly means the southern tropical width derived from the water vapour distribution of MPIC OMI and ERA5 along with the HC width derived from different methodologies using the ERA5 data set and separated into different categories: (**a**) atmospheric dynamics (STJ, PSI, and MSL), (**b**) geophysical variables (E-P and OLR), and (**c**) water vapour.

data and that it is also independent of the choice of threshold values. While it must be taken into account that the correlations, at least for the southern hemisphere, are so high mainly because of the dominant seasonal cycle, the correlations of the TCWV metric with the PSI or E-P metric in the northern hemisphere indicate great potential for further investigations, as the seasonal cycle of the TCWV metric is significantly weaker there.

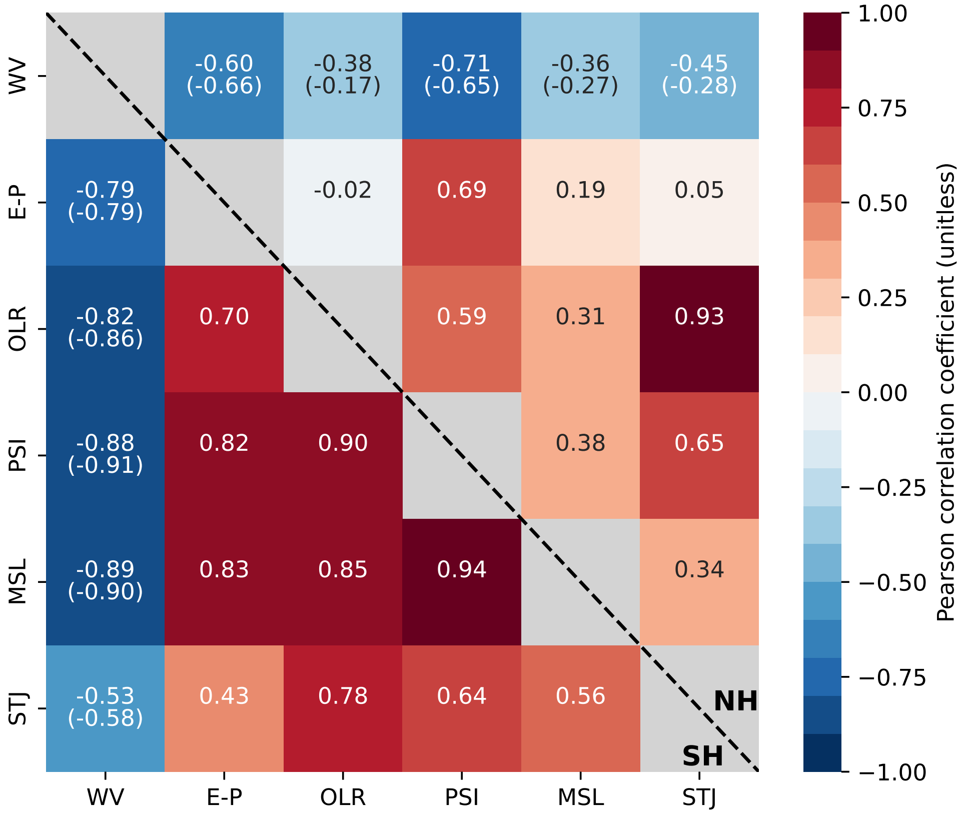

Figure 5.7: Correlation matrix of the monthly mean northern and southern tropical width derived from the TCWV distribution from MPIC OMI (and ERA5) against the tropical width derived from other methodologies using the ERA5 reanalysis. Values in parentheses indicate correlation of tropical width derived via the TCWV distribution from ERA5.

5.3.3 Trends

From the time series of the tropical width metrics, trends for the time range January 2005 to December 2020 have been calculated following the trend analysis scheme presented in Sect. 4.2. The results of these analyses are summarized in Tab. 5.1.

For the northern hemisphere, the expansion trends from the TCWV distribution yield values of 0.0° for MPIC OMI and 0.05°N per decade for ERA5. In contrast, the trends of the other metrics are much stronger: trends of 0.29°N per decade are obtained for the E-P and OLR metrics, with the trends of the OLR metric even being statistically significant (at the significance level of 5%). Surprisingly, negative trends of –0.15°, –0.20°, and –0.48°N per decade are obtained for the PSI, MSL, and STJ metrics, respectively, i.e. the tropical belt does not expand in the selected period, but contracts. However, it must be taken into account that the MSL metric is influenced by outliers and that systematic gaps appear in the time series of the PSI metric.

For the southern hemisphere, the TCWV metric yields expansion trends of 0.10°S per decade for MPIC OMI and 0.07°S per decade for ERA5, with both trend results being statistically significant. In contrast to the northern hemisphere, the trend results of the E-P, MSL, and PSI metrics are of the same order of magnitude as the results of the TCWV metric. Only the STJ and OLR metric show distinctively stronger trends of 0.24° and 0.32°S per decade, which is again statistically significant for the OLR metric .

For the location of the center parameter μ of the TCWV metric, trends were also determined and amount to 0.10°N per decade for MPIC OMI (statistically significant) and 0.08°N per decade for ERA5.

If the μ parameter is set to 0, distinctive changes in the expansion trends of the TCWV metric occur. The trends for the northern expansion increase, whereas those for the southern expansion decrease and are no longer statistically significant. This clear difference shows the strong influence of this parameter and illustrates that when investigating expansion trends, it is important to also consider the location of their center of mass. However, if this were to be done for the other metrics, it would only be feasible for the PSI metric.

For the sake of completeness, Tab. 5.2 presents the trend results of tropical width for the time period January 1990 to December 2020 only using the ERA5 data. Since the time series now covers several decades, a climate index for the so-called Pacific Decadal Oscillation (Mantua et al., 1997; Zhang et al., 1997) has been included in the trend analyses in addition to the teleconnection indices from Sect. 4.2. It should be noted, though, that the trend results (at least for the southern hemisphere) were only negligibly affected by the addition of this further teleconnection.

For this longer time period, the trends in tropical width from the TCWV metric are close to 0°, although the expansion trends for the southern hemisphere are still statistically significant at 0.03°S per decade. For the trends from the other metrics, the picture is more complex: depending on the hemisphere and metric, the trends are sometimes similar in magnitude to the trends based on the TCWV metric, but sometimes more than an order of magnitude stronger. For instance, the E-P metric yields a zero-trend for the northern hemisphere but a statistically significant trend of 0.24°S per decade for the southern hemisphere. At least the trends with the STJ metric seem to be of the same order of magnitude as the trends with the TCWV metric for the northern and southern hemispheres.

To summarize, over longer time periods the tropical expansion varies between 0.00–0.19°N per decade and 0.04–0.38°S per decade, respectively, with trends for E-P, PSI, and MSL metrics being statistically significant for the southern hemisphere. However, the wide range of trend results for both the long and short time period also shows that there is a high uncertainty in the determination of tropical expansion and it is therefore unclear how strong the expansion of tropical width (or Hadley cell) actually is.

Table 5.1: Summary of the trends of the tropical width derived from the time series of different monthly mean metrics for the time range January 2005 to December 2020. The trend results based on the TCWV parameterizsation are given for the case with all 3 parameters and for the case with $\mu = 0$. Numbers marked with an asterisk (*) indicate a statistically significant trend to the significance level of 5%.

Metric	Northern hemisphere (°N per decade)	Southern hemisphere (°S per decade)	Center of mass (°N per decade)
MPIC WV	0.00	0.10*	+0.10*
ERA WV	–0.05	0.07*	+0.08
MPIC WV ($\mu = 0$)	0.04	0.06	
ERA WV ($\mu = 0$)	0.01	0.03	
E-P	0.29	0.08	
OLR	0.29*	0.32*	
PSI	–0.15	0.08	
MSL	–0.48	0.07	
STJ	–0.20	0.24	

Table 5.2: Summary of the trends of the tropical width derived from the time series of different monthly mean metrics for the time range January 1990 to December 2020. Numbers marked with an asterisk (*) indicate a statistically significant trend to the significance level of 5%.

Metric	Northern hemisphere (°N per decade)	Southern hemisphere (°S per decade)	Center of mass (°N per decade)
ERA WV	–0.02	0.03*	+0.03*
ERA WV ($\mu = 0$)	0.01	0.02	
E-P	0.00	0.24*	
OLR	0.19*	0.09	
PSI	0.04	0.38*	
MSL	0.16	0.21*	
STJ	0.05	0.04	

5.4 Changes in regional tropical width

So far, only changes in the zonally averaged meridional (Hadley) overturning circulation have been considered. However, Nguyen et al. (2018) showed that the poleward expansion of the Hadley circulation is not uniform or does not occur at every longitude. Hence, the question naturally arises to what extent changes in the regional meridional circulation (RC) occur, which could allow a clearer assessment of the social impact (e.g. subtropical aridification) of the meridional expansion of the tropics. For this purpose, the zonal means of the metrics are no longer investigated here, but the RC width is determined from the metrics for each individual longitude for each month and finally trends are calculated.

5.4.1 Regional tropical changes from TCWV metrics

Figure 5.8 illustrates the estimated trends of the location of the tropical center derived from the TCWV distribution of OMI (red line) as well as of ERA5 (blue line). Significant trends are indicated by crosses (for OMI) and circles (for ERA5), respectively. In general, positive trends can be observed, i.e. the center of the TCWV distribution for OMI and ERA5 is moving northwards. Statistically significant northward shifts occur in particular over the East Pacific (around 150°W to 110°W), the African/European continent (0°E to 30°E) and parts of East Asia (eastwards of 90°E) with values of around +0.3°N per decade.

Figure 5.9 depicts the expansion trends of the northern and southern branch of the tropical belt derived from OMI and ERA5 (red and blue line, respectively). For both OMI and ERA5, the northward expansion trends (Fig. 5.9a) mostly vary around values of 0.0°N per decade in the region from -180°E to 0°E (except distinctive northward trends close to the dateline for OMI). Eastwards of 30°E (statistically) insignificant contraction trends can be observed, i.e. the northern RC branch is apparently moving southwards. Over East Asia (eastwards of 90°E), significant expansion trends are observable for the OMI TCWV data set with values up to 0.3°N per decade. Interestingly, these significant northward expansion trends are not present within ERA5. However, the results obtained for the MPIC OMI TCWV data are probably influenced by missing data due to land ice contamination for instance over Siberia or the Himalayan mountains.

Contrary to the northern expansion trends, distinctive and statistically significant southward expansion trends can be observed across the complete Pacific Ocean with values around 0.2-0.4°S per decade within both TCWV data sets (Fig. 5.9b). For the rest of the globe, southward expansion trends remain close to values between 0.0–0.2°S per decade (except for a few significant southward trends at around 45°W and 20°E). Therefore, these results together with findings for the shift of the center of mass suggest that the northward movement of the trop-

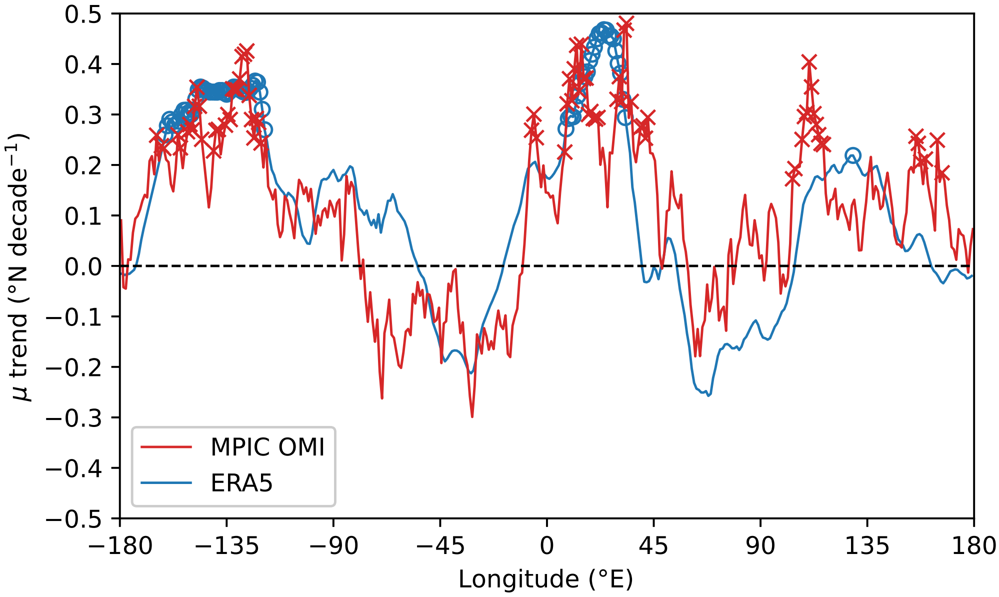

Figure 5.8: Longitudinal distribution of the results of the trend analyses of the parameter μ for the shift of the center of mass from the TCWV distribution of MPIC OMI and ERA5 for the time range of January 2005 to December 2020. Solid red lines represent the results of the MPIC OMI TCWV data set and blue lines the results from ERA5. Significant trends are depicted by crosses and circles for MPIC OMI and ERA5, respectively.

ics in the Pacific Ocean is eventually balanced by an expansion of the southern branch of the regional overturning circulation.

The effects of the non-consideration of the μ parameter in the calculation of regional trends are shown in Fig. 5.10. The longitudinal patterns of the expansion trends have remained almost the same, but all northern and southern expansion trends have shifted northwards by about +0.05°N per decade. Due to this shift, in the southern hemisphere the trends from the ERA5 data are now also no longer statistically significant in the Western Pacific, yet for MPIC OMI the locations of statistically significant trends have not changed a lot.

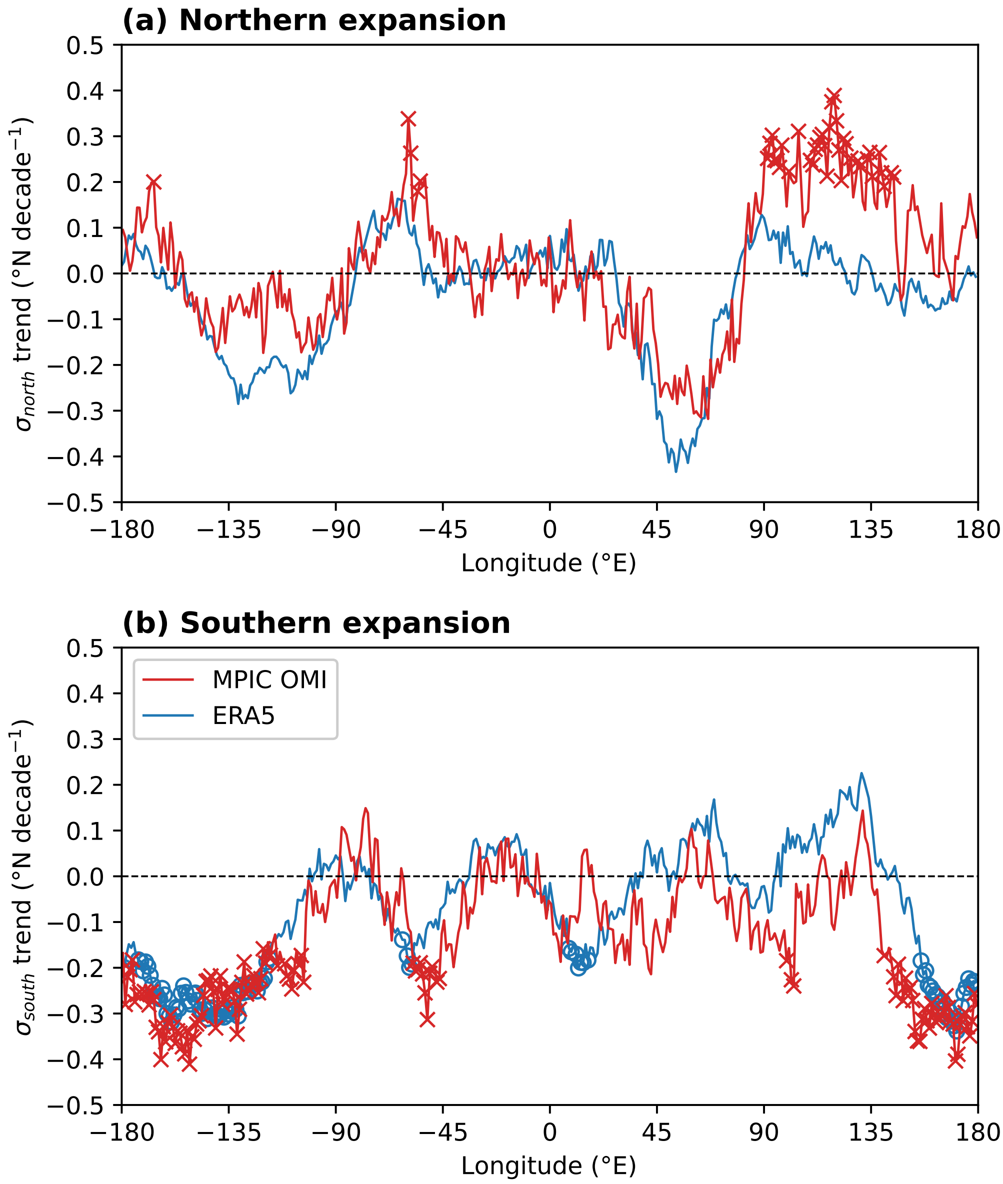

Figure 5.9: Longitudinal distribution of the results of the trend analyses of the parameters for the tropical width from the TCWV distribution of MPIC OMI and ERA5 for the time range of January 2005 to December 2020. Panels **(a)** and **(b)** illustrate the decadal expansion trends of the northern and southern branches, respectively. Solid red lines represent the results of the OMI TCWV data set and blue lines the results from ERA5. Significant trends are depicted by crosses and circles for MPIC OMI and ERA5, respectively.

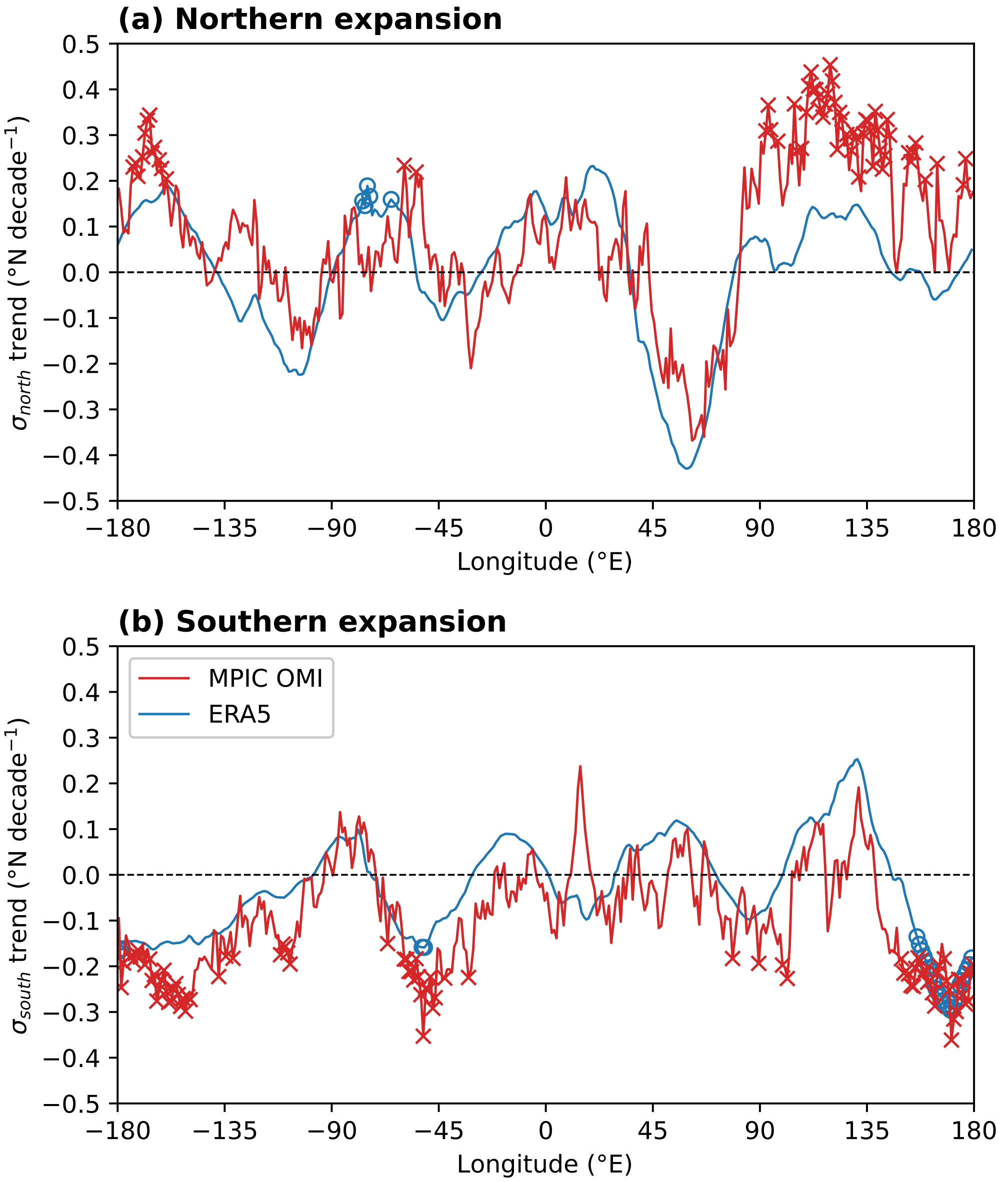

Figure 5.10: Same as Fig. 5.9, but now with μ parameter explicitly set to 0.

5.4.2 Regional tropical changes from other metrics

Similar to the TCWV metric, the RC width was determined for the other metrics presented in Sect. 5.3.2 for each longitude and month and trends were then calculated.

In the case of the streamfunction, the approach of Schwendike et al. (2014) is applied, i.e. only the divergent component of the meridional wind is considered for the calculation of the streamfunction (Keyser et al., 1989). The rationale for this approach is that much of the vertical motion in the tropics and subtropics is due to the meridional divergence and that horizontal rotational wind features are filtered which produce enhanced Hadley cell-wise flow (Staten et al., 2019). To calculate the divergent component of the meridional wind from the ERA5 wind fields, the "windspharm" package (Dawson, 2016) is used.

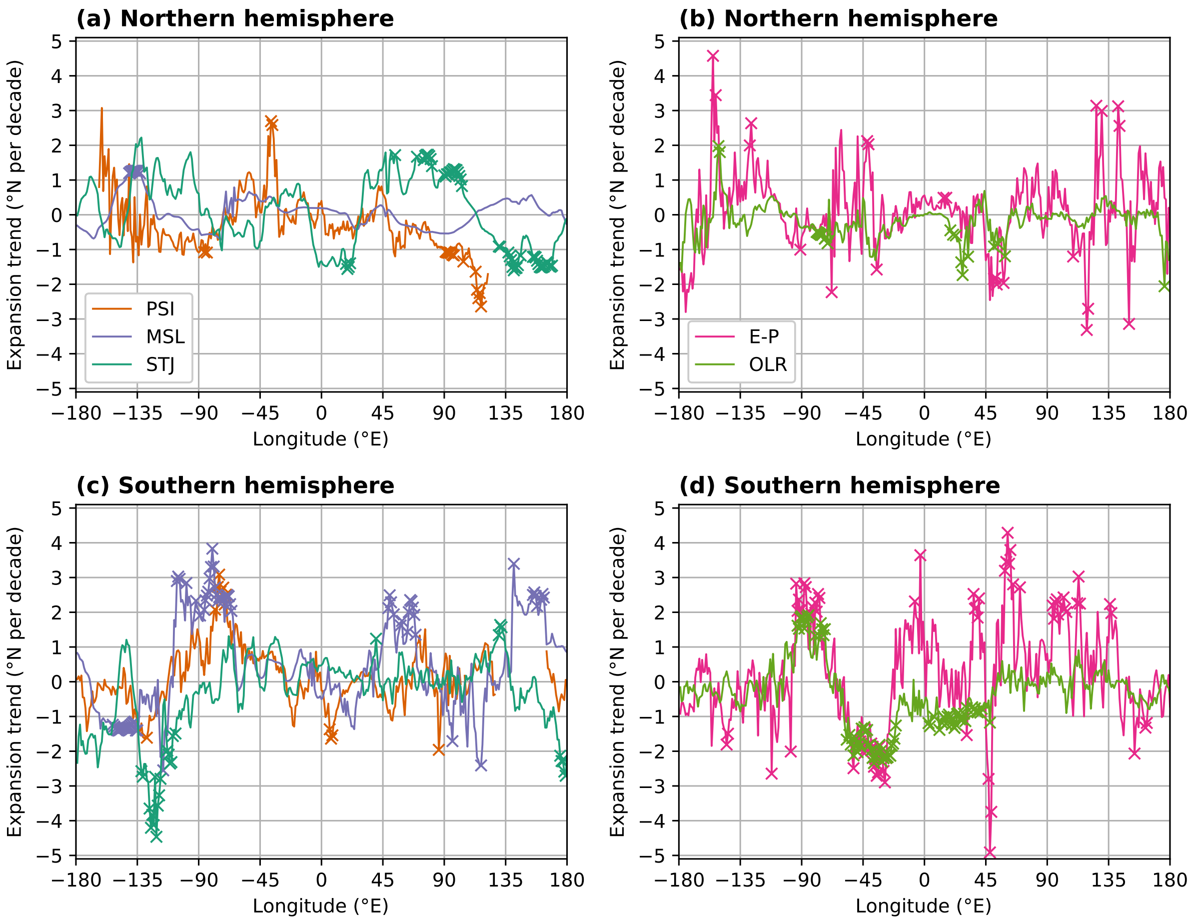

Figure 5.11: Longitudinal distribution of the results of the trend analyses of the additional RC metrics for the time range of January 2005 to December 2020 for the northern (Panels a & b) and southern hemisphere (Panels c & d). The metrics are categorised by the respective atmospheric variable through which they were determined: STJ, PSI, and MSL metric into atmospheric dynamics (left column, Panels a & c) and E-P and OLR into other geophysical variables (right column, Panels b & d). Significant trends are depicted by crosses.

Figure 5.11 shows the longitudinal distribution of expansion trends for the other metrics for the northern (top row) and southern (bottom row) hemisphere, again separated into the geophysical variables on which the respective metrics are based. As with the zonally averaged trends in Sect. 5.3, the trends of the longitudinal distribution are almost an order of magnitude stronger than the trends based on the TCWV metric.

For the northern hemisphere (Fig. 5.11a & b), the distributions strongly fluctuate with longitude and only rarely show the same tendency of trends over larger longitudinal bands. For example, the E-P metric shows some statistically significant trends around 135°E, but these jump from positive to negative and back again. Only for the STJ metric a constant (statistically) significant widening of about +2°N per decade is observable in the longitude range 45°E to 90°E, but also a significant contraction of −2°N per decade for longitudes between 135°E to 180°E.

The picture for the southern hemisphere (Fig. 5.11c & d) is almost similar to that for the northern hemisphere, i.e. the longitudinal trends are highly variable over large areas. However, the MSL metric shows a wide range of significant contraction of more than 2°N per decade between -90°E and -45°E. Similarly, the OLR metric shows a wide band of statistically significant expansion trends around −2 to −1°N per decade between -45°E and 45°E.

5.4.3 Zonal averages of the regional expansion trends

Table 5.3 summarizes the zonally averaged trends from the longitudinal distributions. Similar to the trends from the zonal means, no clear trends of tropical expansion can be discerned from the trends of the various metrics.

For the trends from the TCWV metric one obtains a trend in the globally averaged shift of the center of mass μ of about +0.10°N per decade for the MPIC OMI TCWV data set (+0.09°N for ERA5), a northward expansion trend of around +0.04°N per decade (−0.05°N) and a southward expansion trend of +0.13°S per decade (+0.07°S per decade) for the time range 2005 to 2020. Likewise, a similarly good agreement can be found for the trends without the μ parameter. Thus, the zonally averaged trends are generally consistent with the trends from the zonal means.

In contrast, a different picture emerges for the trends of the other width metrics: either the zonally averaged trends are significantly weaker or stronger (e.g. for the E-P metric) or in some cases have completely different signs than the trends of the zonal means (e.g. OLR metric). Only the trends of the PSI metric seem to be consistent for both approaches. These different results could indicate that some metrics are not applicable on a regional scale, leading to grossly erroneous values that affect the globally averaged trends. Apparently for these metrics, first global averaging is necessary to smooth out the fluctuations along the longitudes before the trend calculation.

Table 5.3: Summary of zonally averaged regional trends in the tropical expansion for the time range January 2005 to December 2020.

Metric	northern hemisphere (°N per decade)	southern hemisphere (°S per decade)	Center of mass (°N per decade)
MPIC WV	0.04	0.13	+0.10
ERA WV	–0.05	0.07	+0.09
MPIC WV ($\mu = 0$)	0.07	0.09	
ERA WV ($\mu = 0$)	0.01	0.03	
E-P	0.13	0.18	
OLR	–0.17	–0.33	
PSI	–0.26	0.11	
MSL	0.05	0.43	
STJ	0.12	–0.27	

Overall, it is difficult to say which metric is best suited to investigate trends in tropical expansion on both global and regional scales. However, if consistency is a selection criterion, the PSI metric and the TCWV metric seem to be superior to all other metrics.

5.5 Conclusions

In this chapter changes in the meridional overturning circulation were determined on a global and on a regional scale by means of the global water vapour distribution from satellite measurements and reanalysis models. To this end, metrics were first established from the meridional normalised TCWV distribution to characterize the northern and southern width and the location of the Hadley cell. These were then applied to the monthly means of the zonally averaged TCWV distribution. The resulting time series of the Hadley cell metrics were compared with the time series of other established Hadley cell metrics and temporal trends were determined. Finally, all these metrics were applied to the regional scale (i.e. for each longitude), again trends were determined and then the zonal distributions of the changes in regional meridional overturning circulation were examined.

The correlation analysis of the time series of the metrics reveals that the results of the TCWV metric is negatively correlated to all other metrics. For the northern hemisphere only a moderate correlations to the other metrics has been obtained, but for the southern hemisphere the correlations are much stronger, typically reaching values of around –0.8. However, it should be noted that the high correlation in the southern hemisphere is probably mainly due to the annual cycle.

The comparisons of the temporal trends of the expansion metrics calculated from the zonal means show an unclear picture, as the trends of all metrics are sometimes positive and sometimes negative. If a longer time period is chosen (1990-2020), the tendency of the trends is the same, but the magnitude of the trends remains highly variable.

To investigate the extent to which the meridional circulation changes on a regional scale, first the HC metrics were determined for each longitude and month. Then trends were for each longitude determined from these results and their zonal distribution was examined. The distribution of the RC width trends from the TCWV metric shows a statistically significant southward expansion of the RC over the entire Pacific of about 0.3°S per decade. But of course, the striking structure in the trends of the TCWV metric in the southern hemisphere leaves open the question of the extent to which these trends do not simply arise from natural variability, even though a wide variety of teleconnection indices are considere in the trend analysis.

This particular pattern in the southern hemisphere is not found in the distributions of the trends of the other metrics, instead their zonal distribution is mostly highly fluctuating. Only for the OLR metric a broad band of significant trends can be identified across the Atlantic Ocean for the southern hemisphere. Thus, the zonal means of these trends rarely coincide with the trends of the zonal means (and thus with the expansion trends of the Hadley circulation). Only the trends of the TCWV metric and possibly the PSI metric seem to provide consistent results.

Because of these consistent results, it can be concluded that the great advantage of this new metric based on the TCWV distribution is the ability to provide reasonable, robust, and independent results in a straightforward manner with a high degree of reliability. Unlike other approaches based on observational data (e.g. tropopause height, outgoing longwave radiation, or total column ozone), it is independent of the choice of arbitrary thresholds. Also, in contrast to approaches considered consistent and reliable (e.g. stream function), it is based exclusively on measured data and does not have to be derived from (reanalysis) model data. Thus, one can conclude that the presented metric is expected to be favorable for many applications as it is independent of the choice of the model as well as input and parametrizations used therein.

The expected further poleward expansion of the Hadley circulation will affect the world's population differently: On the one hand, the expansion of the subtropical dry zones will lead to an increasing population affected by water scarcity. On the other hand, the higher latitudes will face an increasing number of hazards related to tropical cyclones. In this context, the new metric can provide an important contribution to a better understanding of changes in the global water cycle and global warming.

6 Conclusions and outlook

In this work, the changes in the long-term global water vapour distribution were investigated on the basis of global satellite measurements. For this purpose, the following main tasks were carried out: First, a satellite algorithm was developed to retrieve total column water vapour (TCWV) using measurements in the visible blue spectral range from the state-of-the-art TROPOspheric Monitoring Instrument (TROPOMI). TROPOMI is particularly well-suited for the development of retrieval algorithms as it combines a high signal-to-noise ratio with an unprecedented spatial resolution and a daily global coverage and thus allows for the identification of shortcomings in the retrieval. The developed retrieval was then modified and applied to the long-term measurement time series of TROPOMI's predecessor, the Ozone Monitoring Instrument (OMI), and a climate data record was created from the OMI measurements. Based on this climate TCWV data set, a study was carried out in which the local trends in the water vapour distribution were determined on a global scale. In addition, the extent to which the global water vapour distribution can be used to detect changes in the global atmospheric circulation was investigated.

For the TROPOMI TCWV retrieval, for the first time an iterative vertical column conversion scheme was implemented, which is based on a novel parameterisation of the water vapour profile shape by the TCWV itself. This successfully replaced the approach of a prescribed, constant profile shape. To characterize the retrieval, the largest error sources were identified within a comprehensive uncertainty analysis. The total retrieval error consists of an error in the slant column density (SCD) and an error in the airmass factor (AMF) which vary from region to region and sometimes one error dominates the other and vice versa. It turned out that the main SCD uncertainty is the fit error of the spectral analysis and that the main AMF uncertainties are caused by uncertainties in the surface albedo, cloud properties, and the water vapour profile shape. For the H_2O VCD or TCWV of a single satellite pixel a typical total relative error of around 10–20% is estimated for observations under favourable conditions (clear-sky conditions, over ocean surface, and low solar zenith angles) and 20–50% under unfavourable conditions (cloudy-sky conditions, over land surface, and high solar zenith angles). An extensive validation study demonstrated that the retrieval is in very good agreement to reference data sets over ocean surface. Over land surface a distinctive underestimation of +10 % was observed. Nevertheless, as this underestimation is mainly related to an underestimation in the input cloud top heights, updates in these input parameters should lead to an improved agreement.

To create a TCWV climate data record (CDR), the TROPOMI retrieval was applied to long-term measurements from the OMI instrument (2005-2020), which required some modifications in the spectral analysis (e.g. the use of an Earthshine reference instead of a solar reference spectrum). In addition to the generation of the data set, its sampling errors were investigated with regard to spatiotemporal representativeness and a potential clear-sky bias. Overall, a sampling error of −10 % was found, which is mainly due to the clear-sky bias. The data set was also compared with various reference data sets from satellite measurements, reanalysis models, and radiosonde observations which revealed a very good agreement especially over ocean. Over land surfaces, however, a systematic overestimation was identified, which can reach values of around +24 %, especially in the tropics. This overestimation mainly occurs in those tropical regions that are frequently affected by cloud cover, indicating that the obtained biases are due to uncertainties in the input cloud information. Nevertheless, the bias does not affect trend studies, since these studies focus on the relative TCWV trend and the bias is eliminated during the normalisation process. Aside from that, the temporal stability of the MPIC OMI TCWV CDR was also assessed. No significant deviation trends were found with respect to ERA5 and RSS SSM/I. Furthermore, the CDR also fulfills the latest stability criteria according to GCOS requirements.

Various trend analyses were applied to the novel MPIC OMI TCWV data set, taking into account the effects of the corresponding temporal autocorrelation of the fit residuals. Moreover, the local changes in relative humidity (RH), their relationship to precipitation and the changes in the water vapour residence time (WVRT) were investigated on a global scale. The trend analysis reveals an average increase in TCWV of approximately +0.054 $kg\,m^{-2}\,yr^{-1}$ or +0.21 $\%\,yr^{-1}$ globally for the time period of January 2005 until December 2020. After application of several significance criteria, almost all remaining trends are positive and distributed across the globe. The analysis of relative RH trends revealed distinctive increases and decreases over large areas of the ocean and land surface, but these decreases or increases are not limited to arid or humid regions, respectively. These results show that the assumption of temporally constant relative humidity is not always fulfilled over land and sometimes not even over ocean. Moreover, it was found that the expected predictions of the "dry-gets-drier, wet-gets-wetter" paradigm do not agree with the direct and indirect trends in precipitation or that these observed trends occasionally even contradict the paradigm. Additionally, the investigations of WVRT changes reveal an increase in the global turnover time of about 0.18 d, which implies that the global atmospheric branch of the hydrological cycle is slowing down.

The novel OMI TCWV data set was also used to investigate possible changes in the meridional circulation. To this end, first a parameterisation was developed from the normalised TCWV distribution. Then, a correlation analysis with established metrics of the Hadley circulation (e.g. the stream function or outgoing longwave radiation) was conducted to find out whether the results obtained on a global scale are meaningful. For the time series of the calculated parameters from the global means, a high (anti-) correlation of −0.8 was found with respect to other Hadley circulation metrics in the southern hemisphere, but only a moderate correlation in the northern hemisphere. When changes are examined on a regional scale, the TCWV parameterisation shows a statistically significant southern expansion trend over the entire Pacific ocean. However, it still remains unclear whether these trends do not simply stem from natural variability. Overall, it can be said that the new metric is a good alternative to the established metrics as the great advantage of this new metric is the ability to provide reasonable and robust results which are independent of the choice of thresholds or (reanalysis) model data.

The development of a TCWV satellite retrieval in the visible blue spectral range, the creation of a climate data record and the investigation of long-term changes provide a new contribution to the understanding of changes in the hydrological cycle. However, it should be noted that the knowledge gained and assumptions made in the past were dependent on the time period considered and the research methodology chosen, and this also applies to this work. A perhaps underestimated factor is the high interannual variability of the water vapour distribution and its (external) influencing factors such as teleconnections of the El Niño-Southern Oscillation or the Pacific Decadal Oscillation. While these influences can be taken into account with teleconnection indices in the trend analysis scheme, the overarching question arises whether these influences themselves are not also part of the climate system? To clarify this, longer periods of probably more than 50 years would have to be investigated, in which the interannual variability no longer has a major influence on the final result. However, this would require correspondingly long-term, consistent and accurate measurement time series on a global scale.

Currently, TCWV retrievals in the visible spectral range cannot yet meet the requirements in terms of accuracy and the necessary global long-term measurements are not yet available. Although the TCWV data set presented here is already of high quality, which has also been confirmed by extensive validation activities, there is still immense potential for improvement.

First of all, a reduction of the retrieval uncertainties would be beneficial. Here, a good starting point may be the choice of the H_2O absorption cross-section, as it is still unclear which H_2O line list for the calculation of the cross-sections is the most trustworthy. Likewise, a reduction of the uncertainties of the retrieval input parameters, especially of cloud information and surface albedo, is highly desirable. As both of these input parameters influence each other, consistent cloud-albedo retrievals are required. Another shortcoming of current TCWV satellite observations is their temporal coverage, which provides measurements only at the overpass time (typically once a day), though this mode of observation is best suited for trend studies. On a regional scale, geostationary satellites could solve this issue and the improved temporal resolution should also help to reduce sampling errors.

Regarding the TCWV retrieval presented in this thesis, another optimisation opportunity would be the further refinement of the parameterisation of the a priori water vapour profile shape. Currently, a simple exponential profile shape is assumed, for which the scale height is estimated by the measured TCWV and other influencing factors. This parameterisation works well over ocean, but has some weaknesses over land. Instead of this (relatively) simple parameterisation, a deep neural network could be trained with the COSMIC profile data and then either the scale height of the exponential profile or perhaps even directly the profile shape could be derived from the same input parameters as in the current retrieval setup. Similarly, further artifical intelligence approaches (such as convolutional neural networks) could be used to improve the retrieved TCWV distribution and might provide reliable results even in the case of high cloud fractions.

Provided that all these improvements are implemented, several satellite missions could be combined to produce a long-term data record. For this, it must be ensured that the combined data have been retrieved with a consistent TCWV algorithm. But this also means that the input data have to be derived from consistent algorithms as well. For the case of the cloud top height, retrieval algorithms that make use of the Ring effect or O_4 absorption might be suitable since these retrievals operate in the same spectral region as the presented TCWV retrieval.

Yet, so far, water vapour retrievals in the visible spectral range are only able to detect water vapour columns, i.e. the vertical integral of the water vapour profile, and hence focus on the (relatively) strong main H_2O absorption bands. Eventually, it might be possible to retrieve vertical information of water vapour as well. For NO_2, initial attempts of a profile inversion have already been addressed, although these are mainly based only on the wavelength dependence of the AMF (Richter and Burrows, 2000; Hilboll et al., 2014; Behrens et al., 2018). For water vapour, however, there are better preconditions: One idea might be to use the strong absorption bands above 500 nm in addition to the absorption band at 442 nm, as well as the weak absorption bands in between, even though currently the results of the weak bands are subject to large uncertainties. As long as the bands are spectrally far enough apart, the differences in radiative transfer could be utilised and the SCDs have slightly different sensitivities to different atmospheric layers. In this way, the SCDs of various weak and strong absorption bands could be combined to determine water vapour profiles by means of an optimal estimation approach. Thus, in contrast to the approaches for NO_2, this would exploit not only the wavelength dependence of the AMF but also the effect of the different absorption strengths of the various bands. However, this retrieval also requires that the corresponding satellite pixels for different wavelengths are collocated. First attempts of such a profile retrieval could thus possibly be tested on the measurements of the GOME, SCIAMACHY or the upcoming TEMPO mission.

All these optimisation approaches could help in the future to improve the observation of the water vapour distribution both on short time scales of a few hours up to longer time scales of several years. Here, the visible blue spectral range can make pioneering contributions, as it allows the creation of globally consistent data sets and its TCWV retrievals have a high sensitivity for the near-surface layers, where the highest water vapour concentrations occur.

As greenhouse gas concentrations continue to rise, near-surface air temperatures are expected to continue to increase, and consequently the corresponding water-holding capacities. As a result, there may soon be regions on Earth where life is no longer possible due to extreme atmospheric conditions and the limited human adaptability to heat stress (Sherwood and Huber, 2010). This highlights that the provision of accurate water vapour observations is not only essential for scientific questions of the past and present, but will be of even greater importance to the general public in a future warmer climate.

Bibliography

Adam, O., Grise, K. M., Staten, P., Simpson, I. R., Davis, S. M., Davis, N. A., Waugh, D. W., Birner, T., and Ming, A.: The TropD software package (v1): standardized methods for calculating tropical-width diagnostics, Geoscientific Model Development, 11, 4339–4357, https://doi.org/10.5194/gmd-11-4339-2018, 2018.

Allan, R. P., Soden, B. J., John, V. O., Ingram, W., and Good, P.: Current changes in tropical precipitation, Environmental Research Letters, 5, 025 205, https://doi.org/10.1088/1748-9326/5/2/025205, 2010.

Anand, J. S., Monks, P. S., and Leigh, R. J.: An improved retrieval of tropospheric NO_2 from space over polluted regions using an Earth radiance reference, Atmospheric Measurement Techniques, 8, 1519–1535, https://doi.org/10.5194/amt-8-1519-2015, 2015.

Anthes, R. A.: Exploring Earth's atmosphere with radio occultation: contributions to weather, climate and space weather, Atmospheric Measurement Techniques, 4, 1077–1103, https://doi.org/10.5194/amt-4-1077-2011, 2011.

Anthes, R. A., Bernhardt, P. A., Chen, Y., Cucurull, L., Dymond, K. F., Ector, D., Healy, S. B., Ho, S.-P., Hunt, D. C., Kuo, Y.-H., Liu, H., Manning, K., McCormick, C., Meehan, T. K., Randel, W. J., Rocken, C., Schreiner, W. S., Sokolovskiy, S. V., Syndergaard, S., Thompson, D. C., Trenberth, K. E., Wee, T.-K., Yen, N. L., and Zeng, Z.: The COSMIC/FORMOSAT-3 Mission: Early Results, Bulletin of the American Meteorological Society, 89, 313–334, https://doi.org/10.1175/BAMS-89-3-313, 2008.

Behrens, L. K., Hilboll, A., Richter, A., Peters, E., Eskes, H., and Burrows, J. P.: GOME-2A retrievals of tropospheric NO_2 in different spectral ranges – influence of penetration depth, Atmospheric Measurement Techniques, 11, 2769–2795, https://doi.org/10.5194/amt-11-2769-2018, 2018.

Beirle, S., Sihler, H., and Wagner, T.: Linearisation of the effects of spectral shift and stretch in DOAS analysis, Atmospheric Measurement Techniques, 6, 661–675, https://doi.org/10.5194/amt-6-661-2013, 2013.

Beirle, S., Lampel, J., Lerot, C., Sihler, H., and Wagner, T.: Parameterizing the instrumental spectral response function and its changes by a super-Gaussian and its derivatives, Atmospheric Measurement Techniques, 10, 581–598, https://doi.org/10.5194/amt-10-581-2017, 2017.

Beirle, S., Lampel, J., Wang, Y., Mies, K., Dörner, S., Grossi, M., Loyola, D., Dehn, A., Danielczok, A., Schröder, M., and Wagner, T.: The ESA GOME-Evolution "Climate" water vapor product: a homogenized time series of H_2O columns from GOME, SCIAMACHY, and GOME-2, Earth System Science Data, 10, 449–468, https://doi.org/10.5194/essd-10-449-2018, 2018.

Bengtsson, L.: The global atmospheric water cycle, Environmental Research Letters, 5, 025 202, https://doi.org/10.1088/1748-9326/5/2/025202, 2010.

Bengtsson, L., Hagemann, S., and Hodges, K. I.: Can climate trends be calculated from reanalysis data?, Journal of Geophysical Research: Atmospheres, 109, https://doi.org/10.1029/2004JD004536, 2004.

Benjamini, Y. and Hochberg, Y.: Controlling the False Discovery Rate: A Practical and Powerful Approach to Multiple Testing, Journal of the Royal Statistical Society: Series B (Methodological), 57, 289–300, https://doi.org/10.1111/j.2517-6161.1995.tb02031.x, 1995.

Bennartz, R. and Fischer, J.: Retrieval of columnar water vapour over land from backscattered solar radiation using the Medium Resolution Imaging Spectrometer, Remote Sensing of Environment, 78, 274–283, https://doi.org/10.1016/S0034-4257(01)00218-8, 2001.

Bevis, M., Businger, S., Herring, T. A., Rocken, C., Anthes, R. A., and Ware, R. H.: GPS meteorology: Remote sensing of atmospheric water vapor using the global positioning system, Journal of Geophysical Research: Atmospheres, 97, 15 787–15 801, https://doi.org/10.1029/92JD01517, 1992.

Bindoff, N., Stott, P., AchutaRao, K., Allen, M., Gillett, N., Gutzler, D., Hansingo, K., Hegerl, G., Hu, Y., Jain, S., Mokhov, I., Overland, J., Perlwitz, J., Sebbari, R., and Zhang, X.: Detection and Attribution of Climate Change: from Global to Regional, book section 10, pp. 867–952, Cambridge University Press, Cambridge, United Kingdom and New York, NY, USA, https://doi.org/10.1017/CBO9781107415324.022, 2013.

Birner, T.: Recent widening of the tropical belt from global tropopause statistics: Sensitivities, Journal of Geophysical Research: Atmospheres, 115, https://doi.org/10.1029/2010JD014664, 2010.

Boersma, K. F., Eskes, H. J., Richter, A., De Smedt, I., Lorente, A., Beirle, S., van Geffen, J. H. G. M., Zara, M., Peters, E., Van Roozendael, M., Wagner, T., Maasakkers, J. D., van der A, R. J., Nightingale, J., De Rudder, A., Irie, H., Pinardi, G., Lambert, J.-C., and Compernolle, S. C.: Improving algorithms and uncertainty estimates for satellite NO_2 retrievals: results from the quality assurance for the essential climate variables (QA4ECV) project, Atmospheric Measurement Techniques, 11, 6651–6678, https://doi.org/10.5194/amt-11-6651-2018, 2018.

Boggs, P. T., Boggs, P. T., Rogers, J. E., and Schnabel, R. B.: User's reference guide for odrpack version 2.01: Software for weighted orthogonal distance regression, techreport NISTIR 92-4834, U.S. Department of Commerce, https://nvlpubs.nist.gov/nistpubs/Legacy/IR/nistir4834.pdf, 1992.

Borger, C., Beirle, S., Dörner, S., Sihler, H., and Wagner, T.: Total column water vapour retrieval from S-5P/TROPOMI in the visible blue spectral range, Atmospheric Measurement Techniques, 13, 2751–2783, https://doi.org/10.5194/amt-13-2751-2020, 2020.

Borger, C., Beirle, S., and Wagner, T.: A 16-year global climate data record of total column water vapour generated from OMI observations in the visible blue spectral range, Earth System Science Data Discussions, 2021, 1–25, https://doi.org/10.5194/essd-2021-319, 2021.

Borger, C., Beirle, S., and Wagner, T.: Detecting the tropical expansion directly from satellite observations of water vapour, to be submitted, 2022a.

Borger, C., Beirle, S., and Wagner, T.: Analysis of global trends of total column water vapour from multiple years of OMI observations, Atmospheric Chemistry and Physics, 22, 10 603–10 621, https://doi.org/10.5194/acp-22-10603-2022, 2022b.

Bosilovich, M. G., Schubert, S. D., and Walker, G. K.: Global Changes of the Water Cycle Intensity, Journal of Climate, 18, 1591 – 1608, https://doi.org/10.1175/JCLI3357.1, 2005.

Bourdin, S., Kluft, L., and Stevens, B.: Dependence of Climate Sensitivity on the Given Distribution of Relative Humidity, Geophysical Research Letters, 48, e2021GL092 462, https://doi.org/10.1029/2021GL092462, e2021GL092462 2021GL092462, 2021.

Bovensmann, H., Burrows, J. P., Buchwitz, M., Frerick, J., Noël, S., Rozanov, V. V., Chance, K. V., and Goede, A. P. H.: SCIAMACHY: Mission Objectives and Measurement Modes, Journal of the Atmospheric Sciences, 56, 127 – 150, https://doi.org/10.1175/1520-0469(1999)056<0127:SMOAMM>2.0.CO;2, 1999.

Bretherton, C. S., Peters, M. E., and Back, L. E.: Relationships between Water Vapor Path and Precipitation over the Tropical Oceans, Journal of Climate, 17, 1517 – 1528, https://doi.org/10.1175/1520-0442(2004)017<1517:RBWVPA>2.0.CO;2, 2004.

Brogniez, H. and Pierrehumbert, R. T.: Intercomparison of tropical tropospheric humidity in GCMs with AMSU-B water vapor data, Geophysical Research Letters, 34, https://doi.org/10.1029/2006GL029118, 2007.

Burrows, J. P., Weber, M., Buchwitz, M., Rozanov, V., Ladstätter-WeiSSenmayer, A., Richter, A., DeBeek, R., Hoogen, R., Bramstedt, K., Eichmann, K.-U., Eisinger, M., and Perner, D.: The Global Ozone Monitoring Experiment (GOME): Mission Concept and First Scientific Results, Journal of the Atmospheric Sciences, 56, 151 – 175, https://doi.org/10.1175/1520-0469(1999)056<0151:TGOMEG>2.0.CO;2, 1999.

Byrne, M. P. and O'Gorman, P. A.: Trends in continental temperature and humidity directly linked to ocean warming, Proceedings of the National Academy of Sciences, 115, 4863–4868, https://doi.org/10.1073/pnas.1722312115, 2018.

Cahalan, R. F., Ridgway, W., Wiscombe, W. J., Bell, T. L., and Snider, J. B.: The Albedo of Fractal Stratocumulus Clouds, Journal of Atmospheric Sciences, 51, 2434 – 2455, https://doi.org/10.1175/1520-0469(1994)051<2434:TAOFSC>2.0.CO;2, 1994.

Cantrell, C. A.: Technical Note: Review of methods for linear least-squares fitting of data and application to atmospheric chemistry problems, Atmospheric Chemistry and Physics, 8, 5477–5487, https://doi.org/10.5194/acp-8-5477-2008, 2008.

Chahine, M. T.: The hydrological cycle and its influence on climate, Nature, 359, 373–380, https://doi.org/10.1038/359373a0, 1992.

Chambers, L. H., Wielicki, B. A., and Evans, K. F.: Accuracy of the independent pixel approximation for satellite estimates of oceanic boundary layer cloud optical depth, Journal of Geophysical Research: Atmospheres, 102, 1779–1794, https://doi.org/10.1029/96JD02995, 1997.

Chan, K. L., Valks, P., Slijkhuis, S., Köhler, C., and Loyola, D.: Total column water vapor retrieval for Global Ozone Monitoring Experience-2 (GOME-2) visible blue observations, Atmospheric Measurement Techniques, 13, 4169–4193, https://doi.org/10.5194/amt-13-4169-2020, 2020.

Cheng, L., Trenberth, K. E., Gruber, N., Abraham, J. P., Fasullo, J. T., Li, G., Mann, M. E., Zhao, X., and Zhu, J.: Improved Estimates of Changes in Upper Ocean Salinity and the

Hydrological Cycle, Journal of Climate, 33, 10 357 – 10 381, https://doi.org/10.1175/JCLI-D-20-0366.1, 2020.

Chiang, J. C. H. and Vimont, D. J.: Analogous Pacific and Atlantic Meridional Modes of Tropical AtmosphereOcean Variability, Journal of Climate, 17, 4143 – 4158, https://doi.org/10.1175/JCLI4953.1, 2004.

Chou, C., Neelin, J. D., Chen, C.-A., and Tu, J.-Y.: Evaluating the “rich-get-richer” mechanism in tropical precipitation change under global warming, Journal of Climate, 22, 1982–2005, https://doi.org/10.1175/2008JCLI2471.1, 2009.

Chou, C., Chiang, J. C. H., Lan, C.-W., Chung, C.-H., Liao, Y.-C., and Lee, C.-J.: Increase in the range between wet and dry season precipitation, Nature Geoscience, 6, 263–267, https://doi.org/10.1038/ngeo1744, 2013.

Collins, M., Knutti, R., Arblaster, J., Dufresne, J.-L., Fichefet, T., Friedlingstein, P., Gao, X., Gutowski, W., Johns, T., Krinner, G., Shongwe, M., Tebaldi, C., Weaver, A., and Wehner, M.: Long-term Climate Change: Projections, Commitments and Irreversibility, book section 12, pp. 1029–1136, Cambridge University Press, Cambridge, United Kingdom and New York, NY, USA, https://doi.org/10.1017/CBO9781107415324.024, 2013.

Dai, A.: Recent climatology, variability, and trends in global surface humidity, Journal of Climate, 19, 3589–3606, https://doi.org/10.1175/JCLI3816.1, 2006.

Danielson, J. J. and Gesch, D. B.: Global multi-resolution terrain elevation data 2010 (GMTED2010), Tech. rep., https://doi.org/10.3133/ofr20111073, report, 2011.

Danne, O., Falk, U., Preusker, R., Brockmann, C., Fischer, J., Hegglin, M., and Schröder, M.: ESA Water Vapour Climate Change Initiative (Water_Vapour_cci): Total Column Water Vapour monthly gridded data over land at 0.5 degree resolution, version 3.2, NERC EDS Centre for Environmental Data Analysis, https://doi.org/10.5285/4a85c0ef880e4f668cd4ec8e846855ef, 2022.

Davis, N. and Birner, T.: On the Discrepancies in Tropical Belt Expansion between Reanalyses and Climate Models and among Tropical Belt Width Metrics, Journal of Climate, 30, 1211 – 1231, https://doi.org/10.1175/JCLI-D-16-0371.1, 2017.

Davis, S. M. and Rosenlof, K. H.: A Multidiagnostic Intercomparison of Tropical-Width Time Series Using Reanalyses and Satellite Observations, Journal of Climate, 25, 1061 – 1078, https://doi.org/10.1175/JCLI-D-11-00127.1, 2012.

Dawson, A.: Windspharm: A High-Level Library for Global Wind Field Computations Using Spherical Harmonics, Journal of Open Research Software, 4, 2016.

Deutschmann, T., Beirle, S., Frieß, U., Grzegorski, M., Kern, C., Kritten, L., Platt, U., Prados-Román, C., Puķıte, J., Wagner, T., Werner, B., and Pfeilsticker, K.: The Monte Carlo atmospheric radiative transfer model McArtim: Introduction and validation of Jacobians and 3D features, Journal of Quantitative Spectroscopy and Radiative Transfer, 112, 1119–1137, https://doi.org/10.1016/j.jqsrt.2010.12.009, 2011.

Didan, K., Munoz, A. B., Solano, R., and Huete, A.: MODIS vegetation index user's guide (MOD13 series), Tech. rep., Vegetation Index and PhenologyLab, https://doi.org/10.5067/MODIS/MYD13C2.006, 2015.

Dirksen, R. J., Sommer, M., Immler, F. J., Hurst, D. F., Kivi, R., and Vömel, H.: Reference quality upper-air measurements: GRUAN data processing for the Vaisala RS92 radiosonde, Atmospheric Measurement Techniques, 7, 4463–4490, https://doi.org/10.5194/amt-7-4463-2014, 2014.

Douville, H., Chauvin, F., Planton, S., Royer, J.-F., Salas-Mélia, D., and Tyteca, S.: Sensitivity of the hydrological cycle to increasing amounts of greenhouse gases and aerosols, Climate Dynamics, 20, 45–68, https://doi.org/10.1007/s00382-002-0259-3, 2002.

Duan, J., Bevis, M., Fang, P., Bock, Y., Chiswell, S., Businger, S., Rocken, C., Solheim, F., van Hove, T., Ware, R., McClusky, S., Herring, T. A., and King, R. W.: GPS Meteorology: Direct Estimation of the Absolute Value of Precipitable Water, Journal of Applied Meteorology, 35, 830–838, https://doi.org/10.1175/1520-0450(1996)035<0830:GMDEOT>2.0.CO;2, 1996.

Dunn, R. J. H., Willett, K. M., Ciavarella, A., and Stott, P. A.: Comparison of land surface humidity between observations and CMIP5 models, Earth System Dynamics, 8, 719–747, https://doi.org/10.5194/esd-8-719-2017, 2017.

Dupuy, E., Morino, I., Deutscher, N. M., Yoshida, Y., Uchino, O., Connor, B. J., De Mazière, M., Griffith, D. W. T., Hase, F., Heikkinen, P., Hillyard, P. W., Iraci, L. T., Kawakami, S., Kivi, R., Matsunaga, T., Notholt, J., Petri, C., Podolske, J. R., Pollard, D. F., Rettinger, M., Roehl, C. M., Sherlock, V., Sussmann, R., Toon, G. C., Velazco, V. A., Warneke, T., Wennberg, P. O., Wunch, D., and Yokota, T.: Comparison of XH2O Retrieved from GOSAT Short-Wavelength Infrared Spectra with Observations from the TCCON Network, Remote Sensing, 8, https://doi.org/10.3390/rs8050414, 2016.

Durre, I., Vose, R. S., and Wuertz, D. B.: Overview of the Integrated Global Radiosonde Archive, Journal of Climate, 19, 53–68, https://doi.org/10.1175/JCLI3594.1, 2006.

Durre, I., Xungang, Y., Vose, R. S., Applequist, S., and Arnfield, J.: Integrated Global Radiosonde Archive (IGRA), Version 2, https://doi.org/10.7289/V5X63K0Q, 2016.

Durre, I., Yin, X., Vose, R. S., Applequist, S., and Arnfield, J.: Enhancing the Data Coverage in the Integrated Global Radiosonde Archive, Journal of Atmospheric and Oceanic Technology, 35, 1753–1770, https://doi.org/10.1175/JTECH-D-17-0223.1, 2018.

Emanuel, K. A., David Neelin, J., and Bretherton, C. S.: On large-scale circulations in convecting atmospheres, Quarterly Journal of the Royal Meteorological Society, 120, 1111–1143, https://doi.org/10.1002/qj.49712051902, 1994.

Eskes, H. J. and Boersma, K. F.: Averaging kernels for DOAS total-column satellite retrievals, Atmospheric Chemistry and Physics, 3, 1285–1291, https://doi.org/10.5194/acp-3-1285-2003, 2003.

Fang, P., Bevis, M., Bock, Y., Gutman, S., and Wolfe, D.: GPS meteorology: Reducing systematic errors in geodetic estimates for zenith delay, Geophysical Research Letters, 25, 3583–3586, https://doi.org/10.1029/98GL02755, 1998.

Fasullo, J.: A mechanism for land–ocean contrasts in global monsoon trends in a warming climate, Climate Dynamics, 39, 1137–1147, https://doi.org/10.1007/s00382-011-1270-3, 2012.

Feng, S. and Fu, Q.: Expansion of global drylands under a warming climate, Atmospheric Chemistry and Physics, 13, 10 081–10 094, https://doi.org/10.5194/acp-13-10081-2013, 2013.

Fennig, K., Schröder, M., Andersson, A., and Hollmann, R.: A Fundamental Climate Data Record of SMMR, SSM/I, and SSMIS brightness temperatures, Earth System Science Data, 12, 647–681, https://doi.org/10.5194/essd-12-647-2020, 2020.

Foster, G. and Rahmstorf, S.: Global temperature evolution 1979–2010, Environmental Research Letters, 6, 044 022, https://doi.org/10.1088/1748-9326/6/4/044022, 2011.

Gaffen, D. J. and Elliott, W. P.: Column Water Vapor Content in Clear and Cloudy Skies, Journal of Climate, 6, 2278 – 2287, https://doi.org/10.1175/1520-0442(1993)006<2278:CWVCIC>2.0.CO;2, 1993.

Gao, B.-C. and Kaufman, Y. J.: Water vapor retrievals using Moderate Resolution Imaging Spectroradiometer (MODIS) near-infrared channels, Journal of Geophysical Research: Atmospheres, 108, https://doi.org/10.1029/2002JD003023, 2003.

Gimeno, L., Eiras-Barca, J., Durán-Quesada, A. M., Dominguez, F., van der Ent, R., Sodemann, H., Sánchez-Murillo, R., Nieto, R., and Kirchner, J. W.: The residence time of water vapour in the atmosphere, Nature Reviews Earth & Environment, 2, 558–569, https://doi.org/10.1038/s43017-021-00181-9, 2021.

Gleisner, H., Lauritsen, K. B., Nielsen, J. K., and Syndergaard, S.: Evaluation of the 15-year ROM SAF monthly mean GPS radio occultation climate data record, Atmospheric Measurement Techniques, 13, 3081–3098, https://doi.org/10.5194/amt-13-3081-2020, 2020.

Gordon, I., Rothman, L., Hill, C., Kochanov, R., Tan, Y., Bernath, P., Birk, M., Boudon, V., Campargue, A., Chance, K., Drouin, B., Flaud, J.-M., Gamache, R., Hodges, J., Jacquemart, D., Perevalov, V., Perrin, A., Shine, K., Smith, M.-A., Tennyson, J., Toon, G., Tran, H., Tyuterev, V., Barbe, A., Császár, A., Devi, V., Furtenbacher, T., Harrison, J., Hartmann, J.-M., Jolly, A., Johnson, T., Karman, T., Kleiner, I., Kyuberis, A., Loos, J., Lyulin, O., Massie, S., Mikhailenko, S., Moazzen-Ahmadi, N., Müller, H., Naumenko, O., Nikitin, A., Polyansky, O., Rey, M., Rotger, M., Sharpe, S., Sung, K., Starikova, E., Tashkun, S., Auwera, J. V., Wagner, G., Wilzewski, J., Wciso, P., Yu, S., and Zak, E.: The HITRAN2016 molecular spectroscopic database, Journal of Quantitative Spectroscopy and Radiative Transfer, 203, 3 – 69, https://doi.org/10.1016/j.jqsrt.2017.06.038, hITRAN2016 Special Issue, 2017.

Gordon, I., Rothman, L., Hargreaves, R., Hashemi, R., Karlovets, E., Skinner, F., Conway, E., Hill, C., Kochanov, R., Tan, Y., Wcislo, P., Finenko, A., Nelson, K., Bernath, P., Birk, M., Boudon, V., Campargue, A., Chance, K., Coustenis, A., Drouin, B., Flaud, J.-M., Gamache, R., Hodges, J., Jacquemart, D., Mlawer, E., Nikitin, A., Perevalov, V., Rotger, M., Tennyson, J., Toon, G., Tran, H., Tyuterev, V., Adkins, E., Baker, A., Barbe, A., Canè, E., Császár, A., Dudaryonok, A., Egorov, O., Fleisher, A., Fleurbaey, H., Foltynowicz, A., Furtenbacher, T., Harrison, J., Hartmann, J.-M., Horneman, V.-M., Huang, X., Karman, T., Karns, J., Kassi, S., Kleiner, I., Kofman, V., Kwabia-Tchana, F., Lavrentieva, N., Lee, T., Long, D., Lukashevskaya, A., Lyulin, O., Makhnev, V., Matt, W., Massie, S., Melosso, M., Mikhailenko, S., Mondelain, D., Müller, H., Naumenko, O., Perrin, A., Polyansky, O., Raddaoui, E., Raston, P., Reed, Z., Rey, M., Richard, C., Tóbiás, R., Sadiek, I., Schwenke, D., Starikova, E., Sung, K., Tamassia, F., Tashkun, S., Vander Auwera, J., Vasilenko, I., Vigasin, A., Villanueva, G., Vispoel, B., Wagner, G., Yachmenev, A., and Yurchenko, S.: The HITRAN2020 molecular spectroscopic database, Journal of Quantitative Spectroscopy and Radiative Transfer, 277, 107 949, https://doi.org/10.1016/j.jqsrt.2021.107949, 2022.

Grainger, J. F. and Ring, J.: Anomalous Fraunhofer Line Profiles, Nature, 193, 762–762, https://doi.org/10.1038/193762a0, 1962.

Greve, P., Orlowsky, B., Mueller, B., Sheffield, J., Reichstein, M., and Seneviratne, S. I.: Global assessment of trends in wetting and drying over land, Nature Geoscience, 7, 716–721, https://doi.org/10.1038/ngeo2247, 2014.

Grossi, M., Valks, P., Loyola, D., Aberle, B., Slijkhuis, S., Wagner, T., Beirle, S., and Lang, R.: Total column water vapour measurements from GOME-2 MetOp-A and MetOp-B, Atmospheric Measurement Techniques, 8, 1111–1133, https://doi.org/10.5194/amt-8-1111-2015, 2015.

Hadley, G.: VI. Concerning the cause of the general trade-winds, Philosophical Transactions of the Royal Society of London, 39, 58–62, https://doi.org/10.1098/rstl.1735.0014, 1735.

Hajj, G., Kursinski, E., Romans, L., Bertiger, W., and Leroy, S.: A technical description of atmospheric sounding by GPS occultation, Journal of Atmospheric and Solar-Terrestrial Physics, 64, 451 – 469, https://doi.org/10.1016/S1364-6826(01)00114-6, 2002.

Hartmann, D., KleinăTank, A., Rusticucci, M., Alexander, L., Brönnimann, S., Charabi, Y., Dentener, F., Dlugokencky, E., Easterling, D., Kaplan, A., Soden, B., Thorne, P., Wild, M., and Zhai, P.: Observations: Atmosphere and Surface, book section 2, pp. 159–254, Cambridge University Press, Cambridge, United Kingdom and New York, NY, USA, https://doi.org/10.1017/CBO9781107415324.008, 2013.

Heise, S., Wickert, J., Beyerle, G., Schmidt, T., and Reigber, C.: Global monitoring of tropospheric water vapor with GPS radio occultation aboard CHAMP, Advances in Space Research, 37, 2222 – 2227, https://doi.org/10.1016/j.asr.2005.06.066, atmospheric Remote Sensing: Earth's Surface, Troposphere, Stratosphere and Mesosphere - II, 2006.

Held, I. M. and Hou, A. Y.: Nonlinear Axially Symmetric Circulations in a Nearly Inviscid Atmosphere, Journal of Atmospheric Sciences, 37, 515 – 533, https://doi.org/10.1175/1520-0469(1980)037<0515:NASCIA>2.0.CO;2, 1980.

Held, I. M. and Soden, B. J.: Water Vapor Feedback and Global Warming, Annual Review of Energy and the Environment, 25, 441–475, https://doi.org/10.1146/annurev.energy.25.1.441, 2000.

Held, I. M. and Soden, B. J.: Robust Responses of the Hydrological Cycle to Global Warming, Journal of Climate, 19, 5686 – 5699, https://doi.org/10.1175/JCLI3990.1, 2006.

Hersbach, H., Bell, B., Berrisford, P., Biavati, G., Horányi, A., Muñoz Sabater, J., Nicolas, J., Peubey, C., Radu, R., Rozum, I., Schepers, D., Simmons, A., Soci, C., Dee, D., and Thépaut, J.-N.: ERA5 hourly data on pressure levels from 1959 to present, Copernicus Climate Change Service (C3S) Climate Data Store (CDS), https://doi.org/10.24381/cds.bd0915c6, (Accessed on 2022-08-09), 2018a.

Hersbach, H., Bell, B., Berrisford, P., Biavati, G., Horányi, A., Muñoz Sabater, J., Nicolas, J., Peubey, C., Radu, R., Rozum, I., Schepers, D., Simmons, A., Soci, C., Dee, D., and Thépaut, J.-N.: ERA5 hourly data on single levels from 1959 to present, Copernicus Climate Change

Service (C3S) Climate Data Store (CDS), https://doi.org/10.24381/cds.adbb2d47, (Accessed on 2022-08-09), 2018b.

Hersbach, H., Bell, B., Berrisford, P., Biavati, G., Horányi, A., Muñoz Sabater, J., Nicolas, J., Peubey, C., Radu, R., Rozum, I., Schepers, D., Simmons, A., Soci, C., Dee, D., and Thépaut, J.-N.: ERA5 monthly averaged data on single levels from 1979 to present, Copernicus Climate Change Service (C3S) Climate Data Store (CDS), https://doi.org/10.24381/cds.f17050d7, (Accessed on: 2021-07-01), 2019.

Hersbach, H., Bell, B., Berrisford, P., Hirahara, S., Horányi, A., Muñoz-Sabater, J., Nicolas, J., Peubey, C., Radu, R., Schepers, D., Simmons, A., Soci, C., Abdalla, S., Abellan, X., Balsamo, G., Bechtold, P., Biavati, G., Bidlot, J., Bonavita, M., De Chiara, G., Dahlgren, P., Dee, D., Diamantakis, M., Dragani, R., Flemming, J., Forbes, R., Fuentes, M., Geer, A., Haimberger, L., Healy, S., Hogan, R. J., Hólm, E., Janisková, M., Keeley, S., Laloyaux, P., Lopez, P., Lupu, C., Radnoti, G., de Rosnay, P., Rozum, I., Vamborg, F., Villaume, S., and Thépaut, J.-N.: The ERA5 global reanalysis, Quarterly Journal of the Royal Meteorological Society, 146, 1999–2049, https://doi.org/10.1002/qj.3803, 2020.

Hilboll, A., Richter, A., and Burrows, J. P.: Vertical information content of nadir measurements of tropospheric NO2 from satellite, https://doi.org/10.5281/zenodo.8746, 2014.

Ho, S.-p., Kuo, Y.-H., Schreiner, W., and Zhou, X.: Using SI-traceable global positioning system radio occultation measurements for climate monitoring [In" State of the Climate in 2009"], Bulletin of the American Meteorological Society, 91, S36–S37, https://doi.org/10.1175/BAMS-91-7-StateoftheClimate, 2010a.

Ho, S.-p., Zhou, X., Kuo, Y.-H., Hunt, D., and Wang, J.-h.: Global Evaluation of Radiosonde Water Vapor Systematic Biases using GPS Radio Occultation from COSMIC and ECMWF Analysis, Remote Sensing, 2, 1320–1330, https://doi.org/10.3390/rs2051320, 2010b.

Hodnebrog, Ø., Myhre, G., Samset, B. H., Alterskjær, K., Andrews, T., Boucher, O., Faluvegi, G., Fläschner, D., Forster, P. M., Kasoar, M., Kirkevåg, A., Lamarque, J.-F., Olivié, D., Richardson, T. B., Shawki, D., Shindell, D., Shine, K. P., Stier, P., Takemura, T., Voulgarakis, A., and Watson-Parris, D.: Water vapour adjustments and responses differ between climate drivers, Atmospheric Chemistry and Physics, 19, 12 887–12 899, https://doi.org/10.5194/acp-19-12887-2019, 2019.

Hu, Y., Huang, H., and Zhou, C.: Widening and weakening of the Hadley circulation under global warming, Science Bulletin, 63, 640–644, https://doi.org/10.1016/j.scib.2018.04.020, 2018.

Huffman, G., Behrangi, A., Bolvin, D., and Nelkin, E.: GPCP Version 3.1 Satellite-Gauge (SG) Combined Precipitation Data Set, NASA GES DISC, https://doi.org/10.5067/DBVUO4KQHXTK, 2020.

Ingmann, P., Veihelmann, B., Langen, J., Lamarre, D., Stark, H., and Courrèges-Lacoste, G. B.: Requirements for the GMES Atmosphere Service and ESA's implementation concept: Sentinels-4/-5 and -5p, Remote Sensing of Environment, 120, 58–69, https://doi.org/10.1016/j.rse.2012.01.023, the Sentinel Missions - New Opportunities for Science, 2012.

Joiner, J., Bhartia, P. K., Cebula, R. P., Hilsenrath, E., McPeters, R. D., and Park, H.: Rotational Raman scattering (Ring effect) in satellite backscatter ultraviolet measurements, Applied Optics, 34, 4513–4525, https://doi.org/10.1364/AO.34.004513, 1995.

Kämpfer, N.: Monitoring Atmospheric Water Vapour: Ground-Based Remote Sensing and In-situ Methods, vol. 10 of *ISSI Scientific Report Series*, Springer Science & Business Media, New York, NY, 1 edn., https://doi.org/10.1007/978-1-4614-3909-7, 2012.

Kao, A., Jiang, X., Li, L., Trammell, J. H., Zhang, G. J., Su, H., Jiang, J. H., and Yung, Y. L.: A Comparative Study of Atmospheric Moisture Recycling Rate between Observations and Models, Journal of Climate, 31, 2389–2398, https://doi.org/10.1175/JCLI-D-17-0421.1, 2018.

Keyser, D., Schmidt, B. D., and Duffy, D. G.: A Technique for Representing Three-Dimensional Vertical Circulations in Baroclinic Disturbances, Monthly Weather Review, 117, 2463 – 2494, https://doi.org/10.1175/1520-0493(1989)117<2463:ATFRTD>2.0.CO;2, 1989.

Kiehl, J. T. and Trenberth, K. E.: Earth’s Annual Global Mean Energy Budget., Bulletin of the American Meteorological Society, 78, 197–197, https://doi.org/10.1175/1520-0477(1997)078<0197:EAGMEB>2.0.CO;2, 1997.

Kim, J., Jeong, U., Ahn, M.-H., Kim, J. H., Park, R. J., Lee, H., Song, C. H., Choi, Y.-S., Lee, K.-H., Yoo, J.-M., Jeong, M.-J., Park, S. K., Lee, K.-M., Song, C.-K., Kim, S.-W., Kim, Y. J., Kim, S.-W., Kim, M., Go, S., Liu, X., Chance, K., Miller, C. C., Al-Saadi, J., Veihelmann, B., Bhartia, P. K., Torres, O., Abad, G. G., Haffner, D. P., Ko, D. H., Lee, S. H., Woo, J.-H., Chong, H., Park, S. S., Nicks, D., Choi, W. J., Moon, K.-J., Cho, A., Yoon, J., kyun Kim, S., Hong, H., Lee, K., Lee, H., Lee, S., Choi, M., Veefkind, P., Levelt, P. F., Edwards, D. P., Kang, M., Eo, M., Bak, J., Baek, K., Kwon, H.-A., Yang, J., Park, J., Han, K. M., Kim, B.-R., Shin, H.-W., Choi, H., Lee, E., Chong, J., Cha, Y., Koo, J.-H., Irie, H., Hayashida, S., Kasai, Y., Kanaya, Y., Liu, C., Lin, J., Crawford, J. H., Carmichael, G. R., Newchurch, M. J., Lefer, B. L., Herman, J. R., Swap, R. J., Lau, A. K. H., Kurosu, T. P., Jaross, G., Ahlers, B., Dobber, M., McElroy, C. T., and Choi, Y.: New Era of Air Quality Monitoring from Space: Geostationary Environment Monitoring Spectrometer (GEMS), Bulletin of the American Meteorological Society, 101, E1–E22, https://doi.org/10.1175/BAMS-D-18-0013.1, 2020.

Kirtman, B., Power, S., Adedoyin, J., Boer, G., Bojariu, R., Camilloni, I., Doblas-Reyes, F., Fiore, A., Kimoto, M., Meehl, G., Prather, M., Sarr, A., Schär, C., Sutton, R., van Oldenborgh, G., Vecchi, G., and Wang, H.: Near-term Climate Change: Projections and Predictability, book section 11, pp. 953–1028, Cambridge University Press, Cambridge, United Kingdom and New York, NY, USA, https://doi.org/10.1017/CBO9781107415324.023, 2013.

Kleipool, Q. L., Dobber, M. R., de Haan, J. F., and Levelt, P. F.: Earth surface reflectance climatology from 3 years of OMI data, Journal of Geophysical Research: Atmospheres, 113, https://doi.org/10.1029/2008JD010290, 2008.

Koelemeijer, R. B. A., de Haan, J. F., and Stammes, P.: A database of spectral surface reflectivity in the range 335–772 nm derived from 5.5 years of GOME observations, Journal of Geophysical Research: Atmospheres, 108, https://doi.org/10.1029/2002JD002429, 2003.

Kreher, K., Van Roozendael, M., Hendrick, F., Apituley, A., Dimitropoulou, E., Frieß, U., Richter, A., Wagner, T., Lampel, J., Abuhassan, N., Ang, L., Anguas, M., Bais, A., Benavent, N., Bösch, T., Bognar, K., Borovski, A., Bruchkouski, I., Cede, A., Chan, K. L., Donner, S., Drosoglou, T., Fayt, C., Finkenzeller, H., Garcia-Nieto, D., Gielen, C., Gómez-Martín, L., Hao, N., Henzing, B., Herman, J. R., Hermans, C., Hoque, S., Irie, H., Jin, J., Johnston, P., Khayyam Butt, J., Khokhar, F., Koenig, T. K., Kuhn, J., Kumar, V., Liu, C., Ma, J., Merlaud, A., Mishra, A. K., Müller, M., Navarro-Comas, M., Ostendorf, M., Pazmino, A., Peters, E., Pinardi, G., Pinharanda, M., Piters, A., Platt, U., Postylyakov, O., Prados-Roman, C., Puentedura, O., Querel, R., Saiz-Lopez, A., Schönhardt, A., Schreier, S. F., Seyler, A., Sinha, V., Spinei, E., Strong, K., Tack, F., Tian, X., Tiefengraber, M., Tirpitz, J.-L., van Gent, J., Volkamer, R., Vrekoussis, M., Wang, S., Wang, Z., Wenig, M., Wittrock, F., Xie, P. H., Xu, J., Yela, M., Zhang, C., and Zhao, X.: Intercomparison of NO_2, O_4, O_3 and HCHO slant column measurements by MAX-DOAS and zenith-sky UV–visible spectrometers during CINDI-2, Atmospheric Measurement Techniques, 13, 2169–2208, https://doi.org/10.5194/amt-13-2169-2020, 2020.

Kursinski, E. R., Hajj, G. A., Schofield, J. T., Linfield, R. P., and Hardy, K. R.: Observing Earth's atmosphere with radio occultation measurements using the Global Positioning System, Journal of Geophysical Research: Atmospheres, 102, 23 429–23 465, https://doi.org/10.1029/97JD01569, 1997.

Kurucz, R. L., Furenlid, I., Brault, J., and Testerman, L.: Solar flux atlas from 296 to 1300 nm, National Solar Observatory Atlas, US. National Solar Observatory, Sunspot, NM, 1984.

Läderach, A. and Sodemann, H.: A revised picture of the atmospheric moisture residence time, Geophysical Research Letters, 43, 924–933, https://doi.org/10.1002/2015GL067449, 2016.

Lampel, J., Pöhler, D., Tschritter, J., Frieß, U., and Platt, U.: On the relative absorption strengths of water vapour in the blue wavelength range, Atmospheric Measurement Techniques, 8, 4329–4346, https://doi.org/10.5194/amt-8-4329-2015, 2015.

Lamsal, L. N., Krotkov, N. A., Vasilkov, A., Marchenko, S., Qin, W., Yang, E.-S., Fasnacht, Z., Joiner, J., Choi, S., Haffner, D., Swartz, W. H., Fisher, B., and Bucsela, E.: Ozone Monitoring Instrument (OMI) Aura nitrogen dioxide standard product version 4.0 with improved surface and cloud treatments, Atmospheric Measurement Techniques, 14, 455–479, https://doi.org/10.5194/amt-14-455-2021, 2021.

Lang, R., Williams, J. E., van der Zande, W. J., and Maurellis, A. N.: Application of the Spectral Structure Parameterization technique: retrieval of total water vapor columns from GOME, Atmospheric Chemistry and Physics, 3, 145–160, https://doi.org/10.5194/acp-3-145-2003, 2003.

Lang, R., Casadio, S., Maurellis, A. N., and Lawrence, M. G.: Evaluation of the GOME Water Vapor Climatology 1995–2002, Journal of Geophysical Research: Atmospheres, 112, https://doi.org/10.1029/2006JD008246, 2007.

Levelt, P. F., van den Oord, G. H., Dobber, M. R., Malkki, A., Visser, H., de Vries, J., Stammes, P., Lundell, J. O., and Saari, H.: The ozone monitoring instrument, IEEE Transactions on Geoscience and Remote Sensing, 44, 1093–1101, https://doi.org/10.1109/TGRS.2006.872333, 2006.

Levelt, P. F., Joiner, J., Tamminen, J., Veefkind, J. P., Bhartia, P. K., Stein Zweers, D. C., Duncan, B. N., Streets, D. G., Eskes, H., van der A, R., McLinden, C., Fioletov, V., Carn, S., de Laat, J., DeLand, M., Marchenko, S., McPeters, R., Ziemke, J., Fu, D., Liu, X., Pickering, K., Apituley, A., González Abad, G., Arola, A., Boersma, F., Chan Miller, C., Chance, K., de Graaf, M., Hakkarainen, J., Hassinen, S., Ialongo, I., Kleipool, Q., Krotkov, N., Li, C., Lamsal, L., Newman, P., Nowlan, C., Suleiman, R., Tilstra, L. G., Torres, O., Wang, H., and Wargan, K.: The Ozone Monitoring Instrument: overview of 14 years in space, Atmospheric Chemistry and Physics, 18, 5699–5745, https://doi.org/10.5194/acp-18-5699-2018, 2018.

Li, J., Wang, P., Han, H., Li, J., and Zheng, J.: On the assimilation of satellite sounder data in cloudy skies in numerical weather prediction models, Journal of Meteorological Research, 30, 169–182, https://doi.org/10.1007/s13351-016-5114-2, 2016.

Li, L., Jiang, X., Chahine, M. T., Olsen, E. T., Fetzer, E. J., Chen, L., and Yung, Y. L.: The recycling rate of atmospheric moisture over the past two decades (1988–2009), Environmental Research Letters, 6, 034 018, https://doi.org/10.1088/1748-9326/6/3/034018, 2011.

Livezey, R. E. and Chen, W. Y.: Statistical Field Significance and its Determination by Monte Carlo Techniques, Monthly Weather Review, 111, 46–59, https://doi.org/10.1175/1520-0493(1983)111<0046:SFSAID>2.0.CO;2, 1983.

Lu, J., Vecchi, G. A., and Reichler, T.: Expansion of the Hadley cell under global warming, Geophysical Research Letters, 34, https://doi.org/10.1029/2006GL028443, 2007.

Lucas, C., Timbal, B., and Nguyen, H.: The expanding tropics: a critical assessment of the observational and modeling studies, WIREs Climate Change, 5, 89–112, https://doi.org/10.1002/wcc.251, 2014.

Manabe, S. and Wetherald, R. T.: Thermal Equilibrium of the Atmosphere with a Given Distribution of Relative Humidity, Journal of Atmospheric Sciences, 24, 241 – 259, https://doi.org/10.1175/1520-0469(1967)024<0241:TEOTAW>2.0.CO;2, 1967.

Mantua, N. J., Hare, S. R., Zhang, Y., Wallace, J. M., and Francis, R. C.: A Pacific Interdecadal Climate Oscillation with Impacts on Salmon Production, Bulletin of the American Meteorological Society, 78, 1069 – 1080, https://doi.org/10.1175/1520-0477(1997)078<1069:APICOW>2.0.CO;2, 1997.

Markowski, P. and Richardson, Y.: Mesoscale Meteorology in Midlatitudes, John Wiley and Sons, https://doi.org/10.1002/9780470682104, 2010.

Martin, R. V., Chance, K., Jacob, D. J., Kurosu, T. P., Spurr, R. J. D., Bucsela, E., Gleason, J. F., Palmer, P. I., Bey, I., Fiore, A. M., Li, Q., Yantosca, R. M., and Koelemeijer, R. B. A.: An improved retrieval of tropospheric nitrogen dioxide from GOME, Journal of Geophysical Research: Atmospheres, 107, ACH 9–1–ACH 9–21, https://doi.org/10.1029/2001JD001027, 2002.

Mears, C. A., Wang, J., Smith, D., and Wentz, F. J.: Intercomparison of total precipitable water measurements made by satellite-borne microwave radiometers and ground-based GPS instruments, Journal of Geophysical Research: Atmospheres, 120, 2492–2504, https://doi.org/10.1002/2014JD022694, 2015.

Mieruch, S., Noël, S., Bovensmann, H., and Burrows, J. P.: Analysis of global water vapour trends from satellite measurements in the visible spectral range, Atmospheric Chemistry and Physics, 8, 491–504, https://doi.org/10.5194/acp-8-491-2008, 2008.

Mudelsee, M.: Climate Time Series Analysis: Classical Statistical and Bootstrap Methods, Atmospheric and Oceanographic Sciences Library, Springer International Publishing, https://doi.org/10.1007/978-3-319-04450-7, 2014.

Munro, R., Lang, R., Klaes, D., Poli, G., Retscher, C., Lindstrot, R., Huckle, R., Lacan, A., Grzegorski, M., Holdak, A., Kokhanovsky, A., Livschitz, J., and Eisinger, M.: The GOME-2 instrument on the Metop series of satellites: instrument design, calibration, and level 1 data processing – an overview, Atmospheric Measurement Techniques, 9, 1279–1301, https://doi.org/10.5194/amt-9-1279-2016, 2016.

Nguyen, H., Hendon, H. H., Lim, E.-P., Boschat, G., Maloney, E., and Timbal, B.: Variability of the extent of the Hadley circulation in the southern hemisphere: a regional perspective, Climate Dynamics, 50, 129–142, https://doi.org/10.1007/s00382-017-3592-2, 2018.

Nielsen, J., Gleisner, H., and Lauritsen, K.: Validation Report: Reprocessed Level 2B and 2C 1D-Var products, Tech. Rep. SAF/ROM/DMI/REP/1DVAR/001, ROMSAF, https://www.romsaf.org/product_documents.php, product version 1.0, 2018.

Noël, S., Buchwitz, M., Bovensmann, H., Hoogen, R., and Burrows, J. P.: Atmospheric water vapor amounts retrieved from GOME satellite data, Geophysical Research Letters, 26, 1841–1844, https://doi.org/10.1029/1999GL900437, 1999.

Noël, S., Buchwitz, M., and Burrows, J. P.: First retrieval of global water vapour column amounts from SCIAMACHY measurements, Atmospheric Chemistry and Physics, 4, 111–125, https://doi.org/10.5194/acp-4-111-2004, 2004.

Palmer, P. I., Jacob, D. J., Chance, K., Martin, R. V., Spurr, R. J. D., Kurosu, T. P., Bey, I., Yantosca, R., Fiore, A., and Li, Q.: Air mass factor formulation for spectroscopic measurements from satellites: Application to formaldehyde retrievals from the Global Ozone Monitoring Experiment, Journal of Geophysical Research: Atmospheres, 106, 14 539–14 550, https://doi.org/10.1029/2000JD900772, 2001.

Peixoto, J. and Oort, A.: Physics of Climate, American Institute of Physics, 1 edn., https://link.springer.com/book/9780883187128, 1992.

Platt, U. and Stutz, J.: Differential Optical Absorption Spectroscopy: Principles and Applications, Physics of Earth and Space Environments, Springer Berlin Heidelberg, https://doi.org/10.1007/978-3-540-75776-4, 2008.

Prais, S. J. and Winsten, C. B.: Trend Estimators and Serial Correlation, Cowles Commission Discussion Paper, 383, https://cowles.yale.edu/sites/default/files/files/pub/cdp/s-0383.pdf, 1954.

Prat, O. P., Nelson, B. R., Nickl, E., and Leeper, R. D.: Global Evaluation of Gridded Satellite Precipitation Products from the NOAA Climate Data Record Program, Journal of Hydrometeorology, 22, 2291 – 2310, https://doi.org/10.1175/JHM-D-20-0246.1, 2021.

Pruppacher, H. R. and Klett, J. D.: Microphysics of Clouds and Precipitation, vol. 18 of *Atmospheric and Oceanographic Sciences Library*, Springer Dordrecht, 2 edn., https://doi.org/10.1007/978-0-306-48100-0, 2010.

Randall, D. A., Wood, R. A., Bony, S., Colman, R., Fichefet, T., Fyfe, J., Kattsov, V., Pitman, A., Shukla, J., Srinivasan, J., Stouffer, R. J., Sumi, A., and Taylor, K. E.: Climate models and their evaluation, in: Climate change 2007: The physical science basis. Contribution of Working Group I to the Fourth Assessment Report of the IPCC (FAR), edited by Solomon, S., Qin, D., Manning, M., Chen, Z., Marquis, M., Averyt, K., Tignor, M., and Miller, H. L., pp. 589–662, Cambridge University Press, 2007.

Rehfeld, K., Marwan, N., Heitzig, J., and Kurths, J.: Comparison of correlation analysis techniques for irregularly sampled time series, Nonlinear Processes in Geophysics, 18, 389–404, https://doi.org/10.5194/npg-18-389-2011, 2011.

Richter, A. and Burrows, J.: A multi wavelength approach to the retrieval of tropospheric NO_2 from GOME measurements, https://www.iup.uni-bremen.de/doas/paper/esa_00_richter.pdf, 2000.

Rohde, R. A. and Hausfather, Z.: The Berkeley Earth Land/Ocean Temperature Record, Earth System Science Data, 12, 3469–3479, https://doi.org/10.5194/essd-12-3469-2020, 2020.

Rosenkranz, P. W.: Retrieval of temperature and moisture profiles from AMSU-A and AMSU-B measurements, IEEE Transactions on Geoscience and Remote Sensing, 39, 2429–2435, https://doi.org/10.1109/36.964979, 2001.

Rothman, L., Gordon, I., Barbe, A., Benner, D., Bernath, P., Birk, M., Boudon, V., Brown, L., Campargue, A., Champion, J.-P., Chance, K., Coudert, L., Dana, V., Devi, V., Fally, S., Flaud, J.-M., Gamache, R., Goldman, A., Jacquemart, D., Kleiner, I., Lacome, N., Lafferty, W., Mandin, J.-Y., Massie, S., Mikhailenko, S., Miller, C., Moazzen-Ahmadi, N., Naumenko, O., Nikitin, A., Orphal, J., Perevalov, V., Perrin, A., Predoi-Cross, A., Rinsland, C., Rotger, M., imeková, M., Smith, M., Sung, K., Tashkun, S., Tennyson, J., Toth, R., Vandaele, A., and Vander Auwera, J.: The HITRAN 2008 molecular spectroscopic database, Journal of Quantitative Spectroscopy and Radiative Transfer, 110, 533 – 572, https://doi.org/10.1016/j.jqsrt.2009.02.013, HITRAN, 2009.

Rothman, L., Gordon, I., Babikov, Y., Barbe, A., Benner, D. C., Bernath, P., Birk, M., Bizzocchi, L., Boudon, V., Brown, L., Campargue, A., Chance, K., Cohen, E., Coudert, L., Devi, V., Drouin, B., Fayt, A., Flaud, J.-M., Gamache, R., Harrison, J., Hartmann, J.-M., Hill, C., Hodges, J., Jacquemart, D., Jolly, A., Lamouroux, J., Roy, R. L., Li, G., Long, D., Lyulin, O., Mackie, C., Massie, S., Mikhailenko, S., Müller, H., Naumenko, O., Nikitin, A., Orphal, J., Perevalov, V., Perrin, A., Polovtseva, E., Richard, C., Smith, M., Starikova, E., Sung, K., Tashkun, S., Tennyson, J., Toon, G., Tyuterev, V., and Wagner, G.: The HITRAN2012 molecular spectroscopic database, Journal of Quantitative Spectroscopy and Radiative Transfer, 130, 4 – 50, https://doi.org/10.1016/j.jqsrt.2013.07.002, HITRAN2012 special issue, 2013.

Rozemeijer, N. and Kleipool, Q.: S5P Mission Performance Centre Level 1b Readme, Tech. Rep. S5P-MPC-KNMI-PRF-L1B, https://sentinel.esa.int/documents/247904/3541451/Sentinel-5P-Level-1b-Product-Readme-File, product version V01.00.00, 2019.

Rushley, S. S., Kim, D., Bretherton, C. S., and Ahn, M.-S.: Reexamining the Nonlinear Moisture-Precipitation Relationship Over the Tropical Oceans, Geophysical Research Letters, 45, 1133–1140, https://doi.org/10.1002/2017GL076296, 2018.

Scheff, J. and Frierson, D. M. W.: Robust future precipitation declines in CMIP5 largely reflect the poleward expansion of model subtropical dry zones, Geophysical Research Letters, 39, https://doi.org/10.1029/2012GL052910, 2012.

Schenkeveld, V. M. E., Jaross, G., Marchenko, S., Haffner, D., Kleipool, Q. L., Rozemeijer, N. C., Veefkind, J. P., and Levelt, P. F.: In-flight performance of the Ozone Monitoring Instrument, Atmospheric Measurement Techniques, 10, 1957–1986, https://doi.org/10.5194/amt-10-1957-2017, 2017.

Schlüssel, P., Hultberg, T. H., Phillips, P. L., August, T., and Calbet, X.: The operational IASI Level 2 processor, Advances in Space Research, 36, 982–988, https://doi.org/10.1016/j.asr.2005.03.008, atmospheric Remote Sensing: Earths Surface, Troposphere, Stratosphere and Mesosphere- I, 2005.

Schneider, A., Borsdorff, T., aan de Brugh, J., Aemisegger, F., Feist, D. G., Kivi, R., Hase, F., Schneider, M., and Landgraf, J.: First data set of H_2O/HDO columns from the Tropospheric Monitoring Instrument (TROPOMI), Atmospheric Measurement Techniques, 13, 85–100, https://doi.org/10.5194/amt-13-85-2020, 2020.

Schneider, M. and Hase, F.: Optimal estimation of tropospheric H_2O and δD with IASI/METOP, Atmospheric Chemistry and Physics, 11, 11 207–11 220, https://doi.org/10.5194/acp-11-11207-2011, 2011.

Schneider, T.: The General Circulation of the Atmosphere, Annual Review of Earth and Planetary Sciences, 34, 655–688, https://doi.org/10.1146/annurev.earth.34.031405.125144, 2006.

Schneider, T., O'Gorman, P. A., and Levine, X. J.: WATER VAPOR AND THE DYNAMICS OF CLIMATE CHANGES, Reviews of Geophysics, 48, https://doi.org/10.1029/2009RG000302, 2010.

Schrijver, H., Gloudemans, A. M. S., Frankenberg, C., and Aben, I.: Water vapour total columns from SCIAMACHY spectra in the 2.36 µm window, Atmospheric Measurement Techniques, 2, 561–571, https://doi.org/10.5194/amt-2-561-2009, 2009.

Schröder, M., Lockhoff, M., Forsythe, J. M., Cronk, H. Q., Haar, T. H. V., and Bennartz, R.: The GEWEX Water Vapor Assessment: Results from Intercomparison, Trend, and Homogeneity Analysis of Total Column Water Vapor, Journal of Applied Meteorology and Climatology, 55, 1633 – 1649, https://doi.org/10.1175/JAMC-D-15-0304.1, 2016.

Schröder, M., Lockhoff, M., Fell, F., Forsythe, J., Trent, T., Bennartz, R., Borbas, E., Bosilovich, M. G., Castelli, E., Hersbach, H., Kachi, M., Kobayashi, S., Kursinski, E. R., Loyola, D., Mears, C., Preusker, R., Rossow, W. B., and Saha, S.: The GEWEX Water Vapor Assessment archive of water vapour products from satellite observations and reanalyses, Earth System Science Data, 10, 1093–1117, https://doi.org/10.5194/essd-10-1093-2018, 2018.

Schwendike, J., Govekar, P., Reeder, M. J., Wardle, R., Berry, G. J., and Jakob, C.: Local partitioning of the overturning circulation in the tropics and the connection to the Hadley and Walker circulations, Journal of Geophysical Research: Atmospheres, 119, 1322–1339, https://doi.org/10.1002/2013JD020742, 2014.

Schwendike, J., Berry, G. J., Reeder, M. J., Jakob, C., Govekar, P., and Wardle, R.: Trends in the local Hadley and local Walker circulations, Journal of Geophysical Research: Atmospheres, 120, 7599–7618, https://doi.org/10.1002/2014JD022652, 2015.

Seager, R., Naik, N., and Vecchi, G. A.: Thermodynamic and Dynamic Mechanisms for Large-Scale Changes in the Hydrological Cycle in Response to Global Warming, Journal of Climate, 23, 4651 – 4668, https://doi.org/10.1175/2010JCLI3655.1, 2010.

Seidel, D. J., Fu, Q., Randel, W. J., and Reichler, T. J.: Widening of the tropical belt in a changing climate, Nature Geoscience, 1, 21–24, https://doi.org/10.1038/ngeo.2007.38, 2008.

Seinfeld, J. H. and Pandis, S. N.: Atmospheric Chemistry and Physics: From Air Pollution to Climate Change, John Wiley & Sons, Hoboken, New Jersey, 3 edn., 2016.

Serdyuchenko, A., Gorshelev, V., Weber, M., Chehade, W., and Burrows, J. P.: High spectral resolution ozone absorption cross-sections – Part 2: Temperature dependence, Atmospheric Measurement Techniques, 7, 625–636, https://doi.org/10.5194/amt-7-625-2014, 2014.

Sharmila, S. and Walsh, K. J. E.: Recent poleward shift of tropical cyclone formation linked to Hadley cell expansion, Nature Climate Change, 8, 730–736, https://doi.org/10.1038/s41558-018-0227-5, 2018.

Sherwood, S. and Fu, Q.: A Drier Future?, Science, 343, 737–739, https://doi.org/10.1126/science.1247620, 2014.

Sherwood, S. C. and Huber, M.: An adaptability limit to climate change due to heat stress, Proceedings of the National Academy of Sciences, 107, 9552–9555, https://doi.org/10.1073/pnas.0913352107, 2010.

Sherwood, S. C., Roca, R., Weckwerth, T. M., and Andronova, N. G.: Tropospheric water vapor, convection, and climate, Reviews of Geophysics, 48, https://doi.org/10.1029/2009RG000301, 2010.

Siegel, A. F.: Robust regression using repeated medians, Biometrika, 69, 242–244, https://doi.org/10.1093/biomet/69.1.242, 1982.

Sihler, H., Beirle, S., Dörner, S., Gutenstein-Penning de Vries, M., Hörmann, C., Borger, C., Warnach, S., and Wagner, T.: MICRU: an effective cloud fraction algorithm designed for UV–vis satellite instruments with large viewing angles, Atmospheric Measurement Techniques, 14, 3989–4031, https://doi.org/10.5194/amt-14-3989-2021, 2021.

Simmons, A. J., Willett, K. M., Jones, P. D., Thorne, P. W., and Dee, D. P.: Low-frequency variations in surface atmospheric humidity, temperature, and precipitation: Inferences from reanalyses and monthly gridded observational data sets, Journal of Geophysical Research: Atmospheres, 115, https://doi.org/10.1029/2009JD012442, 2010.

Singh, H. K. A., Bitz, C. M., Donohoe, A., Nusbaumer, J., and Noone, D. C.: A Mathematical Framework for Analysis of Water Tracers. Part II: Understanding Large-Scale Perturbations in the Hydrological Cycle due to CO2 Doubling, Journal of Climate, 29, 6765 – 6782, https://doi.org/10.1175/JCLI-D-16-0293.1, 2016.

Smith, E. K. and Weintraub, S.: The Constants in the Equation for Atmospheric Refractive Index at Radio Frequencies, Proceedings of the IRE, 41, 1035–1037, https://doi.org/10.1109/JRPROC.1953.274297, 1953.

Sodemann, H.: Beyond Turnover Time: Constraining the Lifetime Distribution of Water Vapor from Simple and Complex Approaches, Journal of the Atmospheric Sciences, 77, 413 – 433, https://doi.org/10.1175/JAS-D-18-0336.1, 2020.

Sohn, B.-J. and Bennartz, R.: Contribution of water vapor to observational estimates of longwave cloud radiative forcing, Journal of Geophysical Research: Atmospheres, 113, https://doi.org/10.1029/2008JD010053, 2008.

Solomon, A., Polvani, L. M., Waugh, D. W., and Davis, S. M.: Contrasting upper and lower atmospheric metrics of tropical expansion in the Southern Hemisphere, Geophysical Research Letters, 43, 10,496–10,503, https://doi.org/10.1002/2016GL070917, 2016.

Staten, P. W., Lu, J., Grise, K. M., Davis, S. M., and Birner, T.: Re-examining tropical expansion, Nature Climate Change, 8, 768–775, https://doi.org/10.1038/s41558-018-0246-2, 2018.

Staten, P. W., Grise, K. M., Davis, S. M., Karnauskas, K., and Davis, N.: Regional Widening of Tropical Overturning: Forced Change, Natural Variability, and Recent Trends, Journal of Geophysical Research: Atmospheres, 124, 6104–6119, https://doi.org/10.1029/2018JD030100, 2019.

Staten, P. W., Grise, K. M., Davis, S. M., Karnauskas, K. B., Waugh, D. W., Maycock, A. C., Fu, Q., Cook, K., Adam, O., Simpson, I. R., Allen, R. J., Rosenlof, K., Chen, G., Ummenhofer, C. C., Quan, X.-W., Kossin, J. P., Davis, N. A., and Son, S.-W.: Tropical Widening: From Global Variations to Regional Impacts, Bulletin of the American Meteorological Society, 101, E897 – E904, https://doi.org/10.1175/BAMS-D-19-0047.1, 2020.

Steffensen, J. F.: Remarks on iteration., Scandinavian Actuarial Journal, 1933, 64–72, https://doi.org/10.1080/03461238.1933.10419209, 1933.

Stephens, G. L. and Ellis, T. D.: Controls of Global-Mean Precipitation Increases in Global Warming GCM Experiments, Journal of Climate, 21, 6141 – 6155, https://doi.org/10.1175/2008JCLI2144.1, 2008.

Stevens, B.: ATMOSPHERIC MOIST CONVECTION, Annual Review of Earth and Planetary Sciences, 33, 605–643, https://doi.org/10.1146/annurev.earth.33.092203.122658, 2005.

Stevens, B. and Bony, S.: What Are Climate Models Missing?, Science, 340, 1053–1054, https://doi.org/10.1126/science.1237554, 2013.

Studholme, J. and Gulev, S.: Concurrent Changes to Hadley Circulation and the Meridional Distribution of Tropical Cyclones, Journal of Climate, 31, 4367 – 4389, https://doi.org/10.1175/JCLI-D-17-0852.1, 2018.

Sulla-Menashe, D., Gray, J. M., Abercrombie, S. P., and Friedl, M. A.: Hierarchical mapping of annual global land cover 2001 to present: The MODIS Collection 6 Land Cover product, Remote Sensing of Environment, 222, 183 – 194, https://doi.org/10.1016/j.rse.2018.12.013, 2019.

Susskind, J., Barnet, C., and Blaisdell, J.: Retrieval of atmospheric and surface parameters from AIRS/AMSU/HSB data in the presence of clouds, IEEE Transactions on Geoscience and Remote Sensing, 41, 390–409, https://doi.org/10.1109/TGRS.2002.808236, 2003.

Thalman, R. and Volkamer, R.: Temperature dependent absorption cross-sections of O2-O2 collision pairs between 340 and 630 nm and at atmospherically relevant pressure, Phys. Chem. Chem. Phys., 15, 15 371–15 381, https://doi.org/10.1039/C3CP50968K, 2013.

Tilstra, L. G., Tuinder, O. N. E., Wang, P., and Stammes, P.: Surface reflectivity climatologies from UV to NIR determined from Earth observations by GOME-2 and SCIAMACHY, Journal of Geophysical Research: Atmospheres, 122, 4084–4111, https://doi.org/10.1002/2016JD025940, 2017.

Trenberth, K. E.: Atmospheric Moisture Residence Times and Cycling: Implications for Rainfall Rates and Climate Change, Climatic Change, 39, 667–694, https://doi.org/10.1023/A:1005319109110, 1998.

Trenberth, K. E.: Changes in precipitation with climate change, Climate Research, 47, 123–138, https://doi.org/10.3354/cr00953, 2011.

Trenberth, K. E. and Shea, D. J.: Relationships between precipitation and surface temperature, Geophysical Research Letters, 32, https://doi.org/10.1029/2005GL022760, 2005.

Trenberth, K. E. and Stepaniak, D. P.: Indices of El Niño Evolution, Journal of Climate, 14, 1697 – 1701, https://doi.org/10.1175/1520-0442(2001)014<1697:LIOENO>2.0.CO;2, 2001.

Trenberth, K. E., Fasullo, J., and Smith, L.: Trends and variability in column-integrated atmospheric water vapor, Climate Dynamics, 24, 741–758, https://doi.org/10.1007/s00382-005-0017-4, 2005.

Trenberth, K. E., Smith, L., Qian, T., Dai, A., and Fasullo, J.: Estimates of the Global Water Budget and Its Annual Cycle Using Observational and Model Data, Journal of Hydrometeorology, 8, 758 – 769, https://doi.org/10.1175/JHM600.1, 2007.

Trenberth, K. E., Fasullo, J. T., and Kiehl, J.: Earth's Global Energy Budget, Bulletin of the American Meteorological Society, 90, 311 – 324, https://doi.org/10.1175/2008BAMS2634.1, 2009.

van der Ent, R. J. and Tuinenburg, O. A.: The residence time of water in the atmosphere revisited, Hydrology and Earth System Sciences, 21, 779–790, https://doi.org/10.5194/hess-21-779-2017, 2017.

Van Geffen, J., Boersma, K., Eskes, H., Maasakkers, J., and Veefkind, J.: TROPOMI ATBD of the total and tropospheric NO2 data products, Tech. Rep. S5P-KNMI-L2-0005-RP, Royal Netherlands Meteorological Institute, https://sentinel.esa.int/documents/247904/2476257/Sentinel-5P-TROPOMI-ATBD-NO2-data-products, 2019.

van Geffen, J., Eskes, H., Compernolle, S., Pinardi, G., Verhoelst, T., Lambert, J.-C., Sneep, M., ter Linden, M., Ludewig, A., Boersma, K. F., and Veefkind, J. P.: Sentinel-5P TROPOMI NO_2 retrieval: impact of version v2.2 improvements and comparisons with OMI and ground-based data, Atmospheric Measurement Techniques, 15, 2037–2060, https://doi.org/10.5194/amt-15-2037-2022, 2022.

Vandaele, A., Hermans, C., Simon, P., Carleer, M., Colin, R., Fally, S., Merienne, M., Jenouvrier, A., and Coquart, B.: Measurements of the NO2 absorption cross-section from 42 000 cm- 1 to 10 000 cm- 1 (238–1000 nm) at 220 K and 294 K, Journal of Quantitative Spectroscopy and Radiative Transfer, 59, 171 – 184, https://doi.org/10.1016/S0022-4073(97)00168-4, atmospheric Spectroscopy Applications 96, 1998.

Veefkind, J., Aben, I., McMullan, K., Förster, H., de Vries, J., Otter, G., Claas, J., Eskes, H., de Haan, J., Kleipool, Q., van Weele, M., Hasekamp, O., Hoogeveen, R., Landgraf, J., Snel, R., Tol, P., Ingmann, P., Voors, R., Kruizinga, B., Vink, R., Visser, H., and Levelt, P.: TROPOMI on the ESA Sentinel-5 Precursor: A GMES mission for global observations of the atmospheric composition for climate, air quality and ozone layer applications, Remote Sensing of Environment, 120, 70–83, https://doi.org/10.1016/j.rse.2011.09.027, the Sentinel Missions - New Opportunities for Science, 2012.

Veefkind, J. P., de Haan, J. F., Sneep, M., and Levelt, P. F.: Improvements to the OMI O_2–O_2 operational cloud algorithm and comparisons with ground-based radar–lidar observations, Atmospheric Measurement Techniques, 9, 6035–6049, https://doi.org/10.5194/amt-9-6035-2016, 2016.

Ventura, V., Paciorek, C. J., and Risbey, J. S.: Controlling the Proportion of Falsely Rejected Hypotheses when Conducting Multiple Tests with Climatological Data, Journal of Climate, 17, 4343–4356, https://doi.org/10.1175/3199.1, 2004.

von Storch, H.: Misuses of Statistical Analysis in Climate Research, in: Analysis of Climate Variability, edited by von Storch, H. and Navarra, A., pp. 11–26, Springer Berlin Heidelberg, Berlin, Heidelberg, 1999.

Wagner, T., Heland, J., Zöger, M., and Platt, U.: A fast H_2O total column density product from GOME - Validation with in-situ aircraft measurements, Atmospheric Chemistry and Physics, 3, 651–663, https://doi.org/10.5194/acp-3-651-2003, 2003.

Wagner, T., Beirle, S., Grzegorski, M., and Platt, U.: Global trends (1996–2003) of total column precipitable water observed by Global Ozone Monitoring Experiment (GOME) on ERS-2 and their relation to near-surface temperature, Journal of Geophysical Research: Atmospheres, 111, https://doi.org/10.1029/2005JD006523, 2006.

Wagner, T., Beirle, S., Deutschmann, T., Grzegorski, M., and Platt, U.: Satellite monitoring of different vegetation types by differential optical absorption spectroscopy (DOAS) in the red spectral range, Atmospheric Chemistry and Physics, 7, 69–79, https://doi.org/10.5194/acp-7-69-2007, 2007.

Wagner, T., Beirle, S., and Deutschmann, T.: Three-dimensional simulation of the Ring effect in observations of scattered sun light using Monte Carlo radiative transfer models, Atmospheric Measurement Techniques, 2, 113–124, https://doi.org/10.5194/amt-2-113-2009, 2009.

Wagner, T., Beirle, S., Sihler, H., and Mies, K.: A feasibility study for the retrieval of the total column precipitable water vapour from satellite observations in the blue spectral range, Atmospheric Measurement Techniques, 6, 2593–2605, https://doi.org/10.5194/amt-6-2593-2013, 2013.

Wagner, T., Beirle, S., Dörner, S., Borger, C., and Van Malderen, R.: Identification of atmospheric and oceanic teleconnection patterns in a 20-year global data set of the atmospheric water vapour column measured from satellites in the visible spectral range, Atmospheric Chemistry and Physics, 21, 5315–5353, https://doi.org/10.5194/acp-21-5315-2021, 2021.

Wang, H., Liu, X., Chance, K., González Abad, G., and Chan Miller, C.: Water vapor retrieval from OMI visible spectra, Atmospheric Measurement Techniques, 7, 1901–1913, https://doi.org/10.5194/amt-7-1901-2014, 2014.

Wang, H., Souri, A. H., González Abad, G., Liu, X., and Chance, K.: Ozone Monitoring Instrument (OMI) Total Column Water Vapor version 4 validation and applications, Atmospheric Measurement Techniques, 12, 5183–5199, https://doi.org/10.5194/amt-12-5183-2019, 2019.

Wang, J., Dai, A., and Mears, C.: Global Water Vapor Trend from 1988 to 2011 and Its Diurnal Asymmetry Based on GPS, Radiosonde, and Microwave Satellite Measurements, Journal of Climate, 29, 5205 – 5222, https://doi.org/10.1175/JCLI-D-15-0485.1, 2016.

Wang, P., Stammes, P., van der A, R., Pinardi, G., and van Roozendael, M.: FRESCO+: an improved O_2 A-band cloud retrieval algorithm for tropospheric trace gas retrievals, Atmospheric Chemistry and Physics, 8, 6565–6576, https://doi.org/10.5194/acp-8-6565-2008, 2008.

Ware, R. H., Fulker, D. W., Stein, S. A., Anderson, D. N., Avery, S. K., Clark, R. D., Droegemeier, K. K., Kuettner, J. P., Minster, J. B., and Sorooshian, S.: SuomiNet: A real-time national GPS network for atmospheric research and education, Bulletin of the American Meteorological Society, 81, 677–694, https://doi.org/10.1175/1520-0477(2000)081<0677:SARNGN>2.3.CO;2, 2000.

Waugh, D. W., Grise, K. M., Seviour, W. J. M., Davis, S. M., Davis, N., Adam, O., Son, S.-W., Simpson, I. R., Staten, P. W., Maycock, A. C., Ummenhofer, C. C., Birner, T., and Ming, A.: Revisiting the Relationship among Metrics of Tropical Expansion, Journal of Climate, 31, 7565 – 7581, https://doi.org/10.1175/JCLI-D-18-0108.1, 2018.

Weatherhead, E. C., Reinsel, G. C., Tiao, G. C., Meng, X.-L., Choi, D., Cheang, W.-K., Keller, T., DeLuisi, J., Wuebbles, D. J., Kerr, J. B., Miller, A. J., Oltmans, S. J., and Frederick, J. E.: Factors affecting the detection of trends: Statistical considerations and applications to environmental data, Journal of Geophysical Research: Atmospheres, 103, 17 149–17 161, https://doi.org/10.1029/98JD00995, 1998.

Weaver, C. P. and Ramanathan, V.: Deductions from a simple climate model: Factors governing surface temperature and atmospheric thermal structure, Journal of Geophysical Research: Atmospheres, 100, 11 585–11 591, https://doi.org/10.1029/95JD00770, 1995.

Wendland, W. and Steinbach, O.: Analysis: Integral- und Differentialrechnung, gewöhnliche Differentialgleichungen, komplexe Funktionentheorie, Lehrbuch : Mathematik, Vieweg+Teubner Verlag, https://doi.org/10.1007/978-3-322-82962-7, 2005.

Wentz, F. J.: A well-calibrated ocean algorithm for special sensor microwave / imager, Journal of Geophysical Research: Oceans, 102, 8703–8718, https://doi.org/10.1029/96JC01751, 1997.

Wentz, F. J.: A 17-Yr Climate Record of Environmental Parameters Derived from the Tropical Rainfall Measuring Mission (TRMM) Microwave Imager, Journal of Climate, 28, 6882 – 6902, https://doi.org/10.1175/JCLI-D-15-0155.1, 2015.

Wessel, P. and Smith, W. H. F.: A global, self-consistent, hierarchical, high-resolution shoreline database, Journal of Geophysical Research: Solid Earth, 101, 8741–8743, https://doi.org/10.1029/96JB00104, 1996.

Wilks, D. S.: On "Field Significance" and the False Discovery Rate, Journal of Applied Meteorology and Climatology, 45, 1181 – 1189, https://doi.org/10.1175/JAM2404.1, 2006.

Wilks, D. S.: "The Stippling Shows Statistically Significant Grid Points": How Research Results are Routinely Overstated and Overinterpreted, and What to Do about It, Bulletin of the American Meteorological Society, 97, 2263 – 2273, https://doi.org/10.1175/BAMS-D-15-00267.1, 2016.

Wilks, D. S.: Statistical Methods in the Atmospheric Sciences, Elsevier, Amsterdam, 4 edn., https://doi.org/10.1016/C2017-0-03921-6, 2019.

Willett, K. M., Dunn, R. J. H., Thorne, P. W., Bell, S., de Podesta, M., Parker, D. E., Jones, P. D., and Williams Jr., C. N.: HadISDH land surface multi-variable humidity and temperature record for climate monitoring, Climate of the Past, 10, 1983–2006, https://doi.org/10.5194/cp-10-1983-2014, 2014.

Willett, K. M., Dunn, R. J. H., Kennedy, J. J., and Berry, D. I.: Development of the HadISDH.marine humidity climate monitoring dataset, Earth System Science Data, 12, 2853–2880, https://doi.org/10.5194/essd-12-2853-2020, 2020.

Xue, Y., Li, J., Menzel, W. P., Borbas, E., Ho, S.-P., Li, Z., and Li, J.: Characteristics of Satellite Sampling Errors in Total Precipitable Water from SSMIS, HIRS, and COSMIC Observations, Journal of Geophysical Research: Atmospheres, 124, 6966–6981, https://doi.org/10.1029/2018JD030045, 2019.

Zhang, Y., Wallace, J. M., and Battisti, D. S.: ENSO-like Interdecadal Variability: 190093, Journal of Climate, 10, 1004 – 1020, https://doi.org/10.1175/1520-0442(1997)010<1004:ELIV>2.0.CO;2, 1997.

Zoogman, P., Liu, X., Suleiman, R., Pennington, W., Flittner, D., Al-Saadi, J., Hilton, B., Nicks, D., Newchurch, M., Carr, J., Janz, S., Andraschko, M., Arola, A., Baker, B., Canova, B., Miller, C. C., Cohen, R., Davis, J., Dussault, M., Edwards, D., Fishman, J., Ghulam, A., Abad, G. G., Grutter, M., Herman, J., Houck, J., Jacob, D., Joiner, J., Kerridge, B., Kim, J., Krotkov, N., Lamsal, L., Li, C., Lindfors, A., Martin, R., McElroy, C., McLinden, C., Natraj, V., Neil, D., Nowlan, C., O'Sullivan, E., Palmer, P., Pierce, R., Pippin, M., Saiz-Lopez, A., Spurr, R., Szykman, J., Torres, O., Veefkind, J., Veihelmann, B., Wang, H., Wang, J., and Chance, K.: Tropospheric emissions: Monitoring of pollution (TEMPO), Journal of Quantitative Spectroscopy and Radiative Transfer, 186, 17–39, https://doi.org/10.1016/j.jqsrt.2016.05.008, satellite Remote Sensing and Spectroscopy: Joint ACE-Odin Meeting, October 2015, 2017.

Authorships in peer review publications

Peer review publications as lead author

Borger, C., Beirle, S., Dörner, S., Sihler, H., and Wagner, T.: Total column water vapour retrieval from S-5P/TROPOMI in the visible blue spectral range, Atmospheric Measurement Techniques, 13, 2751–2783, https://doi.org/10.5194/amt-13-2751-2020, 2020.

Borger, C., Beirle, S., and Wagner, T.: A 16-year global climate data record of total column water vapour generated from OMI observations in the visible blue spectral range, Earth System Science Data Discussions, 2021, 1–25, https://doi.org/10.5194/essd-2021-319, 2021.

Borger, C., Beirle, S., and Wagner, T.: Analysis of global trends of total column water vapour from multiple years of OMI observations, Atmospheric Chemistry and Physics, 22, 10 603–10 621, https://doi.org/10.5194/acp-22-10603-2022, 2022.

Peer review publications as co-author

Beirle, S., **Borger, C.**, Dörner, S., Li, A., Hu, Z., Liu, F., Wang, Y., and Wagner, T.: Pinpointing nitrogen oxide emissions from space, Science Advances, 5, eaax9800, https://doi.org/10.1126/sciadv.aax9800, 2019.

Beirle, S., **Borger, C.**, Dörner, S., Eskes, H., Kumar, V., de Laat, A., and Wagner, T.: Catalog of NO_x emissions from point sources as derived from the divergence of the NO_2 flux for TROPOMI, Earth System Science Data, 13, 2995–3012, https://doi.org/10.5194/essd-13-2995-2021, 2021.

Beirle, S., **Borger, C.**, Dörner, S., Kumar, V., and Wagner, T.: Calculating the vertical column density of O_4 during daytime from surface values of pressure, temperature, and relative humidity, Atmospheric Measurement Techniques, 15, 987–1006, https://doi.org/10.5194/amt-15-987-2022, 2022.

Herrmann, M., Schöne, M., **Borger, C.**, Warnach, S., Wagner, T., Platt, U., and Gutheil, E.: Ozone depletion events in the Arctic spring of 2019: a new modeling approach to bromine emissions, Atmospheric Chemistry and Physics, 22, 13 495–13 526, https://doi.org/10.5194/acp-22-13495-2022, 2022.

Küchler, T., Noël, S., Bovensmann, H., Burrows, J. P., Wagner, T., **Borger, C.**, Borsdorff, T., and Schneider, A.: Total water vapour columns derived from Sentinel 5P using the AMC-DOAS method, Atmospheric Measurement Techniques, 15, 297–320, https://doi.org/10.5194/amt-15-297-2022, 2022.

Lange, K., Richter, A., Schönhardt, A., Meier, A. C., Bösch, T., Seyler, A., Krause, K., Behrens, L. K., Wittrock, F., Merlaud, A., Tack, F., Fayt, C., Friedrich, M. M., Dimitropoulou, E., Van Roozendael, M., Kumar, V., Donner, S., Dörner, S., Lauster, B., Razi, M., **Borger, C.**, Uhlmannsiek, K., Wagner, T., Ruhtz, T., Eskes, H., Bohn, B., Santana Diaz, D., Abuhassan, N., Schüttemeyer, D., and Burrows, J. P.: Validation of Sentinel-5P TROPOMI tropospheric NO_2 products by comparison with NO_2 measurements from airborne imaging, ground-based stationary, and mobile car DOAS measurements during the S5P-VAL-DE-Ruhr campaign, Atmospheric Measurement Techniques Discussions, 2022, 1–45, https://doi.org/10.5194/amt-2022-264, 2022.

Pukite, J., **Borger, C.**, Dörner, S., Gu, M., Frieß, U., Meier, A. C., Enell, C.-F., Raffalski, U., Richter, A., and Wagner, T.: Retrieval algorithm for OClO from TROPOMI (TROPOspheric Monitoring Instrument) by differential optical absorption spectroscopy, Atmospheric Measurement Techniques, 14, 7595–7625, https://doi.org/10.5194/amt-14-7595-2021, 2021.

Pukite, J., **Borger, C.**, Dörner, S., Gu, M., and Wagner, T.: OClO as observed by TROPOMI: a comparison with meteorological parameters and polar stratospheric cloud observations, Atmospheric Chemistry and Physics, 22, 245–272, https://doi.org/10.5194/acp-22-245-2022, 2022.

Sihler, H., Beirle, S., Dörner, S., Gutenstein-Penning de Vries, M., Hörmann, C., **Borger, C.**, Warnach, S., and Wagner, T.: MICRU: an effective cloud fraction algorithm designed for UV–vis satellite instruments with large viewing angles, Atmospheric Measurement Techniques, 14, 3989–4031, https://doi.org/10.5194/amt-14-3989-2021, 2021.

Wagner, T., Beirle, S., Dörner, S., **Borger, C.**, and Van Malderen, R.: Identification of atmospheric and oceanic teleconnection patterns in a 20-year global data set of the atmospheric water vapour column measured from satellites in the visible spectral range, Atmospheric Chemistry and Physics, 21, 5315–5353, https://doi.org/10.5194/acp-21-5315-2021, 2021.

Acknowledgements – Danksagung